earthsciences.nz

Regional landslide-debris-inundation analysis for West Coast Emergency Management

KJ Leith
CI Massey
SJ de Vilder
B Lukovic

GNS Science Consultancy Report 2025/28
October 2025

Earth Sciences New Zealand

DISCLAIMER

Use of Data:

Date that Earth Sciences New Zealand can use associated data: October 2025

BIBLIOGRAPHIC REFERENCE

Leith KJ, de Vilder SJ, Massey CI, Lukovic B. 2025. Regional landslide-debris-inundation analysis for West Coast Emergency Management. Lower Hutt (NZ): Earth Sciences New Zealand. 152 p. GNS Science Consultancy Report 2025/28. Prepared for West Coast Emergency Management.

CONTENTS

FIGURES

TABLES

APPENDICES

APPENDIX FIGURES

APPENDIX TABLES

EXECUTIVE SUMMARY

West Coast Regional Council (on behalf of West Coast Emergency Management Group [WCEM], formerly known as West Coast Civil Defence & Emergency Management Group) commissioned GNS Science – now a business unit of Earth Sciences New Zealand – to identify areas overseen by WCEM that could potentially be affected by landslides generated by earthquakes and/or rainfall and so potentially present a risk to property and life.

Earth Sciences New Zealand has carried out a regional-scale basic quantitative landslide-debris-inundation hazard and risk analysis for the region overseen by WCEM. The project has been undertaken in two phases, as outlined in GNS Science Proposal Q31872684 (2 March 2022). Stage 1 of this project identified landslide-debris-inundation hazard-footprint areas (outlined in Leith and de Vilder [2022]), while Stage 2 integrated the models developed in Stage 1 with probabilistic models of landslide initiation and runout in order to evaluate annual building loss risks associated with earthquake- and rainfall-induced landslide-debris-inundation events. This study has benefitted from model development and data derived from the Ministry of Business, Innovation & Employment (MBIE)-funded GNS Science Extreme Weather Strategic Science Investment Fund (SSIF) uplift following the impacts of Cyclone Gabrielle (Leith et al., in prep.).

The landslide hazard metrics adopted in this study are landslide-debris flux and probability of inundation (P_i).

- **Landslide-debris flux** quantifies the average volume of landslide debris that can be expected to pass a given location either in a given year or, alternatively, in response to a given earthquake or rainfall scenario. A value of 1 indicates that an average of 1 m^3 of landslide debris can be expected to pass through ('inundate') each square metre of land either per year or in response to a given scenario.
- $\boldsymbol{P_i}$ quantifies the probability of debris from any size of landslide passing a given location in a given year. A value of 1 indicates that an unspecified volume of landslide debris can be expected to pass through ('inundate') a given location on an annual basis.

We use Annual Property Loss Risk (APLR), derived from the landslide-debris-flux hazard, to demonstrate present-day risk from landslide-debris inundation and how this may change under a future climate scenario.

- **APLR** represents the annual probability that landslide debris will damage a generic ('undifferentiated') building beyond economic repair. A value of 1 indicates that landslide debris can be expected to cause total damage to a hypothetical building at a given location on an annual basis.

The methods used to estimate landslide-debris flux, P_i and APLR are based on assessing both the probability of debris being generated at a given location and its potential to inundate downslope areas when transported as part of a landslide. This represents a new methodology in which the landslide hazard calculation is based on an assessment of the processes that generate landslide debris and transport it through the landscape. This differs from more traditional scenario-based landslide-hazard modelling approaches in which the probability of inundation is most commonly assessed with respect to a given number of discrete hypothetical landslide sources and runout paths.

This new hazard assessment method provides a more spatially comprehensive quantitative analysis of regional landslide-debris-inundation hazard and ensures that calculated volume and probability of inundation is constrained by probable rates of geomorphological and geological processes. The methodology, where appropriate, follows applicable parts of the Landslide Risk Management Guidelines (AGS 2007).

The level of detail of the analysis is similar to a 'Level D' basic quantitative hazard and risk analysis, as outlined in Table 4.2 of the Landslide Planning Guidance (de Vilder et al. 2024), although we employ a novel method to calculate hazard. Due to uncertainties in input data, as well as the adopted resolution of the analysis, the outputs are primarily suitable for screening purposes (equivalent to the 'Level A' or 'Level B' analyses described in de Vilder et al. [2024]). In order to ensure homogeneity in the outputs, this regional-scale analysis employs spatially consistent datasets and has been undertaken at a nominal resolution of 25 m. Residual uncertainties vary spatially, and we recommend adopting an uncertainty level of at least ±1.25 orders of magnitude when evaluating hazard and risk outputs under present-day climate conditions and of ±2.75 orders of magnitude for future Representative Concentration Pathway (RCP) 6 (2018–2100) climate conditions.

In areas where the level of hazard or risk exceeds tolerance thresholds determined for given activities, more detailed analysis may be necessary to provide sufficient certainty for decision-making.

The conclusions of this study are that:

1. Landslide-debris-inundation hazard and risk are highest close to steeper slopes, within channels and gullies and on debris fans. Regionally, hazards are greatest in areas where rates of annual landslide-debris production are most rapid.
2. The main contributor to landslide hazard is rainfall-induced landsliding along range-front areas and earthquake-induced landsliding in areas to the northeast of Greymouth. This reflects the main triggering factor of landsliding in each setting.
3. APLR at the location of existing buildings is greatest for debris flows, debris avalanches and rock avalanches (considered here as 'flow'-type landslide movements), while relatively few buildings are exposed to inundation by debris slides ('avalanche'-type movements). This reflects the greater reach of debris resulting from flow-type movements, as well as historical urban planning that may have limited development in areas prone to less mobile landslides .
4. 95% of APLR is carried by approximately 2% of existing residential buildings in the region overseen by WCEM.
5. The susceptibility of hill slopes to landsliding in response to RCP6 2081–2100 climate-change conditions is expected to increase APLR to existing residential buildings by at least 50%.
6. Residual uncertainties are spatially variable and increase with increasing distance from landslide sources. These are particularly large in areas adjacent to small-scale topography with spatial extents less than 100,000 m^2, which is poorly represented in the national digital elevation model (DEM).
7. In order of impact on calculated APLR, the largest uncertainties in this analysis result from constraints on:
    a. The accuracy of the national DEM (LINZ 2014) employed in this study.
    b. The relatively low resolution (25 m) of the landslide-debris-inundation analysis.
    c. The volume of sediment available to develop into landslides each year. This is particularly poorly understood in the future climate-scenario models.
8. Replacing the national DEM with a Light Detecting and Ranging (LiDAR)-derived DEM (LINZ 2022) can reduce residual uncertainties to ±0.75 orders of magnitude.

A guide to applying these results, including references to relevant previous examples and a list of recommended next steps, is provided in Section 5. We recommend that further engineering geological / geotechnical engineer, risk and land-use planning advice is sought in relation to specific applications of the analysis presented in this report.

We suggest that land-use planning documents referring to the results of this study should include provisions whereby site-specific information for a site/dwelling could be used to re-evaluate the landslide risk, thus allowing the given site to be re-classified. This may include the utilisation of more accurate, or higher-resolution, topographic data; collection of site-specific hazard information; incorporation of more detailed landslide-debris-inundation models; and/or re-evaluation of the vulnerability of affected structures.

Application of Results for Planning Purposes

Key Metrics

- **Landslide-debris flux** (m^3/m^2/year): Volume of debris expected to pass through a location annually.
- **Probability of inundation (P_i)** (1/year): Likelihood that debris reaches a location in a given year.
- **Annual Property Loss Risk (APLR)** (loss/year): Probability that a generic building at a location will be damaged beyond economic repair annually.

Risk-Tolerance Thresholds

- A risk-tolerance threshold for acceptability of **APLR = 1×10^{-5}/year** (1 in 100,000) is recommended as a starting point for existing risks.
- Thresholds may vary depending on activity type, societal norms and planning level.

Uncertainty Interpretation

- Adopt uncertainties consistent with the **1-sigma** (standard deviation) (84th percentile) confidence interval.
- **Present-day climate:** APLR uncertainty at 1-sigma is **±1.25 orders of magnitude**.
- **RCP6 2081–2100 climate scenario:** APLR uncertainty at 1-sigma is **±2.75 orders of magnitude**.

Practical Implication

- When applying a risk tolerance threshold, uncertainty must be included.
  For example, if the threshold is **1×10^{-5}/year** and uncertainty is **±1.25 orders of magnitude**, then any location with **APLR less than 5.6×10^{-7}/year** is statistically unlikely to exceed the threshold.
- This means that locations with APLR values below the threshold adjusted for uncertainty can be considered as having **Acceptable Risk** under the current planning framework.

Use of Results for Planning Purposes (refer to Table 5.1).

- Residual uncertainties limit the application of outputs for specific planning activities (see Table 5.2).
- Raster datasets should be presented at a maximum zoom of **1:500,000** for publicly facing GIS applications and/or down-sampled to a minimum pixel size of **150 m**.
- Current outputs are suitable for **Level A screening** and possibly **Level B** planning purposes.
- Reducing uncertainty by using new LiDAR data may make outputs suitable for **Level B–C** applications.
- Outputs are not suitable for planning applications considered for **Level D** assessments without site-specific refinement.
- Where risk exceeds thresholds or uncertainty is high, further analysis should:
  - Re-evaluate using higher-resolution data (e.g. 8 m LiDAR).
  - Incorporate local geotechnical and hazard information.
  - Re-classify sites based on refined risk metrics.

Refer to **Section 5.3.3.2** for the decision-making framework and **Sections 5.4** and **5.5** for recommended next steps and re-evaluation procedures.

1.0 Introduction

West Coast Regional Council (on behalf of West Coast Emergency Management Group [WCEM], formerly known as West Coast Civil Defence & Emergency Management) commissioned GNS Science – now a business unit of Earth Sciences New Zealand – to identify areas overseen by WCEM (Figure 1.1) that could potentially be affected by landslides generated by earthquakes and/or rainfall and so potentially present a risk to property and life. This report accompanies data deliverables resulting from completion of the West Coast landslide-debris-Inundation assessment (contract no. Q31872684). This provides a probabilistic assessment of 'debris flow', 'debris slide', 'debris avalanche' and 'rock avalanche' hazards, as well as associated landslide-debris-inundation risk to buildings. This report describes the modelling and hazard assessment methodologies, an overview of the results and a discussion of these in the context of regional landslide-debris-inundation risk to buildings. In addition, we provide guidance with respect to the application of hazard- and risk-model results for regional land-use planning applications. This study has benefitted from model development and data derived from the Ministry of Business, Innovation & Employment (MBIE)-funded GNS Science Extreme Weather Strategic Science Investment Fund (SSIF) uplift following the impacts of Cyclone Gabrielle (Leith et al., in prep.).

It is our understanding that the results from this project may inform future Te Tai o Poutini Plan (One Plan) Change processes, as well as response and recovery plans for future severe weather events, major earthquakes and cascading hazard events. These outputs will provide a basis for determining critical, or high-risk, areas that may require further local or site-specific analysis.

The scope of work and study area were outlined in GNS Science proposal Q31872684, which was approved by WCEM on 31 March 2022.

It was agreed that this work be carried out in two stages:

- **Stage 1:** Generate models of landslide susceptibility and associated debris runout in order to identify the potential footprint of landslide-debris-inundation hazards across the region. These were essential inputs for Stage 2, although high uncertainties mean that these are not suitable for planning purposes. Outcomes of Stage 1 are outlined in Leith and de Vilder (2022).
- **Stage 2:** Integrate models generated in Stage 1 with probabilistic models of landslide initiation and debris runout in order to describe the probability of landslide debris inundation and associated risks across the region (preliminary outputs were provided to WCEM in a letter report [Leith 2024]).

Earth Sciences New Zealand has carried out a regional-scale basic quantitative landslide-debris-inundation hazard and risk analysis for the region overseen by WCEM, as shown in Figure 1.1.

The object of this study is to inform WCEM of the spatial distribution of potential landslide-debris-inundation hazards and associated risk to buildings across the region.

1.1 Methodology Overview

Assessing landslide-debris-inundation hazards over the vast expanse of the region overseen by WCEM (approximately 25,000 km^2) requires innovative approaches due to the computational demands of modelling such events at a regional scale. This regional-scale analysis utilises the relevant datasets that are consistently available across the entire West Coast region.

To address this, Earth Sciences New Zealand has developed a new 'process-based' methodology that combines geomorphological process rates with established hazard- and risk-estimation techniques.

Within the framework of a traditional event-based quantitative landslide hazard and risk analysis, landslide hazard and risk are typically assessed using a scenario-based methodology. In this approach, a finite number of hypothetical landslides are defined with specific source areas and volumes, and runout models are applied to simulate the resulting inundation footprints. These scenario footprints are then linked to the estimated frequency of landslides of corresponding size in order to calculate the probability of impact at a given location (e.g. Massey et al. 2021b).

In contrast, the process-based methodology developed here derives the probability of inundation events without relying on a limited set of scenarios. Instead, it models the continuous production of landslide debris through time, then simulates the movement of debris downslope (the ‘flux’) by assigning rules consistent with a range of different landslide types. Hazard is expressed in terms of debris flux (volume per unit area per year) and probability of inundation, providing a spatially comprehensive assessment without the requirement to consider discrete landslide footprints.

In the process-based methodology, the magnitude and frequency of landslide hazards are regulated by debris-production rates, informed by the rate of geomorphic processes (e.g. tectonic uplift, erosion), landslide inventories and a geotechnical landslide source model. Spatial impact is calculated with empirical and physically based debris-transport models, using conventional approaches to derive model inputs from international datasets and landslide behaviours in the study area. We employ a deterministic model of characteristic landslide-debris flux to convert the spatial hazard output to a magnitude-frequency relationship for landslide-debris inundation. When, for example, the annual debris flux at a location equals the characteristic debris flux, we expect to observe landslide events passing that location on an annual basis.

For example, if landslide-debris flux indicates that landsliding from hill slopes will result in an average of 0.3 m^3 of debris passing a given downslope location annually, and the characteristic inundation volume at that location is 30 m^3, the annual probability of debris inundation would be 0.01, or 1%. This approach shifts the focus from assigning uniform probabilities to discrete landslide runout paths and allows a regionally consistent assessment of spatially variable landslide-debris-inundation hazard and risk throughout the study region.

Although the new approach employed here sacrifices a degree of accuracy in terms of reproducing dynamic aspects of individual runout events, it has several advantages over standard methods to estimate landslide risk:

- Landslide runout is simulated from every potential source location over a wide spatial area.
- Minimum landslide size can be smaller than the modelled grid resolution.
- Landslide-debris-inundation hazard and risk scales directly with the potential number of landslides passing a given location.
- Calculation of potential hazard and risk incorporates a combination of short-term observational data and long-term geological data, reducing reliance on invariably incomplete landslide records.
- Algorithms are computationally efficient, allowing for large areas to be modelled at one time.

The following tasks were undertaken during this project:

1. Collate reference datasets required to undertake a regional landslide-susceptibility assessment (Stage 1.1), regional debris-runout assessment (Stage 1.2), regional assessment of landslide probability (Stage 2.1) and regional assessment of debris-inundation probability (Stage 2.2).
2. Develop earthquake- and rainfall-induced landslide susceptibility models based on the methods presented in Massey et al. (2021a) and Rosser et al. (2021).
3. Derive landslide frequency-volume relationships for earthquake- and rainfall-induced landslide catalogues in the study region.

4. Determine an appropriate landslide-debris-production model for the study region.
5. Develop geospatial landslide-hazard models based on local susceptibility, frequency-volume and debris-production estimates.
6. Develop geospatial landslide-risk models based on landslide-hazard model results and appropriate vulnerability datasets.
7. Carry out field validation of the regional hazard- and risk-analysis results.
8. Provide guidance on the adoption of hazard- and risk-analysis results for regional land-use planning purposes.

Where applicable, the methods employed here follow appropriate parts of the Australian Geomechanics Society framework for landslide risk management (AGS 2007); see Appendix 8.

Three primary metrics are employed to describe landslide-debris-inundation hazard and risk:

- **Hazard magnitudes** are described using the metric of landslide debris flux. This is expressed as the average volume of debris that can be expected to pass through one square metre of land, either on an annual basis (considering a full year) or for a specific trigger scenario (such as heavy rainfall or an earthquake). Landslide-debris-inundation hazard magnitudes are measured in m^3/m^2/year for annualised outputs or m^3/m^2/event for scenario-based outputs.
- **Hazard frequencies** are described using the metric of probability of inundation (P_i). This is expressed as the probability that any volume of landslide debris will pass through a location, either on an annual basis (considering a full year) or for a specific trigger scenario (such as heavy rainfall or an earthquake). Landslide-debris-inundation hazard frequencies are measured by 1/year for annualised outputs or 1/event for scenario-based outputs.
- **Risks** are described using the metric of Annual Property Loss Risk (APLR), which is expressed as the probability that a generic hypothetical building present at a particular location will sustain damage such that the re-instatement cost exceeds the replacement value (Massey et al. 2019). Landslide-debris-inundation risks are measured by loss/year for annualised outputs or loss/event for scenario-based outputs, where 100% loss indicates that the re-instatement cost of a building footprint within the cell exceeds its replacement value.

This study does not include any assessment of hazards associated with river-related (fluvial) erosion or flooding, tsunami, rockfall, ground deformation as a result of slow-moving landslides or slippage, or earthquake rupture.

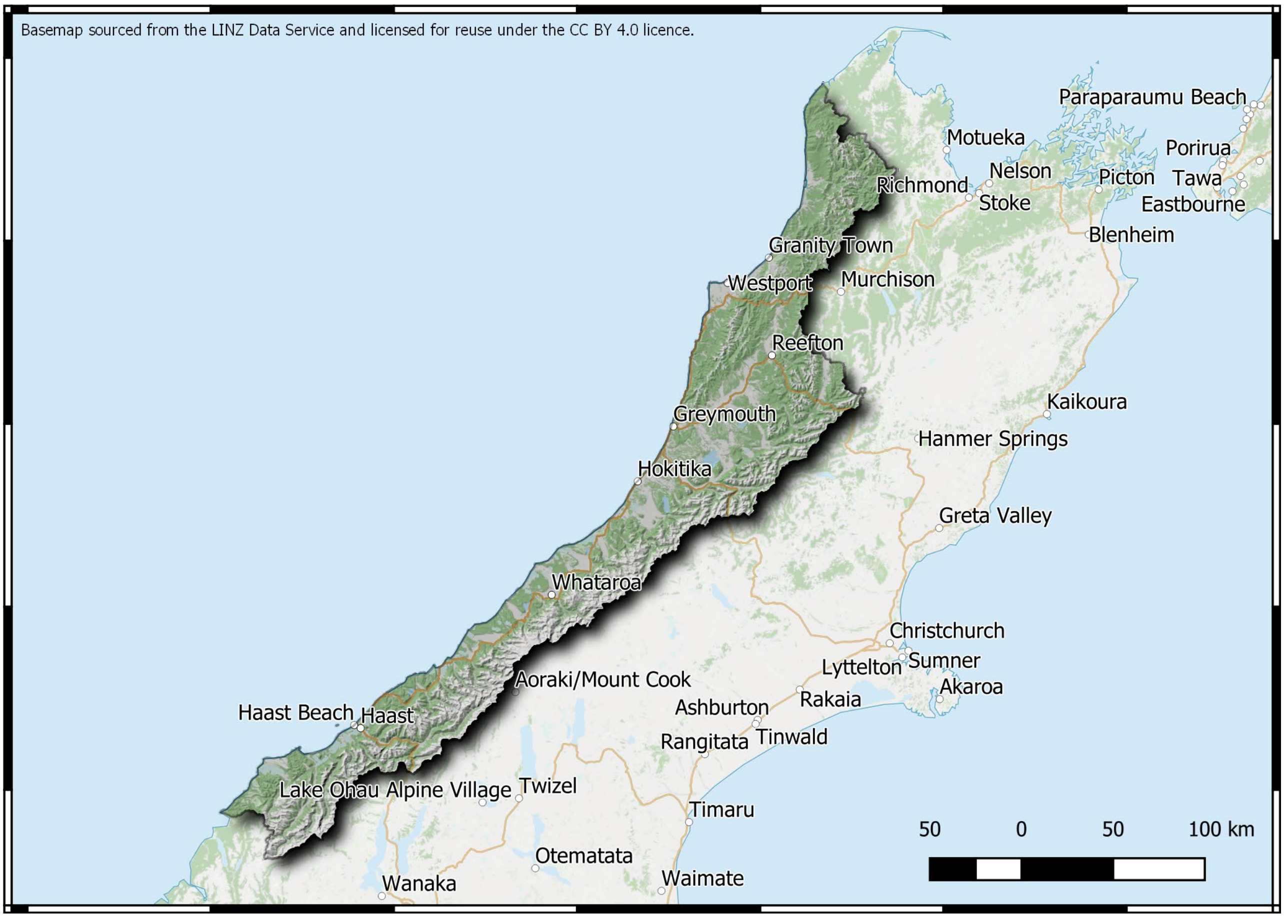

Figure 1.1 Overview of the project area.

1.2 Report Structure

This report has been structured into six sections:

1. Introduction:
   - Project background
   - Overview of landslide hazards
2. Landslide-debris-inundation modelling methodology:
   - Conceptual overview of the modelling method
   - Determination of landslide source susceptibility
   - Calculation of landslide sediment production
   - Landslide-debris-runout modelling
   - Calculation of risk to buildings
3. Discussion:
   - Consistency with actual experience
   - Sensitivity to key uncertainties
4. Description of project deliverables:
   - Landslide-hazard deliverables
   - Landslide-risk deliverables.
5. Applying these results:

- Applications for landslide-hazard data
- Applications for landslide-risk data
- Recommended next steps

6. Summary and conclusions.

Sections 1–5 of the report provide a high-level overview of the landslide-debris-inundation hazard methodology. Detailed descriptions of input data and the methodology employed can be found in Appendices 1–7.

1.3 Personnel

This report has been prepared by Kerry Leith, Saskia de Vilder, Chris Massey and Biljana Lukovic (Earth Sciences New Zealand). The risk calculations and calculation route were reviewed by Sally Dellow (Earth Sciences New Zealand). This report was independently reviewed by Dr Feiko van Zadelhoff and Dr Andrew Neverman (Manaaki Whenua – Landcare Research; see Appendix 9 for review and responses). Kerry Leith and Sam McColl visited study areas during 10–12 August 2023 to carry out field-validation surveys of the risk models and input data and to meet with West Coast Regional Council staff to discuss the results and input variables to be used in the hazard and risk model.

1.4 Landslide Hazards

1.4.1 Terminology

Landslides are defined as the movement of rock, soil or debris downslope (Evans 2001). A landslide hazard is defined as a landslide that has the potential to cause an undesirable outcome. A landslide-hazard assessment provides a quantitative measure of the probability of a hazardous landslide occurring within a defined time period and area (Corominas et al. 2023). Landslide hazards (as defined in the Building Act 2004) can be divided into two broad categories:

1. ‘Slippage’, which includes the movement or loss (including partial loss) of land from a slope when this occurs beneath a structure (e.g. dwelling, garage, road, shed).
2. ‘Falling debris’, which includes soil, rock, vegetation, snow or ice that may fall and ‘runout’ onto a property (e.g. dwelling, garage, shed and/or land) from up-slope (the landslide source area), inundating the property.

In this project, we assess landslide hazards associated with falling debris, as defined in the Building Act 2004. The ‘landslide-debris-inundation area’ refers to the runout path that is inundated by soil and/or rock, which includes the debris source, transport and deposit zones (Figure 1.2).

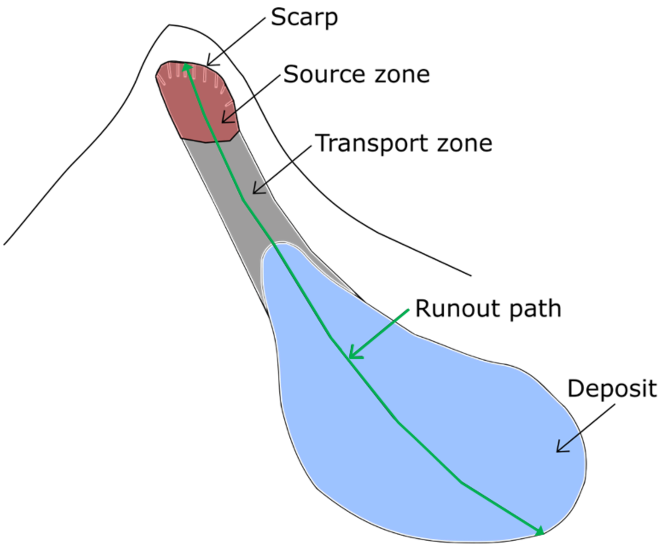

Figure 1.2 Schematic representation of the source and debris-inundation areas (source, transport and deposit zones) of a landslide. Illustration modified from Mitchell et al. (2020).

1.4.2 Landslide Types Assessed and Associated Definitions

Evaluating the hazards associated with landslide debris inundation requires an understanding of the types of landslide that may occur at a given location. The typical behaviour of each type of landslide (e.g. velocity of displacement, re-occurrence, travel distance) will affect both the extent of areas impacted and the nature of that impact. Based on the classification by Hungr et al. (2014), the rapidly moving landslide types to be assessed in this project are: (1) debris flows, (2) debris avalanches and (3) rock avalanches. These rapidly moving landslides present a threat to life and property, with the speed of movement of the landslide limiting the ability for evasion and evacuation to occur. Inundation by slow-moving landslides or rockfall events is not assessed as part of this study.

1.4.2.1 Debris Flows

Debris flows can be defined as a "very rapid to extremely rapid surging flow of saturated debris in a steep channel" (Hungr et al. 2014). Entrainment of material and water from the flow path can occur along the runout path. Debris flows often occur simultaneously with floods. The debris flow may be initiated by a debris slide, debris avalanche or rockfall from a steep bank, or by spontaneous instability of the steep stream bed. The sediment concentration of debris flows exceeds 40% (typically 50–70%), and their volume can be up to 1,000,000,000 m^3 (Iverson et al. 2011). Figure 1.3 shows the result of a mobile channelised debris flow.

Once saturated material begins to move in a steep channel, the volume of a debris flow can change due to entrainment (Iverson et al. 2011). Entrainment results from scour of channel-bed sediment or collapse of stream banks. The bulk of the material involved in a debris-flow event can sometimes originate from entrainment within the runout path. Changes in debris-flow volume and momentum due to entrainment have the potential to influence the debris-flow velocity and travel distance (Iverson et al. 2011).

Following Hungr et al. (2014), 'debris flow' refers exclusively to a channelised landslide, whereas a landslide consisting of flowing debris on an open slope is referred to as a 'debris avalanche'. It is possible that debris flows become debris avalanches (Section 1.4.2.4) if the channel these flow down becomes less confined, and, conversely, a debris avalanche may become debris flows if the debris enters a channel. Where the long-term rate of debris-flow sediment deposition outpaces the rate of long-term sediment transport, the deposits from multiple debris flows form debris fans. Debris fans provide geomorphic evidence of the extent of debris-flow hazards.

Figure 1.3 Debris flows generated by rain in Eastbourne, Wellington, in November 2006. The source areas of the debris flows are in the left of the photograph. The debris travelled down-slope several hundreds of metres, where it impacted the dwellings shown in the right of the photograph. Photograph by G Hancox, GNS Science.

1.4.2.2 Fan

Fans are cone-shaped landforms that are generated when confined watercourses (e.g. gullies, creeks, rivers) become wider and the water-course less confined, for example, when water-courses enter valleys, plains or lakes. The resulting decrease in flow velocity promotes sediment deposition. The dynamic nature of such landforms poses a hazard to people and infrastructure located on these, as areas that were inactive (and have since been built on) can re-activate and start actively eroding or receiving sediments. Davies and McSaveney (2008) have discussed some of the considerations for sustainable development on fans. They also discussed that fans can be divided into two end-members: (1) alluvial fan – dominated by deposition of sediment from fluvial processes; and (2) debris-flow fan – dominated by deposition of sediment from debris flows and debris floods.

1.4.2.3 Debris Slides

A debris slide is defined by Hungr et al. (2014) as:

> *"sliding of a mass of granular material on a shallow, planar surface parallel with the ground. Usually, the sliding mass is a veneer of colluvium, weathered soil, or pyroclastic deposits sliding over a stronger substrate. Many debris slides become flow-like after moving a short distance and transform into extremely rapid debris avalanches."*

Debris slides are not analysed separately in this project, and this definition is only provided to describe the initial stage of a debris avalanche (Section 1.4.2.4).

1.4.2.4 Debris Avalanches

A debris avalanche is defined by Hungr et al. (2014) as a "very rapid to extremely rapid shallow flow of partially or fully saturated debris on a steep slope, without confinement in an established channel". Hungr et al. (2014) also describe debris avalanches as initiating as debris slides (Section 1.4.2.3) and are associated with failures of residual soil, colluvial, pyroclastic or organic veneer.

The important distinction between debris avalanches and rockfalls is that the latter comprise individual fragments, which move as independent rigid bodies interacting with the substrate by means of episodic impacts. By contrast, debris avalanches move in a flow-like manner as masses of interacting fragments and water. Figure 1.4 provides examples of debris avalanches from the West Coast region.

Figure 1.4 Debris avalanches on Whataroa Highway generated by the 2019 West Coast storm. Photograph by D Townsend, Earth Sciences New Zealand.

1.4.2.5 Rock Avalanches

A rock avalanche is defined by Hungr et al. (2014) as:

> *"an extremely rapid (>5 m/s), massive, flow-like motion of fragmented rock from a large rock slide or rock fall. Large rock avalanches have a degree of mobility that exceeds the behaviour of a smaller-volume frictional flow of dry, angular, broken rock."*

The mobility of rock avalanches, which affects the runout distance, increases systematically with the volume of the event. To capture the increase of mobility as a function of volume, the current project restricted the use of rock avalanches to landslides having a volume greater than 100,000 m^3. Figure 1.5 provides examples of a rock avalanche from the Kaikōura district.

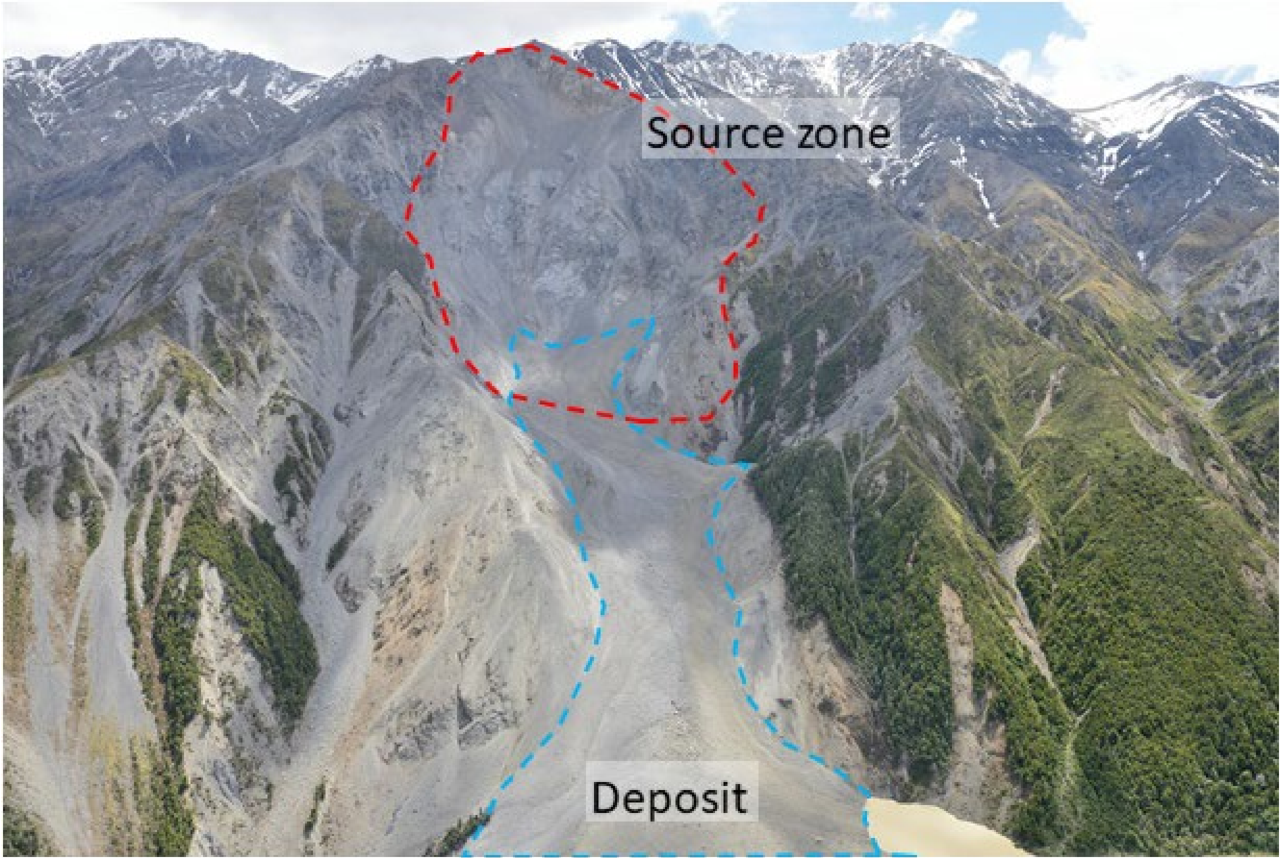

Figure 1.5 Hapuku rock avalanche generated by the 2016 Kaikōura earthquake. The deposit extends outside the current field of view. Photograph by D Townsend, Earth Sciences New Zealand.

2.0 Landslide-Debris-Inundation Modelling

Landslides directly impact both the natural and built environment by mobilising soil and rock on steep hill slopes and efficiently moving it downslope. A landslide-hazard assessment includes evaluation of the spatial and temporal contributors to landslide processes that pose a risk to people or property. This assessment involves determining the likelihood of landslide initiation, the extent of potential debris movement and the frequency and magnitude of debris inundation at a specific site. In this context, a landslide-debris-inundation risk analysis builds on hazard assessment by considering the vulnerability of structures in the area in order to quantify the potential impacts from landslide events.

Developing a full probabilistic workflow capturing landslide hazard and building risk requires an understanding of (1) the probability of a given type of slope failure in a given event, (2) the probability of debris originating from a landslide source reaching a given location and (3) the probability of damage due to inundation by landslide debris.

In this section, we provide a brief overview of the methods adopted in this study, describe the components of the hazard and risk assessment alongside examples of results and key uncertainties, outline the process employed to undertake calculations for Representative Concentration Pathway (RCP) 6 2081–2100 future climate scenarios and describe field-reconnaissance activities.

2.1 Landslide Source to Inundation Process Model Overview

Given the large spatial scale of the West Coast, and the associated computational cost of running multiple landslide runout models over such a wide area, we employ a new Landslide Source to Inundation Process Model (LS-IPM) methodology developed by Earth Sciences New Zealand for regional-scale analysis of landslide-debris-inundation hazards, incorporating a consideration of geomorphological process rates.

We assume that the past is a guide for the future, and the calculation of landslide hazard and risk is then based on the limit of the number of landslide-debris-inundation events of a given volume occurring in a given area over a given period of time. We assume that the rate of landslide-debris production is a limiting factor and that, as such, the frequency of occurrence is directly related to the source volume of contributing landslides – the greater the expected proportion of large landslides, the less frequent landsliding will need to be in order to maintain the rate of debris production. We account for future climate scenarios by adjusting the limiting rate of landslide-debris production in concert with expected changes in landslide-event frequency. This differs from a traditional frequentist interpretation of landslide probability, which would typically use observations of previous landslide frequencies to determine the limit of the number of discrete landslide events expected to occur in a given area over a given period of time. Although traditional frequentist approaches may include a consideration of landslide-event size, the debris production rate is rarely, if ever, considered a limiting factor. The approach used here allows the integration of geological, geomorphological and geophysical data to account for processes that influence landslides, providing constraint on landslide occurrence beyond the limited historical record of landslide events, as employed in frequentist approaches. This helps to provide a more accurate and detailed understanding of regional landslide hazard and risk.

We explicitly tie inundation hazard to a combination of (1) the production of debris by landslides of given size ranges and (2) the manner in which the debris is distributed as it travels to the inundation location. As our hazard metrics describe the probability of a volume of landslide debris passing a given location (rather than the number of discrete landslides that could potentially inundate that location), we calculate the annual probability of inundation by landslides of a given size (irrespective of trigger) as:

$$annual\ probability\ (landslide\ inundation) = \frac{mean\ annual\ landslide\ debris\ flux}{characteristic\ landslide\ inundation\ volume}$$

where the mean annual landslide-debris flux for a given landslide volume range is based on the amount of landslide debris that we expect can be generated up-slope of a given location, as well as the proportion of that debris that can be expected to travel down-slope past the given location (allowing for potential deposition, spreading or channelisation along the route). The characteristic landslide-inundation volume is derived from a combination of the initial landslide geometry and assumed spreading characteristics as material travels down-slope to the given location. For example, if modelled runout of house-sized (up to 1000 m^3) landslides from all possible contributing hill slopes results in an average of 0.3 m^3 of debris passing a given location each year, and the actual expected volume of debris from a single house-sized landslide passing that location is just 30 m^3 (i.e. a fraction of the initial source volume), then:

$$annual\ probability\ (landslide\ inundation) = \frac{0.3\ m^3/yr}{30\ m^3}$$

$$= 0.01, or\ 1\%\ per\ year$$

When assessing the chance of an event happening each year, it is important to understand what 'annual probability' really means. For example:

1. A 1% chance of occurrence similarly means a 99% chance that an event will not occur.
   - If an event has a 1% (0.01) chance of occurring in a given year, there is also a 99% chance that it will not occur that year.
   - This probability resets each year and does not carry over from one year to the next.
2. '1% per year' does not mean 'once every 100 years'.
   - Having a 1% annual probability does not guarantee that the event will happen exactly once in 100 years. It simply means that there is a 1% chance of it happening in any given year. Alternatively, this means that there is a 63% chance that it will occur ***at least once*** in that 100-year period.
3. Events with very low probabilities can be expected to occur in the region every year.
   - For example, if 100,000 locations each have an annual probability of 10^{-5} (0.001%), then:

     $100{,}000 \times 10^{-5} = 1$
   - On average, you would expect about one event each year across those 100,000 locations.

The assumptions we require to determine the rate of landslide-debris production constitute a 'degree of belief' interpretation and, although constrained by regional datasets, are subject to engineering geological/geomorphological judgement. For example, we assume that all primary erosion that occurs on hill slopes capable of generating landslides occurs as a result of landsliding (see Section 2.3.1.1). This is supported by evidence from regional landslide studies (see Section A4.1.1); however, both the rate of debris production and proportion of debris eroded through landsliding are not well constrained in the study region. We therefore evaluate the uncertainty associated with this, as well as other input parameters, by calculating the change in landslide-debris-inundation risk from our favoured (or 'most likely') solution by testing a range of values for variables controlling both erosion rates and the proportion of erosion that contributes to landslide-debris production (see Section 2.3.1). Uncertainties associated with all key assumptions are evaluated in a similar manner (see Sections A7.1–A7.5), and we employ a Monte Carlo approach to evaluate the combined impact of all input uncertainties and assumptions on calculated APLR at various distances from potential landslide sources (see Section A7.6.1). Finally, we estimate uncertainties associated with the accuracy of the topographic model and analysis resolution by comparing the calculated risk from the 25 m regional digital elevation model (DEM) against risks calculated using a recent Light and Detecting Ranging (LiDAR)-derived DEM at both 25 m and 8 m resolutions (see Section A7.6.2).

2.1.1 Consideration of Hazard and Risk

This LS-IPM is based on a combined workflow that provides quantitative forecasts of landslide sediment distribution from hillslopes to populated regions. The workflow incorporates four sub-model components, namely the:

1. Landslide source-susceptibility model (LSS).
2. Landslide sediment-production model (LSP).
3. Landslide sediment-distribution model (LSD).
4. Landslide debris-inundation-risk model (LDIR).

The LSS model describes the probability of slope failure for a range of triggering scenarios and combines outputs from the Rainfall-Induced Landslide (RIL) Tool (Rosser et al. 2021) and Earthquake-Induced Landslide (EIL) Tool (Massey et al. 2021a) to generate both mean annual and scenario-based probabilities of failure for a range of landslide volume classes. The LSP forecast model provides estimates of the volume of debris generated from all feasible landslides and incorporates data describing assumed landslide erosion rates, as well as observed landslide-size characteristics derived from mapped landslides in the study region. The LSD model simulates the movement of landslide debris downslope and can be used to quantify the landslide-debris-inundation probability throughout the study region. The LDIR model incorporates an estimate of building vulnerability in order to derive APLR estimates.

This workflow is briefly described in the following sections. For a detailed description of the model components and assumptions, see Appendices 3–6. Model uncertainties are discussed in detail in Appendix 7.

2.1.2 Quantification of Regional Landslide-Debris-Inundation Hazards

The hazard equation provides a means of describing hazard events, such as landslides, floods or earthquakes, based on factors related to the event's probability and potential intensity or magnitude. In general, the hazard equation can be expressed as:

$$Hazard = Probability\ of\ Occurrence \times Intensity\ or\ Magnitude$$

We can break down the relative components as:

- **Probability of Occurrence:** The likelihood that a specific hazard event will occur in a given area within a specified time period.
- **Intensity or Magnitude:** The severity or strength of the hazard event (e.g. earthquake magnitude, flood depth, landslide volume).

This equation provides a way to quantify the level of hazard by combining how likely the event is to occur with how severe it could be. For probabilistic models, hazard is often represented through recurrence intervals (e.g. a '100-year flood') or exceedance probabilities (e.g. a 1% chance of occurrence per year). In this section, we briefly introduce the key elements of the hazard-modelling approach.

The landslide-debris-inundation hazard assessment is based on a geomorphologically consistent evaluation of landslide-sediment production and distribution across the region by landslide processes. We consider the volume and rate of landslide initiation to be limited by the rate of debris production on hill slopes (Figure 2.1). Once initiated, landslide debris then travels through the hill-slope system as primary 'runout' (i.e. as debris flows or debris avalanches from the landslide source) and is either directly deposited in river channels, which then flush the sediment from the landscape, or deposited on hill slopes before being moved to river channels by secondary debris-transport processes such as sheet wash, rilling, gullying and other fluvial or glacial mechanisms. These secondary processes are not considered in the current study; however, these play an important role in the geomorphological system, as they act as a buffer between landslide deposits and the river system. As secondary transport processes operate at a more or less constant rate through time (e.g. Croissant et al. 2019), we can expect average rates of sediment transport in rivers, for example, to reflect long-term rates of landslide-debris production in the contributing landscape.

We assume that hill-slope debris inputs (through weathering and strength degradation) and outputs (through delivery to glaciers, rivers or coastlines) are balanced over millennial timescales and therefore employ a sediment-production (or erosion-rate) model developed from a combination of uplift, erosion and fluvial sediment-load data to constrain the maximum rate of landslide-source debris production in the landscape. This approach draws parallels to that of Neverman et al. (2023), in which a derivative of the same specific-fluvial-sediment-yield dataset was employed to help constrain rates of shallow rainfall-induced landslide sediment delivery to fluvial networks across New Zealand.

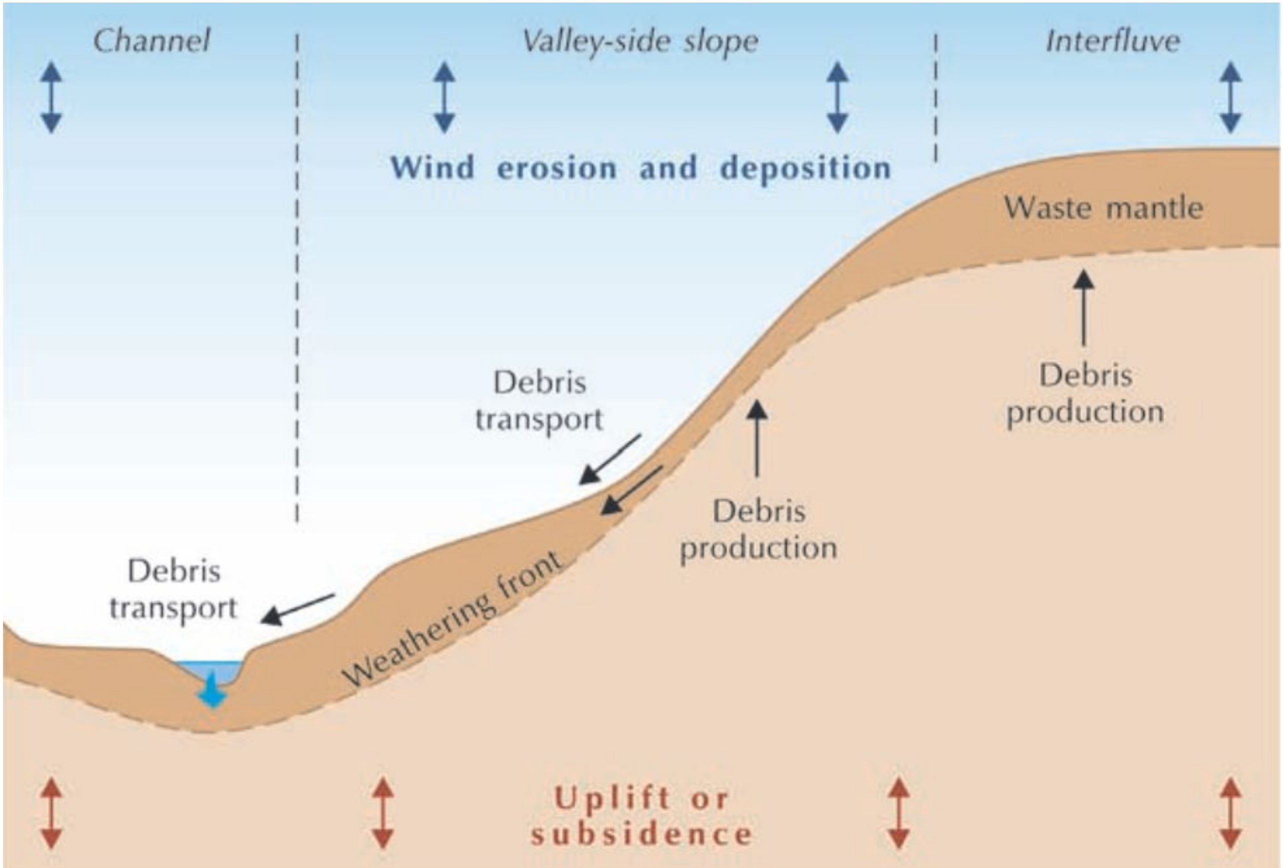

Figure 2.1 Geomorphological model of a hill-slope system. The model includes inputs (e.g. debris production through fracturing and weathering, as well as deposition by wind), storage (e.g. the waste mantle), throughputs (e.g. debris transport by hill-slope processes) and outputs (e.g. evacuation of debris by the fluvial system). Modified after Huggett and Shuttleworth (2012).

Rates of landslide-sediment production, transport and deposition in active landscapes are ultimately limited by the rate at which unstable sediment becomes available. On geomorphologically active hill slopes, the generation of unstable sediment is regulated by the rate of relief production (through a combination of tectonic uplift and fluvial or glacial erosion) and rock-strength degradation (through weathering and fracturing), while landslide-sediment transport is regulated by the frequency of landslide-inducing events and the mobility of the resulting landslides.

We quantify landslide hazard at a given location in terms of both mean annual and scenario-based landslide-debris flux, a measure of the volume of landslide debris that can be expected to pass a given location as a result of all possible triggers, source volumes and movement modes. Fundamentally, the landslide-debris flux at a given location is a function of the landslide-sediment production up-slope of the site, as well as the potential for that sediment to travel down-slope past the location. While the location and potential volume of landslides is derived from the LSS and LSP models, the travel distance needs to be calculated using an LSD model. The distance that a landslide travels (and therefore the potential for it to pass a given location) depends on (1) the initial gravitational potential energy of material in the landslide source and (2) the rate at which energy is gained and lost as the debris moves through the landscape. The initial energy of the landslide is a function of its initial volume and release elevation, while energy may be gained by entraining debris along the travel path. The rate of energy loss is a function of (among other factors) the materials that the landslide is composed of, the material along the travel path, the mode of movement and the topography along the runout path. As it is currently impractical to model these complex physical relationships at a regional scale, inputs to the LSD model employed here adopt empirical statistical relationships to account for key physical parameters controlling runout processes. We account for different modes of movement by adopting modelling methods suited for both ‘avalanche’- and ‘flow’-type movements.

The landslide-debris flux metric derived from the LSD model provides an integrated measure of both mean annual and scenario-based hazard intensity by combining the calculated frequency and magnitude of all potential landslides capable of inundating a site. As such, landslide-debris flux does not provide a measure of landslide-debris-inundation risk (which requires intensity and frequency to be separated). Intermediate outputs of the LSD model (representing individual triggers, return intervals and volume classes) are used to calculate the probability of inundation (P_i) and APLR in the LDIR model. This is described in the following section.

2.1.3 Derivation of Debris-Inundation Probability and Annual Property Loss Risk

The frequency and magnitude of landslide-source events can be determined by evaluating a combination of susceptibility to failure, sediment-production rates and probable landslide-size characteristics. However, deriving the frequency and magnitude of inundation events at a given down-slope location is more complicated. The amount of debris that travels to a site is closely tied to the geographic position of the site, the initial volume of the landslide and the characteristics of the travel path between the source and inundation location. A site on a debris-flow fan far from a landslide source may, for example, only experience inundation events when channelisation on the fan coincides with the location of the site – at which point the magnitude of landslide debris passing the location (the debris flux) may equal the full volume of the landslide source (or more, if debris is entrained during runout). In contrast, a site on an open hill slope close to a landslide source may experience inundation events every time a landslide occurs, although the inundation volume is likely less than the total landslide source volume, as only a portion of the original failure may intersect the site. In order to calculate the frequency of inundation by representative landslide volumes at a given location, we employ a probabilistic approach to compare the mean annual landslide-debris flux to an estimated characteristic flux from contributing landslide sources. This method is described in detail in Appendix A6.2.

APLR is a function of the frequency of various magnitudes of landslide inundation events occurring and the vulnerability of buildings to those inundation hazards. The level of detail in the LS-IPM analysis is similar to a ‘Level D’ basic quantitative hazard and risk analysis, as outlined in Table 4.2 of the Landslide Planning Guidance (de Vilder et al. 2024), including regional analysis of the size and frequency of landslides that could occur for given scenarios, regional modelling of the runout for the full range of landslide sizes and basic analysis of the vulnerability of buildings to inundation by different landslide sizes. A novel approach has been employed to calculate landslide debris-inundation hazard. We note that the input datasets for the LSS and LSP models have been selected to maintain regional consistency and, as such, the residual uncertainties exclude the application of outputs for ‘Level D’ planning and consenting purposes (see Section 5.4 for further discussion on uncertainties and application of these results). The LS-IPM workflow incorporates physically constrained statistical methods appropriate for regional hazard and risk analysis, although this should not be considered a substitute for local hazard and risk analysis.

The general equation for risk in the context of natural hazards can be expressed as:

$$Risk = Hazard \times Vulnerability \times Exposure$$

We can break down the relative components as:

- **Hazard:** The probability or likelihood of a natural or man-made event of a given magnitude occurring (e.g. landslide, flood, earthquake).
- **Vulnerability:** The degree to which people, infrastructure or assets are susceptible to damage from the hazard. This includes factors such as structural resilience, preparedness and capacity to respond.
- **Exposure:** The presence of people, assets, infrastructure or resources in areas where these could be affected by the hazard.

Thus, risk quantifies the potential impact of a hazard, taking into account the likelihood of the event, the vulnerability of affected entities and the extent to which these are exposed. In this section, we briefly introduce the key elements of the LDIR model as these relate to the general risk equation presented above. Section 2.5 provides further details on the LDIR model, associated outputs and key uncertainties.

The vulnerability of buildings to landslide inundation depends on the magnitude or intensity of an inundation event, the type of structure and the nature of the impact (e.g. falling debris through a roof or gradual burial by debris flows) and the consequence to the element(s) being impacted. As vulnerability is a key element of the general risk equation above, calculated landslide-debris-inundation risk is only relevant for the type of element considered in the risk calculation. Here, we adopt an economic approach to quantify the vulnerability of buildings in terms of a ‘damage ratio’, describing the ratio between the cost to repair damage and the cost to replace the damaged structure. This approach is supported by an empirical damage function derived by Massey et al. (2019) from a New Zealand and international dataset of undifferentiated building types, which relates the landslide-debris height observed following inundation events to the assessed damage ratio at each site.

2.1.4 Climate-Change Scenarios and Event-Specific Hazard Assessment

As well as considering mean annual hazard and risk, we also evaluate landslide-debris-inundation hazard and risk associated with four credible landslide-inducing scenarios. These include:

- **Scenario 1:** Present-day precipitation triggers based on 50-, 100- and 250-year annual return interval (ARI) 24-hour precipitation totals derived from the National Institute of Water & Atmospheric Research (NIWA)’s High Intensity Rainfall Design System (HIRDS) V4[1] model.

1 https://hirds.niwa.co.nz/

- **Scenario 2:** Future precipitation triggers based on 50-, 100- and 250-year ARI 24-hour precipitation totals derived from the HIRDS V4 model rainfall projections for a future RCP6 scenario (Carey-Smith et al. 2018).
- **Scenario 3:** A regional earthquake trigger based on 100-, 250-, 500- and 1000-year ARI peak ground accelerations (PGA) derived from the New Zealand National Seismic Hazard Model (NSHM) 2022 (Gerstenberger et al. 2022).
- **Scenario 4:** An Alpine Fault earthquake event (e.g. based on PGA derived from the AlpineF2K rupture model [Bradley et al. 2017]).

We note that, aside from the Alpine Fault earthquake event, these scenarios do not reflect the landslide inundation associated with a specific triggering event but rather the probable debris production and inundation hazard associated with the precipitation or ground accelerations representing various return intervals throughout the region.

2.1.5 Quantification of Results and Uncertainties

In order to demonstrate the spatial variability of some model outputs, we adopt a representative study region in the vicinity of The Doughboy/Kokiraki (-42.92, 171.06). The Kokiraki study region encompasses a catchment of approximately 4500 km^2, incorporating a range of topographic settings representative of the wider region overseen by WCEM. By focusing on this area, we can illustrate how factors such as terrain steepness, geology and land cover influence both the estimated landslide probabilities and associated uncertainties. Unless a result specifically refers to the vicinity of Kokiraki, all results can be assumed to apply to the entire region overseen by WCEM.

Uncertainties relating to the assumptions and input parameters in this study are quantified by assessing the effects of model-input variations and assumptions on calculated landslide-debris-inundation results using a simple 1D model. Specifically, changes in key inputs to the LSS, LSP, LSD and LDIR models are evaluated in relation to the calculated APLR at multiple locations down-slope of a theoretical landslide source. Electing to use a 1D, instead of 2D, model enables a broad exploration of the parameter space while minimising computational costs. While the model is conceptual and simplifies geographic complexities, it effectively captures the magnitudes and trends of impact. This model is described in detail in Sections A7.1–A7.5.

Employing this 1D model, we systematically adjust key variables (e.g. landslide size, probability, debris characteristics and runout parameters) and evaluate how this changes the APLR from its ‘most likely’ value at several locations down-slope of a hypothetical landslide source. The ‘most likely’ APLR at each location represents the calculated risk assuming ‘best estimate’ input parameters selected for this study. Although this framework does not replicate specific real-world conditions, it captures both the magnitude and trends of potential impacts. By identifying which parameters most strongly affect the results, as well as evaluating the total uncertainty at each down-slope location, the study provides guidance on interpreting the hazard estimates in the context of data limitations and potential under- or over-estimates at local scales. This model is described in detail in Section A7.6.1.

Uncertainties relating to the accuracy of the DEM employed in the LSP and LSD models are quantified by comparing 2D APLR results from the area around Greymouth against results generated using a LiDAR-derived DEM. We select an area in the vicinity of Greymouth, rather than in the Kokiraki region, due to the full LiDAR data coverage in this area. We assume that this DEM provides an accurate representation of present-day topography and are therefore able to isolate the impacts of inaccuracies in the national DEM (LINZ 2014), as well as the effect of down-sampling the DEM to a lower resolution prior to running the LSP and LSD models. Although this analysis is undertaken in a limited area, and we do not test the impact of changing model assumptions and parameters, we expect that the analysis effectively captures the magnitude and trends of impacts associated with spatial accuracy of the model. This model is described in detail in Section A7.6.2.

Further details regarding uncertainties relating to each model component are presented in Sections 2.3–2.5 and summarised in Section 3.2.

2.2 Landslide Source-Susceptibility Model

2.2.1 Overview

The LSS model is used to evaluate the relative probability of a landslide occurring at a given location as a result of a given trigger (rainfall or earthquake) and associated return interval. The model assumes that all landslides occurring at a given location are the result of either an earthquake or heavy rainfall and calculates the annual probability of failure by integrating outputs from earthquake-induced landslide (Massey et al. 2021a) and rainfall-induced landslide (Massey et al. 2021b) source-susceptibility models, trained using catalogues of landslides mapped following earthquake- or rainfall-induced events.

The shaking data used to create earthquake-induced landslide outputs was derived from the New Zealand NSHM 2022 (Gerstenberger et al. 2022), and landslide susceptibilities were calculated using PGAs for ARIs of 100-, 250-, 500- and 1000-year earthquakes. The earthquake-induced landslide susceptibility for an Alpine Fault earthquake event is based on PGAs derived from the AlpineF2K rupture model (Bradley et al. 2017).

Rainfall data used to create the rainfall-induced landslide susceptibility forecasts was derived from the NIWA HIRDS V4 model, which simulates rainfall intensity at a 5 km grid resolution for a given range of ARIs. The landslide susceptibilities were calculated using 24-hour rainfall for ARIs of 50, 100 and 250 years (see Appendix 3 for further details). We note that there is no direct correlation between landslide occurrence and 24-hour rainfall accumulation and landslides may be triggered as result of longer or shorter rainfall intervals. However, we do find a reasonable correlation between landslide occurrence and 24-hour rainfall and therefore adopt this interval as a necessary simplification.

The LSS model output describes the mean annual probability of a given location being fully occupied by either a rainfall- or earthquake-induced landslide source in a given year. This was calculated by integrating the product of the susceptibility to a triggering event, as well as the frequency of triggering event, over the representative event return interval for all earthquake- and rainfall-induced landslide outputs. Expressed as $m^2/m^2/kyr$ (per thousand years), a value of 0.5 kyr^{-1} indicates that either 50% of the area is expected to be associated with a landslide source within a 1000-year period, or, alternatively, the entire area is expected to be associated with a landslide source over a 2000-year period (see Appendix A3.4 for further details).

2.2.2 Results and Uncertainties

Mean annual rainfall- and earthquake-induced landslide probabilities, as well as total annual probabilities of landslide initiation, are presented in Figure 2.2. Overall, the LSS model indicates that the greatest earthquake- and rainfall-induced landslide probabilities are in areas with steep topography, primarily in the region between Fox Glacier and Kokiraki. Relative probabilities for the two triggers vary across the study region, with rainfall-induced landslide probabilities being generally higher along the Southern Alps and earthquake-induced landslide probabilities being higher in the north of the region. Overall, mean annual rainfall-induced landslide probabilities are more variable, with maximum values commonly an order of magnitude greater than earthquake-induced landslide probabilities at the same location. However, this difference reduces when averaged across an area, and the spatially averaged rainfall-induced landslide probabilities are more commonly double those of earthquake-induced landslides. For example, the predicted mean annual rainfall-induced landslide probability in the Kokiraki area is approximately 0.30 kyr^{-1} (per thousand years), while the mean annual earthquake-induced landslide probability in the same area is approximately 0.10 kyr^{-1} (Figure 2.2a–c). However, it is important to note that both the magnitude and relative probability of rainfall- and earthquake-induced landslide occurrence varies across the region. In areas northeast of Greymouth, for example, earthquake-induced landslide probability exceeds rainfall-induced landslide probability, although the overall probability of landslide occurrence is much lower than along the range front (Figure 2.2d–f).

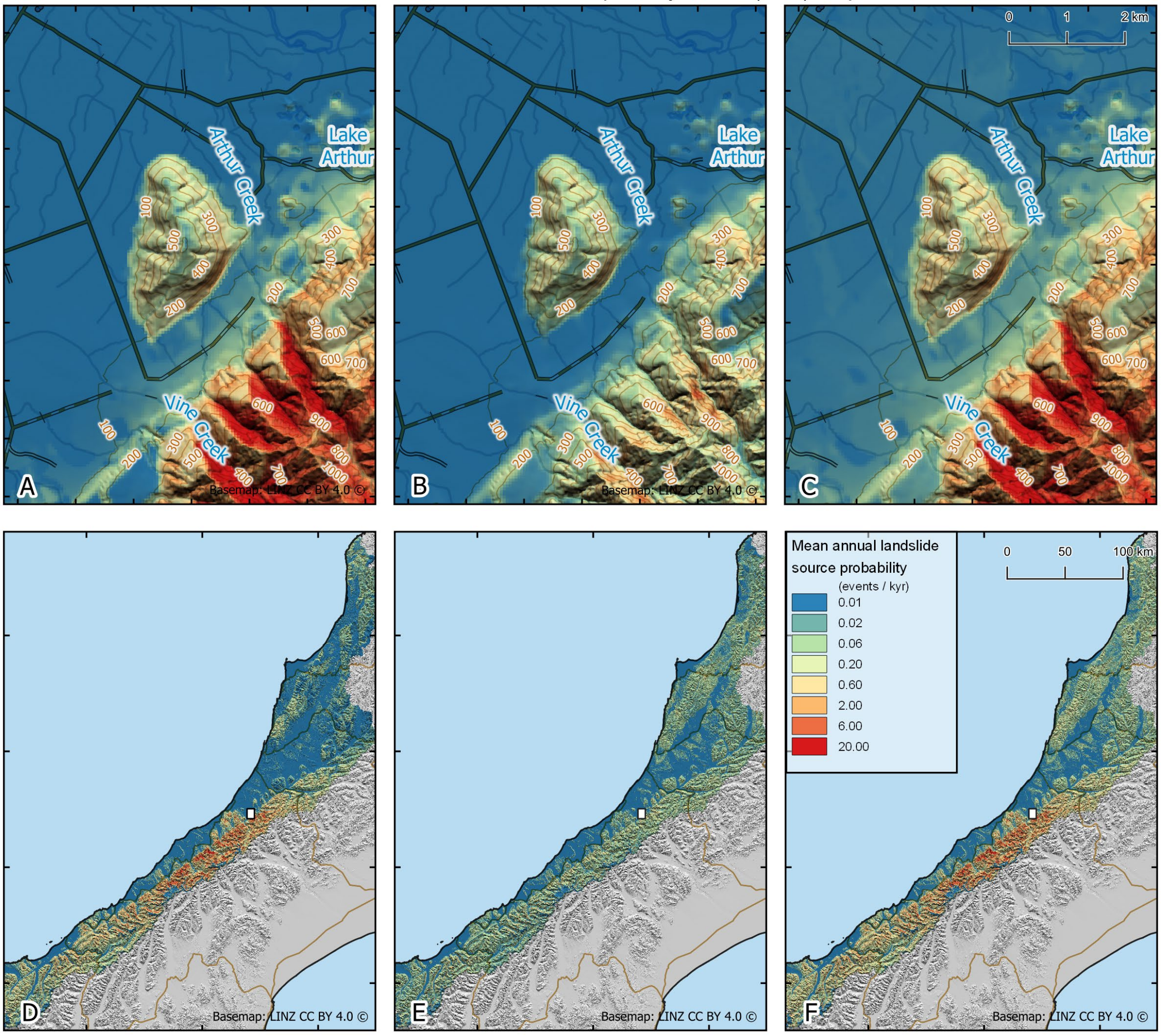

Figure 2.2 Selection of landslide source-susceptibility model outputs. (a, d) Mean annual rainfall-induced landslide probability. (b, e) Mean annual earthquake-induced landslide probability. (c, f) Total mean annual source probability. Legend categories are consistent across all maps. The location of the Kokiraki maps (a–c) are indicated by a white box on the regional overview maps.

The LSS model probabilities for rainfall- and earthquake-induced landslides determine how landslide-sediment production is distributed across the LSD model runout simulations (described in Section 2.3). While these probabilities do not affect the total amount of debris produced in a given cell, they do influence how debris is allocated across 112 individual runout simulations in the LSD model (described in Section 2.4). These simulations represent various combinations of landslide triggers, return intervals and landslide-size classes.

For example, if the probability of a rainfall-induced landslide is higher than that of an earthquake-induced landslide, a greater proportion of the annual sediment production will be assigned to rainfall-induced landslides. Within the category of rainfall-induced landslides, the specific amount of debris assigned to each return interval depends on its relative probability of landsliding, meaning that return intervals with a greater probability of landsliding will receive a larger share of the debris allocation (see Section A4.5 for a full description).

As landslide volumes, and therefore runout extents, vary for each runout simulation, the LSS model probabilities affect the distribution of landslide debris down-slope of landslide sources. For example, as earthquake-induced landslides are larger, and therefore overall more mobile than rainfall-induced landslides, locations with a greater probability of earthquake-induced landsliding will have a higher proportion of debris assigned to larger, more mobile landslides. This will lead to:

1. A lower APLR in locations close to landslide sources due to a reduction in landslide frequency (for a given erosion rate, the frequency of larger landslides must be less than that of smaller failures).
2. A higher APLR at locations far from source areas, as larger volumes are more mobile and therefore travel further from the source.

Uncertainties in the inputs used to calculate LSS probabilities have a moderate impact on the predicted APLR. Depending on the input, these uncertainties could cause a variation of up to 0.01× the 'most likely' APLR. This variation is strongest both close to the landslide source (where increasing the proportion of smaller rainfall-induced landslides will increase the inundation frequency) and far from the source (where increasing the proportion of larger, more mobile, earthquake-induced landslides will increase the probability of inundation). The impact of LSS model uncertainties is further discussed in Section A7.2.

2.3 Landslide Sediment-Production Model

2.3.1 Overview

The LSP model provides a means of estimating the volume of landslide sediment likely to be generated by events of a given trigger and return interval. In steep hill-slope terrains, landsliding is a primary driver of long-term erosion rates. By rapidly mobilising and transporting a mixture of sediment sizes, landslides contribute significantly to overall sediment flux and landscape evolution. The material exposed and deposited by landslides is further weathered and re-distributed by secondary processes such as sheet wash, rilling, gullying and piping, which contribute to the ongoing erosion of the landscape. Over time, the frequency and magnitude of landslides and high-magnitude rainfall events, combined with these secondary processes, shape long-term erosion and sediment-transport rates in the region.

2.3.1.1 Mean Annual Landslide Debris-Production Rate

We assume that landslides are the sole driver of mass wasting (the initial mobilisation and movement of soil or rock material) on hill slopes where landslides are determined to be kinematically feasible. Landslide-debris production is therefore assumed to be equal to the long-term erosion rate. We derive the long-term erosion rates from a combination of suspended-sediment-yield observations, estimates of soil and rock densities and measures of long-term tectonic uplift and erosion. This is a necessary simplification, and, while observational evidence suggests that landslides dominate mass wasting processes in much of the region, processes such as slope creep, gully formation, glacial erosion or fluvial under-cutting can also contribute to initial movement of soil and rock. Once sediment is mobilised, additional erosion processes (such as gullying and fluvial transport) contribute to the long-term transport of sediment through the landscape.

We base our estimation of erosion rates on previous studies quantifying specific sediment yield from hill slopes to rivers across New Zealand, as well as the specific density of geological units mapped throughout the country. This is calibrated against rates of long-term erosion and tectonic uplift. Hicks et al. (2011) undertook a detailed measurement campaign in order to determine mean annual sediment fluxes for 233 catchments across New Zealand. They then developed a 100-m-resolution spatially consistent specific-sediment-yield model to estimate sediment-delivery rates from topography within these catchments using a range of weighted-input variables, including precipitation, local slope and erosion terrain (encompassing geology, soil cover and physiography). In order to convert the Hicks et al. (2011) specific-sediment-yield model into total erosion rates, we converted mass-based sediment loads to volumetric erosion rates using source-material densities from the digital rock-density catalogue of Tenzer et al. (2011). As Hicks et al. (2011) did not evaluate bed-load transport within the sampled rivers, calculating total sediment yield (and therefore total erosion in the contributing catchments) required that we determine a scaling factor to account for the additional component of sediment transport. We achieved this by comparing predicted suspended sediment yields with measured longer-term erosion rates in West Coast catchments (Hovius et al. 1997; Larsen et al. 2014; Roda-Boluda et al. 2023). We found that a constant suspended to total sediment-yield scaling factor of 1.5 was required to correlate specific sediment yields based on suspended sediment measurements to basin-averaged erosion rates within the study region (see Section A4.1 for further details).

The long-term erosion rate is assumed to be maintained by discrete landslide events generated in response to earthquake or heavy rainfall events. We therefore proportion the mean annual erosion at a given location across a full range of ‘kinematically feasible’ landslide volumes at that location, assigning a greater proportion of the annual erosion to the most commonly occurring landslide volumes. ‘Kinematic feasibility’ ensures that our hypothetical landslide sources have the physical characteristics required to slide down slope, and are not (for example) too flat or blocked by topographic features. The maximum feasible landslide volumes are calculated from the 25 m DEM, while the allocation of sediment production to smaller volume classes is based on empirical landslide frequency-magnitude relationships derived from landslides mapped in the study region. These aspects are discussed further in the following section; see Appendix 4 for a full description of LSP model inputs.

Once landslide sediment is generated on a hill slope, the movement of a landslide results in the generation of landslide debris with an associated volumetric expansion as cracks and voids form within the material. We therefore convert landslide sediment-production rates to equivalent debris-production rates by multiplying the former by a sediment bulking factor to capture the reduction in density as a result of weathering and disaggregation. We adopted a bulking factor of 1.3 based on the relative densities of rock and soil in the region. See Section A4.1.3 for full details of this calculation.

Results and Uncertainties

Calculated sediment-production rates for the present-day scenario are presented in Figure 2.3a, d. Calculated rates are highest along the range front to the east of the Alpine Fault and increase up to 30 mm/yr in the Mount Cook region, although are generally closer to 6 mm/yr along the range front. Calculated sediment production rates to the north of the region are considerably lower, in the order of 0.25 mm/yr, as may be expected given the regional geomorphological setting (e.g. Adams 1980).

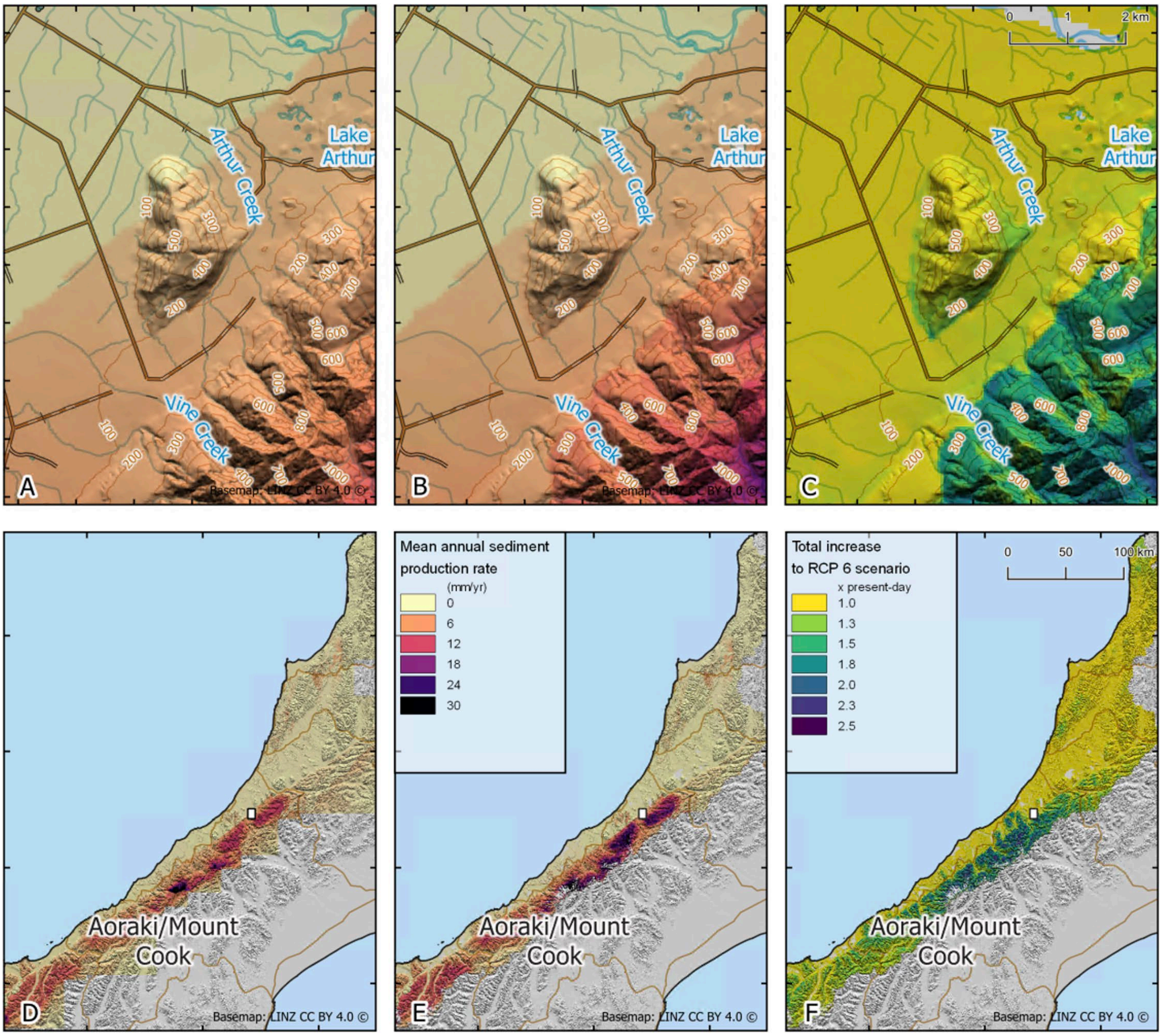

Figure 2.3 Selection of landslide sediment-production model outputs. (a, d) Mean annual sediment production. (b, e) Mean annual sediment production for the RCP6 2081–2100 climate scenario. (c, f) Change in total mean annual sediment production. Legend categories are consistent across maps (a), (b), (d) and (e) and maps (c) and (f). The location of the Kokiraki maps are indicated by a white box on the regional overview maps.

Catchment-averaged sediment-production rates derived from the regional erosion model adopted in this study compare favourably with bedrock-uplift rates derived from geological constraints (Adams 1980). This supports our assumptions that the rates adopted here likely reflect long-term averages spanning several thousand years and suggests that the landscape is in a state of ‘dynamic equilibrium’, such that long-term uplift and erosion are in balance. We find a similar favourable comparison between calculated landslide-derived erosion rates determined from a catalogue of thousands of landslides mapped along the range front (Hovius et al. 1997) and our adopted landslide-erosion model. This supports our assumption that the majority of erosion on slopes on which landsliding is kinematically feasible is driven by landslide processes. See Appendix A4.1.1 for further details on these comparisons.

The landslide debris-production rate directly affects the volume of source material available in LSD model simulations. As such, it has a dominant impact on both the calculated mean annual landslide-debris flux and the related frequency of inundation events. For consistency, the datasets employed in this study prioritise spatial uniformity. This necessitates a trade-off between local accuracy and spatial coverage. The primary input to the LSP model is suspended sediment yield, based on estimates from Hicks et al. (2011). The associated uncertainties are estimated to be more than an order of magnitude at a 100 m resolution, decreasing to approximately 2× as sediment yields are averaged over larger areas (Hicks et al. 2011). Given that sediment yield dictates the rate of debris production in the landslide-source area (rather than debris runout), these uncertainties impact how accurately the LSP model captures the frequency of landsliding events across landforms of varying scales. Uncertainty can be expected to be higher for landslides originating from smaller landforms and lower for those originating from larger areas. Specifically, standard errors in debris-production rates (and therefore inundation frequencies and associated APLR) from areas smaller than 1000 m^2 can be expected to be greater than an order of magnitude. Although this will have little effect on the extent of inundation, care should be taken when adopting hazard or risk metrics for planning purposes in the vicinity of smaller landslide source areas.

We find that uncertainties associated with inputs affecting landslide debris-production rates have little impact on the extent of landslide-debris-inundation hazard, although these can lead to APLR variations in affected areas up to 3× the ‘most likely’ estimate. This is, unsurprisingly, one of the largest impacts on APLR, reflecting the primary link between landslide-debris production and inundation hazard. The impact of LSP model uncertainties is further discussed in Section A7.3.

2.3.1.2 Kinematic-Source Model

The possibility for landslides of a given volume class range to occur at a location is informed by a simple ‘kinematic’ model that ensures that sufficient topographic relief and geometric freedom is available for an appropriately sized landslide to occur. As we limit our analysis to avalanche- and flow-type landslides, and do not consider falls (i.e. rockfall), we do not evaluate kinematic potential for ‘fall’-type movements. Where insufficient relief is available for a given landslide volume class range, the total landslide-sediment production is distributed across all smaller volume classes. The amount of debris assigned to various volume classes is determined based on the probability distribution of earthquake- and rainfall-induced landslides observed in the region. Combined with data relating to erosion rates, this approach allows us to estimate the total landslide sediment production at a given location for all landslide volume ranges, considered triggers and return intervals.

An ‘excess topography’ condition is employed to determine the spatial extent and maximum possible depth of slope failure units, while ‘area-volume scaling’ is employed to determine the potential depth of failure within these units. The excess topography condition adopts a 20° angle to define the position of the deepest possible failure surface, reflecting the potential frictional strength of weak joints within the rock mass. Although likely to vary throughout the region, this value falls within the 8–27° frictional strength range for landslides with volume classes greater than 1, derived from a survey of landslides in similar soil and rock conditions in Western Oregon (e.g. Alberti et al. 2022).

The depth of failure close to the landslide margins is controlled by an area-volume scaling relationship based on limit-equilibrium principles. This allows us to relate the landslide-source geometry to cohesive strength properties of the landslide-source material (see Section A5.2). We adopt a representative cohesive strength of 50 kPa toward the upper limit of back-calculated cohesive strengths presented in Alberti et al. (2022), although well below the cohesive strength of fractured greywacke rock masses (commonly 400–1000 kPa, e.g. Read et al. [1999]). As the cohesive strength is used to determine scaling characteristics for all landslide volume classes and, as such, must represent landslides in both soils, as well as in weathered and fractured rock, selecting a low to intermediate value is appropriate for this regional study. We model eight landslide-source volume-class ranges with upper limits fixed at order-of-magnitude intervals (see Table 2.1 for further details). Section A5.2 provides associated calculations and further discussion of input variables.

An example of potential source areas is provided in Figure 2.4. The maximum landslide volume class in each kinematically feasible failure unit is determined by comparing the mean depth of all cells within a unit (see Figure 2.4a) to the representative mean depth of landslides within each volume-class range. Figure 2.5 presents maximum volume classes for each kinematically feasible unit. We note that the kinematic-source model should not be considered a substitute for detailed geotechnical assessment and is neither an exhaustive, nor prescriptive, description of potential landslide-source areas. Individual landslides may be more or less extensive than the maximum feasible failure units defined using this method.

We explore uncertainties associated with the derivation of potential source areas in the following section and recommend the incorporation of local geotechnical data in locations where uncertainties are greater than acceptable limits. In particular, the incorporation of material or site-specific constraints on friction and cohesion parameters, including the manner in which these parameters change with depth, can significantly reduce associated uncertainties. This data is not available on a regional scale and is therefore not incorporated in this study.

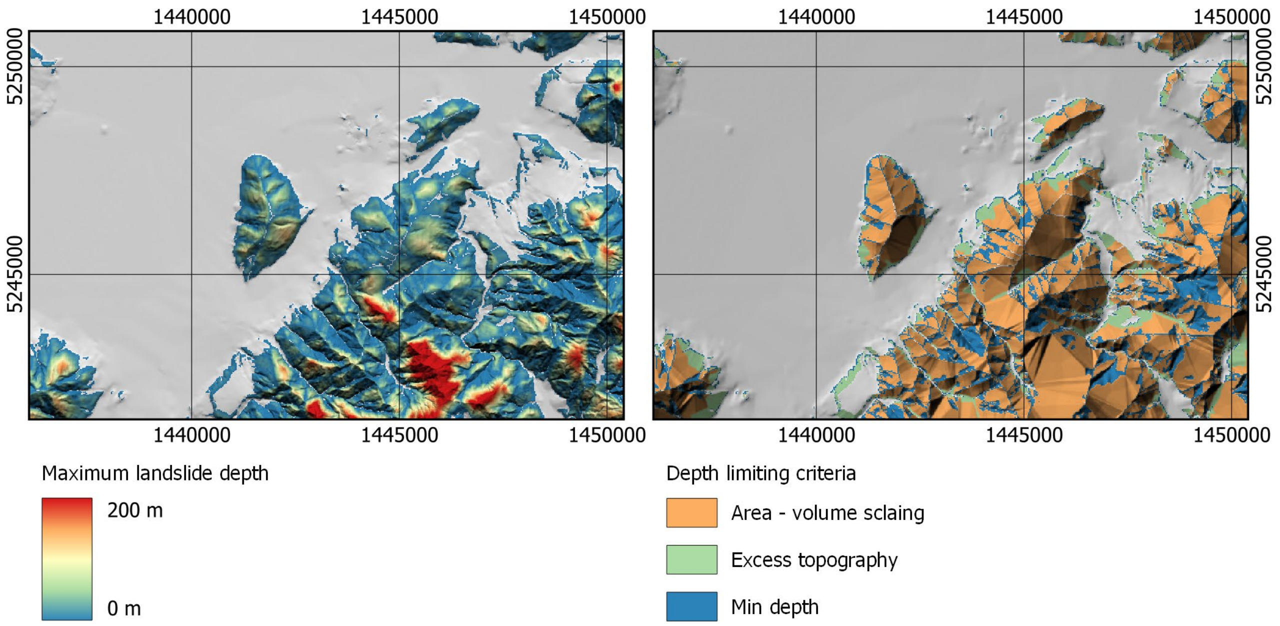

Figure 2.4 Calculated maximum landslide depths based on kinematic models (left) and depth-limiting criteria employed in the kinematic model (right). The hillshade image representing topography for the maximum depth figure is based on present-day topography, while the hillshade image representing topography for the depth-limiting criteria is derived from the calculated maximum-depth failure surfaces.

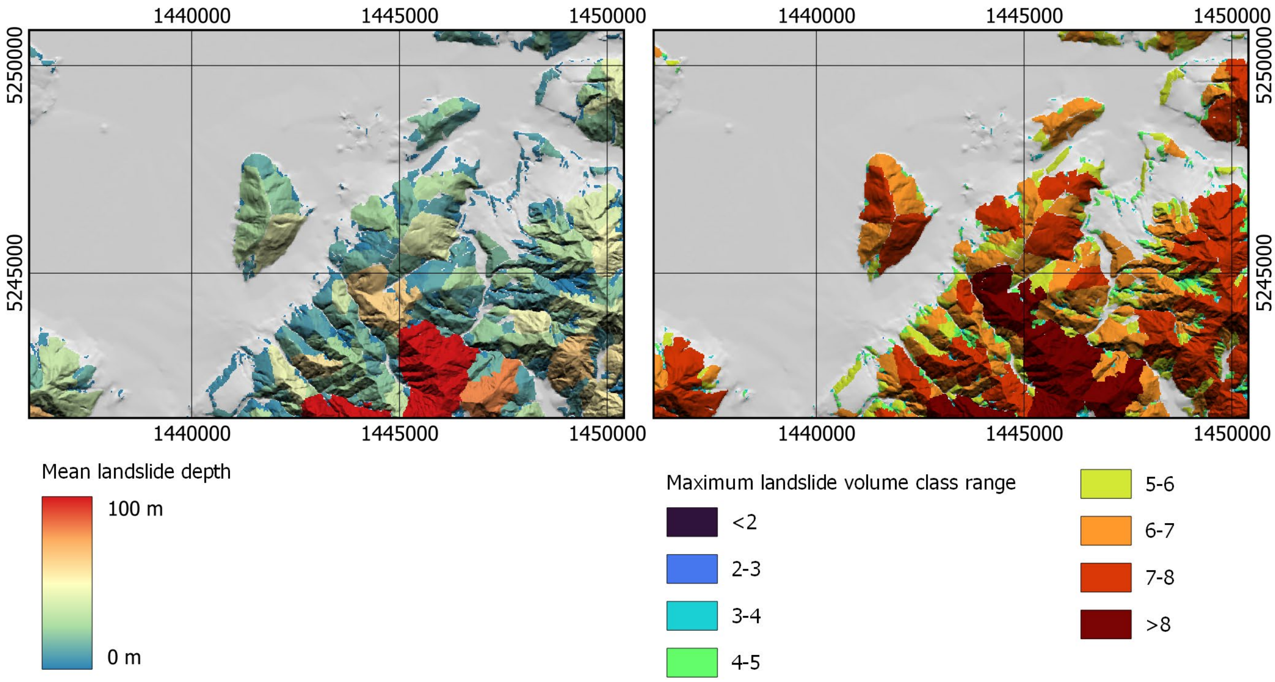

Figure 2.5 Depth to the kinematically feasible failure surface (left) and volume classes used to determine the maximum feasible volumes for the landslide sediment-production model (right).

Results and Uncertainties

We evaluate the probability of landslides of all volumes occurring within susceptible cells by dividing the landscape into kinematically feasible failure units and applying landslide frequency-volume statistics consistent with global observations of landslide occurrence (see Figure 2.6). The national DEM adopted in this study (LINZ 2014) is based on data derived from aerial photographs collected in the 1940s and has been down-sampled to 25 m resolution to meet computational constraints for this regional analysis. This raises significant uncertainties in the identification of landslide-source regions, particularly for landforms with areas less than 100,000 m^2, and can lead to debris inundation from smaller source areas not being identified (and therefore associated APLR not being calculated) and/or calculated runouts being less extensive than these would otherwise be with larger topography. Although not solely the result of the kinematic model, we estimate that the impact of inaccurate terrain representation in the national DEM can lead to a variation in APLR from that derived from a recent LiDAR DEM (LINZ 2022) by at least 0.79 orders of magnitude, while the nominal 25 m resolution for both the LSP and LSD analyses can be expected to result in uncertainties of at least 0.58 orders of magnitude. This is further discussed in Sections A7.3 and A7.6.2.

2.3.1.3 Landslide-Volume Distributions

Once a maximum landslide volume is determined for a given location, we employ empirical frequency-volume distributions to assign debris to all feasible volume-class ranges. As a first step, we compiled all mapped earthquake-induced (n = 6359) and rainfall-induced (n = 7269) landslide polygon datasets available for the region overseen by WCEM for which coverage can be reasonably assumed to be complete for given triggering events (see Table A1.2 in Appendix 1 for a complete list of datasets used). Mapped polygons were separated into source and runout by assuming that the source occupies a proportion of the total elevation range, and the volume of each individual landslide source was then calculated from the 8 m DEM using the same kinematic model described in the previous section. Resulting landslide frequency-volume distributions were found to be approximately log-normally distributed, similar to previous observations in international datasets (e.g. Brunetti et al. 2009). The calculated geometric mean volume of earthquake-induced landslides on a $\log_{10}$ scale was 4.55 ± 0.60 (m^3) and for rainfall-induced landslides was 3.92 ± 0.68 (m^3) (see Appendix A4.3 for further details).

Results and Uncertainties

Table 2.1 presents a summary of calculated landslide areas and depths for each landslide volume-class range alongside proportional landslide-volume distributions derived from West Coast region landslides.

Table 2.1 Key attributes of volume-class ranges used for the landslide sediment-production, sediment-distribution and debris-inundation-risk models. RIL = rainfall-induced landslides, EIL = earthquake-induced landslides, CBD = central business district.

Class	Class Range	Geometric Mean			Proportional Contribution of Sediment (per m^2) (%)	
		Landslide Volume $\log_{10}$ (m^3)	Landslide Area (m^2)	Landslide Depth (m)	RIL	EIL
Family car or smaller	<1	0.5	3	1.1	<0.01	<0.01
Car to bus or large truck	1–2	1.5	16	1.9	0.02	0.00
Bus to house	2–3	2.5	89	3.6	2.56	0.05
House to Olympic swimming pool	3–4	3.5	484	6.5	34.44	7.09
Pool to supermarket	4–5	4.5	2630	12.0	53.29	60.13
Supermarket to container ship	5–6	5.5	14,295	22.1	9.48	31.69
Ship to CBD of typical city	6–7	6.5	77,711	40.7	0.19	1.04
CBD to large hill or small mountain	7–8	7.5	422,454	74.9	<0.01	<0.01

As larger landslides travel further than smaller landslides and are likely more damaging to buildings, the extent of APLR tends to increase where topography can support larger maximum volume-class ranges (a function of both geometric-mean volumes and standard deviations). In contrast, limiting the maximum potential volume at a given location will shift debris production to smaller volume class ranges, resulting in more frequent events and therefore increased inundation risk close to hill slopes. We find that uncertainties associated with both the geometric mean and standard deviation of volumes can significantly influence the predicted APLR, leading to variations of between 0.5× the most likely APLR at locations close to the landslide source and 0.001× at more distal locations. Uncertainties associated with the geometric-mean volume have the greatest impact on calculated APLR at distal locations, while changes in the standard deviation tend to more strongly affect APLR closer to the source. The impact of LSP model uncertainties is further discussed in Section A7.3.

2.3.1.4 Proportional Landslide Erosion for All Triggers, Return Intervals and Volume Classes

We assume that discrete landslide events induced by earthquakes or heavy rainfall maintain the long-term erosion rate. To estimate the erosion contributed by each trigger, we first compare the total probability of failure at a given location with the probability of failure for each LSS model scenario (i.e. each trigger and return interval combination). We then distribute the annual debris production associated with each LSS model scenario across kinematically feasible volume classes using the previously mentioned landslide frequency-volume distributions. In other words, we allocate the proportion of annual erosion associated with each trigger to a range of possible landslide volumes based on the proportions of landslides of given volumes observed to have previously occurred in the region. This is described in full in Appendix 4.

Results and Uncertainties

Figure 2.6 presents spatially averaged landslide debris-production rates for kinematically feasible hill slopes in the vicinity of Kokiraki. Overall, landslide sediment-production rates in this area approximate a log-normal distribution, consistent with input frequency-volume distributions (see Figure A4.5). However, these are skewed slightly (approximately half a volume class) toward larger volumes, as areas in the vicinity of Kokiraki associated with greater topographic relief, and therefore larger maximum possible volumes (see Figures 2.5 and A4.8), are also associated with higher erosion (and therefore landslide sediment-production) rates. This effect is a function of the extreme contrast in both relief and erosion rates specific to the vicinity of Kokiraki and is negligible when considering landslide debris-production rates across the entire WCEM study region.

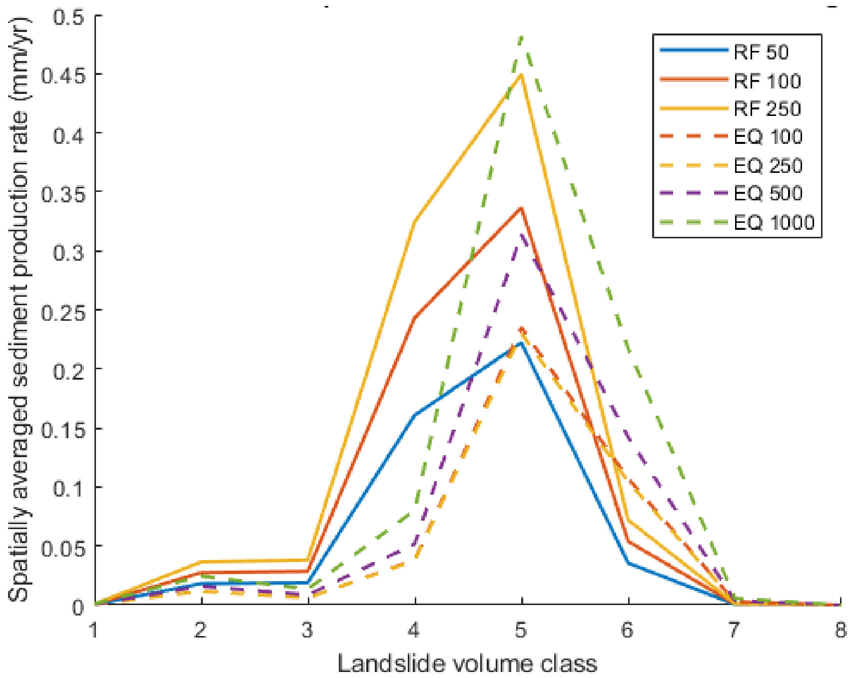

Figure 2.6 Landslide sediment-production frequency-magnitude relationships derived for the vicinity of Kokiraki using the landslide sediment-production model. Solid lines represent the mean annual sediment production by rainfall-induced landslides and dashed lines represent the mean annual sediment production by earthquake-induced landslides of various volume classes.

Uncertainties associated with the proportional distribution of debris volumes are related to the assumption that, where landsliding is kinematically feasible, long-term erosion rates are maintained by landslide events. As this assumption directly affects the rate of landslide-debris production, associated uncertainties behave in an essentially identical manner to those described for the mean annual landslide debris-production rate in Section 2.3.1.1, and APLR will tend to decrease proportionally with decreasing contributions of landslide erosion to the total erosion rate. However, we do note that the regional-scale datasets utilised in this study do not capture local or site-specific effects and, as such, may overlook sources of rapid debris generation, leading to potential under-estimation of localised landslide debris production. Areas with active erosion (such as fluvial and coastal erosion), ongoing slope instability (e.g. creeping or deep-seated landslides), temporary susceptibility increases (e.g. from vegetation loss) and recent human modifications (such as quarries and road cuts) often produce landslide sediment at much higher rates than regional erosion estimates. Such areas may exhibit local landslide debris-production rates several orders of magnitude above the regional values presented in this report. Further discussion on these limitations, variability in debris production and the impact of localised factors is provided in Section A7.3.

2.3.1.5 Sediment Production for Event Scenarios

Event-specific hazard assessments for Scenarios 1–3 (Section 2.1.4) are based on 24-hour precipitation totals derived from the relevant HIRDS V4 and New Zealand NSHM 2022 ARIs. As such, these do not represent specific trigger events but rather the potential debris production in a given location, if local precipitation or ground accelerations meet that of the ARI for the given location. The Alpine Fault scenario (Scenario 4) is based on a specific event forecast derived from the AlpineF2K rupture model (Bradley et al. 2017).

We calculate the volume of landslide debris generated in a scenario by comparing the probability of failure from the scenario-specific LSS model to the annual probability of failure at a location from all potential trigger events (derived from the annual LSS model). As we assume that all primary erosion is a result of landsliding, the total annual probability of landsliding represents sediment production at the annual rate. If the probability of failure as a result of a trigger is twice that of the mean annual probability (for example), then we can therefore assume that the volume of landslide debris produced will be twice the annual debris-production rate. To estimate sediment production for each scenario (e.g. Alpine Fault earthquake or heavy rainfall), we can therefore first calculate the ratio of the scenario-specific probability of failure to the mean annual probability of failure at each location. By multiplying the calculated mean annual sediment-production rate by this interval, we can then derive the probable total event-driven landslide-debris production for all feasible landslide volumes at the given location. See Appendix A4.6 for further details of this calculation.

2.3.1.6 Sediment Production for the RCP6 2081–2100 Climate-Change Scenario

In this study, we limit our assessment of future climate impacts to the data currently available. This is a necessary simplification and may not accurately capture the diverse effects of a future climate scenario. We opt to fix the earthquake-induced landslide sediment-production rates for the RCP6 2081–2100 climate-change scenario and increase the rainfall-induced landslide sediment-production rate in concert with the change in mean annual landslide probability from the present-day scenario. This ensures that the distribution of landslide volumes is maintained, while the frequency of future rainfall-induced landsliding increases without a commensurate reduction in the frequency of earthquake-induced landsliding. See Appendix A4.7 for full details of this calculation.

Results and Uncertainties

Calculated sediment-production rates for the RCP6 2081–2100 climate scenario are presented in Figure 2.3 (b, e). Figure 2.3 (c, f) demonstrates the predicted increase in sediment production from the calculated long-term erosion rates as a result of increased susceptibility to landsliding. As the increase in rate is directly tied to the increase in susceptibility derived from the LSS model output, the scale and distribution of increased erosion is similar to that that presented in Figure 2.11, with increases of up to 2.5× concentrated on the range front.

LSS model outputs for the RCP6 2081–2100 climate-change scenario indicate an increase in the mean annual probability of rainfall-induced landsliding (Section A3.5). However, these are based partly on present-day observations and cannot therefore account for any of the complex processes likely to drive future rates of landslide-debris production (e.g. weathering, deglaciation, vegetation change, wildfire, etc.). This point is crucial because, if landslides become more likely (i.e. the probability increases), there must be a corresponding change to keep the overall model consistent. Specifically, either the average volume of individual landslides must decrease or the total amount of debris produced must increase – or both. In fact, it is possible that the rapid pace of ongoing climate change will lead to a short-term (perhaps in the order of hundreds to thousands of years) imbalance in the rate of landslide-debris production and its removal from hill slopes through landsliding. The effects of climate change on both the size, and frequency of landslide occurrence are therefore inherently uncertain (see Appendix A4.7 for further discussion).

As uncertainties associated with many potential climate-change impacts are either unknown or cannot be quantified within the scope of this project, we are unable to quantify uncertainties for model outputs that rely on the RCP6 2081–2100 climate scenario. See Section 5.3.2 for recommendations regarding adoption of suitable uncertainty estimates.

2.4 Landslide Sediment-Distribution Model

2.4.1 Overview

The distance that a landslide travels (and therefore the potential for it to pass a given location) depends on (1) the initial gravitational potential energy of material in the landslide source and (2) the rate at which energy is gained or lost as the debris moves through the landscape. The initial energy of the landslide is a function of its initial volume and release elevation, while the rate of energy loss is a function of (among other factors) the materials that the landslide is composed of, the material along the travel path, the mode of movement and the topography along the runout path. Landslides may gain energy by entraining additional debris along the runout path. In this study, the location and potential volume of landslides is derived from the LSS and LSP models. The travel distance is then calculated using the LSD model.

Regional landslide-debris-inundation potential was modelled using the Gravitational Path Process (GPP) model developed by Wichmann (2017). This model simulates the movement of mass down-slope through a DEM from an initiation point (e.g. landslide-source area) to a deposition cell (e.g. landslide-runout area) using the single-flow-direction path-finding approach coupled with a random walk algorithm. We account for different modes of movement by modelling all trigger and source-volume cases using ‘fahrböschung’ (Heim 1932) methods for avalanche-type movements, while a two-parameter friction model (Perla et al. 1980) method is employed to represent flow-type movements.

The following sections briefly describe the derivation of inputs and modelling methods, while Appendix 5 provides a detailed description of the model implementation.

2.4.1.1 Avalanche-Type Movements

The ‘fahrböschung’ module (Heim 1932) of the GPP model was adopted to model avalanche-type movements in the region overseen by WCEM. We employ dry open-slope debris avalanche and rock avalanche fahrböschung angles for all landslide volume ranges derived from international and New Zealand datasets (Brideau et al. 2021b). For each volume class modelled, we adopt the 50th percentile fahrböschung representing the geometric mean of that volume class, recognising that we are not simulating runout of a single landslide volume but rather all possible volumes within the associated volume-class range (e.g. 10 up to 100 m^3). The same volume-fahrböschung relationships are employed for both earthquake- and rainfall-induced avalanche-type movements.

2.4.1.2 Flow-Type Movements

The commonly named ‘PCM’ module (Perla et al. 1980) of the GPP model was adopted to model flow-type movements in the region overseen by WCEM. The PCM method is commonly used to represent debris-flow-type runouts (e.g. Gamma 1999; Mergili et al. 2012; Goetz et al. 2021). In the absence of any local data relating to the PCM model parameterisation for flow-type landslides, we have selected a conservative approach to parameterisation and adopt a drag coefficient that varies with catchment area (allowing increased mobility of channelised flows), as well as literature parameters derived for debris flows in Switzerland (Gamma 1999; Wichmann 2017). These have been qualitatively validated against mapped West Coast landslide-debris extents (see Section A5.5.2 for further details) to ensure that runouts from ‘flow’ models for both rainfall- and earthquake-induced landslides extend across debris-flow fans throughout the region (see Section A5.5.3 for further details).

2.4.1.3 'Avalanche' versus 'Flow' Ratio

As no data are available to constrain the probability of a given type of movement occurring in the region overseen by WCEM, we base our estimate of the relative probability of these two movement modes on observations following Cyclone Gabrielle (Leith et al., in prep.). This dataset indicates that the probability of avalanche-type movements is approximately 66%, while flow-type landslides occur 33% of the time. As no similar dataset is available for the study region, we assume that the relative probability of rainfall-induced landslide movement types is the same in this region. Anecdotal evidence suggests that flow-type movements are less common in association with earthquake triggers, so we therefore assume that flow-type movements are half as probable for earthquake-induced landslides (i.e. a ratio of 83% versus 17%). We note that this is a necessary simplification, and gathering additional data to better constrain the proportion of various movement types in the study region could significantly reduce uncertainties associated with this estimate (see Section A5.2 for further discussion).

2.4.1.4 Model Configurations

The landslide-debris-inundation hazard model accounts for both sediment transport and deposition. Each model run is configured such that the total volume of sediment released from each source point represents the total erosion by a given trigger and volume class integrated over a representative time interval. Sediment is introduced progressively from all designated source locations. This approach allows debris from multiple landslides of similar volume, and sharing a common runout path, to contribute to filling topographic depressions and forming depositional landforms. Maximum depositional depths are commonly in the order of a few metres, consistent with the scale of topography in the areas subject to landslide hazards. Finally, we run the LSD model in two separate configurations:

1. **Mean annual landslide-sediment distribution** resulting from all possible volume-class ranges, triggers and movement types.
2. **Scenario-based landslide-sediment distribution** resulting from sediment generated by a given trigger scenario. We adopt the same methods for combining the effects of all source volumes and movement types as described above.

Although the parameters controlling sediment delivery (or runout) in each configuration are essentially identical, the manner in which the location and volume of source debris is determined is unique for each configuration, as discussed in in Sections 2.3.1.5 and 2.3.1.6.

Each LSD model output consists of an ensemble of 112 separate GPP model simulations to cover all considered triggers, volume classes, return intervals and movement types. The inputs for each model run were informed by mean annual sediment-production rates from the LSP model, as well as inputs specifically configured for the LSD model (see Appendix 5 for further details). In order to calculate the mean annual landslide-debris flux, we added together all calculated debris fluxes for all avalanche- and flow-type models, then applied a weighting to reflect the relative proportion of avalanche- and flow-type movements in the landscape before adding the output of both movement types together (see Section A5.7 for full details).

2.4.2 Results and Uncertainties

The mean annual landslide-debris flux for all considered triggers, volume classes, return intervals and movement modes in the vicinity of Kokiraki is presented in Figure 2.7. This indicates that, in general, landslide-debris flux is greater on steep slopes, close to the base of landforms with significant relief, and along the axis of convergent landforms (e.g. valleys), where debris is concentrated by the runout process. This is consistent with general observations in all geomorphologically active landscapes and provides confidence that the LSS, LSP and LSD models are capturing the most fundamental elements of landslide-debris-inundation hazards in this setting.

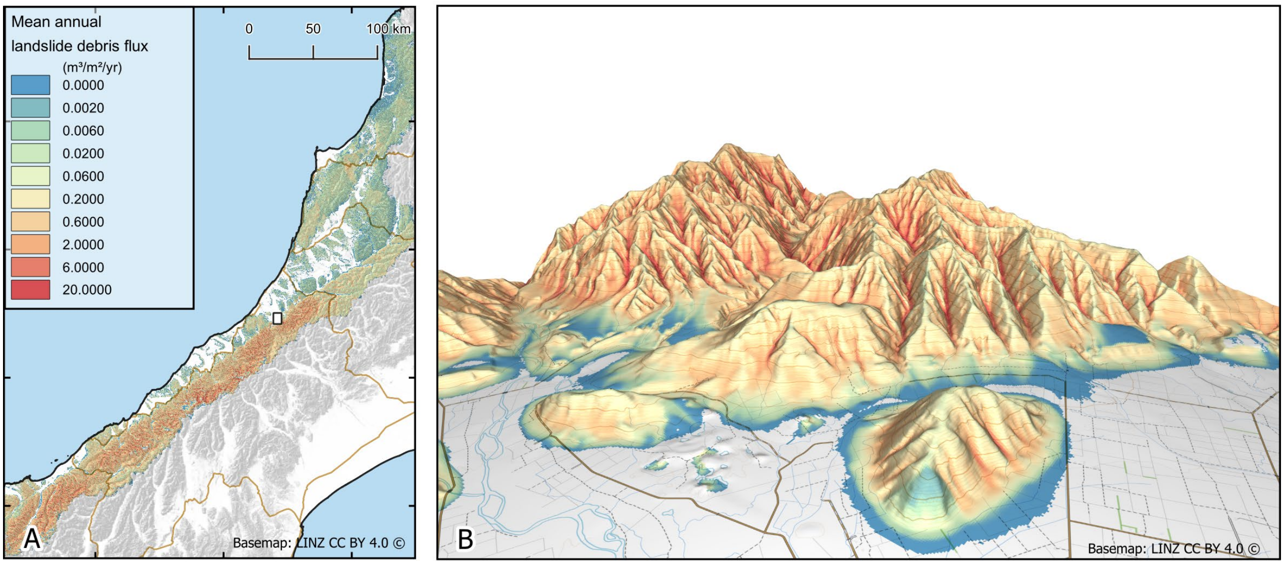

Figure 2.7 Present-day mean annual landslide-debris flux in the vicinity of Kokiraki (vertical exaggeration 1.5×).

Mean annual debris flux is fundamentally a function of landslide-debris production and landslide mobility. As a result, the magnitude of landslide-debris flux is greatest in areas where erosion rates are highest and slope gradients are sufficient to facilitate the down-slope movement of debris. The maximum extent of landslide-debris flux provides an indication of the maximum probable extent of landslide inundation from all kinematically feasible landslide-source regions. In most cases, this is defined by the largest (and therefore most mobile) feasible landslide source(s) in the contributing area, as determined by the kinematic-source model described in Section 2.3.1.2.

The magnitude of landslide-debris flux at a given location provides an integrated measure of landslide hazard in terms of the volume of landslide debris likely to pass a given location, although does not allow separation of the frequency or magnitude of potential debris-inundation events (hazard being defined here as the product of frequency and magnitude). As such, landslide-debris flux is particularly useful for assessing scenario- or event-specific hazards for which the inundation frequency is essentially 1 (assuming that all debris is released simultaneously), and the landslide-debris flux can therefore be considered to be the average magnitude of inundation at any given location. We note that the hazard assessment in this study uses a probabilistic model, and, unlike deterministic models, it therefore does not track specific landslide sources and runouts. As a result, debris flux observed at the location of discrete landslides following a triggering event is likely higher than the average landslide-debris flux estimated here. However, when summing the landslide-debris flux along a segment of a contour line (e.g. a road at the base of a slope), the cumulative flux can be expected to reflect the total debris that crosses that section. The longer the integration interval, the more accurately this cumulative landslide-debris flux represents actual debris volumes expected across the hill slope.

Aside from uncertainties associated with previously discussed LSS and LSP model inputs, landslide-debris flux outputs are a function of (1) the input variables used to define the fahrböschung ('avalanche') and PCM ('flow') model behaviours, (2) the general GPP model parameters and (3) the DEM used to simulate the runout paths. The source of uncertainties, and their effect on APLR, is discussed in detail in Section A5.9. Uncertainties in the fahrböschung model have the greatest impact on APLR near the landslide source (with a variation of up to 0.01× the most likely value at the closest location) but little effect near the maximum extent of the landslide-debris-inundation hazard zone, as more mobile flow-type movements commonly determine the inundation hazard far from the source. PCM-related uncertainties generally have minimal impact on APLR, as debris flow halts soon after the slopes become too gentle to support movement.

The random-walk component of the GPP model includes terms for debris spreading and persistence, reflecting how intact or fragmented the landslide mass is (see Section A5.3.2 for further details). These uncertainties can change the most likely APLR by up to 0.06× the most likely result near the source and by more than one million times at distant locations (where most-likely values are extremely small, so small variations therefore make large differences). However, as APLR at the most distant sites is usually negligible, such changes generally do not affect risk-tolerance thresholds for planning (see Section 5.4 for further details on risk-tolerance thresholds).

As landforms represented by the DEM determine the travel path of landslide debris, inaccuracies resulting from (for example) topographic changes since the original elevation data were generated in the 1940s (see Section 2.3.1.2), digital noise, interpolation errors or failure to accurately resolve landforms with lesser spatial extents can significantly change the travel path of debris sourced from smaller landslides. Smoothing of the DEM to improve runout-model performance for larger landslides mitigates much of the uncertainty associated with this input data (see Section A5.3.1 for further details). The accuracy of the national DEM employed here is estimated to generate spatial uncertainties of more than 6× the most likely APLR, while the 25 m resolution of the regional study is expected to generate uncertainties greater than 4× the most likely result. These two factors are the largest single source of uncertainty in this study, and care must therefore be taken when interpreting results (for example) in locations subject to inundation by smaller landslides, down-slope or smaller landforms (<100,000 m^2) or where topographic changes may significantly alter the path of landslide debris runout. See Sections A7.4 and A7.6.2 for further discussion on DEM-related LSD model uncertainties, as well as mitigation strategies involving the use of up-to-date LiDAR datasets.

2.5 Landslide Debris-Inundation-Risk Model

2.5.1 Overview

The LDIR model is employed to both determine the probability of landslide-debris-inundation events (*Pi*) and evaluate associated APLR across the region overseen by WCEM.

Mean annual landslide-debris flux is the product of contributing landslide-event frequencies and magnitudes. It is therefore not possible to directly derive inundation-event frequency and magnitude (as is required for risk assessment) from LSD model outputs. Instead, the frequency of inundation events can be determined by comparing the landslide-debris flux at a given location to the volume of debris that is expected to pass that location if a landslide were to occur. Termed the ‘characteristic landslide debris flux’, we calculate the volume of debris that is expected to pass through the DEM at every location for every volume-class range. By dividing the mean annual landslide-debris flux by the characteristic flux, we are then able to calculate the total frequency of inundation by summing that of every trigger, volume, return interval and volume-class range. We then convert the inundation event frequency (1/year) to an annual probability of inundation (1) by employing a Poisson probability formula. Details of this calculation, and a benchmarking of the characteristic landslide-debris flux estimation method, are presented in Section A6.2.

APLR provides a measure of the likelihood that, within a given year (or for a given event), the damage to a building due to landslide-debris inundation will be significant enough that the cost of repairing or restoring the property (re-instatement cost) exceeds the cost of completely replacing it (replacement cost) (see Section 2.1.3 for details). This risk measure assesses the probability that the damage reaches a threshold where repair is no longer economically viable, making full replacement the more cost-effective option. We employ an empirical estimate of undifferentiated building vulnerability compiled in Massey et al. (2019) from New Zealand and international data, where the vulnerability of buildings to landslide damage has been related to landslide-inundation depth (see Section A6.3). We assume that inundation depth is equal to the geometric-mean depth of the landslide source for each volume-class range and calculate APLR by converting the inundation-event frequency to an annual probability, multiplying this by the building vulnerability for each volume-class range. Given that all but the two smallest landslide volume-class ranges modelled in this study are assumed to generate inundation depths close to, or above, those required to cause 100% building damage, APLR varies from the inundation-probability metric only in areas where smaller ('family car'- or 'bus'-sized) landslides are dominant. Further details on this calculation are presented in Sections A6.3 and A6.4.

2.5.2 Results and Uncertainties

The annual probability of landslide-debris inundation for all considered triggers, volume classes, return intervals and movement modes is presented in Figure 2.8. This indicates that, in general, inundation probability is greatest within steep alpine catchments, where landslide debris-production rates are highest, as well as within convergent landforms (e.g. valley axes) and near the base of steep slopes, where the relatively steep path between the debris source and inundation location ensures that even smaller landslide events can reach the given location.

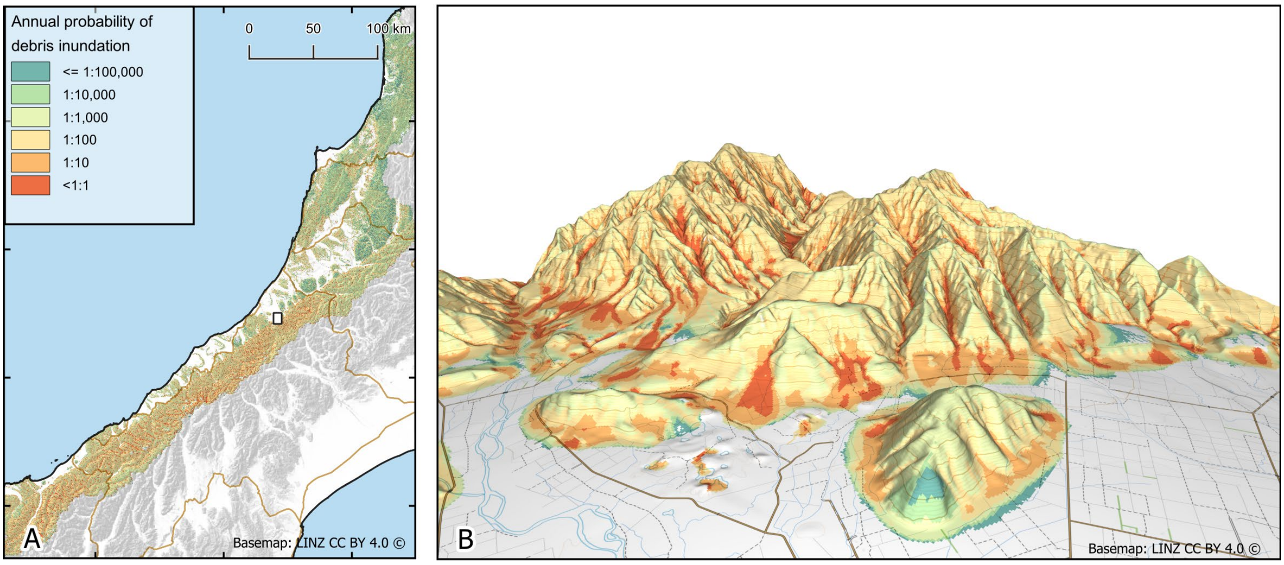

Figure 2.8 Annual probability of landslide-debris inundation in the vicinity of Kokiraki (vertical exaggeration 1.5×).

Landslide debris-production rates (presented in Figure 2.3) and landslide-debris flux (presented in Figure 2.7) both demonstrate a strong contrast between high rates in the mountainous terrain to the east of the Alpine Fault and significantly lower rates in less rugged topography towards the coast (west of the Alpine Fault). However, annual landslide debris-inundation probabilities demonstrate significantly less contrast between these two regions (Figure 2.8), as the lesser topographic relief west of the Alpine Fault limits debris production to smaller landslide classes. This effectively increases the predicted frequency of landslide events, as more small landslides are required to maintain a given debris-production rate. Despite significantly lower debris-production rates to the west of the fault, the probability of inundation therefore remains relatively high, as a relative increase in predicted frequencies partially balances the lesser availability of landslide debris in these areas (e.g. north of Greymouth).

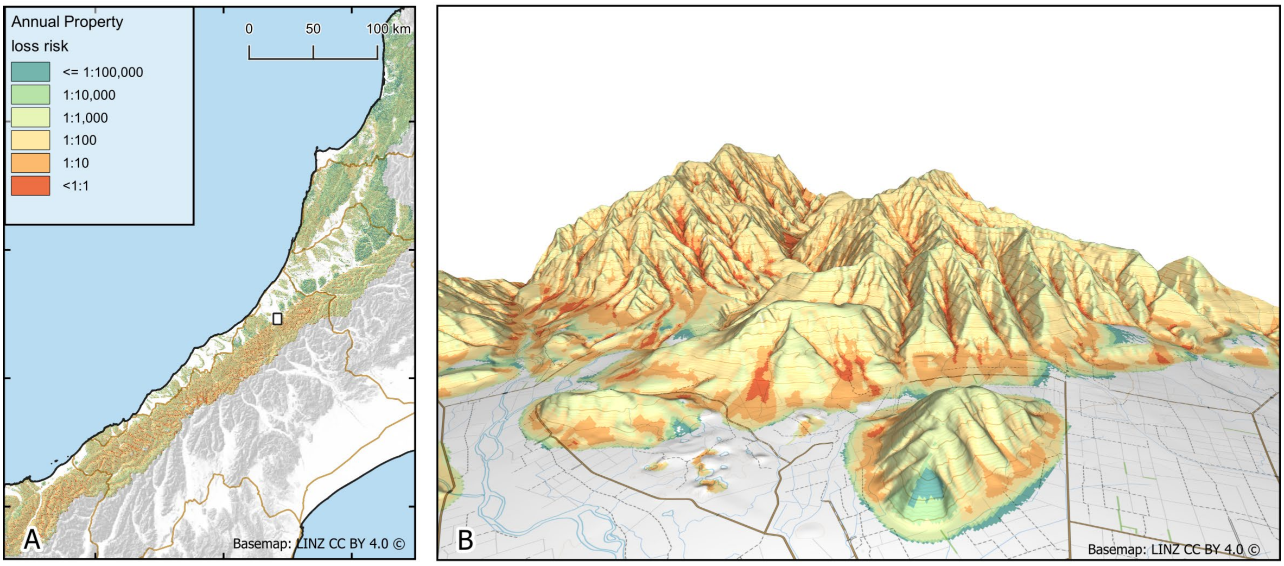

Figure 2.9 Calculated annual property loss risk in the vicinity of Kokiraki (vertical exaggeration 1.5×).

As APLR is closely tied to inundation probability, the two measures follow a very similar pattern across the region overseen by WCEM, with APLR typically slightly lower than P_i, reflecting the lesser vulnerability of buildings to smaller events (Figure 2.9). The most significant deviations between P_i and APLR occur in areas in which these smaller landslide classes dominate the risk calculation, such as adjacent to slopes from which only smaller landslides can be generated, and in debris-flow channels adjacent to steep slopes, where landslide debris flux is accumulated from a large number of cells generating shallow landslides.

APLR in the vicinity of Kokiraki is presented in Figure 2.9. Here, the annual probabilities of potentially destructive inundation events occurring along the axis of large debris-flow channels are commonly as high as 5% (0.05 1/yr), indicating that, on average, potentially destructive inundation events can be expected to occur in debris-flow channels every 20 years. With approximately 20 large debris-flow channels in the Kokiraki area, we may therefore expect to observe potentially destructive debris flows somewhere in the region every year. APLR in smaller debris channels and on planar slopes or convex fans tends to be between 0.1% and 2%, indicating that potentially destructive inundation events on individual slopes are likely to occur with a frequency of one in every period of 50–1000 years. This is consistent with general observations of event frequencies in this region and provides confidence that the LDIR model is capturing the most fundamental inundation processes in this setting (see Section 3.1 for further discussion on the frequency of damaging inundation events).

The LDIR model has uncertainties related to estimating the characteristic landslide-debris-inundation event magnitude down-slope of landslide sources, the assumed inundation depths for each volume class and the vulnerability of structures to debris inundation. While the first factor affects both probability and APLR calculations, the latter two only influence APLR. Uncertainty in event magnitude is difficult to quantify due to its dependence on debris-travel paths. However, a conservation-of-mass approach helps constrain characteristic fluxes, keeping event-frequency variation within one order of magnitude (see Section A6.2). Testing uncertainties in inundation depth and structure vulnerability by varying the critical depth from 2 m to 10 m shows a minimal impact on APLR – with a variation of up to 0.03× the most likely value at all locations (see Sections A6.5 and A7.5 for further details).

Figure 2.10 Landslides and debris flows generated by the December 2019 West Coast storm. The property in the foreground has a calculated present-day APLR of 5.3%. The calculated APLR for an RCP6 scenario is 5.7%. The risk from earthquake-induced flow-type movements is similar. There is no risk associated with avalanche-type movements from either earthquake- or rainfall-induced landslide events, as these do not travel as far as the property's location. We note that this assessment is based on a regional analysis and refer readers to Section 5.5 for further details on site-specific considerations. (Photo credit D Townsend, Earth Sciences New Zealand).

2.6 RCP6 2081–2100 Climate-Change Scenario

Consideration of the RCP6 2081–2100 climate-change scenario requires an adjustment of both the LSS model, in order to capture the spatio-temporal effects of increased landslide-induced precipitation on landslide-source generation, and the LSP model, in order to capture the effect of increased debris production as a result of more frequent landsliding.

To evaluate the change in probability of rainfall-induced landsliding for the RCP6 2081–2100 climate-change scenario, we increase 24-hour precipitation estimates for each LSS model scenario in line with NIWA's recommendations for the HIRDS V4 precipitation model (see Section A3.5 for further details). Figure 2.11 presents landslide-source probabilities for this climate scenario, as well as a comparison of the total change in landslide-source probability from present-day.

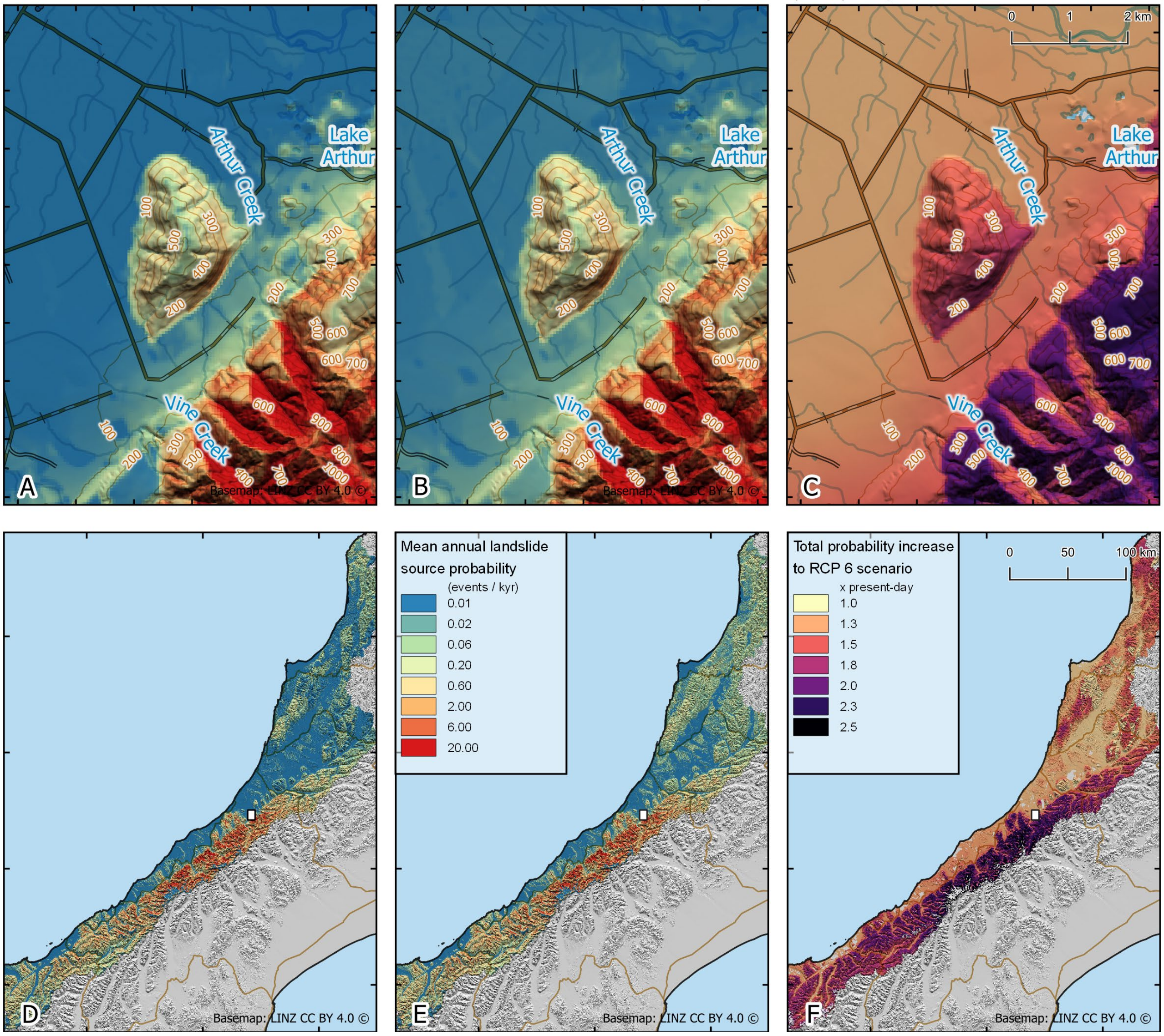

Figure 2.11 Selection of landslide source-susceptibility model outputs for the RCP6 2081– 2100 climate scenario. (a, d) Mean annual probability of rainfall-induced landslide initiation. (b, e) Total mean annual probability of landslide initiation, (c, f) Change in total mean annual source probability from present-day probability. Legend categories are consistent across maps (a), (b), (d) and (e) and maps (c) and (f). The location of the Kokiraki maps are indicated by a white box on the regional overview maps.

Due to the lack of regional data on how sediment-production and -transport rates may change under various climate-change scenarios, we use the change in LSS model rainfall-induced landslide probability – from present day to the RCP6 2081–2100 climate scenario – as an indicator for potential increases in erosion rates relative to long-term averages. We assume that (1) sediment-production rates from earthquake-induced landslides will remain consistent with present-day levels under the RCP6 2081–2100 climate scenario and (2) landslide-volume distributions will remain consistent with present-day observations. We then calculate the relative increase in rainfall-induced landslide debris production as a function of increased landslide susceptibility. This method is similar to that of Reid and Page (2003) and Neverman et al. (2023). Scaling the present-day rainfall-induced landslide debris-production rate with the LSS RCP6 2081–2100 climate scenario model output therefore enables us to capture the predicted immediate spatio-temporal increase in sediment production as existing unstable sources are exhausted. See Section A4.7 for a full description of landslide debris-production rates for this climate scenario.

The average increase in mean annual landslide sediment production derived from this method is approximately 50%. Unsurprisingly, this is not dissimilar to the predicted 31% increase in sediment yields for the same climate-change scenario in the West Coast region reported in Neverman et al. (2023). Figure 2.12 presents a comparison of mean annual debris flux for the present-day and RCP6 2081–2100 climate scenarios. In general, the maximum extent of landslide-debris inundation does not vary significantly, as the location and characteristics of the largest kinematically feasible landslides are unchanged. However, within this extent, the magnitude of mean annual debris flux is increased by up to an order of magnitude on the steep, linear slopes in the mountains in the southeast of the area. Although landslide debris production in this area only increases by approximately 2×, the cumulative effect of this debris running out downhill can cause the overall landslide hazard on these slopes to increase by an order of magnitude or more. That said, the increase in mean annual debris flux on debris fans extending from the range front is much more in line with the 2× increase in debris production. This latter increase is similar to observations throughout the region, where debris fans extending from relatively short, moderate gradient hill slopes demonstrate an approximate doubling of landslide-debris flux as a result of more debris being assigned to larger volume landslides in the source areas.

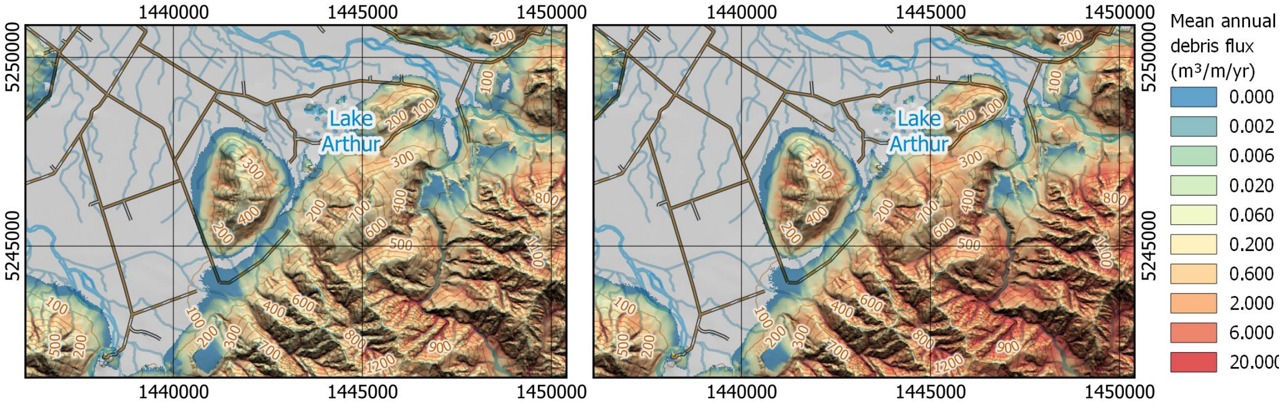

Figure 2.12 Left: Present-day mean annual landslide debris flux. Right: RCP6 2081–2100 mean annual debris flux derived from the ensemble of landslide sediment-distribution model results.

Changes in APLR in the RCP6 2081–2100 climate scenario are primarily a function of the landslide-debris flux and vulnerability of buildings to future landsliding. As we assume that landslide-volume distributions remain unchanged in the RCP6 2081–2100 climate scenario, neither the mobility of landslides nor the vulnerability of structures to inundation changes. As a result, the change in APLR is closely tied to that of landslide-debris flux, and we observe an approximate doubling of APLR in moderate- to low-gradient hill slopes where vulnerable structures are most commonly located. This is discussed further in Section 3.1.4. As mentioned in Section 2.3.1.6, a lack of constraints on input variables associated with the RCP6 2081–2100 climate scenario preclude the explicit quantification of uncertainties related to this scenario in this study. Instead, we recommend adopting the 2-sigma uncertainty for equivalent present-day outputs as the estimated 1-sigma uncertainty for the RCP6 2081–2100 scenario. See Sections 5.3.2 and A7.5 for further discussion on this topic.

2.7 Field Reconnaissance

Field reconnaissance was undertaken by a team of two GNS Science engineering geologists during 10–12 August 2023. The purpose of this reconnaissance was to (1) validate preliminary LSS and LSD model results, (2) consider characteristic debris-flux indicators and (3) identify additional risk contributors not considered to date. The reconnaissance focused on areas presenting a range of geomorphic characteristics and associated hazard scenarios and covered a region extending from Hokitika River in the south to Mokihinui in the north. An overview of the 89 localities visited during the field reconnaissance is presented in Figure 2.13. Geolocated observational data was recorded in a custom mobile application for later integration in GIS (geographic information system), alongside

182 geo-located reference photographs. Observations were classified as relating to (1) landslide source locations (13 entries), (2) landslide runout and/or fan extents (36 entries) and (3) commentary on the geomorphological setting or preliminary landslide-debris-inundation model performance (40 entries). See Section A5.5.3 for further details on the application of field observations to runout model validation.

Figure 2.13 Overview of field data collection during 10–12 August 2023. (a, b) Field photo locations and observation categories overlain on mean annual landslide-debris flux. (c) Debris-flow fan south of Lake Arthur (looking south). Calculated mean annual landslide-debris flux at the photo location is 0.8 x 10^{-3} $m^3/m^2/yr$, and the mean annual APLR is 0.19%. (d) Shallow landslides on hillsides to the north of Lake Kaniere (looking northeast). Calculated mean annual landslide-debris flux at the photo location is 2.2 x 10^{-5} $m^3/m^2/yr$ and APLR is 0.0012%. Landslide-debris flux at the location of the observed landslides is 6 x 10^{-3} $m^3/m^2/yr$ and APLR is approximately 0.0013%. Legend categories are consistent across (a) and (b). The location of the Kokiraki maps are indicated by a white box on the regional overview maps.

3.0 Discussion

3.1 Consistency with Actual Experience

3.1.1 Alpine Fault Scenario Impacts

A comparison of the total sediment deposition resulting from the Alpine Fault scenario model and estimates of probable sediment production as a result of an Alpine Fault magnitude 8 (AF8) event provides a test for the LSP and LSD models. Robinson and Davies (2013) evaluated the probable total volume of landslide debris generated by an AF8 event based on a comparison with global earthquake-induced landslide catalogues. They estimated that over 1 billion m^3 of landslide debris was likely to be created by the event. Based on results from the Alpine Fault LSD model presented this study, the expected total landslide-sediment deposition is approximately 17 billion m^3. Although a broad range, these two values are within 1.25 orders of magnitude. Given the uncertainties inherent in both methods, and differences in the data used (i.e. the AF8 susceptibility model was derived separately from the EIL models used to calculate annual landslide susceptibility), we consider the results to be within error.

3.1.2 Rainfall-Induced Landslide Damage

In order to evaluate the performance of the risk models presented here, we compare the predicted rate of annual building loss for all residential buildings in the study region to annualised records of natural landslide damage within the Natural Hazards Commission (NHC) Toka Tū Ake claims database.

We make use of a compilation of property data for the region (Scheele et al. 2023), based on CoreLogic property data, Land Information New Zealand (LINZ) property outlines and LINZ property parcels in order to classify the usage category for buildings across the region. We assume that all records classified as the 'Residential' or 'Lifestyle' use classes are residential buildings and that all listed claims are associated with rainfall events. In total, the dataset contains 48,000 buildings in the study area, of which 15,000 can be classified as residential. In order to evaluate the predicted average annual number of residential APLR events in the area, we sampled APLR at the centroid of all buildings and converted these into loss-event frequencies for both present day and RCP6 2081–2100 model climate scenarios. Results for both scenarios are presented in Figure 3.1.

In order to understand the principal driver of risk at all building locations in the study region, we separated out the building-loss frequencies associated with earthquake- and rainfall-induced avalanches and slides. The annual earthquake-induced landslide risk is approximately 7× that of rainfall-induced landslides. Figure 3.1a indicates that risk at the location of residential buildings is dominated by inundation from flow-type movements for both rainfall- and earthquake-induced landslides. This is perhaps unsurprising, given the significantly greater travel distance of this movement mode, but the very low relative proportion of avalanche-type movements intersecting building locations is reassuring, as these hazards are commonly associated with the presence of steep slopes and are therefore perhaps more readily recognised and avoided when selecting residential building sites.

The sum of modelled complete economic loss-event frequencies for rainfall-induced landslides under present-day climate conditions indicates an average of 1.6 residential-building losses across the study region per year. This compares favourably with the NHC Toka Tū Ake claims data for the study region, which shows that private-property owners have registered a total of 52 natural-landslide-related claims since 1997. On average, this equates to 2.0 claims per year, and, although no data are available to determine the proportion of economic loss associated with these claims, we expect many to be less than full-loss events. This higher frequency of claims therefore aligns with our estimate of the equivalent number of complete building losses. Given that there have been no significant landslide-inducing earthquakes since 1997, we are satisfied that (1) the NHC Toka Tū Ake landslide-related claims reflect rainfall events and (2) the APLR calculated in this study is adequately capturing the broader risk to existing residential-building stock. We note this is a statistical analysis of regional trends, appropriate for the regional-scale hazard and risk analysis presented here.

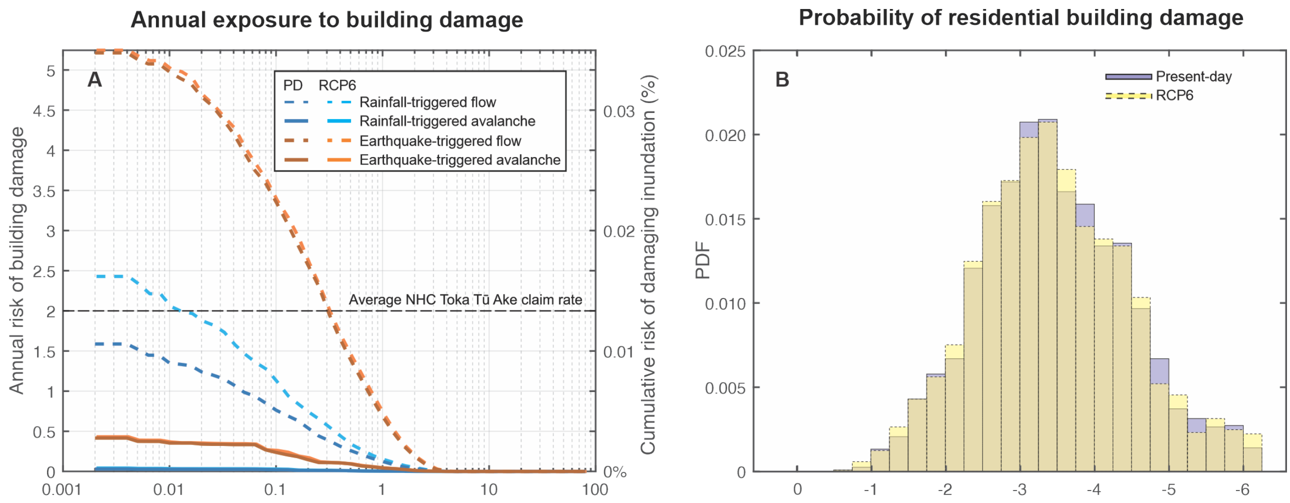

Figure 3.1 Annual property loss risk sampled at residential-building locations throughout the region overseen by West Coast Emergency Management. (a) Annual exposure to building damage: illustrates how the progressive exclusion of high-risk-building locations affects the overall annual property loss risk, showing that rainfall- and earthquake-induced flow movements dominate the risk profile. The risk is further differentiated between present-day (PD) and future (RCP6) climate scenarios. Values on the left *x* axis indicate risk in terms of equivalent number of buildings with 100% damage, while the axis to the right indicates the total proportion of residential buildings with 100% damage. (b) Probability of residential building damage: represents the probability density function (PDF) of building-damage event-return intervals, indicating little systematic change in inundation probabilities under future climate conditions (RCP 6), as the majority of risk is associated with earthquake-induced landslides (which we assume are unaffected by climate change).

We evaluate the exposure profile of all residential buildings across the region by progressively excluding the highest risk structures from the datasets. This indicates that approximately 2% of all residential buildings (~300 structures) account for almost all rainfall-induced landslide risk. A slightly larger proportion (~3%) of structures account for the majority of earthquake-induced landslide risk, likely reflecting the greater reach of the generally larger volume events.

The annual risk of building damage from rainfall-induced landslides under the RCP6 2081–2100 climate-change scenario is estimated to be approximately 50% higher than present-day (Figure 3.1a). This is broadly in line with the increased landslide susceptibility and landslide-debris production in areas where the majority of the population lives. The estimated risk from earthquake-induced landslides at the location of residential buildings is unchanged under this future climate scenario. This reflects our assumptions that allow for greater rainfall-induced debris production under the future climate scenario, while leaving earthquake-induced landslide debris production unchanged. However, we note that significant uncertainties are associated with these assumptions and therefore suggest that this result should be treated with caution (see Sections 2.3.1.6 and 5.3.2).

3.1.3 Insights into an Alpine Fault Magnitude 8 Scenario

To evaluate the potential impact of an AF8 scenario on property damage, we can assess APLR at CoreLogic residential-building locations (Scheele et al. 2023) for this scenario. Results indicate that total APLR in the region equates to the equivalent of 477 buildings classified as either ‘Residential dwelling’ or ‘Lifestyle’ suffering total economic loss in the region. The majority of APLR is associated with flow-type movements (83%), while a lesser percentage is associated with avalanche-type movements (17%; see Figure 3.2a). In total, we find that 2400 ‘Residential dwelling’ or ‘Lifestyle’ buildings are located within the maximum extent of the AF8 APLR. As discussed in Section 2.5.1, APLR provides an indication of the proportion of damage that a building is likely to sustain, rather than the number of buildings that suffer complete damage. As such, it is possible that all buildings within the maximum extent of the AF8 APLR suffer some degree of inundation damage. Figure 3.2b indicates the distribution of APLR across all of these buildings, indicating that, of the buildings that may be inundated by debris, the majority can be expected to incur damage equalling approximately 30% (i.e. APLR of 0.3) of their replacement cost. Uncertainties associated with these calculations are discussed in detail in Section A7.5.

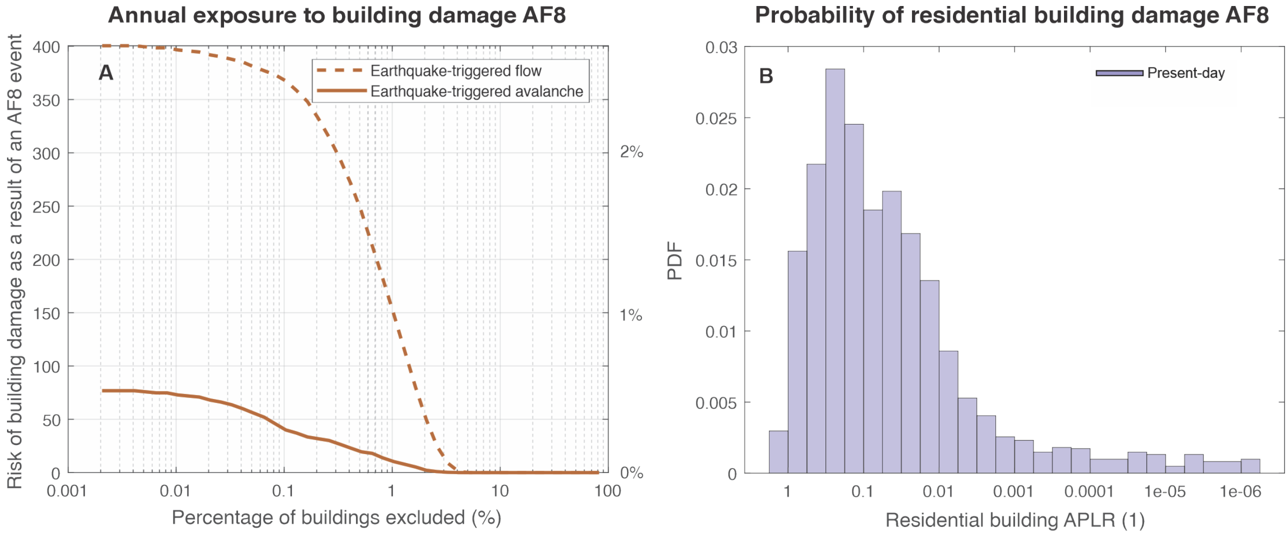

Figure 3.2 Expected annual property loss risk (APLR) for residential buildings in the region overseen by West Coast Emergency Management.

3.1.4 Insights into Overall Landslide Debris-Inundation Risk

As well as sampling present-day and future APLR at the location of residential buildings, we can gain insight into the hazard and potential risk across the landscape by sampling potential APLR at random points across the region (i.e. not just at building locations). In this case, we sampled 10,000 random points and, as with the residential-building analysis, separated out rainfall- and earthquake-induced flows and avalanches for the present-day and future climate scenarios. In order to maintain consistency with the insights presented in Sections 3.1.1–3.1.3, we employed APLR as our risk metric, although it is not expected that a building will be present at any of the random locations. The results of this landscape-wide assessment are presented in Figure 3.2. Similar to APLR sampled at building locations, we observe significantly higher risks associated with flow- rather than avalanche-type movements. However, we also observe a number of distinct differences, including that:

- The probability of damage to hypothetical buildings at random locations is between 3× and 10× higher than that of actual residential-building locations for most triggers and movement types. This suggests a general mitigation (intentional or otherwise) of associated hazards by good building-site selection.
- In terms of the relative proportion of flow- versus avalanche-type movements, the random locations indicate a much higher proportion of APLR associated with avalanche-type landslides. Again, this indicates that good, or fortuitous, site selection has largely mitigated avalanche-type landslide hazards at building locations.
- APLR associated with flow- and avalanche-type rainfall-induced landslides at random locations increases by approximately 60%,and 100%, respectively, under the RCP6 2081–2100 climate-change scenario. Risks associated with earthquake-induced landslides are unchanged, as should be expected based on the model inputs and assumptions.

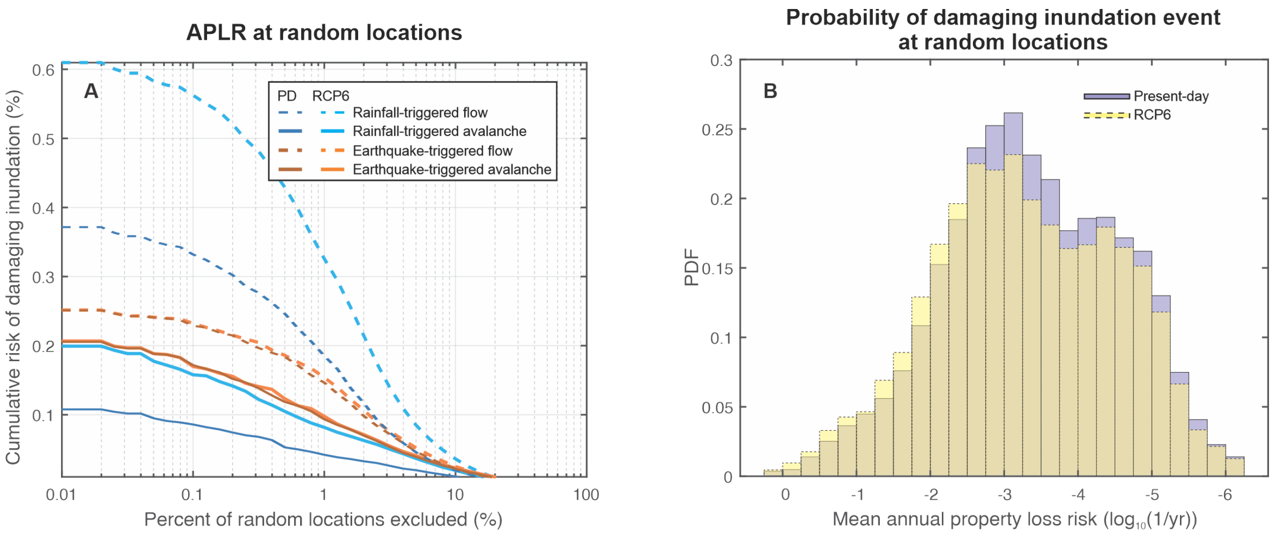

Figure 3.3 Hypothetical annual property loss risk (APLR) sampled at random locations throughout the region overseen by West Coast Emergency Management.

3.2 Landslide Source to Inundation Process Model Sensitivity to Key Uncertainties

The regional landslide-debris-inundation assessment presented here has been undertaken within the constraints of the datasets described in Appendix 2. In order to ensure consistency across the region, we limit our analysis to regionally consistent datasets. As a result, the current dataset contains a number of limitations, which may lead to under- or over-estimation of local hazard extents and associated risk. Sensitivities associated with LSS, LSP, LSD and LDIR model inputs and assumptions are mentioned alongside results in Section 2; expanded upon in Sections A3.6, A4.8 and A5.9; and discussed in detail in Appendix 7.

In order to quantitatively assess the impact of uncertainties associated with individual variables, we evaluate changes in calculated APLR at a series of locations distributed down-slope of a theoretical landslide source in a simplified 1D model (introduced in Section 2.1.5). This allows us to efficiently explore the input-parameter space without undue computational cost. However, we do note that this is a simplified model, designed to capture magnitude and trends in impacts, and is not designed to explicitly simulate inundation in a given geographic setting (see Appendix 7 for further details). Key findings from this assessment are discussed in the remainder of this section.

The down-slope movement of landslide debris is the principal hazard considered in this study, and, as such, uncertainties associated with factors controlling the potential size of landslides and long-term landslide debris-production rates have some of the greatest impacts on modelled APLR. These uncertainties include those associated with determining kinematic feasibility and deriving long-term debris-production rates, quantifying variability across the landscape (e.g. due to recent erosion, excavation or rejuvenation of existing creeping landslides) and forecasting the impact of climate change on future fracturing, weathering and erosion rates. Associated individual variable uncertainties can cause variations in the calculated APLR of up to about 2× the most likely value or more, depending on the scale of the landform, its history of modification or instability and the location of elements at risk.

As well as debris-production rates, variables affecting the volume of potential landslide sources also have considerable impact on the calculated APLR. In particular, the geometric-mean volume of earthquake- and rainfall-induced landslides, as well as the cohesion of critical joints, affect the potential volume distribution of landslides and where these may occur in the landscape. As larger landslides have the potential to travel greater distances, uncertainties associated with these variables indirectly control the distance that landslide debris travels and can cause variations in the calculated APLR of up to about 0.5× the most likely value.

As the LSD model simulates the movement of landslide debris down-slope through a DEM, uncertainties associated with the manner in which the DEM represents present-day topography can have a significant impact on the trajectory and extent of modelled landslide runout. In general, debris tends to travel farther, with less change in direction, on a coarser-resolution DEM. As a result, the extent of APLR can be greater on a lower-resolution (smoother) DEM, although the channelisation of debris, and therefore inundation hazard, along preferential travel paths will tend to be under-estimated. In addition, a more accurate DEM can be expected to better capture smaller landforms capable of re-directing or channelising debris, increasing deposition along the runout path and reducing the ability of the landslide runouts to spread. Both effects will reduce the spatial risk of landslide debris inundation.

The location and potential volume of landslide-source areas is based on an analysis of topography represented by the DEM employed in the LSP model. In this study, the national DEM (LINZ 2014) is derived from aerial photographs captured in the 1940s and has been down-sampled to 25 m resolution, consistent with the contracted specification. Failure of the DEM to accurately capture present-day topography can lead to mis-representation, or non-identification, of potential landslide-source areas. A local comparison of APLR results based on the national DEM with those calculated using a recent LiDAR-derived DEM in the Greymouth area indicates that the accuracy of the national DEM alone introduces uncertainties of ±0.79 orders of magnitude (see Sections A7.6.2 and A7.6.3). Substituting the DEM used in this study with a LiDAR-derived DEM and running the analysis at a higher (8 m) resolution can be expected to reduce the geometric mean APLR by approximately 3.4×, while also reducing uncertainty by more than half an order of magnitude (see Section A7.6).

The uncertainties stated here are valid only for APLR outputs. Additional analysis is required to calculate uncertainties on other outputs (e.g. landslide-debris flux and probability of inundation).

4.0 Project Deliverables

The landslide-debris-inundation hazard and risk analysis evaluates the probability of landslide initiation and debris travel as (1) the mean annual product of foreseeable rainfall- and earthquake-inducing events and (2) a result of three credible landslide-inducing scenarios. These include:

- **Scenario 1:** Present-day precipitation triggers based on 50-, 100- and 250-year ARI 24-hour precipitation totals derived from the HIRDS V4 model.
- **Scenario 2:** Future precipitation triggers based on 50-, 100- and 250-year ARI 24-hour precipitation totals derived from the HIRDS V4 model rainfall projections for a future RCP6 scenario (Carey-Smith et al. 2018).
- **Scenario 3:** A regional earthquake trigger based on 100-, 250-, 500- and 1000-year ARI PGA derived from the New Zealand NSHM 2022 (Gerstenberger et al. 2022).
- **Scenario 4:** An Alpine Fault earthquake event (e.g. based on PGA derived from the AlpineF2K rupture model [Bradley et al. 2017]).

All model outputs are provided as geolocated rasters at a nominal spatial resolution of 25 m. The mean annual landslide-debris flux, mean annual probability of inundation (P_i) and mean APLR may be the most useful datasets in terms of hazard and risk, respectively.

- **Landslide-debris flux:** This dataset describes the average volume of landslide debris likely to pass a given location in a given year or in response to a given trigger. Landslide-debris flux can be useful for determining landslide-hazard zones (i.e. areas that have the potential for debris inundation) and scoping the scale of mitigation and/or remedial options in areas where inundation risk is deemed unacceptable.
- **Probability of inundation (P_i):** This dataset describes the annual probability of landslide debris of any volume inundating a given location. It can be useful for determining areas at risk of (or 'susceptible' to) any inundation events. P_i does not consider the vulnerability of elements in the study region.
- **APLR:** This dataset describes the annual probability of landslide debris damaging a hypothetical building beyond repair. It can be useful for determining areas at risk of (or 'susceptible' to) significant inundation events. APLR cannot be directly transferred to evaluate risk to elements with differing vulnerabilities (e.g. people, vehicles or isolated power/telecommunications infrastructure).

Due to uncertainties associated with the calculation of landslide debris-inundation hazard and risk in this study (see Section A7.6), we recommend that a maximum zoom be fixed at 1:500,000 for publicly facing GIS applications and/or data be down-sampled to a minimum pixel size of 150 m. These limitations may be relaxed where model results are derived from LiDAR-based DEM products (see Section A7.6.2).

Key landslide-debris flux and APLR deliverables are briefly described in the following section.

4.1 Deliverables for Landslide-Debris Flux

4.1.1 Mean Annual Hazard Maps (25 m resolution raster)

These maps indicate mean annual landslide-debris-flux hazard throughout the regions integrated over all foreseeable rainfall- and earthquake-inducing events (e.g. how much debris is likely to pass a specific location *in a given year* [m^3/m^2]).

To view the present-day mean annual landslide-debris flux for the region overseen by WCEM, see the dataset named '*WCEM_PD_MaterialFlux_MeanAnnual_25m*'.

4.1.2 **Hazard Maps for Scenarios 1–4** (25 m resolution raster)

These maps indicate landslide-debris-flux hazard throughout the region as a result of landslides generated by events in Scenarios 1–4 (e.g. how much debris is likely to pass a specific location *for a given event* [m^3/m^2]).

To view the present-day landslide-debris flux associated with a HIRDS V4 50-year ARI precipitation event for the region overseen by WCEM, see the dataset named '*WCEM_PD_MaterialFlux_HIRDS_ARI50_25m*'.

4.2 Deliverables for Probability of Inundation

4.2.1 **Mean Annual Probability Maps** (25 m resolution raster)

These maps delineate mean annual probability of inundation by any volume of landslide debris (e.g. the probability of some debris passing this location *in a given year*).

To view the RCP6 2081–2100 climate-scenario mean annual probability of inundation for the region overseen by WCEM, see the dataset named '*WCEM_RCP6_PI_MeanAnnual_25m*'.

4.2.2 **Scenario-Specific Maps** (25 m resolution raster)

These maps delineate the probability of inundation by any volume of landslide debris in a given scenario (e.g. the probability of some debris passing this location *in this scenario*).

To view the RCP6 2081–2100 climate-scenario AF8 scenario-specific probability of debris inundation for the region overseen by WCEM, see the dataset named '*WCEM_RCP6_PI_AF8_25m*'.

4.3 Deliverables for Annual Property Loss Risk

4.3.1 **Mean Annual Risk Maps** (25 m resolution raster)

These maps delineate mean annual probability that a hypothetical building will sustain damage such that it is uneconomic to repair (e.g. the *probability of a building being destroyed* in a given year).

To view the present-day mean annual APLR risk for the region overseen by WCEM, see the dataset named '*WCEM_PD_APLR_MeanAnnual_25m*'.

4.3.2 **Scenario-Specific Risk Maps** (25 m resolution raster)

These maps delineate the probability that a hypothetical building will sustain damage in a given scenario such that it is uneconomic to repair (e.g. the *probability of a building being destroyed* in a given scenario).

To view the present-day mean annual scenario-specific APLR risk for the region overseen by WCEM, see the dataset named '*WCEM_PD_APLR_AF8_25m*'.

5.0 Applying these Results

Application of Results for Planning Purposes
Key Metrics
• **Landslide-debris flux** (m^3/m^2/year): Volume of debris expected to pass through a location annually. • **Probability of inundation (P_i)** (1/year): Likelihood that debris reaches a location in a given year. • **Annual Property Loss Risk (APLR)** (loss/year): Probability that a generic building at a location will be damaged beyond economic repair annually.
Risk-Tolerance Thresholds
• A risk-tolerance threshold for acceptability of **APLR = 1×10^{-5}/year** (1 in 100,000) is recommended as a starting point for existing risks. • Thresholds may vary depending on activity type, societal norms and planning level.
Uncertainty Interpretation
• Adopt uncertainties consistent with the **1-sigma** (standard deviation) (84^{th} percentile) confidence interval. • **Present-day climate:** APLR uncertainty at 1-sigma is **±1.25 orders of magnitude**. • **RCP6 2081–2100 climate scenario:** APLR uncertainty at 1-sigma is **±2.75 orders of magnitude**.
Practical Implication
• When applying a risk tolerance threshold, uncertainty must be included. For example, if the threshold is **1×10^{-5}/year** and uncertainty is **±1.25 orders of magnitude**, then any location with **APLR less than 5.6×10^{-7}/year** is statistically unlikely to exceed the threshold. • This means that locations with APLR values below the threshold adjusted for uncertainty can be considered as having **Acceptable Risk** under the current planning framework.
Use of Results for Planning Purposes (refer to Table 5.1).
• Residual uncertainties limit the application of outputs for specific planning activities (see Table 5.2). • Raster datasets should be presented at a maximum zoom of **1:500,000** for publicly facing GIS applications and/or down-sampled to a minimum pixel size of **150 m**. • Current outputs are suitable for **Level A screening** and possibly **Level B** planning purposes. • Reducing uncertainty by using new LiDAR data may make outputs suitable for **Level B–C** applications. • Outputs are not suitable for planning applications considered for **Level D** assessments without site-specific refinement. • Where risk exceeds thresholds or uncertainty is high, further analysis should: - Re-evaluate using higher-resolution data (e.g. 8 m LiDAR). - Incorporate local geotechnical and hazard information. - Re-classify sites based on refined risk metrics.
Refer to **Section 5.3.3.2** for the decision-making framework and **Sections 5.4** and **5.5** for recommended next steps and re-evaluation procedures.

5.1 Overview

Application of results from landslide-hazard or -risk analyses requires careful consideration. This report presents a ‘regional-scale basic quantitative landslide-debris-inundation hazard and risk analysis’. Where applicable, the methods employed here follow appropriate parts of the Australian Geomechanics Society framework for landslide-risk management (AGS 2007); key differences relate to the metric used to describe the frequency of landsliding and to derive the probability of spatial impact (see Appendix 8 for further details). The level of detail of the analysis is similar to ‘Level D’ basic quantitative hazard and risk analysis, as outlined in Table 4.2 of the Landslide Planning Guidance (de Vilder et al. 2024), although we note that a novel approach has been employed to calculate landslide debris-inundation hazard. We suggest that the level of residual uncertainty currently limits the application of results to 'Level A' or 'Level B' planning purposes (de Vilder et al. 2024). We discuss determination of the required level of certainty, associated applicability of results and risk-acceptance thresholds for various applications in the following sections.

The application of LDIR model results should be evaluated in terms of hazard and risk, uncertainty and statistical confidence. Specifically, these can be defined as:

- **Risk:** The potential impact of a hazard, taking into account the likelihood of the event, vulnerability of affected entities and extent to which these are exposed. Expressed as an annual probability of occurrence, for example, 10^{-5} per annum.
- **Uncertainty:** The degree to which a value, prediction or outcome is unknown or variable. Expressed as an expected variation in the value of the prediction, for example, ± 1 order of magnitude.
- **Statistical confidence:** A statistical measure of the percentage of results that can be expected to fall within a specified range. Expressed as a percentage of all results, for example, 95%.

Although commonly used interchangeably, 'uncertainty' and 'statistical confidence' are distinctly different aspects of a hazard- or risk-based dataset. Here, the application of results from such datasets should therefore include determination of acceptable/tolerable thresholds for all three aspects. Figure 5.1 illustrates confidence intervals associated with a standard normal distribution. These statistical confidence intervals describe the proportion of data that falls within a given range of the mean (for example) in a normally distributed dataset. The value of the uncertainty represents the absolute magnitude of the variation at a given confidence level and must be derived from the dataset itself. In the following sections, we outline hazard and risk outputs from this study and suggest methods for determining appropriate risk, uncertainty and confidence thresholds.

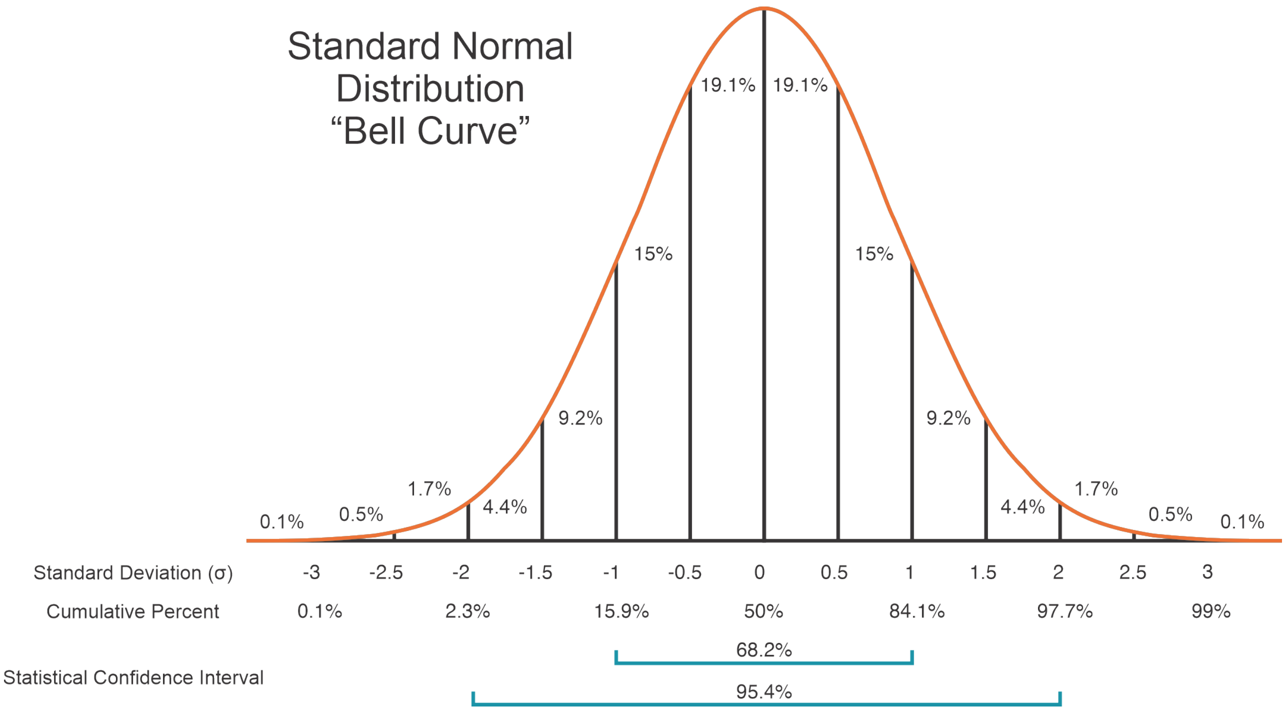

Figure 5.1 Standard normal distribution displaying the relationship between statistical confidence intervals described as standard deviations (sigma), cumulative percentage and central coverage probabilities.

Table 5.1 Five levels of susceptibility, hazard and risk analysis, with recommended applications (modified after Table 4.2 in de Vilder et al. [2024]).

Level	Description	Uncertainty / Confidence Level	Application
A	Susceptibility analysis	‘Significant uncertainty remains over the frequency of landslides … the impact of climate change …’	This is the gateway assessment that determines where further assessment is required and where it will not be required.
B	Hazard analysis	‘Significant uncertainty remains regarding potential consequences … Uncertainty may also remain regarding landslide frequency …’	This is the recommended minimum for plan-making and plan changes for rural (rural lifestyle and settlement), commercial and mixed use, industrial, residential (large lot or low density) and future urban zones.
C	Semi-quantitative risk analysis	‘Uncertainty remains regarding landslide risk …’	This is the recommended minimum for plan-making and plan changes for general residential, medium- and high-density residential and tertiary education zones.
D	Basic quantitative risk analysis	‘… a moderate degree of confidence.’	This can form the basis for district plans, as well as site-specific analysis.
E	Detailed quantitative risk analysis	‘… a high degree of confidence.’	This can form the basis for district plans; plan changes; and land-use, subdivision and building consents.

The Landslide Planning Guidance (de Vilder et al. 2024) outlines five levels of landslide susceptibility, hazard and risk analysis, providing methodological guidance, residual uncertainty estimates and potential applications. An extract of this outline is provided in Table 5.1, highlighting the five analysis levels and their description, the associated uncertainty or confidence level and possible applications for the analysis at each level. While this table can be interpreted sequentially from left to right – implying that a ‘Level D’ analysis ‘can form the basis for district plans, as well as site-specific analysis’ – uncertainties associated with the chosen analysis techniques or datasets may lead to a mis-match between the analysis level, magnitude of uncertainty and interpretation of an appropriate uncertainty level by the end user (e.g. ‘significant uncertainty’ may correspond to *some specific* order of magnitude, depending on the tolerance of the user group or application).

Where the stated uncertainty of an analysis does not meet the user’s interpretation of ‘significance’, it may not be appropriate to match the application to the analysis level in the corresponding row. Instead, users should first determine the maximum acceptable uncertainty (and confidence) for each application level (e.g. ±1.25 orders of magnitude at one standard deviation [1-sigma] for Level A and ±0.5 orders of magnitude at two standard deviations [2-sigma] for Level E), then determine the applicability of a given hazard or risk dataset based on whichever is more limiting; the described analysis level or the reported uncertainty. This ensures that decision-making considers both methodological rigor and the practical implications of uncertainty in real-world applications.

The following sections outline recommendations regarding the determination of appropriate data outputs, risk-tolerance thresholds and associated uncertainties, as well as next steps and opportunities to re-evaluate hazard and risk.

5.2 Landslide-Debris-Flux Summary

The landslide-debris-flux outputs for the present-day climate scenario provide a ‘most likely’ landslide-debris-inundation hazard across the region. These are derived from our ‘best estimates’ of landslide susceptibility, debris production and sediment distribution. In terms of inundation extent, these are slightly conservative, as landslide-sediment distribution has been modelled at 25 m resolution, while our sensitivity analyses indicate a general decrease in landslide travel distance with increasing model resolution. In terms of inundation magnitude, the relative smoothness of the 25-m-resolution DEM tends to reduce variability in the magnitude of debris flux, thereby slightly under-estimating the maximum flux in channels and over-estimating on gentle ridges and slightly convex landforms.

Landslide-debris flux is particularly useful for scenario-specific hazard assessments, where the inundation frequency is assumed to be 1 (i.e. all debris is released simultaneously). In such cases, landslide-debris flux represents the expected average magnitude of inundation at a given location.

As this study employs a 'process-based' hazard model rather than an 'event-based' approach (see Section 1.1 for details), individual landslide sources and runout paths are not explicitly tracked. As a result, the debris flux observed in association with specific landslide events following a given trigger is likely higher than the average landslide-debris-flux values presented here. However, when summing landslide-debris flux along a defined segment of terrain – such as a road at the base of a slope – the cumulative debris flux provides a more representative estimate of the total volume of debris crossing that section. The longer the segment used for integration, the more accurately this cumulative landslide-debris flux reflects actual debris volumes expected across the hill slope.

This makes landslide-debris flux a valuable tool for identifying areas with high debris-flow potential, assessing infrastructure vulnerability and supporting hazard-based land-use planning.

5.3 Summary of Annual Property Loss Risk

5.3.1 Present-Day Climate Conditions

The APLR outputs for the present-day climate scenario provide a 'most likely' APLR to hypothetical buildings in the area exposed to landslide debris-inundation hazards. These represent our 'best estimates' of landslide susceptibility, debris production, sediment distribution and property vulnerability. These are slightly conservative, as landslide-sediment distribution has been modelled at 25 m resolution, while our uncertainty analysis suggests that, on average, this may over-estimate risk by at least 2×.

We explore uncertainties resulting from model assumptions and input parameter ranges by testing combinations of 29 key input parameters and evaluating their impact at various locations along a hypothetical 1D profile. Uncertainties relating to the accuracy of the DEM and resolution of the LS-IPM analysis are evaluated by comparing results derived from the national DEM (LINZ 2014) against those derived from a recent LiDAR DEM (LINZ 2022) at resolutions of 8 m and 25 m. Based on results of these analyses, and allowing for uncertainties unable to be captured by these methods, we suggest that 68% of APLR results can be considered to fall within ±1.25 orders of magnitude of the 'most likely' output, while 95% of APLR results can be considered to fall within ±2.75 orders of magnitude. Although uncertainties are not normally distributed, we recommend treating these ranges as equivalent to 1- and 2-sigma intervals (i.e. the 84th and 98th percentiles), respectively.

These uncertainty bounds imply that an APLR of 10^{-4} per year, as presented in this report, could reasonably vary between $10^{-5.25}$ and $10^{-2.75}$ per year. However, it is important to note that values outside of this range are also possible. Specifically, there is a 5% chance that APLR values will be less than $10^{-6.75}$ or greater than $10^{-1.25}$ per year.

5.3.2 RCP6 2081–2100 Climate-Change Scenario

APLR maps for the RCP6 2081–2100 climate-change scenario represent a 'best estimate' based on 'most likely' estimates for all parameters for which the uncertainty can reasonably be determined. As all uncertainties on constrained parameters are identical to those of the present-day model, the associated uncertainty may be expected to remain unchanged. However, a number of unconstrained input parameters for the RCP6 climate scenario do not allow for a complete evaluation of uncertainties (see Section 2.3.1.6 for further discussion). As such, it is possible that APLR may exceed our 'best estimate' by several orders of magnitude. Given these limitations, we conservatively recommend adopting a 1-sigma (84th percentile) uncertainty estimate of ±2.75 orders of magnitude for hazard and risk outputs relating to this scenario, which is equivalent to the 2-sigma statistical confidence interval of the present-day model. This can be reduced to ±1.75 orders of magnitude with the incorporation of a LiDAR-derived DEM and a ±1.00 order-of-magnitude if the model resolution is also increased to 8 m or more (see Section A7.7). The 2-sigma (98th percentile) uncertainty cannot be constrained without additional data to better characterise input variability.

5.3.3 Applying Risk Metrics

5.3.3.1 Determining Tolerance Criteria

Risk evaluation is inherently uncertain. When using hazard- or risk-model outputs for specific applications – such as emergency preparedness or land-use planning, including plan changes, notices of requirement and consenting – it is essential to consider both the indicated risk level and associated uncertainty at an appropriate statistical confidence level.

For life-safety-critical structures, it is standard practise to adopt a precautionary approach, meaning that risk assessments should prioritise the upper bound of estimated risk rather than the central or lower values. Figure 5.2 provides a framework for evaluating both existing and new risks while accounting for residual uncertainty in risk calculations.

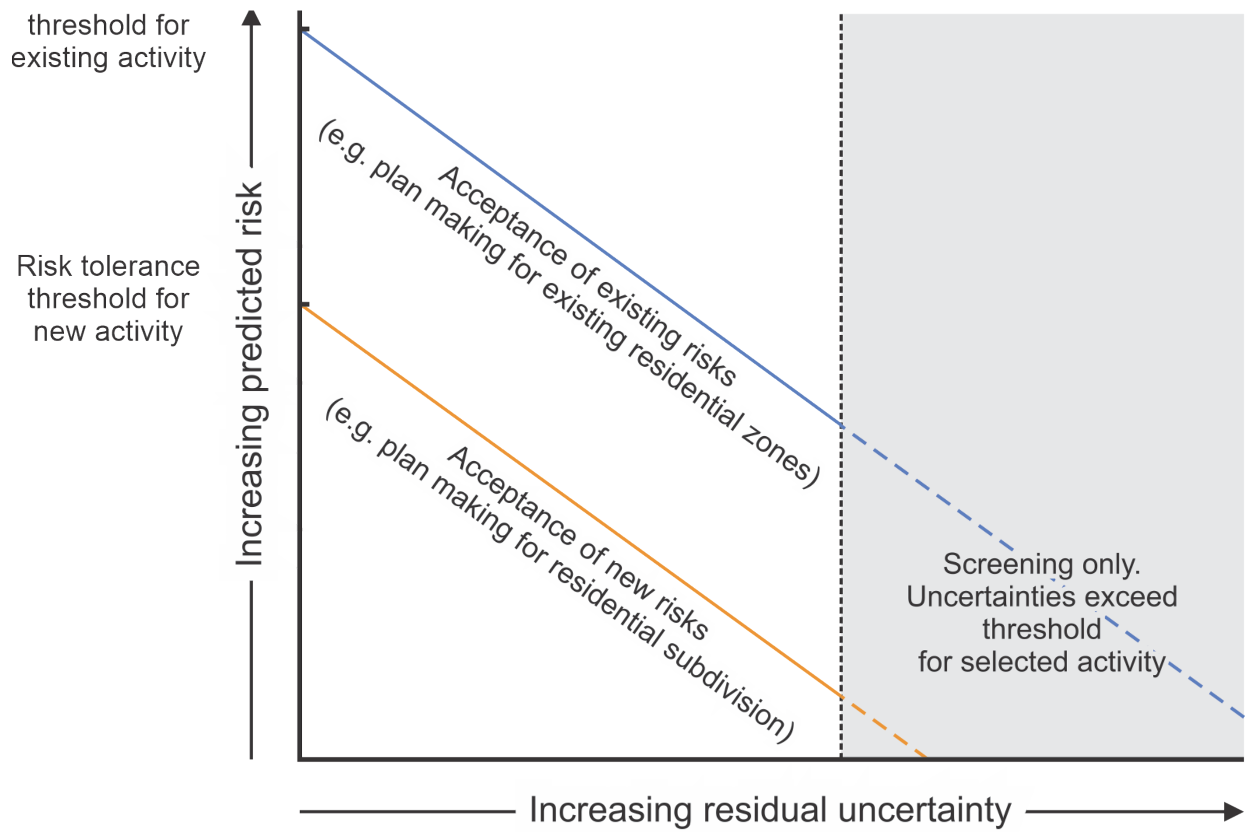

Figure 5.2 A framework for considering predicted risk (e.g. modelled annual property loss risk in this study) and associated uncertainty when planning for existing and new activities (adapted from a figure initially published by USBR [2025]). The acceptance threshold for existing risks (blue line) can be higher than that for new risks (orange line) for the same activity (e.g. residential housing). Predicted risks that fall below the respective acceptance threshold are considered acceptable for the given use case. If uncertainty is deemed too significant, risk predictions may be unsuitable for planning decisions. Instead, these can be used for screening and guidance where additional assessment is needed to refine risk estimates.

In this framework, the risk-acceptance threshold may be higher for existing risks than for new ones. This reflects the reality that existing developments may have different tolerances due to historical approvals, economic constraints or established land use, a concept adopted in the Proposed Otago Regional Policy Statement (Otago Regional Council 2021).

Adopting a precautionary approach, the appropriate predicted risk level at which a given activity can be considered acceptable decreases with increasing residual uncertainty. The gradient of each threshold represents a precautionary reduction in acceptable risk as uncertainty increases. Critical facilities (e.g. hospitals, emergency infrastructure) may require stricter standards, such as using a 2-sigma rather than 1-sigma uncertainty bound. This will result in the adoption of a greater representative uncertainty, and therefore a steeper gradient, meaning that the acceptable predicted risk will reduce more aggressively.

For example, if a study states a ±1 order of magnitude uncertainty at 1-sigma, the acceptable predicted risk may be:

- equal to the risk acceptance threshold for less critical applications; or
- one order of magnitude lower than the threshold for more critical applications where the 84th percentile is deemed acceptable; or
- for the most critical applications, reduced by an uncertainty corresponding to the 98th percentile. If the corresponding uncertainty is too large, alternative options may need to be considered before proceeding.

This structured approach ensures that both uncertainty and confidence are explicitly accounted for in risk-based decision-making.

5.3.3.2 Creation of Regional Landslide-Debris-Inundation Hazard or Risk Maps

The following steps outline a process by which lifelines and service organisations may use datasets presented in this report to categorise landslide-debris-inundation risk for a given activity (e.g. a new development):

1. Determine an appropriate hazard or risk acceptance threshold (e.g. 10^{-5} per annum).
2. Define the maximum allowable uncertainty threshold (e.g. two orders of magnitude).
3. Determine an appropriate statistical confidence interval (e.g. 1-sigma).
4. Select a dataset that best represents landslide-debris-inundation hazard or risk for the activity (e.g. mean annual APLR). If the dataset represents a risk output, it is essential to ensure that the applied vulnerability function is appropriate to the considered activity (see Section 2.1.3).
5. Select a representative uncertainty from the dataset by referencing the statistical confidence interval determined in Step 3 to the reported statistical uncertainties of the dataset (e.g. ±1.25 orders of magnitude at the 1-sigma confidence interval for mean annual APLR).
6. Check that the representative uncertainty reported for the dataset (e.g. ±1.25 orders of magnitude; from Step 5) is less than the maximum allowable uncertainty for the activity (two orders of magnitude; defined in Step 2).
7. If the representative uncertainty exceeds the maximum allowable for the activity (which it does not in this example), application of the dataset may be limited to 'screening' purposes. Explore options to reduce either global or local uncertainties before proceeding. These may include increasing DEM accuracy and/or model resolution, refining model inputs, gathering additional data or adjusting assumptions. If the uncertainty is within acceptable limits, proceed to Step 8.
8. Calculate an 'adjusted tolerance threshold' by reducing the hazard- or risk-acceptance threshold determined in Step 1 by the representative uncertainty (identified in Step 5) (e.g. $10^{-6.25}$ per annum).

9. Compare the predicted hazard or risk from the dataset to the adjusted tolerance threshold and classify outputs as ‘Significant’, ‘Tolerable’ or ‘Acceptable’ (as proposed in Otago Regional Council [2021], or similar terminology from the provisional New National Policy Statement [Ministry for the Environment 2025]) based on whether the predicted level is above, near or below the adjusted tolerance threshold (in this example, the activity is likely to be considered acceptable in areas where APLR values are less than $10^{-6.25}$ per annum).

This approach provides a clear and transparent path for decision-making and allows for consistent application of guidance based on calculated risk and uncertainties, independent of the method employed to derive risk estimates.

5.4 Recommended Next Steps

Risk criteria established in other contexts, along with data on natural hazards and risk tolerance in New Zealand, can help inform the development of risk metrics and criteria for representative authorities in relation to landslide-debris-inundation risk within the study area. Such information can guide the definition of quantitative thresholds that align with existing practises and reflect New Zealanders' observed tolerance (or lack thereof) for risk associated with similar hazards (e.g. Taig et al. 2012; Kilvington and Saunders 2015; Massey et al. 2021b; Toka Tū Ake EQC 2023; de Vilder et al. 2024; ResOrgs [2025]).

Define a Sustainable Risk Threshold

Representative authorities should consider defining risk criteria to assess the tolerability of landslide-debris-inundation risk based on societal acceptance of comparable risk levels for given activities from other sources.

In this study, we calculate risk based on economic loss to hypothetical buildings (APLR), as this is more readily verifiable than life-based metrics at the regional scale. However, landslides do have the potential to cause fatalities, and life-based metrics such as Annual Individual Fatality Risk (AIFR) can be equally appropriate in local-scale studies. Where both metrics are known, a first-past-the-post principle in risk re-categorisation can eventually be employed to ensure that decisions prioritise whichever of the two metrics – fatalities or property damage – poses the higher threat.

In the proposed Otago Regional Policy Statement (Otago Regional Council 2021), the same tolerance threshold is currently proposed for both APLR and AIFR. Following this guidance, as well as other international and national risk-tolerance threshold examples (e.g. Toka Tū Ake EQC 2023; de Vilder et al. 2024) a sustainable APLR threshold may fall within the range of 1×10^{-6} to 1×10^{-4} per year (depending on whether the development is new or existing), in line with both New Zealand risk tolerances and international regulatory practises. A reasonable starting point for deliberation could be **1×10^{-5} per year** (equivalent to a 1 in 100,000 annual probability of property loss).

Define an Appropriate Level of Confidence

Risk-tolerability assessments should incorporate acceptable levels of confidence, recognising that all risk estimates have inherent uncertainty. Representative authorities should specify whether risk thresholds are based on mean values or 1- or 2-sigma (84th or 98th percentile) confidence bounds. Using Intergovernmental Panel on Climate Change terminology, the chance that true annual risk exceeds the 1-sigma threshold can be described as *Unlikely*, while exceedance of the 2-sigma threshold would be *Exceptionally unlikely* (Mastrandrea et al. 2010). The acceptable confidence should reflect the criticality of the activity, with more conservative confidence ranges (e.g. 2-sigma) required for high-risk applications (e.g. emergency infrastructure, densely populated areas). For context, Massey et al. (2021b) were requested to provide data describing the 1-sigma confidence level for the evaluation of AFIR as a result of landslide debris inundation in the Kaikōura district.

We suggest that adopting a **1-sigma** confidence interval is likely to be appropriate for most regional landslide-risk applications, as the cost associated with generating data sufficient to constrain 2-sigma uncertainties to acceptable thresholds is likely to outweigh benefits gained through the improved accuracy of the prediction.

Determine an Acceptable Uncertainty Threshold

There is an inherent trade-off between the spatial scale of a dataset and its absolute uncertainty at the local level. The representative authorities should determine a threshold at which uncertainty becomes significant enough to prevent the reasonable determination of acceptable risk for given activities. If the uncertainty on a model output is greater than the determined significance threshold, the results should instead be used for the identification of areas in which tighter constraints are required ('screening') before determining acceptability of certain activities.

As there is little precedent for setting specific uncertainty thresholds for different activities, we provide guidance based on expert opinion in Table 5.2. The table provides a starting point for determining approximate thresholds that can be used to evaluate data suitability, assuming a general 0.25 order-of-magnitude decrease in residual uncertainty across application levels A–D. For the most critical applications ('Level E'), the underlying uncertainty is not reduced further; instead, the required confidence is increased (e.g. from 1-sigma to 2-sigma) so that rare but extreme events are more reliably captured. These thresholds will inevitably vary depending on society's tolerance for uncertainty and the consequences of exceedance. Accordingly, West Coast Regional Council should carefully consider which thresholds are most appropriate for local planning purposes.

Table 5.2 Indicative order-of-magnitude uncertainty thresholds and associated confidence levels that may be applied to determine the utility of Annual Property Loss Risk datasets for a range of planning purpose levels.

Level	Approximate Uncertainty Threshold	Confidence	Example Implication	Application
A	> ±1.25	1-sigma (84th percentile)	It is *unlikely* that the true annual number of events in an area will exceed about 18× the expected value.	This is the gateway assessment that determines where further assessment is required and where it will not be required.
B	±1.00	1-sigma (84th percentile)	It is *unlikely* that the true annual number of events in an area will exceed about 10× the expected value.	This is the recommended minimum for plan-making and plan changes for rural (rural lifestyle and settlement), commercial and mixed use, industrial, residential (large lot or low density) and future urban zones.
C	±0.75	1-sigma (84th percentile)	It is *unlikely* that the true annual number of events in an area will exceed about 6× the expected value.	This is the recommended minimum for plan-making and plan changes for general residential, medium- and high-density residential and tertiary education zones.
D	±0.50	1-sigma (84th percentile)	It is *unlikely* that the true annual number of events in an area will exceed about 3× the expected value.	This can form the basis for district plans, as well as site-specific analysis.
E	±0.50	2-sigma (98th percentile)	It is *exceptionally unlikely* that the true annual number of events in an area will exceed about 3× the expected value.	This can form the basis for district plans; plan changes; and land-use, subdivision and building consents.

Comparing the uncertainties for present-day and RCP6 APLR datasets provided with this report (both **greater than ±1.25** orders of magnitude) with approximate uncertainty thresholds detailed in Table 5.2, we suggest that **present-day APLR outputs** are suitable to be employed for **'Level A'** or **'Level B'** planning applications, if presented at an appropriate spatial resolution (see Section 4). RCP6 2018–2100 climate-change-scenario outputs should be limited to **'Scoping'**, or possibly **'Level A'** planning purposes, unless spatial uncertainties are minimised by repeating the analysis using an 8 m resolution LiDAR DEM (see Section 5.3.2).

Communicate the Implications for this Hazard and Risk Analysis through the One Plan Process

Representative authorities should consider how to communicate the implications for landslide-debris-inundation hazard and risk through future Te Tai o Poutini Plan (One Plan) Change processes. As detailed in this section, landslide-debris flux and APLR outputs can form the basis for a range of planning applications, depending on the confidence, uncertainty and risk criteria adopted for various activities by representative authorities. Less-critical activities may include:

- Identifying land 'susceptible' to land-debris-inundation hazards in overlays and providing indications of where further analysis should be undertaken.

More-critical activities may include plan-making and plan changes in:

- Rural (rural lifestyle and settlement), commercial and mixed use, industrial, residential (large lot or low density) and future urban zones.
- General residential, medium- and high-density residential and education zones, as well as open space.

And as the District Plan moves from development to implementation:

- Site-specific analysis and consenting input.

Where stated APLR uncertainties do not meet the statistical confidence and uncertainty thresholds determined by West Coast Regional Council for selected activities, outputs may be used as a screening tool to guide where local refinement or more site-specific analyses are required (e.g. see Figures 6.1b and 6.1c of de Vilder et al. [2024] describing the process for resource and building consents).

Incorporate Event-Specific Landslide-Debris-Flux Outputs into Emergency-Management Plans

Datasets describing scenario-specific landslide-debris flux can be employed in a range of emergency-management applications. As these datasets provide an indication of the volume of material that may be expected to pass a given location in a given scenario, the outputs could be used, for example, for estimating probable volumes of landslide debris passing through sections of highway or entering river networks in response to heavy rainfall or earthquake events.

5.5 Re-Evaluation of Hazard and Risk and Re-Classification of Sites

Given the regional scale of the hazard and risk models provided with this report, a provision should be included whereby site-specific information for a site/dwelling could be used to re-evaluate the landslide risk, thus allowing the given site to be re-classified (e.g. changing its hazard-area status through a certification process). This process was allowed for in Christchurch City Council's replacement District Plan (Quigley et al. 2020). In 2016, the Independent Hearings Panel agreed to this provision, provided that any re-assessment should follow the same method and approach adopted for the district-wide assessments.

The regional-scale basic quantitative landslide-debris-inundation hazard and risk analysis presented here is specifically configured to provide a physically based, adaptable and scalable regional hazard and risk analysis. Results should be expected to vary with the inclusion of higher-resolution or site-specific data.

When evaluating the potential impact of additional datasets on model uncertainties, we recommend that users reference Sections A7.1 and A7.6.3. Section A7.1 provides an indication of the relative change in uncertainties associated with each input variable in the LS-IPM assessment. Section A7.6.3 provides an evaluation of the relative impacts of improving DEM accuracy and model resolution. Incorporating data to more tightly constrain variables with the greatest uncertainty and largest impact on calculated APLR can be expected to result in the most impactful change in landslide hazard and risk. These should therefore be initial targets when considering refinement of results to allow re-classification of sites.

The effect of locally increasing the resolution of landslide-debris-flux and APLR predictions is particularly easy to test, and an example is presented for the Greymouth area in Figure A7.4 (see Section A7.6.2). Increasing the resolution of the LSP and LSD models can provide better representation of potential landslide sources and improve the tracking of potential landslide-debris-inundation paths. This is most relevant for locations close to hill slopes, down-slope of landforms with spatial extents less than 100,000 m^2 and areas of subtle channelisation. Incorporation of a more accurate topographic model may result in both increases and decreases in APLR, depending on the scale and variability of local landforms and their representation in the DEM. However, we overall find that reducing from 25 m to 8 m resolution and employing a recent LiDAR-derived DEM can be expected to reduce the mean APLR by approximately 3.4×, while also reducing 2-sigma (95th percentile) uncertainties from ±2.75 to ±1.0 order of magnitude (see Section A7.7).

In addition to a fundamental change in the DEM accuracy and model resolution, additional datasets may allow the revision of hazard and risk outputs by:

- Better constraining long-term sediment-production rates, for example, with the aid of sedimentological data, improved specific-sediment-yield estimates (possibly including Dymond et al. [2010], Hicks et al. [2019] and Neverman et al. [2023]), dating of depositional landforms or determination of local erosion rates.
- Better constraining landslide susceptibility with the aid of geotechnical data and/or mapping of historical landslides and improved observations of source geometry and/or runout characteristics.
- Better characterising landslide-source geometries. In particular, explicitly accounting for spatially variable, depth-dependent cohesion and friction estimates based on geological data.
- Better constraining the spatial distribution of potential landslide-source volumes by updating kinematic-source models for every landslide volume-class range.
- Generating characteristic landslide-debris-inundation frequency-magnitude distributions tailored to local site conditions with the aid of sedimentological, geotechnical or dynamic landslide-modelling data.
- Better constraining susceptibility estimates with refined or updated rainfall or earthquake scenarios.
- Refine estimates of building vulnerability using numerical or physical analogue models.

We recommend discussion with a geotechnical expert prior to undertaking any additional investigations.

6.0 Summary and Conclusions

WCEM commissioned GNS Science, now part of Earth Sciences New Zealand, to assess landslide hazards and risks across its jurisdiction, focusing on landslides generated by earthquakes and rainfall that potentially present a risk to property and life.

This study presents a regional-scale basic quantitative landslide-debris-inundation hazard and risk analysis, conducted in two phases:

- Stage 1 identified landslide-debris-inundation hazard-footprint areas (Leith and de Vilder 2022).
- Stage 2 integrated these hazard models with probabilistic landslide-initiation and -runout models to estimate annual building loss risks.

The study leverages advances from the MBIE-funded GNS Science Extreme Weather SSIF uplift, developed in response to Cyclone Gabrielle (Leith et al., in prep.).

Landslide-hazard metrics employed include:

- **Landslide-debris flux:** Quantifies the expected volume of debris passing a location per year or per event.
- **Probability of Inundation (P_i):** Represents the likelihood of debris reaching a location annually.
- **APLR:** Estimates the probability of a generic building sustaining damage beyond economic repair.

The methodology differs from traditional landslide-hazard and -risk models by considering debris movement from all potential source cells, rather than relying on a limited number of predefined landslide sources. This approach provides a spatially comprehensive regional assessment and aligns with applicable sections of the Australian Geomechanics Society Landslide Risk Management Guidelines (AGS 2007).

This analysis was conducted using spatially consistent datasets at 25 m resolution, aligning with a ‘Level D’ basic quantitative hazard and risk analysis (de Vilder et al. 2024). However, residual uncertainties vary spatially, necessitating the adoption of at least ±1.25 orders of magnitude of uncertainty for present-day conditions and ±2.75 orders of magnitude for future RCP6 (2018–2100) climate conditions. These uncertainty levels suggest that outputs are likely to be suitable for screening purposes (equivalent to ‘Level A’ or ‘Level B’ planning purposes as described in de Vilder et al. [2024]), and their use in higher-criticality decision-making should be carefully evaluated. West Coast Regional Council is advised to establish required confidence levels and associated uncertainty thresholds for various activities before applying landslide-debris-inundation outputs to planning decisions or policy changes.

We find that:

1. Landslide-debris-flux, P_i and APLR values are highest in areas near steep slopes, channelised gullies and debris fans in regions where annual landslide debris-production rates are greatest.
2. Rainfall-induced landslides dominate landslide-debris flux in range-front areas, while earthquake-induced landslides are the primary contributor northeast of Greymouth. This reflects the dominant landslide triggers in each setting.
3. Existing buildings are most exposed to debris flows, debris avalanches and rock avalanches (flow-type landslides), while fewer are at risk from debris slides (avalanche-type movements). This is due to the greater runout distances of flow-type landslides and historical urban planning that have limited development in areas prone to less mobile landslides.
4. 95% of APLR is concentrated in just 1% of existing buildings in the region overseen by WCEM.

5. Under RCP6 (2081–2100) climate-change scenarios, APLR for rainfall-induced landslides at existing buildings is projected to increase by approximately 50%.
6. Residual uncertainties vary spatially and increase with distance from landslide sources. These are particularly large in areas adjacent to topography with spatial extents less than 100,000 m^2.
7. The largest uncertainties are associated with the quality of the DEM used for runout modelling, spatial resolution of the modelling and sediment availability for landsliding.
8. Sediment availability and landslide-volume distributions are particularly uncertain for future climate scenarios.
9. Planning decisions should allow for site-specific assessments to refine hazard classifications. This may include:
    a. Substituting the national DEM with improved topographic data.
    b. Increasing the nominal spatial resolution of the LS-IPM analysis.
    c. Site-specific hazard assessments.
    d. More-detailed landslide-debris-inundation models.
    e. Re-assessment of vulnerability functions for structures.

This study provides a spatially comprehensive assessment of landslide risk in the region overseen by WCEM, offering critical insights for regional planning and emergency management. It is recommended that West Coast Regional Council carefully consider hazard and/or risk thresholds, appropriate confidence levels and acceptable uncertainty thresholds prior to the implementation of study results in future Te Tai o Poutini Plan (One Plan) Change processes and emergency-management planning.

7.0 Acknowledgements

The authors would like to acknowledge reviews by Dr Feiko van Zadelhoff and Dr Andrew Neverman (Manaaki Whenua – Landcare Research, now part of the Bioeconomy Science Institute), Sally Dellow (Earth Sciences New Zealand) and Dr Sam McColl (Earth Sciences New Zealand), as well as input provided by Edith Bretherton (Earth Sciences New Zealand) and Scott Kelly (Earth Sciences New Zealand).

8.0 References

Adams J. 1980. Contemporary uplift and erosion of the Southern Alps, New Zealand. *GSA Bulletin*. 91(1_Part_II):1–114. https://doi.org/10.1130/GSAB-P2-91-1

[AGS] Australian Geomechanics Society. 2007. Practice note guidelines for landslide risk management. *Australian Geomechanics*. 42(1):63–114.

Alberti S, Leshchinsky B, Roering J, Perkins J, Olsen MJ. 2022. Inversions of landslide strength as a proxy for subsurface weathering. *Nature Communications*. 13(1):6049. https://doi.org/10.1038/s41467-022-33798-5

Blöthe JH, Korup O, Schwanghart W. 2015. Large landslides lie low: excess topography in the Himalaya-Karakoram ranges. *Geology*. 43(6):523–526. https://doi.org/10.1130/G36527.1

Bradley BA, Bae SE, Polak V, Lee RL, Thomson EM, Tarbali K. 2017. Ground motion simulations of great earthquakes on the Alpine Fault: effect of hypocentre location and comparison with empirical modelling. *New Zealand Journal of Geology and Geophysics*. 60(3):188–198. https://doi.org/10.1080/00288306.2017.1297313

Brideau MA, Massey CI, Lukovic B, Morgenstern R. 2020. Deterministic mapping of potential landslide debris inundation in the Kaikoura District. Lower Hutt (NZ): GNS Science. 37 p. Consultancy Report 2019/102. Prepared for Canterbury Regional Council.

Brideau M-A, de Vilder S, Massey C, Mitchell A, McDougall S, Aaron J. 2021a. Empirical relationships to estimate the probability of runout exceedance for various landslide types. In: Guzzetti F, Mihalić Arbanas S, Reichenbach P, Sassa K, Bobrowsky PT, Takara K, editors. *Understanding and reducing landslide disaster risk Volume 2: from mapping to hazard and risk zonation*. Cham (CH): Springer International Publishing. p. 321–327. https://doi.org/10.1007/978-3-030-60227-7_36

Brideau M-A, de Vilder S, Massey C, Mitchell A, McDougall S, Aaron J. 2021b. V1.0 empirical landslide runout relationships, compiled from international examples, for various landslide types. Austin (TX): DesignSafe-CI; [accessed 2025 Jun]. https://doi.org/10.17603/ds2-9qbx-n796

Brunetti MT, Guzzetti F, Rossi M. 2009. Probability distributions of landslide volumes. *Nonlinear Processes in Geophysics*. 16(2):179–188. https://doi.org/10.5194/npg-16-179-2009

Budimir MEA, Atkinson PM, Lewis HG. 2015. A systematic review of landslide probability mapping using logistic regression. *Landslides*. 12(3):419–436. https://doi.org/10.1007/s10346-014-0550-5

Carey-Smith T, Henderson R, Singh S. 2018. High Intensity Rainfall Design System. Version 4. Wellington (NZ): National Institute of Water & Atmospheric Research. 73 p. Client Report 2018022CH. Prepared for Envirolink. https://niwa.co.nz/sites/default/files/2018022CH_HIRDSv4_Final.pdf

Chan H-C, Chen P-A, Lee J-T. 2018. Rainfall-induced landslide susceptibility using a rainfall-runoff model and logistic regression. *Water*. 10(10):1354. https://doi.org/10.3390/w10101354

Christen M, Bühler Y, Bartelt P, Leine R, Glover J, Schweizer A, Graf C, McArdell B, Gerber W, Deubelbeiss Y, et al. 2012. Integral hazard management using a unified software environment. In: *12th Congress Interpraevent;* 2012 Apr 23–26; Grenoble, France. Klagenfurt (AT): International Research Society. p. 77–86.

Corominas J. 1996. The angle of reach as a mobility index for small and large landslides. *Canadian Geotechnical Journal*. 33(2):260–271. https://doi.org/10.1139/t96-005

Corominas J, Einstein H, Davis T, Strom A, Zuccaro G, Nadim F, Verdel T. 2015. Glossary of terms on landslide hazard and risk. In: Lollino G, Giordan D, Crosta GB, Corominas J, Azzam R, Wasowski J, Sciarra N, editors. *Engineering geology for society and territory – volume 2: landslide processes*. Cham (CH): Springer International Publishing. p. 1775–1779. https://doi.org/10.1007/978-3-319-09057-3_314

Corominas J, Guzzetti F, Lan H, Macciotta R, Marunteranu C, McDougall S, Strom A. 2023. Revisiting landslide risk terms: IAEG commission C-37 working group on landslide risk nomenclature. *Bulletin of Engineering Geology and the Environment*. 82(12):450. https://doi.org/10.1007/s10064-023-03474-z

Croissant T, Steer P, Lague D, Davy P, Jeandet L, Hilton RG. 2019. Seismic cycles, earthquakes, landslides and sediment fluxes: linking tectonics to surface processes using a reduced-complexity model. *Geomorphology*. 339:87–103. https://doi.org/10.1016/j.geomorph.2019.04.017

Davies TR, McSaveney MJ. 2008. Principles of sustainable development on fans. *Journal of Hydrology (New Zealand)*. 47(1):43–65.

Davies TR, McSaveney MJ, Doscher C. 2005. Project No. 03/499: monitoring and effects of landslide-induced aggradation in the Poerua Valley, Westland. Wellington (NZ): Earthquake Commission; [accessed 2025 Jun]. https://www.naturalhazards.govt.nz/assets/Publications-Resources/4339-Monitoring-and-effects-assessment-of-landslide-induced-aggradation-in-the-Poerua-Valley-Westland-compressed.pdf

de Vilder S, Massey C, Taig T, Lukovic B, Archibald G, Morgenstern R. 2021. Quantitative risk analysis of earthquake-induced landslides. In: Tiwari B, Sassa K, Bobrowsky PT, Takara K, editors. *Understanding and reducing landslide disaster risk: volume 4 testing, modeling and risk assessment*. Cham (CH): Springer International Publishing. p. 465–470. https://doi.org/10.1007/978-3-030-60706-7_50

de Vilder SJ, Brideau MA, Massey CI. 2022. Empirical and physics-based runout models. Lower Hutt (NZ): GNS Science. 42 p. (GNS Science report; 2019/38). https://doi.org/10.21420/HYMS-9W10

de Vilder SJ, Kelly SD, Buxton RB, Allan S, Glassey PJ. 2024. Landslide planning guidance: reducing landslide risk through land-use planning. Lower Hutt (NZ): GNS Science. 77 p. (GNS Science miscellaneous series; 144). https://doi.org/10.21420/R2X8-FJ49

Dymond JR, Betts HD, Schierlitz CS. 2010. An erosion model for evaluating regional land-use scenarios. *Environmental Modelling & Software*. 25(3):289–298. https://doi.org/10.1016/j.envsoft.2009.09.011

Efron B, Tibshirani RJ. 1994. An introduction to the bootstrap. New York (NY): Chapman and Hall / CRC. 456 p. https://doi.org/10.1201/9780429246593

Emberson R, Hovius N, Galy A, Marc O. 2016. Oxidation of sulfides and rapid weathering in recent landslides. *Earth Surface Dynamics*. 4(3):727–742. https://doi.org/10.5194/esurf-4-727-2016

England KA. 2011. A GIS approach to landslide hazard management for the West Coast region, New Zealand [MSc thesis]. Christchurch (NZ): University of Canterbury. 163 p. + appendices. https://doi.org/10.26021/6979

Evans SG. 2001. Landslides. In: Brooks GR, editor. *A synthesis of geological hazards in Canada*. Ottawa (ON): Geological Survey of Canada. p. 43–79. (Geological Survey of Canada bulletin; 548).

Fan X, Domènech G, Scaringi G, Huang R, Xu Q, Hales TC, Dai L, Yang Q, Francis O. 2018. Spatio-temporal evolution of mass wasting after the 2008 M_W 7.9 Wenchuan earthquake revealed by a detailed multi-temporal inventory. *Landslides*. 15(12):2325–2341. https://doi.org/10.1007/s10346-018-1054-5

Friedman JH, Hastie T, Tibshirani R. 2010. Regularization paths for generalized linear models via coordinate descent. *Journal of Statistical Software*. 33(1):1–22. https://doi.org/10.18637/jss.v033.i01

Gamma P. 1999. Dfwalk – ein Murgang-Simulationsprogramm zur Gefahrenzonierung [Dfwalk – a debris simulation program for hazard zoning]. Bern (CH): University of Bern. 144 p. German.

Gerstenberger MC, Van Dissen RJ, Rollins C, DiCaprio C, Chamberlain C, Christophersen A, Coffey GL, Ellis SM, Iturrieta P, Johnson KM, et al. 2022. The Seismicity Rate Model for the 2022 New Zealand National Seismic Hazard Model. Lower Hutt (NZ): GNS Science. 156 p. (GNS Science report; 2022/47). https://doi.org/10.21420/2EXQ-NP48

Goetz J, Kohrs R, Parra Hormazábal E, Bustos Morales M, Araneda Riquelme MB, Henríquez C, Brenning A. 2021. Optimizing and validating the Gravitational Process Path model for regional debris-flow runout modelling. *Natural Hazards and Earth System Sciences*. 21(8):2543–2562. https://doi.org/10.5194/nhess-21-2543-2021

Guzzetti F, Ardizzone F, Cardinali M, Rossi M, Valigi D. 2009. Landslide volumes and landslide mobilization rates in Umbria, central Italy. *Earth and Planetary Science Letters*. 279(3):222–229. https://doi.org/10.1016/j.epsl.2009.01.005

Hancox GT, Ries WF, Lukovic B, Parker RN. 2014. Landslides and ground damage caused by the M_W 7.1 Inangahua earthquake of May 1968 in northwest South Island, New Zealand. Lower Hutt (NZ): GNS Science. 1 map + 89 p. (GNS Science report; 2014/06).

Hancox GT, Ries WF, Parker RN, Rosser BJ. 2016. Landslides caused by the MS 7.8 Murchison earthquake of 17 June 1929 in northwest South Island, New Zealand. Lower Hutt (NZ): GNS Science. 4 maps + 131 p. (GNS Science report; 2015/42).

Heim A. 1932. Landslides & human lives. Skermer N, translator. Vancouver (BC): BiTech Publishers. 195 p.

Hermanns RL, Oppikofer T, Anda E, Blikra LH, Böhme M, Bunkholt H, Crosta GB, Dahle H, Devoli G, Fischer L, et al. 2012. Recommended hazard and risk classification system for large unstable rock slopes in Norway. Trondheim (NO): Norges Geologiske Undersokelse. NGU report 2012.029; [accessed 2025 Jun]. https://www.ngu.no/publikasjon/recommended-hazard-and-risk-classification-system-large-unstable-rock-slopes-norway

Heron DW, custodian. 2020. Geological map of New Zealand: digital vector data [map]. 3rd ed. Lower Hutt (NZ): GNS Science. 1 USB, scale 1:250,000. (GNS Science geological map; 1).

Hicks DM, Shankar U, McKerchar AI, Basher L,Lynn I, Page M, Jessen M. 2011. Suspended sediment yields from New Zealand rivers. *Journal of Hydrology (New Zealand)*. 50(1):81–142.

Hicks M, Semadeni-Davies A, Haddadchi A, Shankar U, Plew D. 2019. Updated sediment load estimator for New Zealand. Christchurch (NZ): National Institute of Water & Atmospheric Research. 190 p. Client Report 2018341CH. Prepared for the Ministry for the Environment. https://environment.govt.nz/assets/Publications/Files/updated-sediment-load-estimator-for-nz.pdf

Hilton RG, Meunier P, Hovius N, Bellingham PJ, Galy A. 2011. Landslide impact on organic carbon cycling in a temperate montane forest. *Earth Surface Processes and Landforms*. 36(12):1670–1679. https://doi.org/10.1002/esp.2191

Hovius N, Stark CP, Allen PA. 1997. Sediment flux from a mountain belt derived by landslide mapping. *Geology*. 25(3):231–234. https://doi.org/10.1130/0091-7613(1997)025<0231:SFFAMB>2.3.CO;2

Howarth JD, Fitzsimons SJ, Norris RJ, Langridge RM, Vandergoes MJ. 2016. A 2000 yr rupture history for the Alpine fault derived from Lake Ellery, South Island, New Zealand. *Geological Society of America Bulletin*. 128(3–4):627–643. https://doi.org/10.1130/B31300.1

Huggett R, Shuttleworth E. 2022. Fundamentals of geomorphology. 5th ed. London (GB): Routledge. 682 p. https://doi.org/10.4324/978100325115

Hungr O, McDougall S. 2009. Two numerical models for landslide dynamic analysis. *Computers & Geosciences*. 35:978–992. https://doi.org/10.1016/j.cageo.2007.12.003

Hungr O, Leroueil S, Picarelli L. 2014. The Varnes classification of landslide types, an update. *Landslides*. 11(2):167–194. https://doi.org/10.1007/s10346-013-0436-y

Iverson RM, Reid ME, Logan M, LaHusen RG, Godt JW, Griswold JP. 2011. Positive feedback and momentum growth during debris-flow entrainment of wet bed sediment. *Nature Geoscience*. 4(2):116–121. https://doi.org/10.1038/ngeo1040

Kilvington M, Saunders WSA. 2015. "I can live with this": the Bay of Plenty Regional Council public engagement on acceptable risk. Lower Hutt (NZ): GNS Science. 71 p. (GNS Science miscellaneous series; 86).

Klar A, Aharonov E, Kalderon-Asael B, Katz O. 2011. Analytical and observational relations between landslide volume and surface area. *Journal of Geophysical Research: Earth Surface*. 116(F2). https://doi.org/10.1029/2009JF001604

Kober F, Hippe K, Salcher B, Ivy-Ochs S, Kubik PW, Wacker L, Hählen N. 2012. Debris-flow–dependent variation of cosmogenically derived catchment-wide denudation rates. *Geology*. 40(10):935–938. https://doi.org/10.1130/G33406.1

Larsen IJ, Montgomery DR, Korup O. 2010. Landslide erosion controlled by hillslope material. *Nature Geoscience*. 3(4):247–251. https://doi.org/10.1038/ngeo776

Larsen IJ, Almond PC, Eger A, Stone JO, Montgomery DR, Malcolm B. 2014. Rapid soil production and weathering in the Southern Alps, New Zealand. *Science*. 343(6171):637–640. https://doi.org/10.1126/science.1244908

Larsen IJ, Eger A, Almond PC, Thaler EA, Rhodes JM, Prasicek G. 2023. The influence of erosion and vegetation on soil production and chemical weathering rates in the Southern Alps, New Zealand. *Earth and Planetary Science Letters*. 608:118036. https://doi.org/10.1016/j.epsl.2023.118036

Leith KJ. 2024. West Coast landslide debris inundation assessment: preliminary data delivery. Lower Hutt (NZ): GNS Science. 15 p. Consultancy Report 2024/24LR. Prepared for the West Coast Civil Defence & Emergency Management Group.

Leith KJ, de Vilder SJ. 2022. Deterministic mapping of potential landslide debris inundation hazards in the West Coast region. Lower Hutt (NZ): GNS Science. 36 p. Consultancy Report 2022/116. Prepared for the West Coast Civil Defence & Emergency Management Group.

Leith K, McColl S, Robinson T, Massey CI, Townsend DB, Rosser BJ, Smith H, Barrell DJA, Zoeller A, Lukovic B, et al. In prep. Ex-Tropical Cyclone Gabrielle (12–16 February 2023): landslide inventory for North Island New Zealand, version 1.0. Lower Hutt (NZ): GNS Science. (GNS Science report; 2025/02). https://doi.org/10.21420/MMFP-S330

Li T. 1983. A mathematical model for predicting the extent of a major rockfall. *Zeitschrift fur Geomorphologie*. 27(4):473–482. https://doi.org/10.1127/zfg/27/1983/473

Lin Q, Lima P, Steger S, Glade T, Jiang T, Zhang J, Liu T, Wang Y. 2021. National-scale data-driven rainfall induced landslide susceptibility mapping for China by accounting for incomplete landslide data. *Geoscience Frontiers*. 12(6):101248. https://doi.org/10.1016/j.gsf.2021.101248

[LINZ] Toitū Te Whenua Land Information New Zealand. 2014. NZ 8m Digital Elevation Model (2012). Wellington (NZ): LINZ; [updated 2023 Nov 30; accessed 2025 Jun]. https://data.linz.govt.nz/layer/51768-nz-8m-digital-elevation-model-2012/

[LINZ] Toitū Te Whenua Land Information New Zealand. 2022. West Coast LiDAR 1m DEM (2020–2024). Wellington (NZ): LINZ; [updated 2025 Feb 25; accessed 2025 Jun]. https://data.linz.govt.nz/layer/110163-west-coast-lidar-1m-dem-2020-2024/

Lombardo L, Mai PM. 2018. Presenting logistic regression-based landslide susceptibility results. *Engineering Geology*. 244:14–24. https://doi.org/10.1016/j.enggeo.2018.07.019

LRIS Portal. 2019. LCDB v5.0 – Land Cover Database version 5.0, mainland, New Zealand. Lincoln (NZ): Manaaki Whenua Landcare Research; [updated 2024 Nov 15; accessed 2025 Jun]. https://lris.scinfo.org.nz/layer/104400-lcdb-v50-land-cover-database-version-50-mainland-new-zealand/

Marc O, Hovius N, Meunier P, Uchida T, Hayashi S. 2015. Transient changes of landslide rates after earthquakes. *Geology*. 43(10):883–886. https://doi.org/10.1130/G36961.1

Marc O, Hovius N, Meunier P, Gorum T, Uchida T. 2016. A seismologically consistent expression for the total area and volume of earthquake-triggered landsliding. *Journal of Geophysical Research: Earth Surface*. 121(4):640–663. https://doi.org/10.1002/2015JF003732

Massey CI, Thomas K-L, King AB, Singeisen C, Taig T, Horspool NA. 2019. SLIDE (Wellington): vulnerability of dwellings to landslides (Project No. 16/SP740). Lower Hutt (NZ): GNS Science. 76 p. (GNS Science report; 2018/27). https://doi.org/10.21420/G2DD2Q

Massey CI, Townsend D, Jones K, Lukovic B, Rhoades D, Morgenstern R, Rosser B, Ries W, Howarth J, Hamling I, et al. 2020a. Volume characteristics of landslides triggered by the M_w 7.8 2016 Kaikōura Earthquake, New Zealand, derived from digital surface difference modeling. *Journal of Geophysical Research: Earth Surface*. 125(7):e2019JF005163. https://doi.org/10.1029/2019JF005163

Massey CI, Townsend DT, Lukovic B, Morgenstern R, Jones K, Rosser B, de Vilder S. 2020b. Landslides triggered by the M_W7.8 14 November 2016 Kaikōura earthquake: an update. *Landslides*. 17(10):2401–2408. https://doi.org/10.1007/s10346-020-01439-x

Massey CI, Lukovic B, Huso R, Buxton R, Potter SH. 2021a. Earthquake-induced landslide forecast tool for New Zealand: version 2.0. Lower Hutt (NZ): GNS Science. 77 p. (GNS Science report; 2018/08). https://doi.org/10.21420/G2TP9V

Massey CI, de Vilder SJ, Lukovic B, Townsend DB, Rosser BJ. 2021b. District-scale landslide risk analysis of debris inundation for the Kaikōura District. Lower Hutt (NZ): GNS Science. 117 p. Consultancy Report 2021/89. Prepared for Environment Canterbury; Kaikōura District Council.

Massey C, Lukovic B, Dellow S. 2022a. A prototype earthquake-induced landslide forecast tool for New Zealand. In: Towhata I, Wang G, Xu Q, Massey C, editors. *Coseismic landslides: phenomena, long-term effects and mitigation*. Singapore (SG): Springer. p. 617–631. https://doi.org/10.1007/978-981-19-6597-5_17

Massey C, Wolter A, Huso R, Lukovic B, Brideau M-A. 2022b. Coseismic landslide susceptibility and triggering analyses. In: Towhata I, Wang G, Xu Q, Massey C, editors. *Coseismic landslides: phenomena, long-term effects and mitigation*. Singapore (SG): Springer. p. 633–679. https://doi.org/10.1007/978-981-19-6597-5_18

Mastrandrea MD, Field CB, Stocker TF, Edenhofer O, Ebi KL, Frame DJ, Held H, Kriegler E, Mach KJ, Matschoss PR, et al. 2010. Guidance note for lead authors of the IPCC Fifth Assessment Report on consistent treatment of uncertainties. Geneva (CH): Intergovernmental Panel on Climate Change; [accessed 2025 Sep]. https://www.ipcc.ch/site/assets/uploads/2018/05/uncertainty-guidance-note.pdf

McDougall S. 2017. 2014 Canadian Geotechnical Colloquium: landslide runout analysis – current practice and challenges. *Canadian Geotechnical Journal*. 54(5):605–620. https://doi.org/10.1139/cgj-2016-0104

Medwedeff WG, Clark MK, Zekkos D, West AJ. 2020. Characteristic landslide distributions: an investigation of landscape controls on landslide size. *Earth and Planetary Science Letters*. 539:116203. https://doi.org/10.1016/j.epsl.2020.116203

Merghadi A, Yunus AP, Dou J, Whiteley J, ThaiPham B, Bui DT, Avtar R, Abderrahmane B. 2020. Machine learning methods for landslide susceptibility studies: a comparative overview of algorithm performance. *Earth-Science Reviews*. 207:103225. https://doi.org/10.1016/j.earscirev.2020.103225

Mergili M, Fellin W, Moreiras SM, Stötter J. 2012. Simulation of debris flows in the Central Andes based on open source GIS: possibilities, limitations, and parameter sensitivity. *Natural Hazards*. 61(3):1051–1081. https://doi.org/10.1007/s11069-011-9965-7

Ministry for the Environment. 2025. Proposed provisions – new National Policy Statement for Natural Hazards. Wellington (NZ): Ministry for the Environment; [accessed 2025 Sep 25]. https://environment.govt.nz/publications/attachment-1-8-proposed-provisions-new-national-policy-statement-for-natural-hazards/

Mishra AK, Placzek C, Jones R. 2019. Coupled influence of precipitation and vegetation on millennial-scale erosion rates derived from 10Be. *PLOS ONE*. 14(1):e0211325. https://doi.org/10.1371/journal.pone.0211325

Mitchell A, McDougall S, Nolde N, Brideau MA, Whittall J, Aaron JB. 2020. Rock avalanche runout prediction using stochastic analysis of a regional dataset. *Landslides*. 17(4):777–792. https://doi.org/10.1007/s10346-019-01331-3

Montgomery DR, Brandon MT. 2002. Topographic controls on erosion rates in tectonically active mountain ranges. *Earth and Planetary Science Letters*. 201(3–4):481–489. https://doi.org/10.1016/S0012-821X(02)00725-2

Moreno M, Steger S, Tanyas H, Lombardo L. 2023. Modeling the area of co-seismic landslides via data-driven models: the Kaikōura example. *Engineering Geology*. 320:107121. https://doi.org/10.1016/j.enggeo.2023.107121

Neverman AJ, Donovan M, Smith HG, Ausseil A-G, Zammit C. 2023. Climate change impacts on erosion and suspended sediment loads in New Zealand. *Geomorphology*. 427:108607. https://doi.org/10.1016/j.geomorph.2023.108607

Otago Regional Council. 2021. Proposed Otago Regional Policy Statement June 2021: integrating the management of Otago's natural and physical resources. Appeals Version. Dunedin (NZ): Otago Regional Council; [updated 2025 May 7; accessed 2025 Jun]. https://www.orc.govt.nz/media/s1xo42oh/clean-appeals-version-porps-21-forwebsite.pdf

Perla R, Cheng TT, McClung DM. 1980. A two-parameter model of snow-avalanche motion. *Journal of Glaciology*. 26(94):197–207. https://doi.org/10.3189/S002214300001073X

Quigley MC, Saunders W, Massey C, Van Dissen R, Villamor P, Jack H, Litchfield N. 2020. The utility of earth science information in post-earthquake land-use decision-making: the 2010–2011 Canterbury earthquake sequence in Aotearoa New Zealand. *Natural Hazards and Earth System Sciences*. 20(12):3361–3385. https://doi.org/10.5194/nhess-20-3361-2020

Read SAL, Richards LR, Perrin ND. 1999. Applicability of the Hoek-Brown failure criterion to New Zealand greywacke rocks. In: Vouille G, Berest P, editors. *International Congress on Rock Mechanics: proceedings*; 1999 Aug 25–28; Paris, France. [Place unknown]: International Society for Rock Mechanics. p. 655–660.

Reichenbach P, Rossi M, Malamud BD, Mihir M, Guzzetti F. 2018. A review of statistically-based landslide susceptibility models. *Earth-Science Reviews*. 180:60–91. https://doi.org/10.1016/j.earscirev.2018.03.001

Reid LM, Page MJ. 2003. Magnitude and frequency of landsliding in a large New Zealand catchment. *Geomorphology*. 49(1–2):71–88. https://doi.org/10.1016/S0169-555X(02)00164-2

[ResOrgs] Resilient Organisations. [2025]. Let's talk about risk: building greater capability for risk conversations between local authorities and communities. Christchurch (NZ): ResOrgs; [accessed 2025 Sep 25]. https://www.resorgs.org.nz/our-projects/risk-communication/lets-talk-about-risk/

Robinson TR, Davies TRH. 2013. Review Article: Potential geomorphic consequences of a future great (M_W = 8.0+) Alpine Fault earthquake, South Island, New Zealand. *Natural Hazards and Earth System Sciences*. 13(9):2279–2299. https://doi.org/10.5194/nhess-13-2279-2013

Robinson TR, Davies TRH, Wilson TM, Orchiston C. 2016. Coseismic landsliding estimates for an Alpine Fault earthquake and the consequences for erosion of the Southern Alps, New Zealand. *Geomorphology*. 263:71–86. https://doi.org/10.1016/j.geomorph.2016.03.033

Roda-Boluda DC, Schildgen TF, Wittmann H, Tofelde S, Bufe A, Prancevic J, Hovius N. 2023. Elevation-dependent periglacial and paraglacial processes modulate tectonically-controlled erosion of the Western Southern Alps, New Zealand. *Journal of Geophysical Research: Earth Surface*. 128(11):e2023JF007271. https://doi.org/10.1029/2023JF007271

Rosser B, Dellow S, Haubrock S, Glassey P. 2017. New Zealand's National Landslide Database. *Landslides*. 14(6):1949–1959. https://doi.org/10.1007/s10346-017-0843-6

Rosser B, Massey C, Lukovic B, Dellow S, Hill M. 2021. Development of a rainfall-induced landslide forecast tool for New Zealand. In: Casagli N, Tofani V, Sassa K, Bobrowsky PT, Takara K, editors. *Understanding and reducing landslide disaster risk Volume 3: monitoring and early warning*. Cham (CH): Springer International Publishing. p. 273–277. https://doi.org/10.1007/978-3-030-60311-3_32

Scheele FR, Syed YI, Hayes JL, Paulik R, Inglis S. 2023. Building inventory and vulnerability functions for risk modelling in New Zealand. Lower Hutt (NZ): GNS Science. 42 p. (GNS Science report; 2023/08). https://doi.org/10.21420/G34N-V958

Scheidegger AE. 1973. On the prediction of the reach and velocity of catastrophic landslides. *Rock Mechanics*. 5(4):231–236. https://doi.org/10.1007/BF01301796

Taig T, Massey CI, Webb TH. 2012. Canterbury earthquakes 2010/11 Port Hills slope stability: principles and criteria for the assessment of risk from slope instability in the Port Hills, Christchurch. Lower Hutt (NZ): GNS Science. 45 p. Consultancy Report 2011/319. Prepared for Christchurch City Council.

Tenzer R, Sirguey P, Rattenbury M, Nicolson J. 2011. A digital rock density map of New Zealand. *Computers & Geosciences*. 37(8):1181–1191. https://doi.org/10.1016/j.cageo.2010.07.010

Toka Tū Ake EQC. 2023. Risk tolerance methodology. Wellington (NZ): Toka Tū Ake EQC; [accessed 2025 Sep]. https://www.naturalhazards.govt.nz/assets/Research/Risk-Tolerance-Methodology_published-version.pdf

[USBR] U.S. Bureau of Reclamation. [2025]. Dam safety. Washington (DC): USBR; [updated 2023 Nov 14; accessed 2025 Mar 7]. https://www.usbr.gov/damsafety/risk/methodology.html

von Ruette J, Papritz A, Lehmann P, Rickli C, Or D. 2011. Spatial statistical modeling of shallow landslides: validating predictions for different landslide inventories and rainfall events. *Geomorphology*. 133(1–2):11–22. https://doi.org/10.1016/j.geomorph.2011.06.010

Wang W, Godard V, Liu-Zeng J, Scherler D, Xu C, Zhang J, Xie K, Bellier O, Ansberque C, de Sigoyer J, et al. 2017. Perturbation of fluvial sediment fluxes following the 2008 Wenchuan earthquake. *Earth Surface Processes and Landforms*. 42(15):2611–2622. https://doi.org/10.1002/esp.4210

Wichmann V. 2017. The Gravitational Process Path (GPP) model (v1.0) – a GIS-based simulation framework for gravitational processes. *Geoscientific Model Development*. 10(9):3309–3327. https://doi.org/10.5194/gmd-10-3309-2017

Wilkinson C, Stahl T, Jones K, Fujioka T, Fink D, Norton KP. 2022. Delayed ^{10}Be dilution in detrital quartz following extensive coseismic landsliding: a 2016 Kaikōura earthquake case study. *Earth and Planetary Science Letters*. 581:117392. https://doi.org/10.1016/j.epsl.2022.117392

Woods RJ, Thomas K-L, Scheele FR, Canessa S, Horspool NA. 2021. Queenstown debris flow and rockfall loss modelling for land-use planning policy options. Auckland (NZ): GNS Science. 35 p. Consultancy Report 2021/07. Prepared for Queenstown Lakes District Council.

Wride M, de Vilder SJ. 2021. Landslides caused by the March 2019 West Coast storm, South Island, New Zealand. Lower Hutt (NZ): GNS Science. 33 p. (GNS Science report; 2020/36). https://doi.org/10.21420/H0ZK-ES93

This page left intentionally blank.

APPENDICES

This page left intentionally blank.

APPENDIX 1 Datasets

The following datasets have been used for development of the landslide-debris-inundation hazard analysis conducted in this study.

Table A1.1 Digital elevation models.

Type	Description	Coverage	Reference
Raster	National digital elevation model (8 m ground resolution)	Full	LINZ (2014)

Table A1.2 Landslide catalogues.

Type	Description	Coverage	Number of Features	Reference
Vector	GNS Science landslide database	Full	1970	Rosser et al. (2017)
Vector	Shallow landslides	Partial	118	Emberson et al. (2016)
Vector	Shallow landslides	Partial	689	Hilton et al. (2011)
Vector	Shallow landslides	Full	7686	Hovius et al. (1997)
Vector	Rainfall- and earthquake-induced landslides	Partial	1643	England (2011)
Vector	2019 rainfall-induced landslides	Partial	1359	Wride and de Vilder (2021)
Vector	Shallow landslides	Partial	836	Leith (unpublished)
Vector	Land Cover Database (v5.0) landslides	Full	1102	LRIS Portal (2019)
Vector	Murchison earthquake landslides	Full	6134	Hancox et al. (2016)
Vector	Inangahua earthquake landslides	Full	1200	Hancox et al. (2014)
Vector	2021 rainfall-induced landslides	Full	669	Bain and Rosser (unpublished)

Table A1.3 Landslide triggers.

Type	Description	Coverage	Reference
Raster	ShakeMapNZ atlas and the New Zealand National Seismic Hazard Model (NSHM) 2022	Full	Gerstenberger et al. (2022)
Raster	Rainfall scenarios from the High Intensity Rainfall Design System (HIRDS) V4	Full	Carey-Smith et al. (2018)

APPENDIX 2 List of Landslide-Debris-Inundation Model Variables

Table A2.1 List of landslide-debris-inundation model variables.

Variable	Description	Value	Unit
A	Planimetric area of a landslide-source polygon	0	m^2
c	Average cohesive strength of landslide failure surface	50	kPa
α	Landslide area-volume scaling multiplier	-	1
γ	Landslide area-volume scaling exponent	1.36	1
V	Predicted volume of landslide source	-	m^3
$r_{(x,y)}$	Horizontal distance to the nearest failure-unit cell boundary	-	m
$D_{(x,y)}$	Maximum possible landslide depth at each pixel	N/A	m
θ_{XST}	Threshold slope angle for excess topography	20	°
θ_{NAT}	Threshold slope angle for surficial failures	20	°
SSY	Suspended sediment yield	-	t/m^2/yr
δ	Multiplier to convert *SSY* to total sediment yield	1.5	1
$\rho_{(x,y)}$	Rock density for constitutive units	-	t/m^3
S_{RIL}	Rainfall-induced landslide susceptibility	-	1/yr
S_{EIL}	Earthquake-induced landslide susceptibility	-	1/yr
dt_{RIL}	Rainfall-induced landslide probability-integration interval	-	yr
dt_{EIL}	Earthquake-induced landslide probability-integration interval	-	yr
$P_{RIL(T_0,T_{max},x,y)}$	Rainfall-induced landslide annual probability	-	1
$P_{EIL(T_0,T_{max},x,y)}$	Earthquake-induced landslide annual probability	-	1
$P_{(x,y)}$	Annual landslide probability	-	1
$\dot{E}_{(x,y)}$	Erosion rate	-	m/yr
ω_L	Proportion of eroded sediment generated through landsliding	1	1
η_L	Landslide-sediment bulking factor	1.3	1
$\rho_{L\,(x,y)}$	Landslide-debris density	-	t/m^3
$\dot{E}_{L(x,y)}$	Rate of sediment produced by landsliding at a given location	-	m/yr
$\dot{E}_{L_D(x,y)}$	Depth-corrected landslide sediment-production rate	-	m/yr
$\overline{D}_{L(x,y)}$	Mean depth of landslide occurrence	-	m
$V_{L(c)}$	Volume of a landslide class (c) size	-	m^3
$A_{L(c)}$	Landslide class area	-	m^2
$\overline{D}_{L(c)}$	Mean landslide class depth	-	m
$K_{L(c)(x,y)}$	Possibility for landslides of each class size to occur	-	T/F
$\dot{E}_{L(c)(T,RI)(x,y)}$	Landslide-induced erosion rate	-	m/yr
$S_{S(x,y)}$	Event-specific landslide susceptibility	-	1
$E_{L_S(x,y)}$	Event-specific landslide-sediment production	-	m
$M_{GPP(c)(T,RI)(x,y)}$	Landslide source-material thickness for each model run	-	m
σ	Landslide source-depth-integration interval	10^4	yr
$\Phi_{GPP(\mu)(c)(T,RI)(x,y)}$	Modelled landslide-material flux (per trigger and movement type)	-	m^3/m^2/yr
$P_{(\mu)(T)}$	Probability of a given movement type occurring (for a given trigger)	-	1

Variable	Description	Value	Unit
Φ_L	Mean landslide-debris flux	-	m^3/m
R	Gravitational Path Process (GPP) model grid resolution	25	m
Subscript	Description	-	-
x,y	Spatial location of pixel centroid	-	-
T_0	Lower limit of temporal-integration interval	-	-
T_{max}	Upper limit of temporal-integration interval	-	-
μ	Runout-model configuration	-	-
c	Landslide-volume class	-	-
T	Landslide trigger type	-	-
RI	Event return interval	-	-
L_S	Landslide-inducing scenario	-	-

APPENDIX 3 Landslide Source-Susceptibility Model

A landslide-susceptibility assessment is a quantitative or qualitative assessment of the spatial distribution of landslides that exist or potentially may occur in an area in response to a given trigger (Corominas et al. 2015). This landslide-susceptibility assessment forms the basis for the landslide-debris-inundation assessment, as it delineates the potential landslide-source areas from which landslide runout can be estimated.

The mean annual probability of failure for a grid cell is calculated by integrating the product of the susceptibility to a triggering event, and frequency of triggering event, over representative return intervals for a combination of foreseeable earthquake- and rainfall-induced landslide events. The shaking data used to create earthquake-induced landslide susceptibility outputs is derived from the New Zealand National Seismic Hazard Model (NSHM) 2022 (Gerstenberger et al. 2022). The landslide susceptibilities are calculated using peak ground accelerations (PGAs) for annual return intervals (ARIs) of 100-, 250-, 500- and 1000-year earthquakes. The rainfall data used to create the rainfall-induced landslide susceptibility forecasts come from the National Institute of Water & Atmospheric Research (NIWA)'s High Intensity Rainfall Design System (HIRDS) V4 model, which simulates the rainfall intensity at a 5 km grid resolution for a given range of ARIs. The landslide susceptibilities are calculated using the 24-hour rainfall for ARIs of 50, 100 and 250 years.

The landslide source-susceptibility (LSS) model is informed by outputs from Earthquake-Induced Landslide (EIL) Tool and Rainfall-Induced Landslide (RIL) Tool outputs trained on the region overseen by West Coast Emergency Management (WCEM). Each of these models is described in the following sections. Key landslide sediment-production (LSP) model assumptions and uncertainties are noted in Section A3.6, and a quantitative sensitivity analysis is undertaken in Section A7.2.

A3.1 Statistical-Modelling Methodology

To undertake the modelling, a sample grid at 32 m ground resolution was defined, and an input grid for each variable was created and aligned with the sample grid. A 32-m-resolution grid size was chosen as it was much less than the typical hill-slope lengths in the regions used for modelling, which can vary from 100 to >>1000 m. This resolution allowed easy aggregation of the inputs derived from the elevation data based upon the New Zealand 8 m Digital Elevation Model obtained from the Land Information New Zealand (LINZ) Data Service (LINZ 2014). For this analysis, only landslide-source areas, not debris trails, from each inventory were used. To reduce sample bias, (1) it was assumed that a grid cell is defined as being a landslide source (LS = 1) if its centroid falls within a landslide-source area, even if the grid cell is not fully occupied by the landslide source; and (2) all landslides within each dataset were used, regardless of their size.

A3.1.1 Model Training

Logistic regression is routinely used to forecast landslide occurrence (e.g. von Ruette et al. 2011; Budimir et al. 2015; Lombardo and Mai 2018) by calculating landslide probability from a series of input 'predictor' variables. The method is used to estimate the coefficients for predicting the probability (P_{LS}) that $Y = 1$, given the values of one or more predictor variables. Here, the condition $Y = 1$ corresponds to the occurrence of a landslide, and $Y = 0$ corresponds to no landslide, within a sample grid cell on the ground. The regression coefficients were estimated using a maximum likelihood criterion. Each model was fitted using the equation:

$$P_{LS} = \frac{1}{1+exp^{-z}} = \frac{exp^{z}}{1+exp^{z}}$$ Equation A3.1

where the probability of a landslide occurrence (P_{LS}) is within the range 0–1 on a sigmoid curve and Z is a linear-fitting function for the set of landslide-related variables tested, expressed in the form of:

$$Z = b_0 + b_1X_1 + b_2X_2 + \dots b_nX_n$$ Equation A3.2

where b_0, b_n and X_n represent the intercept of the model, the partial regression coefficients 'parameter estimates' and the conditioning factors, respectively. The parameter estimates for the different variables were derived by statistically comparing the mapped landslides with the features listed in Section A3.3.2, using the Statistica software (TIBCO Statistica™ 14.0.0[2]). For investigating the variables that best describe the landslide locations, we used an unbalanced dataset, given that the occurrence of a landslide ($Y = 1$) is much rarer than not ($Y = 0$). Therefore, our dataset is inherently biased toward no landslides ($Y = 0$) and, as a result, are naturally unbalanced. The regression coefficients were estimated in Statistica by maximising the likelihood function. The maximisation of the likelihood is achieved by an iterative method called Fisher scoring. The algorithm completes when the convergence criterion is satisfied or when the maximum number of iterations has been reached. Convergence is obtained when the difference between the log-likelihood function from one iteration to the next is less than 0.0000001.

For a variable to be included in the model, it must have a logical and statistically significant influence on P_{LS}. We used a significance level (p-value) of $p < 0.05$ (using the Wald statistic) as the threshold for inclusion in the model. Multiple combinations of variables were iteratively tested. To ensure that the variables included do not exhibit multicollinearity, we used the estimated correlation matrix of estimates between the variables. Note that we use the correlation matrix of estimates rather than the co-variance matrix of estimates. This is because the range of the values within each variable are relatively large – and vary considerably between each variable – which leads to very small co-variance values that are difficult to interpret. However, the correlation values range between -1 and 1, thus making it easier to interpret the correlation relationship between any two variables. Values of >0.5 were avoided by removing the given variable from the model, as these can exhibit multicollinearity. The final variable coefficients used in the models represent those variables that produced the best fit while meeting the significance level and multicollinearity criteria. This was done initially on all data from the combined events to determine the significant variables.

A3.1.2 List of Landslide Source-Susceptibility Model Predictors

Table A3.1 Predictor variables used in the logistic regression model with their ID codes, descriptions and units.

Variable ID	Description	Units
Landslide Susceptibility Factors		
Geology	The geology classification is from the geology layer for the whole of New Zealand and is based on the 'dominant unit' classification within the QMAP data (Heron 2020). The Geology field holds one out of seven possible values based on dominant unit, and a number code was assigned to each Geology classification and stored in the GeolCode field. This number code was used to generate a grid out of polygons using the MAXIMUM_COMBINED_AREA option.	-
Geology 1 (GeolCode 1)	Quaternary sands, silts and gravels. These materials typically form terrace deposits on the top of the steep coastal cliffs, as well as on inland slopes adjacent to the main rivers of the area. Many of these terraces have been incised by rivers.	Categorical
Geology 2 (GeolCode 2)	Neogene limestones, sandstones and siltstones, which are typically weak. These occur along sections of the coast north of Kaikōura and along the coast and inland from Greymouth to Karamea on the West Coast.	Categorical
Geology 3 (GeolCode 3)	Upper Cretaceous – Paleogene rocks, including limestones, sandstones, siltstones and minor volcanic rocks. These are typically weak (like the Neogene limestones and sandstones) and easily erodible, and can also contain thin clay seams, which are volcanic in origin. These rocks are typically exposed in narrow strips overlying the greywacke basement rocks in the Kaikōura region but are more prevalent within the area affected by the Murchison and Inangahua earthquakes.	Categorical

2 https://docs.tibco.com/products/tibco-statistica-14-0-0

Variable ID	Description	Units
Geology 4 (GeolCode 4)	All intrusive and extrusive igneous rocks, ranging in age from Jurassic to Quaternary. Includes andesites, basalts, rhyolites, ignimbrites, dacites, granites and granodiorites. These represent the smallest (in land area) geology group within the area affected by the three earthquakes.	Categorical
Geology 5 (GeolCode 5)	Lower Cretaceous Torlesse (Pahau terrane) ‘basement’ rocks are predominantly sandstones and argillite, also known as greywacke. The greywacke rocks are typically moderately to well bedded and tend to be closely jointed. These form many of the coastal slopes, as well as the steeper inland Kaikōura mountain ranges, and are the dominant rock type affected by the Kaikōura earthquake.	Categorical
Geology 6 (GeolCode 6)	Quaternary lava. Predominantly basalt lavas. Not used in these analyses, as such materials are not present within the training area.	Categorical
Geology 7 (GeolCode 7)	Neogene debris, including landslide debris, alluvium, etc. Not used in these analyses, as such materials are not present within the training area.	Categorical
Land cover categories	The land-cover categories of LCDB v5.0 were obtained from the LRIS Portal. The data were grouped based on the polygon description, a code assigned to each group and the polygons then turned into integer grids using the MAXIMUM_COMBINED _AREA option. The chosen land-cover grid was based on its proximity in time (the closest in time) to the event triggering the landslides and thus is thought to represent the land cover at the time that the storm occurred. For this work, the land-cover grids LC1997 and LC2018 were used – the LC1997 classification for the Coromandel 1981 landslides and study area and LC2018 for the Hunua landslides and study area – as these represent the land-cover types at times closest to when the landslides occurred. To simplify the training, the land-cover grid codes were combined into three categories, see cells below.	Categorical
Land cover code 1 (LCC1)	Group 1 includes deciduous hardwoods and indigenous, exotic and harvested forest.	Categorical
Land cover code 2 (LCC2)	Group 2 includes: bare ground, urban, urban open (parks and open space), transport and landslides.	Categorical
Land cover code 3 (LCC3)	Group 3 includes: alpine vegetation, scrub, grassland and horticulture.	Categorical
$Slope_{MEAN}$	Local hillslope gradient generated in ArcGIS from the LINZ 8 m resolution digital elevation model, adopting the mean value of all 8 m cells that fall within each cell of the 32 m sample grid. This variable is a proxy for the static shear stresses in the slope.	Degrees (°)
$Elev_{MEAN}$	Local hillslope elevation taken from the LINZ 8 m resolution digital elevation model, adopting the mean value of all 8 m cells that fall within each cell of the 32 m sample grid. This variable represents the observation that topography can limit the size of the landslides. For example, slopes that are higher in elevation tend to have larger surface areas and can therefore generate larger landslides than slopes at lower elevations, which tend to have smaller surface areas (Massey et al. 2020a). It could also represent different climatic conditions and erosion processes that could dominate at different elevations.	Metres above mean sea level (mAMSL)
$Aspect_{MEAN}$	Grid-cell aspect re-sampled from the LINZ 8 m digital elevation model. Hill-slope aspect calculated in ArcGIS at 32 m resolution.	Degrees (°) 0–36
$Curv_{MEAN}$	Curvature generated in ArcGIS from the LINZ 8 m resolution digital elevation model. For each cell, the curvature value is calculated as a second derivative of the surface fitted through that cell and its eight surrounding neighbours. A negative value indicates that the surface is upwardly convex at that cell. A positive profile indicates that the surface is upwardly concave at that cell. A value of 0 indicates that the surface is flat. Curvature was aggregated to 32 m resolution, adopting the mean value of all 8 m cells that fell within each cell of the 32 m sample grid. This variable is a proxy for slope ‘hollows’ that represents topographic depressions where surface water might accumulate.	One hundredth (1/100) of a z-unit

Variable ID	Description	Units
Landslide Forcing Factors		
24 hr Rain	Grid of 24-hour rain amounts (from 9:00 am to 9:00 am), derived from NIWA's Virtual Climate Station Network (VCSN) model[3] at 5 km resolution. The rain values were attributed to the sample grid cell by taking the rain value at its centroid using bi-linear interpolation. The rain amount is the maximum value from all 24-hour rain grids that cover the duration of the storm.	mm
SMI	Grid of soil moisture (soil moisture indices; SMI) on the day before the storm, taken from NIWA's VCSN model at 5 km resolution. The SMI values were attributed to the sample grid cell by taking the SMI value at its centroid using bi-linear interpolation. SMI is calculated from 9:00 am to 9:00 am (24-hour period), from rainfall and evapotranspiration. The base value is -150 mm ('permanent wilting point') based on 'soil store capacity'. A value of '0' indicates that the soil is at 'field capacity' (amount of water held in the soil after the excess has drained away). A value greater than '0' indicates runoff. Note on soil moisture calculation: The NIWA model has one parameter, the soil store capacity (S_{max}). Rainfall is assumed to infiltrate into a soil store from which moisture is depleted by evapotranspiration loss. The model keeps track of the soil store for each time-step. When the soil store is full, it is assumed to be saturated and the excess rainfall becomes surface run-off. Evapotranspiration is assumed to continue at its potential rate until the soil water store drops to half capacity. Evapotranspiration then decreases linearly to zero when the store is empty. For the simulations here, an S_{max} value of 150 mm is used for all modelling grids.	mm

A3.1.3 Model Standardisation and Bootstrapping

To test the importance of each variable used in the model, we converted each one to their standard score using the formula:

$$z = \frac{x - \mu}{\sigma} \qquad \text{Equation A3.3}$$

where z is the standard score, x is the data value of the variable, μ is the variables mean and σ is the variables standard deviation. This conversion normalises the distribution of the variable, which in turn allows the model coefficients of each variable to be interpreted as a measure of its importance relative to other variables in the model (Lombardo and Mai 2018). As we standardised each variable prior to use within the regressions, all resulting coefficient values are in the same unit-less scale and can be directly compared. Initial models were fitted using GeolCode as a categorical variable in the regression, and the results showed that GeolCode was statistically significant. Separate models were then fitted using GeolCode as a grouping variable. These GeolCode-grouped models performed statistically better than the model that included the GeolCodes as categorical variables.

Validation of the model results was done using bootstrapping (Efron and Tibshirani 1994), which allowed the variability of the parameter values for each variable to be estimated within each GeolCode group. Bootstrapping is a way to assess the robustness of the coefficients estimated for each variable derived from model fitting. For example, a robust estimate of the value for a given variable should have a narrow variation between the minimum and maximum and standard deviation either side of the mean. Conversely, a poor estimate would be one with a wider variation. In addition, a robust model should show little difference between the areas under the ROC (receiver operating characteristic) curves calculated for each of the 100 bootstrap models. To this end, we repeatedly drew random samples from the respective landslide datasets, where each sample represented 75% of the total GeolCode-specific dataset. A sample was drawn 100 times, logistic-regression models were fitted to the sampled dataset and the result statistics were calculated – minimum, maximum, mean and standard deviation of each variable parameter, along with the specificity, sensitivity and area under the ROC curve (ROC:AUC).

3 https://niwa.co.nz/climate/our-services/virtual-climate-stations

A3.1.4 Logistic Lasso Regression

We then used logistic Lasso (L1) regression to identify and cross-check the main variables that could be used to explain landslide occurrence while reducing over-fitting – this step essentially identifies the minimum number and therefore most important variables that can be used to explain landslide occurrence.

Statistica performs V-fold cross-validation to identify the optimal lambda value (hyper parameter) using minimum average error. The initial run is on the entire data to get the lambda sequence. The cross-validation procedure then splits the input data into 10 folds and runs the algorithm with each fold omitted. The average errors are calculated over each fold and their standard deviations computed. The errors were calculated using the mean squared error, which uses the squared residuals to calculate the mean cross-validated error. The logistic Lasso regression coefficients for the chosen variables were only used for variable selection, as the coefficients produced by the Lasso model are biased.[4]

The Lasso Regression module in Statistica uses a penalised maximum likelihood estimation (MLE) method to fit the linear and logistic regression models. The regularisation is performed over a grid of lambda values, the regularisation parameter (the L1 penalty). The module uses a cyclical coordinate descent to minimise the objective function and likelihood contribution, as well as the penalty, over a grid of lambda values successively (Friedman et al. 2010).

The main advantage of a Lasso regression model is that it can set the coefficients for variables it does not consider interesting to zero. This means that the model decides which variables should and should not be included. Another advantage of a Lasso regression is that the L1 penalty added to the model helps to prevent the model from over-fitting. One of the main disadvantages of Lasso regression is that the coefficients that are produced by a Lasso model are biased. The L1 penalty that is added to the model artificially shrinks the coefficients closer to zero, or, in some cases, all the way to zero. This means that the coefficients from a Lasso model do not represent the true magnitude of the relationship between the variables and the outcome (landslide probability) but rather a shrunken version of that magnitude.

A3.2 Earthquake-Induced Landslide Forecast Model

Version V2.1 of the earthquake-induced landslide-susceptibility model (Massey et al. 2021a) was used to generate the earthquake-induced landslide probability grids used in this report. A landslide-susceptibility model provides a quantitative or qualitative assessment of the volume (or area) and spatial distribution of landslides that exist or potentially may occur in an area (Corominas et al. 2015). For this work, a quantitative susceptibility model is used to estimate the probability (0–1) of landslides occurring under a given set of conditions. This statistical model is based on a logistic regression machine-learning approach, which is described in Massey et al. (2021a, 2022a, 2022b). This model requires several variables as inputs – in grid format, these factors are:

1. **Geology:** The dominant rock/soil type of the grid cell. This was based on linking the 'GeolCodes' used in the earthquake-induced landslide-susceptibility model V2.1 with appropriate geological units based on their mechanical properties. The available geological information was limited in detail and resolution (Table A3.1).
2. **Earthquake shaking:** Adoption of different PGAs from the New Zealand NSHM 2022, adopting the given return periods and a shear wave velocity (V_{S30}) of 750 m/s.
3. **Local slope relief:** The local height of a given gid cell relative to its surrounding grid cells.
4. **Slope angle:** How steep the given grid cell is.

4 https://crunchingthedata.com/when-to-use-lasso/

5. **Elevation:** The elevation of the given grid cell.
6. **Slope curvature:** The shape of the surface area defined by a given, and surrounding, grid cells.

Separate grids were generated for each of the given variables required by the earthquake-induced landslide-susceptibility model within the study area. The LINZ 8 m digital elevation model (DEM) was used to generate all of the variable grids used in the earthquake-induced landslide modelling, with a final grid resolution of 32 x 32 m used for the susceptibility forecasts used in the development of the LSP model. The earthquake-induced landslide-susceptibility model variables and their coefficients are shown in Tables A3.2–A3.6. Results from the model fitting – calculated as the Nagelkerke (pseudo R^2) and ROC: AUC – are shown in Table A3.7.

Table A3.2 GeolCode1 (Quaternary sands, silts and gravels): logistic regression coefficients for the different variables used in the model derived from bootstrapping.

Variable Coefficient	Intercept	Elevation	Slope	Local Slope Relief	Curvature	Peak Ground Acceleration
Minimum	-10.10	-0.0010	0.03	0.06	-0.23	2.64
Maximum	-9.93	-0.0008	0.04	0.07	-0.16	2.79
Mean	-10.00	-0.0009	0.03	0.06	-0.20	2.70
Standard deviation	0.04	0.00002	0.00	0.00	0.01	0.03
Skew	-0.22	0.6448	-0.34	0.27	0.80	0.11

Table A3.3 GeolCode2 (Neogene limestones, sandstones and siltstones): logistic regression coefficients for the different variables used in the model derived from bootstrapping.

Variable Coefficient	Intercept	Elevation	Slope	Local Slope Relief	Curvature	Peak Ground Acceleration
Minimum	-10.03	0.0017	0.05	0.02	-0.11	2.39
Maximum	-9.89	0.0017	0.06	0.02	-0.09	2.46
Mean	-9.97	0.0017	0.05	0.02	-0.10	2.44
Standard deviation	0.03	0.00002	0.00	0.00	0.01	0.02
Skew	0.55	0.2733	-1.02	-0.04	-0.36	-0.56

Table A3.4 GeolCode3 (Upper Cretaceous to Paleogene rocks, including limestones, sandstones and siltstones): logistic regression coefficients for the different variables used in the model derived from bootstrapping.

Variable Coefficient	Intercept	Elevation	Slope	Local Slope Relief	Curvature	Peak Ground Acceleration
Minimum	-8.42	-0.0003	0.03	0.02	-0.14	2.15
Maximum	-8.29	-0.0002	0.04	0.03	-0.12	2.22
Mean	-8.35	-0.0003	0.03	0.03	-0.13	2.19
Standard deviation	0.03	0.00003	0.00	0.00	0.01	0.02
Skew	0.09	-0.2147	-0.21	0.54	-0.66	-0.11

Table A3.5 GeolCode4 (All intrusive and extrusive igneous rocks): logistic regression coefficients for the different variables used in the model derived from bootstrapping.

Variable Coefficient	Intercept	Elevation	Slope	Local Slope Relief	Curvature	Peak Ground Acceleration
Minimum	-8.05	-0.0009	0.01	0.03	-0.16	1.94
Maximum	-7.82	-0.0007	0.01	0.03	-0.12	2.02
Mean	-7.94	-0.0008	0.01	0.03	-0.14	1.97
Standard deviation	0.05	0.00003	0.00	0.00	0.01	0.02
Skew	0.33	0.1051	0.14	0.00	-0.33	0.09

Table A3.6 GeolCode5 (Lower Cretaceous Torlesse [Pahau terrane] 'basement' rocks): logistic regression coefficients for the different variables used in the model derived from bootstrapping.

Variable Coefficient	Intercept	Elevation	Slope	Local Slope Relief	Curvature	Peak Ground Acceleration
Minimum	-10.04	-0.0005	0.04	0.03	-0.11	1.98
Maximum	-9.91	-0.0005	0.05	0.03	-0.09	2.01
Mean	-9.97	-0.0005	0.04	0.03	-0.10	1.99
Standard deviation	0.03	0.00001	0.00	0.00	0.00	0.01
Skew	-0.53	0.0185	0.23	0.23	0.14	0.87

Table A3.7 Results from the model fitting: calculated as the Nagelkerke (pseudo R^2) and area under the random operator characteristic curve (ROC: AUC) (Massey et al. 2021a, 2022a, 2022b).

GeolCode	Pseudo R^2	Mean ROC:AUC
1	0.23	0.91
2	0.28	0.89
3	0.14	0.82
4	0.09	0.76
5	0.17	0.86

A3.3 Western South Island Rainfall-Induced-Landslide Model

This section provides an overview of the development of the rainfall-induced-landslide model for the western South Island, which follows the same methodology adopted to develop the earthquake-induced landslide-susceptibility model. The following key steps were undertaken to establish the rainfall-induced-landslide model and its associated variables and coefficients:

A3.3.1 Area of Interest Definition

To define areas of interest for model training, a polygon was created around two separate landslide datasets. This involved adopting a 100 m buffer around all landslide sources and applying a convex hull interpolation around these buffers. This approach assumed that the mapped landslides accurately represent the full extent of landslides generated by storm events.

The two landslide datasets used were:

- **West Coast 2019**, containing 1395 landslide-source polygons (Wride and de Vilder 2021).
- **West Coast 2021**, containing 951 landslide-source polygons (Bain and Rosser, unpublished).

A3.3.2 Variable Selection

Statistical-based models are most used for mapping landslide susceptibility (Budimir et al. 2015; Reichenbach et al. 2018; Merghadi et al. 2020). Statistical-based modelling of landslide susceptibility is usually performed using classification algorithms to establish an empirical relationship between a binary dependent variable (landslides versus no landslides) and various static environmental factors, such as slope gradient and bedrock lithology (Lin et al. 2021). The established empirical relationship can then be used to estimate a relative spatial landslide-susceptibility index and produce the final landslide-susceptibility map. For this work, we also adopt ‘dynamic’ variables of rain amount and the soil-moisture indices to represent the magnitude of ‘forcing’, as landslide probability should scale with this magnitude (e.g. Chan et al. 2018).

The predictor variables used to train the models were chosen based on variables previously found to influence landslide occurrence (e.g. Budimir et al. 2015; Reichenbach et al. 2018; Chan et al. 2018; Merghadi et al. 2020; Lin et al. 2021). Based on these studies, we reduced the number of predictor variables used in the model training to the following (in no particular order):

1. 24-hour rainfall amount.
2. Soil-moisture indices.
3. Slope angle.
4. Elevation.
5. Slope aspect.
6. Slope curvature.
7. Geology.
8. Land cover.

These predictor variables and the methods used to calculate them are described in Table A3.1.

A3.3.3 Model Results

Once the main variables contributing to the landslide occurrence in each GeolCode were identified from the Lasso models, the chosen variables were then included in separate logistic-regression models using all of the training data within each GeolCode separately. The estimated coefficients for each variable included in the models were then used to forecast landslide occurrence across the entire area of interest using either HIRDS V4 24-hour rainfall amounts for different average recurrence intervals (ARIs) or event-specific ‘scenario’ rainfall amounts.

The chosen variables and their coefficients derived from the 'best-fitting' models are shown in Table A3.8.

Table A3.8 Results from the best-fitting logistic-regression models, their variables and mean coefficients and the model pseudo R^2 and area under the receiver operating characteristic curve (ROC:AUC).

Variable	GeolCode 1			GeolCodes 2 and 3 (Combined)			GeolCode 4			GeolCode 5		
	Mean Coefficient	Standard Error	84^{th}% Coefficient	Mean Coefficient	Standard Error	84^{th}% Coefficient	Mean Coefficient	Standard Error	84^{th}% Coefficient	Mean Coefficient	Standard Error	84^{th}% Coefficient
Intercept	-11.866	0.181	-11.611	-12.313	0.341	-11.834	-9.0031	0.2300	-8.6799	-10.756	0.121	-10.5860
$Elev_{MEAN}$	-0.0011	0.0002	-0.0008	-0.0027	0.0004	-0.0022	-0.0038	0.0002	-0.0035	-0.0027	0.0001	-0.0026
$Slope_{MEAN}$	0.120	0.004	0.125	0.091	0.007	0.100	0.0757	0.0051	0.0828	0.082	0.002	0.0844
$Aspect_{MEAN}$	-0.018	0.005	-0.011	-0.051	0.008	-0.040	-0.0584	0.0054	-0.0508	-0.009	0.002	-0.0065
$Curv_{MEAN}$	-0.256	0.040	-0.199	-0.166	0.060	-0.082	-0.1900	0.0362	-0.1391	-0.095	0.011	-0.0790
24 hr Rain	0.004	0.001	0.005	0.007	0.001	0.009	0.0017	0.0007	0.0026	0.0080	0.0002	0.0084
LCC1	-0.86	0.10	-0.719	N/A	N/A	N/A	N/A	N/A	N/A	-1.027	0.037	-0.975
LCC2	0.47	0.14	0.663	N/A	N/A	N/A	N/A	N/A	N/A	0.801	0.057	0.881
LCC3	1.00	N/A	1.0	N/A	N/A	N/A	N/A	N/A	N/A	1.000	N/A	1.0
Pseudo R^2	0.20			0.08			0.19			0.11		
ROC:AUC	0.917			0.838			0.904			0.846		

These results show that:

- Only GeolCodes 1 and 5 have land cover as a categorical variable.
- GeolCodes 2 and 3 were merged, as these not only had limited data with respect to the numbers of landslides but also because the fitted models had very similar variables and coefficients.
- Overall, the main variables are – in order of importance with respect to explaining landslide probability – GeolCode, rainfall, slope, elevation and then the others such as land cover, soil-moisture indices, aspect and curvature, which tend to have similar but lower levels of importance.
- Elevation is slightly correlated with rainfall but not enough to lead to over-fitting.
- With the exception of GeolCode 4, the soil-moisture indices variable was not shown to be statistically important in any of the other GeolCode regressions. It also had low importance in the GeolCode 4 regression and, when removed from the regressions, had little influence on the coefficients and model 'goodness of fit' statistics. As a result, the soil-moisture indices variable was not included in the final models used to forecast landslide probability.
- The relatively high ROC:AUC values indicate that, overall, the models are fitting the data well. Overall, the statistical models developed here provide a robust forecast of landslide probability at different levels of rainfall.
- However, the results from the models have a low pseudo R^2, indicating that these cannot give accurate forecasts for individual grid cells. These may nevertheless give good overall estimates of the scale 'intensity' of landslide occurrence to be expected in individual rain events.

A3.4 Calculation of Slope Failure Probability

The earthquake- and rainfall-induced landslide models provide insight into the probability of a landslide occurring at a given location in response to rainfall triggers for 50-, 100- and 250-year ARI events, as well as seismic shaking associated with 100-, 250-, 500- and 1000-year ARI events.

In order to calculate the total annual probability of a landslide occurring at a given location [$P_{(x,y)}$], we integrate the rainfall-induced landslide probability (S_{RIL}) and earthquake-induced landslide (S_{EIL}) probabilities, normalised by their respective integration intervals ($dt_{RIL} = T_{RIL\_max} - T_0$ and $dt_{EIL} = T_{EIL\_max} - T_0$, respectively), where T_0 and T_{max} represent the midpoint between subsequent trigger intervals. To convert from the probability of a grid cell containing a landslide (as output from the earthquake- and rainfall-induced landslide models) to the predicted area of landslide sources (required for sediment-production models), we multiply both outputs by the ratio of the earthquake- or rainfall-induced landslide grid-cell area to the geometric-mean area of all landslides associated with that trigger ($\overline{A_{L(T)}}$; the derivation of this area is described later in Section A4.3):

$$P_{RIL(x,y)} = \frac{\int_{T_0}^{T} S_{RIL(T_0,T,x,y)}}{dt_{RIL}} \times \frac{\overline{A_{L(EIL)}}}{32^2} \quad \text{Equation A3.4}$$

$$P_{EIL(x,y)} = \frac{\int_{T_0}^{T} S_{EIL(T_0,T,x,y)}}{dt_{EIL}} \times \frac{\overline{A_{L(RIL)}}}{32^2} \quad \text{Equation A3.5}$$

$$P_{(x,y)} = P_{RIL(x,y)} + P_{EIL(x,y)} \quad \text{Equation A3.6}$$

A3.5 Landslide Source-Susceptibility Model Adjustment for the RCP6 2081–2100 Climate-Change Scenario

To adjust historical HIRDS V4 rainfall depth or intensity surfaces for climate change, we increased rainfall by a specific percentage per degree of warming. We selected this adjustment factor from Table A3.9 below, multiplied it by the chosen temperature increase and applied it to the historical HIRDS V4 rainfall estimates. For example, when estimating a 1-hour, 10-year rainfall event with a historical value of 35 mm, and assuming a temperature increase of 2.1°C, we first selected a percentage increase of 13.1% per degree of warming for this duration and frequency. We then multiplied 13.1% by 2.1 to get 27.5% and applied this to the historical estimate, resulting in a projected rainfall of 45 mm. This consistent percentage increase allowed us to apply the same adjustment across the entire HIRDS V4 grid. For shorter storm durations, we used the 1-hour duration percentage change factors, and, for return periods of over 100 years, we applied the 100-year factors. Temperature change values for different RCPs (Representative Concentration Pathways) and time periods were taken from Table A3.10, so, for RCP6 at the end of the century, we used a value of 1.63°C.

Table A3.9 Percentage-change factors to project rainfall depths derived from the current climate to a future climate that is one degree warmer (Source: Carey-Smith et al. 2018). ARI = Annual Return Interval.

Duration/ ARI	2-Year	5-Year	10-Year	20-Year	30-Year	40-Year	50-Year	60-Year	80-Year	100-Year
1 hour	12.2	12.8	13.1	13.3	13.4	13.4	13.5	13.5	13.6	13.6
2 hours	11.7	12.3	12.6	12.8	12.9	12.9	13.0	13.0	13.1	13.1
6 hours	9.8	10.5	10.8	11.1	11.2	11.3	11.3	11.4	11.4	11.5
12 hours	8.5	9.2	9.5	9.7	9.8	9.9	9.9	10.0	10.0	10.1
24 hours	7.2	7.8	8.1	8.2	8.3	8.4	8.4	8.5	8.5	8.6
48 hours	6.1	6.7	7.0	7.2	7.3	7.3	7.4	7.4	7.5	7.5
72 hours	5.5	6.2	6.5	6.6	6.7	6.8	6.8	6.9	6.9	6.9
96 hours	5.1	5.7	6.0	6.2	6.3	6.3	6.4	6.4	6.4	6.5
120 hours	4.8	5.4	5.7	5.8	5.9	6.0	6.0	6.0	6.1	6.1

Table A3.10 New Zealand land-average temperature increase relative to 1986–2005 for four future emissions scenarios. The three 21st century projections result from the average of six regional climate model simulations (driven by different global climate models). The early 22nd century projections are based only on the sub-set of models that were available and so should be used with caution (source: Carey-Smith et al. 2018).

	2031–2050	2056–2075	2081–2100	2101–2120
RCP 2.6	0.59	0.67	0.59	0.59 (4 model average)
RCP 4.5	0.74	1.05	1.21	1.44 (5 model average)
RCP 6.0	0.68	1.16	1.63	2.31 (CESM1–CAM5 only)
RCP 8.5	0.85	1.65	2.58	3.13 (3 model average)

A3.6 Key Landslide Source-Susceptibility Model Uncertainties and Assumptions

We note a number of constraints for the rainfall-induced landslide-susceptibility calculation:

- The model represents extrapolation of observations from two storm events, just two years apart. While the model results are statistically significant, these only represent the relationships between the variables used and the landslides generated by these two events.
- 24-hour precipitation data for each event are derived from a model and gridded at 5 x 5 km. The accuracy of precipitation totals at each landslide location is unconstrained. Other than for the GeolCode 4 model, the soil-moisture indices variable is not statistically significant in the models and so not included in the final models used for forecasting landslide probability.
- Soil moisture for each event is derived from a model and gridded at 5 x 5 km. The accuracy of soil-moisture indices totals at each landslide location is unconstrained.
- The rainfall totals did not allow sampling of impacts up to a 250-year ARI event. There is therefore no data to support predictions for higher-intensity events.
- The landslide data incorporates 2300 manually mapped landslide-source areas. The completeness of the mapping is unconstrained in terms of both spatial distribution and observed landslide sizes.
- The 2019 landslide catalogue covers landsliding in the northern half of the study area, while the 2021 landslide catalogue covers approximately 5% of the study region centred around the Kokiraki area.
- The catalogues cover similar geomorphological settings and rock types. The impact of precipitation events (in terms of the number of grid cells containing landslide sources) in other geological and geomorphological settings is therefore unconstrained.
- It is unclear whether the area-frequency distribution of landslides from the mapped events is representative of all geomorphological settings.
- It is unclear whether the area-frequency distribution from the mapped events is representative of all triggering-event magnitudes.
- Employing statistical datasets to describe the distribution of possible landslide areas ignores kinematic constraints and would suggest that the relative probability of giant landslides occurring on small hill slopes is equal to that in mountainous areas with similar slope angles.

- The model is trained on a 32 x 32 m grid of pixels containing landslide scars. This neither represents the exact number, nor exact area, of mapped landslides in the dataset. The uncertainty associated with calculating either of these two fundamental metrics from the rainfall-induced landslide output is dependent on grid resolution, landslide-area characteristics and landslide clustering in the landscape. Currently, this uncertainty is only constrained with respect to the training dataset; elsewhere, it is unconstrained.

APPENDIX 4 Landslide Sediment-Production Model

This section describes details of the landslide sediment-production (LSP) model, which is used to determine the volume of landslide debris released from each source pixel for both mean annual and scenario-based models in the present-day and RCP6 2081–2100 climate scenarios.

Key LSP model assumptions and uncertainties are noted in Section A4.8, and a quantitative sensitivity analysis is undertaken in Section A7.3.

A4.1 Determination of Landslide-Erosion Rates

A4.1.1 Determination of Landslide-Sediment Production

As discussed in Section 2.1.2, the selected mean annual erosion rates for this study are derived from regional observations.

We base our estimation of erosion rates on two previous studies quantifying river-borne suspended sediment yields from catchments across New Zealand (Hicks et al. 2011) and the specific density of geological units mapped throughout the country (Tenzer et al. 2011). Hicks et al. (2011) undertook a detailed measurement campaign during the 1990s that provided mean annual sediment fluxes for all 233 catchments. Using this data, along with a classification of catchment lithology and landforms and mean annual precipitation rates, they then calibrated a national model constraining specific sediment yield (SSY) to rivers on a 100 m resolution grid. The national calibration required local adjustments to address outliers in northwest Nelson, the central axial Southern Alps, McKenzie Country and Fiordland.

Spatially consistent erosion rates derived from suspended-sediment-yield and bedrock-density data can be tested against local observations of catchment-integrated denudation rates derived from ^{10}Be concentrations in sediment deposited in river beds. Davies et al. (2005) suggest that suspended sediment may represent 50% of total sediment yield for catchments in this region, and Robinson et al. (2016) therefore elected to multiply the SSY values by a factor of 2. However, more recent measurement of catchment-averaged ^{10}Be denudation rates (Larsen et al. 2014; Roda-Boluda et al. 2023) demonstrate a good correlation with the SSY model data when a factor of 1.5 is used to correct from the suspended component to total sediment yield (Figure A4.1a). This is lower than that earlier adopted by Davies et al. (2005) and Robinson et al. (2016), although well supported by the observational data, so we therefore adopt this value for the current hazard assessment.

Employing recent observations of river-borne sediment yield or denudation rates through ^{10}Be concentrations can raise questions with respect to the influence of earthquake-induced landslide-sediment contributions. Specifically, (1) are observed rates elevated as a result of recent earthquake-induced landsliding? (2) If these do not include a direct earthquake-induced landslide signal, do observed rates exclude the contribution from earthquake-induced landslides?

Regarding question (1): Observations of lacustrine sedimentation in Lake Ellery immediately to the west of the Alpine Fault indicate that seismically generated sediment may temporarily increase mean erosion rates by ~40% (Howarth et al. 2016). This is supported by seismically generated landslide models from Robinson et al. (2016), who suggested that co-seismic landsliding may increase erosion rates in some catchments by around 35%. Global studies indicate that the period of enhanced landslide-sediment production commonly decays exponentially to background levels over a period of up to seven years, depending on the return interval of the triggering event (Marc et al. 2015; Fan et al. 2018), with the phase of enhanced post-seismic sedimentation (incorporating enhanced instability and sediment transport) lasting on average 58 ± 15 years (Howarth et al. 2016). This reflects a period over which landslide deposits directly connected to river networks become exhausted of readily transportable debris (see Croissant et al. [2019] and references therein). Given that the last earthquake to trigger regional landsliding in the region was the 1968 Inangahua earthquake (>56 years ago), suspended sediment yields observed by Hicks et al. (2011) almost certainly reflect rates of inter-seismic sediment transport. As such, these do not carry the short-term 35–40% increase in sediment output associated with fluvially connected post-seismic landslides and instead reflect more or less constant background rates of undifferentiated (earthquake- and rainfall-induced) landslide debris export via the river network. This is facilitated by a combination of secondary sub-aerial and fluvial processes, modulated by climatic factors (Croissant et al. 2019). We can therefore rule out the possibility that observed rates are elevated as a result of recent earthquake-induced landsliding.

Regarding question (2): Accounting for the relatively modest initial increase in earthquake-induced erosion rates, as well as rapid exponential decay, the associated increase in long-term erosion rates can therefore be expected to be approximately 4% over a 100-year seismic cycle, dropping to roughly 1–1.5% for a 300-year cycle (consistent with Alpine Fault recurrence intervals [Howarth et al. 2016]). These increases are negligible when compared to uncertainties associated with erosion-rate estimates in the study region (discussed later in this section). We therefore assume that the observed rates represent the combined transport of earthquake- and rainfall-induced landslide debris through secondary sub-aerial and fluvial processes and thereby capture the contribution of both triggers.

In order to convert the Hicks et al. (2011) SSY model into spatially distributed erosion rates [$\dot{E}_{(x,y)}$], we must account for the additional proportion of sediment transported as bed load and divide the yield [$SSY_{(x,y)}$] by the density of geological units underlying each catchment [$\rho_{\ (x,y)}$]. The digital rock-density catalogue of Tenzer et al. (2011) summarises measured densities of almost 10,000 specimens divided into 123 soil and rock types, consistent with the QMAP classification used in digital geological maps of New Zealand (Heron 2020). Equation A4.1 describes the method used to convert estimated suspended sediment yields to erosion rates in the region:

$$\dot{E}_{(x,y)} = \frac{SSY_{(x,y)} \times \delta}{\rho_{\ (x,y)}} \qquad \text{Equation A4.1}$$

We can test the temporal validity of our adopted sediment-yield model by comparing against long-term geological uplift rates (Adams 1980) and landslide event-driven denudation rates (Hovius et al. 1997). Suspended-sediment-yield observations reflect erosion and sediment-transport processes spanning years to decades, while ^{10}Be sediment-yield calculations most commonly sample the effect of erosional processes over hundreds of years (~275 years in the sample area [Roda-Boluda et al. 2023]), and, although these have been shown to be sensitive to episodic landslide events well-connected to the fluvial system in the years immediately prior to sampling, the impact has been shown to be complex (Kober et al. 2012; Wang et al. 2017; Wilkinson et al. 2022), and, in the case of the Conway River catchment that was affected by the Kaikōura earthquake in 2016, sampling two years after the earthquake demonstrated no deviation from background rates (Wilkinson et al. 2022).

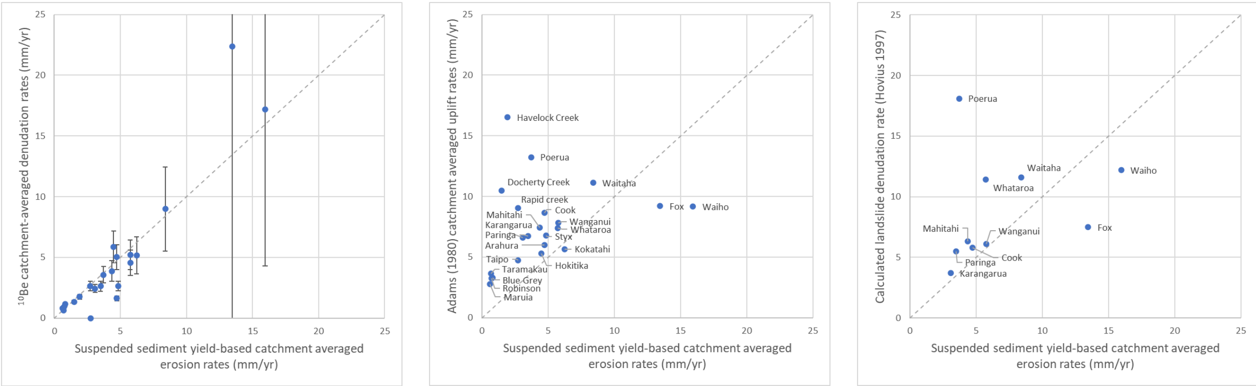

Figure A4.1 Compilation of various indicators of sediment production and erosion compared against mean rates estimated from suspended sediment yield (Hicks et al. 2011), the 1.5× suspended to total sediment-yield correction factor determined in this study and bedrock densities (Tenzer et al. 2011) using the method presented here. (a) ^{10}Be catchment-averaged erosion rates derived for major West Coast drainage basins (Roda-Boluda et al. 2023). (b) Catchment-averaged contemporary bedrock-uplift rates (Adams 1980), which can be considered to be equivalent to erosion rates in steady-state landscapes. (c) Landslide denudation rates derived from mapped landslides (Hovius et al. 1997).

When a landscape is in a steady state, we can expect observed erosion rates to balance long-term bedrock-uplift rates. Adams (1980) developed a map of uplift across the Southern Alps based on a range of geological indicators (e.g. uplifted marine and river terraces) integrating uplift rates over thousands to tens of thousands of years. Aside from strongly glaciated Fox and Waiho river catchments, and the relatively small Poerua and Havelock Creek catchments, a comparison between the erosion rates adopted here and catchment-averaged uplift rates derived from geological indicators demonstrates general agreement between the two datasets, with an apparent systematic over-estimation of 2.5 mm/yr in the data derived from geological sources (Figure A4.1b). This over-estimation may be expected, as the geologically derived observations are biased toward areas in which uplift is occurring (in order to preserve uplifted landforms), and little data can be derived from areas of little or negative uplift regions. Overall, this suggests that the landscape is likely in a steady state, and our adopted erosion rates are consistent with long-term geological uplift rates, although significantly higher in the Fox and Waiho catchments. The discrepancy in these two catchments may reflect a short-term increase in landslide-sediment production or re-working of moraine deposits as a result of glacial retreat.

Directly calculating the proportion of long-term erosion effected by landslide processes from event-based catalogues is complicated due to the lack of temporal and spatial completeness of associated datasets, as well as (in most cases) a lack of direct volumetric measurements. However, Hovius et al. (1997) was able to estimate catchment-wide landslide denudation rates for a portion of the region from a catalogue of 7691 mapped landslides derived from aerial imagery spanning 40 years. The calculated denudation rates are compared against the erosion rates adopted in this study in Figure A4.1c, again indicating a good correlation between suspended-sediment-yield-based erosion rates adopted in this study and event-driven denudation by landslides when averaged across drainage basins. Although the rates calculated for the Fox and Waiho catchments are again higher than those estimated from aerial photo interpretation, the landslide catalogue employed by Hovius et al. (1997) relied on observing disturbances in vegetation and therefore includes almost no landslides on unvegetated slopes. The relatively high proportion of unvegetated or snow-covered slopes in these catchments likely therefore led to an under-estimation of the total landslide-driven erosion in these catchments. While re-mobilisation of moraine material has likely contributed to higher apparent sediment-yield rates in these catchments, the potential for a greater landslide contribution cannot therefore be ruled out. Overall, the good correlation between sediment yield, geological-uplift indicators, ^{10}B and landslide-catalogue-derived denudation rates supports the conclusion of Hovius et al. (1997) that the majority of erosion in the mapped catchments was the result of bedrock landsliding. We are therefore also confident that the erosion rates derived from sediment-yield data adequately capture landslide-sediment production for this regional landslide-debris-inundation assessment.

Uncertainties associated with the determination of erosion rates from these datasets are discussed in Section A4.8.

A4.1.2 Comparison between Adopted Denudation Rates and Global Erosion Datasets

In addition to comparing erosion rates adopted in this study to local datasets, we can gain further insight into potential uncertainties by comparing the basin-averaged erosion rates to observations compiled in global datasets. Long-term landslide-sediment-production rates in mountainous landscapes are a function of increasing local relief through tectonic uplift and fluvial incision, as well as reducing material strength through weathering and fracturing processes. Together, these competing processes lead to the development of 'threshold hillslopes', in which the mean topographic gradient in a drainage basin reflects the balance between constructive and destructive hill-slope processes (Montgomery and Brandon 2002).

Although the processes involved are complex, and both temporally and spatially variable, global compilations of long-term erosion rates derived from ^{10}Be concentrations in river-borne sediments indicate a positive relationship between the mean slope of the contributing river basin and spatially averaged erosion rates, which tend to range from 0.001 to 10 mm/yr (Figure A4.2) (Montgomery and Brandon 2002; Mishra et al. 2019). Although spatial and temporal variability within a basin can be expected to cause local variations of several orders of magnitude, Mishra et al. (2019) recently determined that the majority of spatially averaged erosion-rate observations for a given mean basin slope lie within an order of magnitude of the mean. Where the erosion rate for a given basin sits with respect to the mean depends on a range of physiographic factors, including precipitation (Mishra et al. 2019) and, to a lesser degree, vegetation cover (Larsen et al. 2023). These observations appear to hold for river basins in the region overseen by West Coast Emergency Management (WCEM), and a comparison of erosion rates derived from both suspended-sediment-yield and ^{10}Be observations with mean basin slopes indicate that catchments in the study region consistently plot ~1.5 orders of magnitude above the global mean for the associated basin slopes (Figure A4.2) – as may be expected, given the exceptionally high annual precipitation in this region (c.f. Mishra et al. 2019). The erosion rates adopted in this study are therefore consistent with global datasets and are unlikely to vary by more than an order of magnitude.

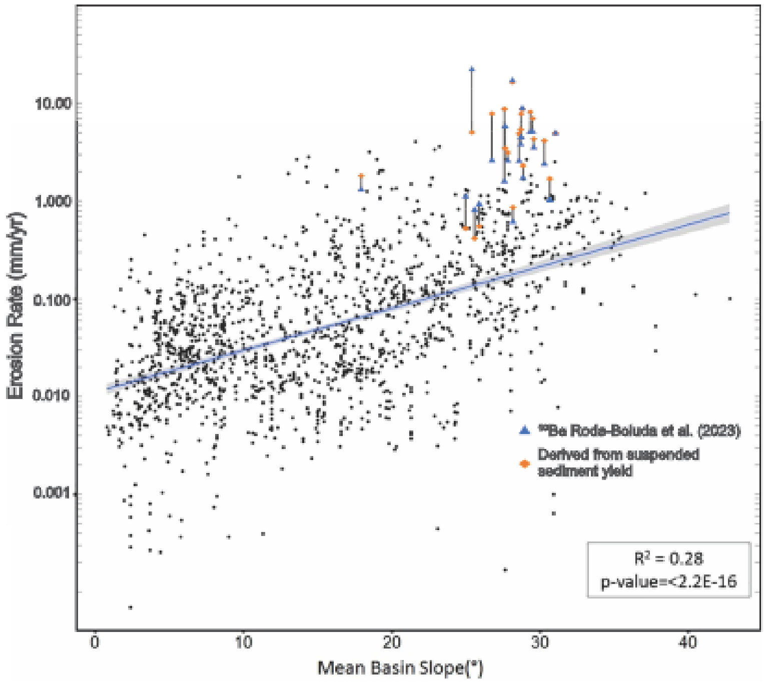

Figure A4.2 A global compilation of ^{10}Be-derived long-term erosion rates compared against the mean gradient in the contributing drainage basin. The ^{10}Be erosion rates and mean basin slope for catchments studied in Roda-Boluda et al. (2023) are indicated by blue triangles; orange diamonds represent estimated erosion rates derived from suspended-sediment yields. Modified after Mishra et al. (2019).

A4.1.3 Estimation of Landslide Sediment-Production Rates

A range of processes are responsible for erosion in steep and/or hilly terrain. These include fluvial and glacial erosion, soil creep, rain-splash erosion and overland flow, animal activity and landsliding. Landslides facilitate erosion by transporting bedrock uplifted through tectonic processes and/or sediments deposited as a result of a range of geomorphic processes down-slope to areas where material is either deposited or subsequently transported by fluvial processes. The long-term average rate of sediment produced by landsliding at a given location [$\dot{E}_{L(x,y)}$] can then be described as a function of the erosion rate at that location and the proportion of that eroded sediment generated through landsliding (ω_L). In the absence of good regional data for non-landslide erosion, we elect to ignore non-landslide erosion processes and treat all primary erosion as being a result of landsliding. This is the most conservative approach and likely leads to an over-estimation of landslide debris-production rates, especially in glacierised catchments. We adopt a bulking factor (η_L) to convert volumes of material produced through rock uplift (approximately 2650 kg/m^3) into lower-density landslide debris (approximately 2000 kg/m^3).

$$\dot{E}_{L(x,y)} = \dot{E}_{(x,y)} \times \omega_L \times \eta_L \quad \text{Equation A4.2}$$

A4.2 Kinematic Landslide Source Model

Identification of potential landslide-source areas was based on an analysis of landscape morphology, with the intention of determining the greatest kinematically feasible landslide-volume classes within the digital elevation model (DEM).

Our kinematic landslide source model allows us to estimate the largest hypothetical landslide that can occur at a given location based on an assumption of basic material-strength parameters (friction and cohesion) and an assessment of required geometric freedom through an analysis of local topography. The purpose of this step is not to evaluate slope stability but rather to define geometric constraints for the largest potential landslide sources. Therefore, we do not explicitly calculate the balance of driving and resisting forces for each hypothetical source.

We then assume that smaller landslides are able to occur anywhere that larger ones can occur. This is a notable simplification, as present-day local topography may have insufficient relief to support the generation of smaller landslides at some locations within a larger landslide body. However, given that (1) larger landslides can only occur on slopes with average gradients in excess of an assumed critical-failure angle (and mean slope angles must therefore equal or exceed this angle) and (2) failure of these slopes may occur progressively (such that future topography may support smaller failures where it is not currently possible), we suggest that this simplification is reasonable for a regional analysis.

We identified regions capable of generating landslides by calculating the ‘excess topography’ (Blöthe et al. 2015) above an assumed critical-failure plane, providing a measure of the thickness of bedrock or sediment overlying the assumed failure plane for every pixel in the DEM (see Figure A4.3; excess topography). This analysis was undertaken by filtering the topography using a moving window twice the diameter of the assumed largest volume class (see Equation A4.6) and a fixed angle (θ_{XST}) representing the assumed threshold basal angle for slope failure (i.e. critical-failure plane). We note that this is a necessary simplification for the current regional analysis, and our results do not preclude the potential for landslide-debris generation from lower basal-failure angles in specific settings. The intersection of resulting excess-topography surfaces defines the boundaries of maximum possible-failure units. We identify the boundaries by selecting all pixels in the resulting DEM with no contributing catchment area, excluding any isolated groups of zero-catchment-area pixels with total connected lengths less than the largest volume-class diameter, as these tend to sub-divide the failure units and limit potential failure volumes.

While the excess-topography criteria defines potential basal-failure planes, landslide area-volume relationships are used to limit the volume of landslides close to the margins of maximum possible-failure units (see Figure A4.3; landslide area-volume scaling). Similar relationships have been used to relate the planform area of mapped landslides to calculated volumes of up to 10,000,000 m^3, although the relationship is best constrained for landslides less than 100,000 m^3 (Guzzetti et al. 2009; Larsen et al. 2010; Massey et al. 2020b). This relationship is commonly described using a power-law equation of the form:

$$V = \alpha A^{\gamma} \qquad \text{Equation A4.3}$$

where V is the total landslide volume, A is planimetric area and α and γ are scaling parameters representing the mean fit for landslides in a given dataset. Comparisons of global landslide datasets indicate that scaling parameters are consistent across a wide range of landslide sizes, locations and triggers. Observations generally indicate that α < 1, and varies on a logarithmic scale, while $\gamma \approx$ 1.4, although this can range between 1 < γ < 1.5 (Guzzetti et al. 2009; Larsen et al. 2010; Massey et al. 2020b). Klar et al. (2011) demonstrated a probable mechanical control underpinning this relationship and developed analytical solutions to relate the scaling parameters to mechanical properties of 2D and 3D landslide geometries for which the analytical solution for the limit-equilibrium equation indicates that (for $\gamma = 1.36$) α can be related to the mechanical properties of the landslide source by the following equation:

$$\alpha = k\left(\frac{c}{\rho_{L\,(x,y)}}\right)^{d} \qquad \text{Equation A4.4}$$

where k is a dimensionless constant, d and γ are derived from empirical datasets, c is the average cohesive strength of the failure surface and $\rho_{L\,(x,y)}$ is the bulk density of the landslide material. We adopt parameters consistent with the more generic 2D model, assuming that the landslide depth is proportional to the length of its source and that k = 0.45, $d = 0.28$ and $\gamma = 1.36$ (Klar et al. 2011).

We select a representative cohesive strength of 50 kPa, which is near the upper limit of back-calculated values reported in Alberti et al. (2022) but remains significantly lower than the cohesive strength typical of fractured greywacke rock masses (400–1000 kPa, as described by Read et al. [1999]). As cohesive strength is used to determine scaling characteristics for all landslide volume classes – covering both soils and weathered or fractured rock – a low to intermediate value is considered appropriate for this regional-scale study. As discussed here, cohesive strength is highly dependent on the type of materials present and their physical condition (compaction, weathering, fracture density, etc.). These properties tend to vary with depth from the surface, and landslide area-volume relationships should therefore theoretically also vary with increasing depth from the surface. Although we currently have no data to better constrain this relationship in the study area, explicitly accounting for spatially variable, depth-dependent cohesion values could reduce uncertainties in the landslide-debris flux and annual property loss risk (APLR) datasets. Further discussion regarding selection of the cohesive strength and associated uncertainties can be found in Section A7.3.

The landslide area-volume scaling relationship described in Equation A4.5 was applied to a grid describing the horizontal distance to the nearest failure-unit cell boundary [$r_{(x,y)}$], where, assuming a representative cylindrical volume, the maximum landslide depth at each pixel [$D_{(x,y)}$] was calculated by:

$$D_{(x,y)} = \frac{V_{(x,y)}}{A_{(x,y)}} = \frac{\alpha\,(\pi\, r_{(x,y)}{}^{2})^{\gamma}}{\pi\, r_{(x,y)}{}^{2}} \qquad \text{Equation A4.5}$$

Landslide ‘scarps’ that form the lateral and upper margins of evacuated landslide-source areas are commonly planar features, defined by the mechanics of failure or pre-existing discontinuities in the rock mass. As such, pre-failure surface topography has little impact on the form of scarps formed adjacent to landslide margins. In order to remove the effect of topography on the geometry of scarps, which we derive from area-volume scaling relationships, we first applied a linear interpolation to generate an envelope between the failure-unit boundaries (i.e. the margins of hypothetical largest possible landslides). We generate planar failure surfaces consistent with the failure-unit margins by subtracting the residual between this plane and the DEM topography (to generate a planar surface within the margin of the failure), then subtracting depths calculated from the area-volume scaling relationship. Although this step will cause an over- or under-estimation of volumes derived from the scaling relationship (as actual topography can lie both above and below the planar surface), the relationship is not meant to provide an accurate representation of landslide geometry, and, as such, it must be treated as a guideline rather than a hard and fast rule. Our approach ensures that we define maximum landslide volumes that are kinematically feasible, while also maintaining approximate area-volume scaling relationships derived from regional landslide observations.

Shallow failures originating from soil or weathered bedrock may initiate on hill slopes with gradients less than that assumed for the kinematic model. In order to capture these features, we assigned a depth of failure equivalent to a Class 1 landslide to all cells not already classified with a surface gradient of more than θ_{NAT} (see Figure A4.3).

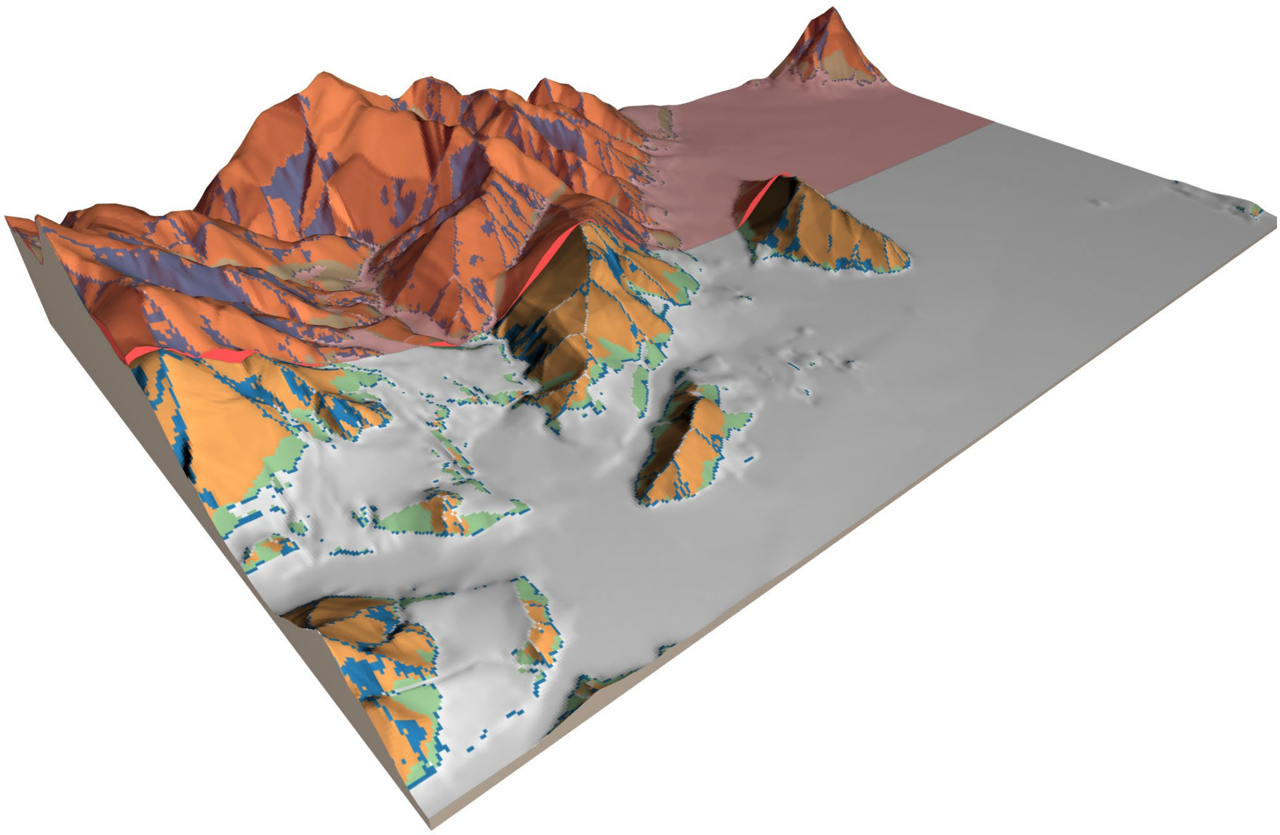

Figure A4.3 Example of the maximum depth surface derived from the kinematic landslide source model (foreground). Surface topography is superimposed in the red-shaded region for comparison (background). Green denotes the threshold slope angle for excess topography (θ_{XST}), orange denotes the landslide area-volume scaling [$D_{(x,y)}$] and blue denotes steep slopes otherwise not captured (θ_{NAT}).

A4.3 Characteristic Landslide-Volume Distributions

The contribution of landsliding to long-term erosion rates varies as a function of the volume of sediment mobilised in the landslide-source area, as well as the total frequency of landslide events. The relative erosional contribution by each landslide-volume class requires additional insight from local landslide inventories. In particular, statistics describing the landslide volume-frequency relationship are required to distribute sediment associated with a given trigger across each of the various landslide-size classes.

Landslide volume-frequency relationships have been shown to demonstrate self-similarity across a range of spatial scales and geographic settings, likely reflecting physical controls associated with slope geometry and soil or rock strength (Brunetti et al. 2009). While some studies have employed empirical area-volume scaling relationships to estimate the total volume of sediment produced from individual triggering events (e.g. Marc et al. 2016), very few employ true volume measurements required to accurately describe the frequency distribution of source volumes. Brunetti et al. (2009) compiled a global database of landslides with known source volumes (Figure A4.4) and found the probability density of landslide volumes to be approximately log-normally distributed about a geometric-mean source volume. This is consistent with recent findings from a number of authors (Medwedeff et al. 2020; Moreno et al. 2023). Although the geometric-mean volume and associated standard deviation varied from location to location, most datasets were centred between 10 and 10,000 m^3, with ranges varying from ±1 to 2 orders of magnitude. In this section, we compare these distributions to those derived from landslide sources in the WCEM study region.

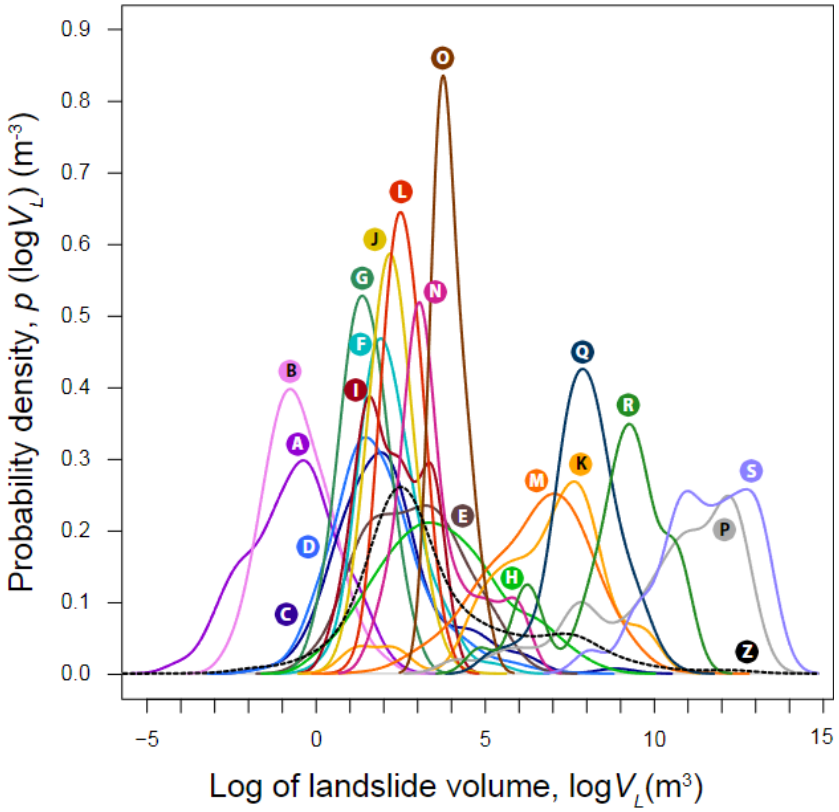

Figure A4.4 Probability-density distributions derived from the log of calculated landslide volumes from a compilation of 19 mapped landslide catalogues from around the globe, as well as planetary observations (Brunetti et al. 2009).

There are few rainfall-induced landslide-source areas accurately mapped in the study region and no accurately mapped earthquake-induced landslide sources. In order to evaluate the landslide area-volume frequency distribution for rainfall- and earthquake-induced landsliding in the region, we therefore compiled all mapped landslide polygon datasets available for the region overseen by WCEM for which the coverage can be reasonably assumed to be complete for given triggering events. Rainfall-induced landslides have been derived from studies incorporating undifferentiated triggering events, with the assumption that a majority are generated by rainfall (Hovius et al. 1997; Hilton et al. 2011; Leith, unpublished; Emberson et al. 2016; Wride and de Vilder 2021), while earthquake-induced landslides are derived from the M_W 7.1 1968 Inangahua and M_W 7.3 1929 Murchison earthquakes (Hancox et al. 2014, 2016).

Where landslides were not mapped with separate source and runout polygons, we used an in-house machine-learning model to categorise landslides, distinguishing between different types of movement based on the shape and topographic characteristics of landslide features and comparing these with the categories represented in IFFI (the Italian Landslide Inventory[5]). Relatively wide landslide polygons with little vertical extent, for example, are more likely representative of (less mobile) rotational landslides, whereas long, narrow polygons with a large vertical extent are more likely to reflect more mobile debris flows. A summary of polygons used to generate source areas is presented in Table A4.1.

Table A4.1 Summary of polygons used for volume estimation and model validation. Polygons were mapped as landslide outlines (including source and runout). We used an in-house machine-learning model to categorise polygons into landslide types based on geometric characteristics of the DEM within the polygons. A transfer-learning model was then used to designate the upper proportion of the polygon as the landslide 'source'. While all landslides were used to determine earthquake- and rainfall-induced volume distributions, only landslides likely to be associated with 'flow' or 'avalanche' movement types were included in the runout model validation (see Section A5.4.4 for details).

	Number of Landslide Polygons	Proportion of Elevation Range Classified as 'Source' (%)	Landslide Category
Included in Model Validation	26	30	Complex rock slide
	1043	34	Rock slide – medium
	146	38	Rock slide – large (rock avalanche)
	414	40	Debris flow
	8746	55	Rock slide – small
Not Included in Model Validation	382	58	Slow earth flow
	23	70	Soil slide – small
	1316	71	Rotational/translational slide
	16	74	Complex landslide
	342	75	Slow earth flow
	403	78	Rotational/translational slide
	90	81	Rotational/translational slide

We used the same machine-learning model to categorise landslide outlines mapped following the 2016 Kaikōura earthquake (Massey et al. 2020a), for which the proportional fall height separating source from runout and deposit is known. This allowed us to determine representative source areas for each landslide category based on the proportional elevation ranges occupied by source areas in the Kaikōura earthquake dataset. Finally, we used the same machine-learning model to classify mapped landslide outlines in the region overseen by WCEM and divide these into source and runout categories based on the elevation ranges derived for the Kaikōura dataset. The probable volume of each landslide source was then calculated from the 25 m DEM using the kinematic-source model described in Section A4.2, with landslide region boundaries defined by the calculated source-area extent. This allowed us to determine source volumes for all mapped earthquake- and rainfall-induced landslides in the study region, as well as build statistical models based on calculated volume distributions (Figure A4.5).

5 https://www.progettoiffi.isprambiente.it/?lang=en

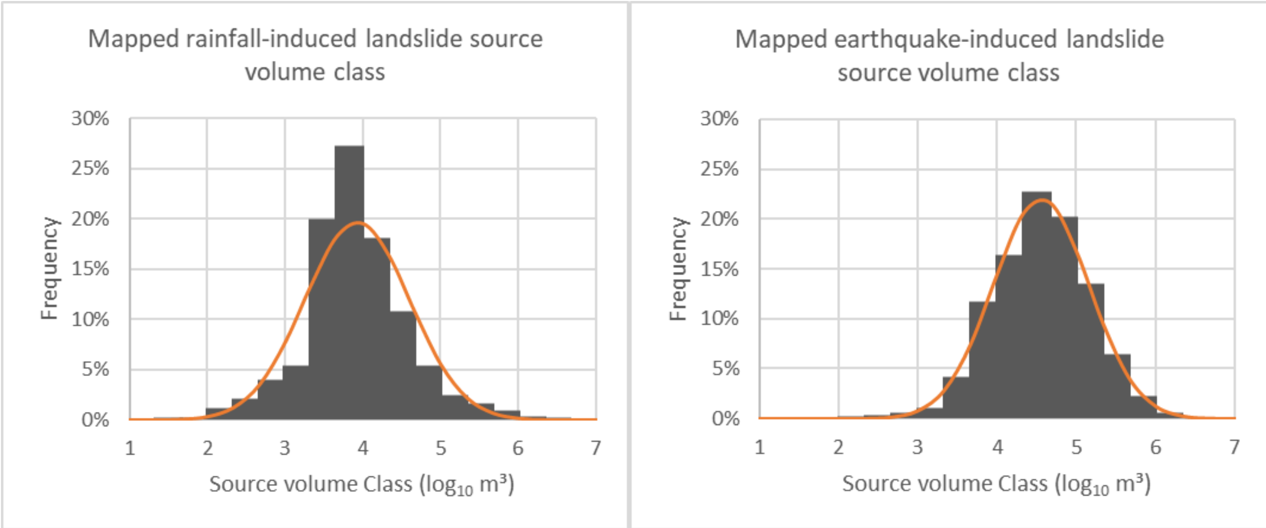

Figure A4.5 Landslide frequency-volume plots for all landslide sources in the rainfall- and earthquake-induced landslide datasets employed in this study (Table A1.2).

In line with the findings of Brunetti et al. (2009), landslide source frequency-volume plots for the West Coast region demonstrate approximate log-normal distribution (Figure A4.5). Overall, we observe a greater mean volume for earthquake-induced landslides, although the ranges for both datasets are similar. This is consistent with observations from international datasets (see Brunetti et al. [2009] and references therein) and likely represents a difference in the trigger process rather than the local impact of topographic or bedrock strength properties (Brunetti et al. 2009). Table A4.2 provides a summary of the observations employed in the dataset, as well as the calculated geometric mean and 1-sigma distribution of the source-volume statistics for earthquake- and rainfall-induced landslide-source volumes in the region.

Table A4.2 Summary landslide frequency-volume statistics for rainfall- and earthquake-induced landslides in the study region.

Trigger	**Observations per Volume Class**								**Volume Distribution (log_{10} m^3)**
	1	**2**	**3**	**4**	**5**	**6**	**7**	**>7**	
Earthquake	0	4.55 ± 0.60	68	1073	3769	1403	39	0	4.55 ± 0.60
Rainfall	4	3.92 ± 0.68	522	3821	2485	358	43	2	3.92 ± 0.68

The geometric mean and standard deviation of landslide-volume distributions for both earthquake- and rainfall-induced landslides are employed to determine the proportion of landslide-debris production assigned to each landslide class range. These are explicitly incorporated in Equations A4.10 and A4.11 in Section A4.5.

A4.4 Landslide-Volume Classes

The LSP and LSD models require potential landslide source volumes to be divided into discrete volume-class ranges. We employ a similar approach to previous studies (de Vilder et al. 2021) and adopt a common logarithm with which to sub-divide the classes. Selecting the full range of volume classes and the range defining each interval requires some trial and error, as significant trade-offs exist between computational performance and accuracy of results. In general, selecting fewer classes with larger volume-range intervals leads to a linear decrease in computation time, as each model can be run in parallel. However, larger intervals tend to lead to an over-estimation of the total material available to slide, as discretising the intervals generates an inherent over-estimation of the material available with respect to the output of the landslide sediment-production model. Although this is primarily controlled by the effects of topographic relief and class boundaries, we find that selecting volume classes spanning order-of-magnitude ranges (i.e. integer limits) tends to lead to an over-estimation of the total volume of debris available by approximately 20%. This effect typically reduces to less than 1% difference between total annual debris production when volume ranges are reduced to 33% of an order of magnitude.

We opt to separate source volumes into order-of-magnitude (i.e. full decadal) ranges between 10 m^3 and 100,000,000 m^3, favouring a three-fold decrease in simulation time, with more conservative estimates of material flux and debris extent as a result. LSD model runs for a 150 km^2 section in the vicinity of Kokiraki indicate that the full order-of-magnitude volume-class ranges lead to a 20% higher mean flux but just 1% greater inundation area with respect to identical models run on 33% order-of-magnitude ranges (see Figure A4.6). We note that, as described in the following section, larger volume landslides are only simulated in the LSD model where the kinematic-source model allows.

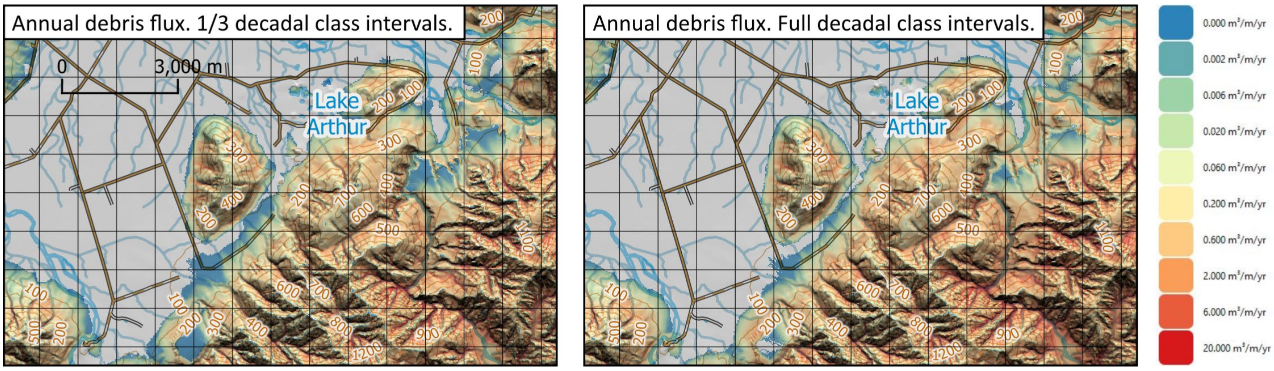

Figure A4.6 Comparison of combined annual landslide-debris-flux outputs from preliminary landslide sediment-distribution model runs incorporating 33% and full decadal class intervals. These outputs are illustrative only and may not reflect landslide-debris-inundation hazards at the indicated location.

A4.5 Mean Annual Landslide-Debris-Production Rates

In order to calculate the mean annual landslide-sediment-production rate for each landslide volume-class range, we employ the characteristic landslide frequency-volume relationships presented in the previous section to distribute calculated annual landslide sediment production across the range of volumes that can be released from each grid cell. This requires that we first convert landslide volumes to representative areas by employing the inverse of the area-volume scaling relationship described in Equation A4.3, i.e.

$$A_{L(c)} = \sqrt[\gamma]{\frac{V_L}{\alpha}} \qquad \text{Equation A4.6}$$

where V_L is landslide volume, A_L is the corresponding area and α and γ are scaling parameters. Calculating the mean depth [$\bar{D}_{L(c)}$] corresponding to each volume-class boundary is then trivial:

$$\bar{D}_{L(c)} = \frac{V_{L(cg)}}{A_{L(cg)}} \qquad \text{Equation A4.7}$$

Comparing the maximum possible landslide depths from the kinematic model with the mean depths for each landslide-class boundary then allows us to identify the possibility for landslides within each class to occur at each pixel location [$K_{L(c)(x,y)}$]. We assume that landslides of a given class range can occur if the mean depth of the upper bounding volume is less than that derived from the kinematic model for each region (see Figure A4.7).

$$K_{L(c)(x,y)} = D_{(x,y)} > \bar{D}_{L(c)} \qquad \text{Equation A4.8}$$

Similarly, the maximum kinematically feasible landslide volume at a given location [$V_{L(max)(x,y)}$, m] can be denoted by:

$$V_{L(max)(x,y)} = max\left(V_{L(c)} \times K_{L(c)(x,y)}\right) \quad \text{Equation A4.9}$$

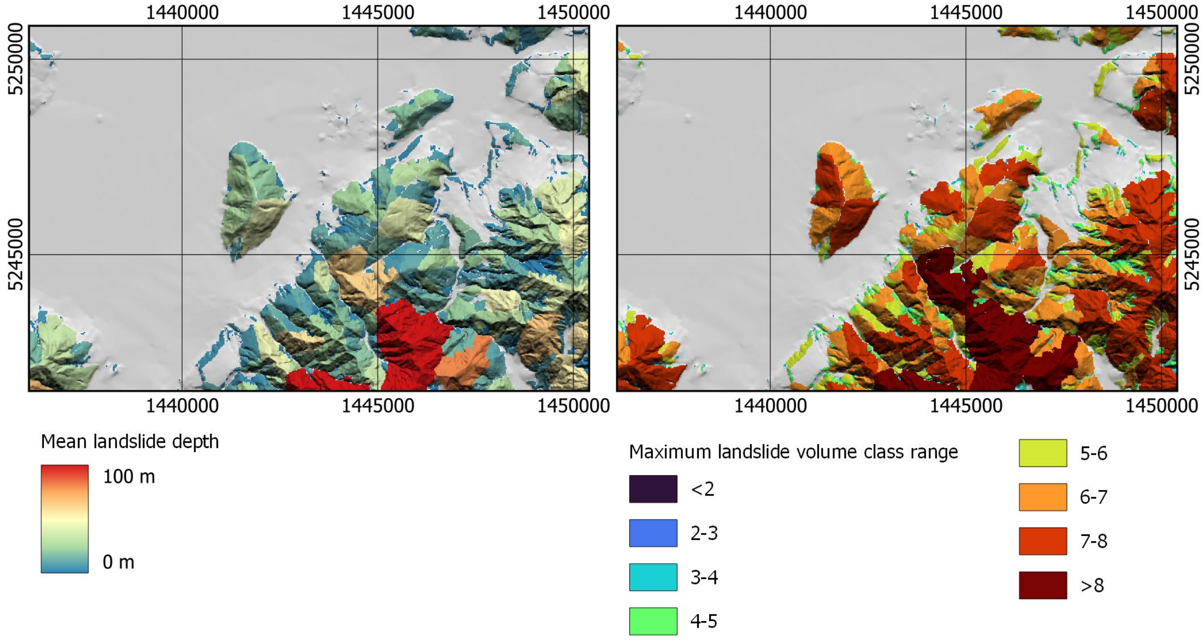

Figure A4.7 Calculated maximum landslide depths based on kinematic models (left) and maximum volume-class ranges based on the mean depth within each kinematically feasible region (right).

Calculating the likelihood of valid volume classes occurring at each location in the landscape then requires the incorporation of characteristic landslide frequency-volume distributions. We opt to describe the likelihood of a landslide of a given volume occurring [$N_{(x,y)(T)}$, 1] using the probability density function (PDF) of the log-normal distribution. This is described in Equation A4.10, below:

$$N_{(x,y)(T)} = \frac{1}{2}\left[1 + erf\left(\frac{V_{L(max)(x,y)} - V_{\mu(T)}}{V_{\sigma(T)}\sqrt{2}}\right)\right] \quad \text{Equation A4.10}$$

Here, $V_{L(max)(x,y)}$ is the maximum kinematically feasible landslide volume at a given location; $V_{\mu(T)}$ is the mean of the landslide volume PDF for a given trigger; $V_{\sigma(T)}$ is the standard deviation of the PDF (derived from observational data; see Section A4.3); and erf denotes the error function, which is a standard mathematical function used in probability and statistics.

We account for increased proportionality of lower-volume landslides at locations in which the kinematic model suggests that larger landslides are infeasible by normalising the PDF by the cumulative distribution function up to the upper depth limit (assuming that lower volumes can occur at any feasible location). The probability of a landslide of a given volume class and trigger occurring at each location [$N_{L(c)(T)(x,y)}$, 1/log$_{10}$(m^3)] is then given by a conditional formula in which proportions are either equal to the volume-range-normalised PDF (when the depth class is kinematically feasible) or set to zero:

$$N_{L(c)(T)(x,y)} = \begin{cases} \dfrac{\frac{1}{\sqrt{2\pi V_{\sigma(T)}{}^2}} e^{-\frac{(V_{L(cg)} - V_{\mu(T)})^2}{2\, V_{\sigma(T)}{}^2}}}{N_{(x,y)(T)}} & if\ 0 \leq \bar{D}_{L(c)} \leq D_{(x,y)} \\ 0 & \end{cases} \quad \text{Equation A4.11}$$

where $V_{L(cg)}$ is the geometric mean of the volume class interval.

In order to determine the proportion of erosion generated by each valid volume-class range [$D_{L(c)(T)(x,y)}$, m³/m²], we calculate the probability of landsliding by integrating the likelihood of occurrence with respect to the breadth of the class range [$\omega_{(c)} = log_{10}(V_{L(c)} - V_{L(c-1)})$, $log_{10}(m^3)$] and multiply by the mean erosional depth of the interval ([$\overline{D}_{L(cg)}$, m], calculated by substituting $V_{L(cg)}$ into Equations A4.7 and A4.8).

$$D_{L(c)(T)(x,y)} = N_{L(c)(T)(x,y)} \times \omega_{(c)} \times \overline{D}_{L(cg)} \quad \text{Equation A4.12}$$

where *c* again denotes the upper limit of the volume-class range, and *cg* represents the geometric mean of the volume-class range.

The normalised proportion of erosion by each volume-class range and trigger [$V_{L(c)(T)(x,y)}$,1] can then be determined by dividing the proportion of erosion generated by each volume-class range by the sum of erosion for all feasible volume-class ranges.

$$V_{L(c)(T)(x,y)} = \frac{D_{L(c)(T)(x,y)}}{\sum_{c_{min}}^{c_{max}} D_{L(c)(T)(x,y)}} \quad \text{Equation A4.13}$$

The mean annual landslide-sediment-production rate for each volume class range, trigger and return interval at each location within the landscape [$\dot{E}_{L(c)(T,RI)(x,y)}$, m/yr] is then calculated by multiplying the mean annual landslide-sediment-production rate (Equation A4.2) by the proportional contribution from each volume class and trigger (Equation A4.13), as well as the mean probability of failure over the temporal integration interval (Equation A4.12), Finally, this needs to be normalised by the total probability of failure (Equation A4.10). This is described in Equation A4.14:

$$\dot{E}_{L(c)(T,RI)(x,y)} = \dot{E}_{L(x,y)} \times \frac{N_{(x,y)(T_{RI-1},T_{RI})} \times V_{L(c)(T)(x,y)}}{N_{(x,y)}} \quad \text{Equation A4.14}$$

This process ensures that the calculated sediment-production rates are accurately scaled and reflect the contributions from different landslide classes, triggers and probabilities of occurrence. The sum of calculated erosion rates for all landslide-size classes, triggers and return intervals, i.e. $\sum \dot{E}_{L(c)(T,RI)(x,y)}$, will then equal the estimated landslide-induced erosion rate, i.e. $\dot{E}_{L(x,y)}$, everywhere that landsliding is feasible based on kinematic constraints. Figure A4.8 presents calculated mean annual landslide-debris-production rates for present-day and future RCP 6 2081–2100 climate-change scenarios. The rates presented in Figure A4.8 differ from long-term sediment-production rates presented in Figure 2.3, as landslide-debris-production rates include the effect of the landslide sediment bulking factor (η_L; see Equation A4.2).

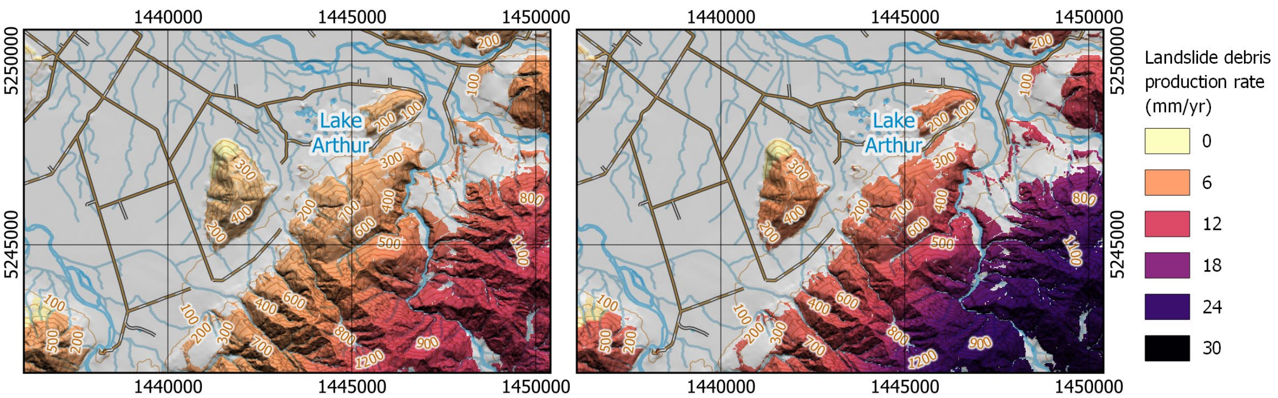

Figure A4.8 Left: Calculated mean annual landslide-debris-production rates for the present-day. Right: A future RCP6 2081–2100 climate-change scenario.

By assessing the range of feasible landslide-size classes in the DEM, it is possible to evaluate the probable erosion by each volume-class range, return interval and trigger. Figure A4.9 presents an example of the mean annual landslide-sediment-production rates calculated for a single pixel in the DEM. Each of the 112 nodes in the plot represents the input sediment contribution for an individual Gravitational Path Process (GPP) model run.

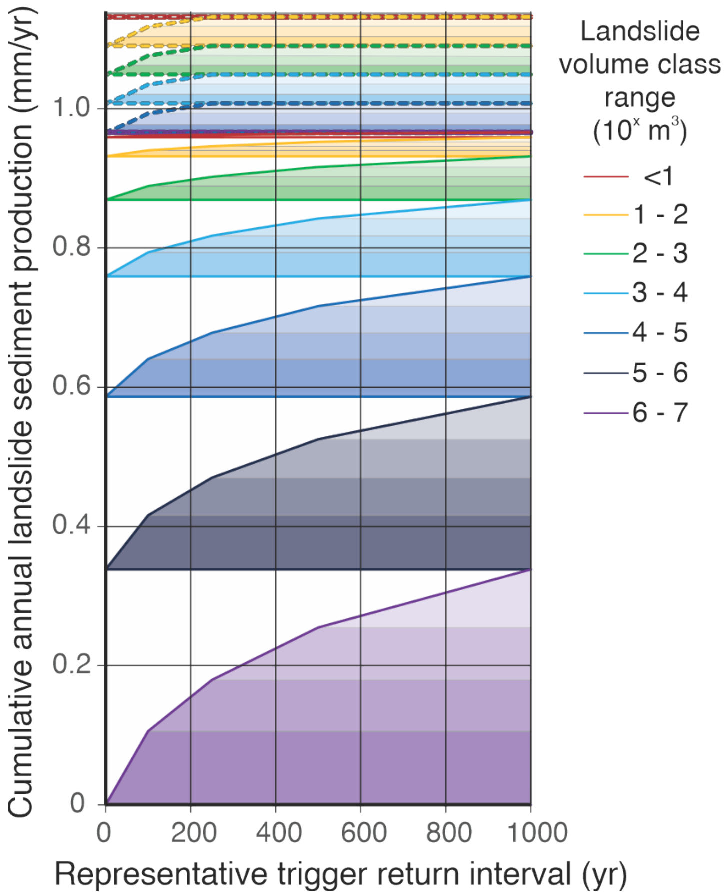

Figure A4.9 Landslide sediment-production (LSP) model output describing cumulative annual sediment production for a given grid cell, separated by landslide volume class (dashed lines = rainfall-induced landslide, solid lines = earthquake-induced landslide). In this case, the calculated landslide erosion rate is 1.1 mm/yr, of which LSP model results predict that approximately 90% is a result of earthquake-induced landsliding (solid lines). The majority of long-term erosion at this location is facilitated by large (Class 6–7) earthquake-induced landslides (violet solid lines) with relatively short (100-year) return intervals (denoted by the darkest violet bar). These large, somewhat frequent, events account for an average sediment production rate of 1 mm/yr at this hypothetical location.

A4.6 Scenario-Specific Landslide-Sediment Production

The probable sediment production for specific landslide-inducing scenarios (e.g. 50-, 100- and 250-year ARI rainfall scenarios and an Alpine Fault magnitude 8 [AF8] scenario) is determined by comparing the event-specific probability of failure to the mean annual probability of failure at a given location. The sediment produced in each scenario [$E_{L_S(x,y)}$] can be calculated by substituting the probability of failure and integration interval in Equation A4.14 with the calculated landslide susceptibility associated with the given scenario [$S_{S(x,y)}$]. As susceptibility is not annualised, this substitution has the effect of altering the resultant units from an annual sediment production (m/yr) to a scenario-specific contribution (m):

$$E_{L_S(x,y)} = \dot{E}_{L(x,y)} \times \frac{S_{S(x,y)}}{N_{(x,y)}} \qquad \text{Equation A4.15}$$

As with the calculation of mean annual sediment production, scenario-specific sediment production models do not allow for the determination of exact locations and volumes of landslide debris. Rather, these indicate the probability that sediment from landslides of given volumes will originate from each cell in the model. The calculated sediment flux, and associated deposition, must therefore be considered as probabilities, rather than predictions for the given scenario.

A4.7 Landslide Sediment-Production Adjustment for the RCP6 2081–2100 Climate-Change Scenario

Without regional data describing the manner in which rates of sediment production and sediment transport are likely to change in response to the diverse impacts of climate change, we adopt the change in the landslide-source-susceptibility (LSS) model rainfall-induced landslide probability from the present-day to RCP6 2081–2100 climate-change scenario as a proxy for increased erosion rates with respect to long-term averages. We assume that earthquake-induced landslide sediment-production rates under an RCP6 climate-change scenario will remain the same as the present-day. This allows us to calculate $P_{RCP6(x,y)}$, the mean annual probability of landsliding under the RCP6 scenario, by substituting appropriate susceptibility values into Equations A3.4–A3.6, such that:

$$P_{RCP6(x,y)} = P_{RIL\_RCP6(x,y)} + P_{EIL(x,y)} \qquad \text{Equation A4.16}$$

In order to maintain earthquake-induced landslide sediment-production rates in the face of increased rainfall-induced landslide susceptibility, we increase the landslide-sediment-production rate in concert with the increase in mean annual landslide probability [i.e. from $P_{(x,y)}$ in Equation A3.6 to $P_{RCP6(x,y)}$ in Equation A4.16] with the help of a weathering-rate multiplier (W):

$$W = 1 + \frac{P_{RCP6(x,y)} - P_{(x,y)}}{P_{(x,y)}} \qquad \text{Equation A4.17}$$

The increase in available sediment due to increased weathering ($\dot{E}_{L\_S\_RCP6(x,y)}$) can then be defined as a function of the long-term erosion rate and weathering-rate multiplier (W):

$$\dot{E}_{L\_S\_RCP6(x,y)} = \dot{E}_{L(x,y)} \times W \qquad \text{Equation A4.18}$$

A4.8 Key Landslide Sediment-Production Model Assumptions and Uncertainties

We note a number of uncertainties associated with the mean annual landslide-sediment-production rate calculation:

- We base our estimates of present-day landslide-sediment-production rates on a derivative of rates of specific sediment yield (SSY) presented in Hicks et al. (2011). They report a standard factorial error (SFE) of between 1.55 and 1.8 for the majority of studied catchments, noting that glaciated catchments on the West Coast may be associated with SFEs of ~2–3 (an SFE of 1.8 is equivalent to a geometric standard deviation of 1.8, meaning one 'sigma' on the log scale corresponds to multiplying or dividing by 1.8). The authors recommend against applying the models to predict sediment yields from catchments less than 10 km^2, raising the question of applicability at the local slope scale, as applied here. In this study, we do not expect SSY, and therefore calculated landslide debris-production rates, to accurately represent present-day activity on individual hill slopes across the approximately 25,000 km^2 of the region overseen by WCEM. However, evidence suggesting that the landscape is in a steady state (see Section A4.1.1) and that, on average, denudation rates derived from SSY estimates represent long-term, spatially integrated erosion rates provides confidence that this dataset is adequately capturing regional variability in landslide debris-production rates. That said, we note that uncertainties associated with SSY inputs generate some of the greatest uncertainties in APLR predictions (see Section 8.3), and therefore identify local refinement of the landslide sediment-production models with appropriate local input data as a high priority for local re-evaluation of hazard and risk (see Section 5.5).

- We assume that present-day rates of landslide-sediment production reflect long-term erosion rates. Although the contributing datasets are regionally consistent, these do not capture spatial and temporal changes in rates associated with destabilisation of slopes by retrogressive landsliding, river erosion, coastal retreat, glacial retreat, anthropogenic activities (e.g. excavation of road cuts, quarrying, mining or removal of retaining structures), vegetation change (deforestation), short-term climatic changes or other effects that may locally enhance or decrease the long-term rate of landslide-sediment production. Although regionally accurate, this may lead to local over- or under-estimation of landslide-debris-inundation hazard.
- We assume that our calculated long-term erosion-rate model reflects long-term erosion rates throughout the study region. Although independent data derived from catchments along the range front support this assumption, there is little data to constrain the accuracy of the model in other areas. This may lead to local over- or under-estimation of landslide-debris-inundation hazard in areas beyond the range front.
- We assume that all erosion is driven by landslide processes where landsliding is kinematically feasible. Adopting the long-term erosion rate as a landslide-sediment-production rate means that the LSP model provides an upper bound on regional landslide-sediment generation.

We note a number of uncertainties associated with the kinematic-model calculation:

- We assume that the threshold gradient used for the excess topography calculation is isotropic and spatially homogeneous. In reality, this is likely to vary with rock or soil strengths, as well as with underlying structural controls. Varying this gradient will alter the distribution of the maximum feasible landslide volumes. A steeper gradient will bias sediment production toward lower volume and more frequent landslide classes.
- We assume that the adopted cohesion is spatially consistent and invariant with landslide volume. In reality, this is likely to vary with rock or soil strengths. Varying the cohesion will alter the distribution of the maximum feasible landslide volumes. A lower cohesion will bias sediment production toward lower volume and more frequent landslide classes.
- We assume that the calculated distribution of maximum landslide volumes is representative of the maximum possible volume of landslides sourced from slopes throughout the study region. We do not explicitly model potential landslide-source areas. This may lead to local over- or under-estimation of landslide-debris-inundation hazard.
- We assume that the topography in the DEM is an accurate representation of the ground surface. The 8 m DEM is derived from the January 2012 Land Information New Zealand (LINZ) Topo50 20 m contours, which largely reflect topography digitised from 1940 aerial photographs. We have down-sampled this data to 25 m resolution for the purposes of this regional study. The DEM therefore likely under-represents the smaller landforms (less than approximately 100,000 m^2), and smaller landslide source areas may therefore not be identified (see Section A7.6.2 for further details on this topic).

We note a number of uncertainties associated with the calculation of landslide-volume distributions:

- We include no directly measured landslide volumes in this study and base our estimated geometric-mean volumes on a combination of mapped landslide areas and DEM analysis. Given the resolution of the source imagery and the base DEM, this is most likely to have resulted in an over- rather than under-estimation of landslide volumes and would result in an over-estimation of landslide hazard.
- We assume that landslide-volume distributions are consistent across the region. As landslide size is a function of a range of factors, including material strength, joint patterns, vegetation strength and geomorphological setting, it is likely that landslides in some areas are consistently larger than assumed, while landslides in other settings will be consistently smaller.

Given the above assumptions and uncertainties, we have elected to adopt 'best estimates' for all input variables while adopting conservative ranges for associated uncertainties. This ensures that LSP model results most closely reflect the input datasets and assumptions described in this report, while conveying the overall level of uncertainty associated with inputs to the LSP model (see Appendix 7). We recommend that West Coast Regional Council consider appropriate precautionary reductions in acceptable hazard or risk metrics based on an evaluation of appropriate confidence intervals and reported model uncertainty (as discussed in Section 5).

APPENDIX 5 Landslide Sediment-Distribution Model

This section describes details of the landslide sediment-distribution (LSD) model used to inform the landslide-debris-inundation risk assessment.

Regional landslide-debris-inundation potential was modelled using the Gravitational Path Process (GPP) model developed by Wichmann (2017). We employ the GPP model in two distinct configurations, employing different runout models to simulate avalanche- and flow-type landslide runouts. In both cases, we use the fully featured GPP model with both material deposition and sink filling enabled as described in Wichmann (2017). The selection of input parameters for each configuration is discussed later in this section.

Key LSD model assumptions and uncertainties are noted in Section A5.9, and a quantitative sensitivity analysis is undertaken in Section A7.4.

A5.1 Landslide-Source-Material Thickness

Landslide source material thicknesses were informed by the calculated probability of sediment production within the study region to assess the combined probability of debris inundation. To achieve this, we ran an ensemble of GPP models capturing the full range of triggers, return intervals, class sizes and runout mechanisms. The landslide source-material thickness and distribution for each model run (M_{GPP}) was determined by multiplying the erosion rate derived for the given input parameters by an integration interval (σ) to infill topography, prevent small depressions from trapping and/or redirecting debris and generate sufficient deposition to mimic single landslide events:

$$M_{GPP(c)(T,RI)(x,y)} = \dot{E}_{L(c)(T,RI)(x,y)} \times \sigma \qquad \text{Equation A5.1}$$

We adopt an integration interval of 10,000 years, reflecting the approximate interval since deglaciation of the region following the Last Glacial Maximum. This effectively ensures that the magnitude of debris deposited in each model run is similar to the scale of post-glacial sedimentary landforms in the region (such as debris-flow fans and incised river channels), enabling modelled runouts to overcome topographic obstacles where sufficient landslide debris is available. While increasing the integration interval is an effective means of reducing the effects of minor topographic features on local flow paths, it has little impact on the overall model output. An increase of two orders of magnitude (from 0.1 to 10 kyr), for example, decreased the mean annual debris flux in a sample region by <1% while increasing the proportional area affected by debris flux by 2.7% (see Section A5.6 for further details).

All volumetric outputs (deposition and material flux) were normalised by the integration interval on completion of each model run (see Equation A5.2).

A5.2 Probability of ‘Avalanche’ versus ‘Flow’ Movement Types

We assume that all landslide-debris transport is a function of either ‘avalanche’- or ‘flow’-type movements. Typically, initial open-slope avalanche-type movements develop into flow-type landslides, and the latter mode of movement can therefore be expected to be generally less common than the parent movement mode. However, few landslide datasets draw a distinction between movement modes for rapid landslides, making the proportional attribution of types of movement complicated. Recently, a catalogue of 140,000 landslides mapped following Cyclone Gabrielle, primarily in soft sedimentary rocks of the Hawke’s Bay region, indicated that 66% of mapped landslides were avalanche-type movements, while 33% were flow-type movements (Leith et al., in prep.). Given that (1) lithologies in the Hawke’s Bay region are better known for flow-type behaviours than generally stronger lithologies in the region overseen by West Coast Emergency Management (WCEM) and (2) lower-gradient topography in Hawke’s Bay favours flow-type movements, we consider it unlikely that flows in the region overseen by WCEM make up more than 33% of the total movement types. As flow-type movements are generally more mobile than avalanche movement types, we conservatively adopt the same relative probability of movement for rainfall-induced landslides observed in the Hawke's Bay region, allowing for a largest-probable proportion of more mobile flow-type movements. Anecdotal evidence suggests the proportion of flow-type movements for earthquake-induced landslides is less than that for rainfall-induced events, and we therefore reduce the relative probability of flows for earthquake-induced landslides by 50% (i.e. 83% 'avalanche' and 16% 'flow'). Uncertainties associated with this assumption are discussed in Section A5.9 and tested in Appendix 7.

A5.3 Landslide-Runout Simulation

A5.3.1 Landslide-Runout Modelling

The distance that landslide debris travels from its source is called the landslide travel (or runout) distance (e.g. McDougall 2017). The debris-inundation area is the ground area covered by debris as it moves, including the source, transport and deposition zones.

There are two main methods to estimate landslide-debris runout: simplified or continuum mechanics-based methods. Simplified methods include empirical, stochastic and physically based modelling approaches and typically use data describing the extent of landslide runout from existing catalogues to calibrate simple physical models based on readily available datasets, such as topographic and volumetric data, making these easier to apply for large-scale studies (e.g. Wichmann 2017). However, their accuracy depends on the quality and quantity of regional datasets, and the ability of these datasets to capture physical aspects of landslide runout is limited.

Continuum mechanics-based methods more directly consider physical factors such as landslide material, properties of the travel path and internal fragmentation processes, requiring detailed data and calibration from representative landslides (e.g. Hungr and McDougall 2009; Christen et al. 2012). The incorporation of key physical considerations in these models means that they can reproduce detailed aspects of landslide runout, more accurately reproducing complex runout paths. However, the increased complexity increases computational requirements, and model accuracy is often constrained by input-data-availability limitations. As a result, simplified methods are still commonly used in situations in preliminary studies or regional investigations.

A5.3.2 Gravitational Path Process Model

The GPP model (Wichmann 2017) employs empirical, stochastic and physics-based approaches in order to simulate the movement of mass down-slope through a DEM from an initiation point to a deposition cell using the single-flow-direction path-finding approach coupled with a random-walk algorithm. This means that source material is moved downslope through the DEM cell-by-cell using a random walk algorithm based on a multiple-flow-direction approach, taking into account particle energy, topography, and a set of user-defined parameters. The model includes components that allow DEM modification through sink filling and material deposition, allowing for example, landslide debris to progressively infill, then overflow basins; or the formation of landslide deposits that alter the path of subsequent failures. The model is open-source and has been successfully used for a number of regional landslide hazard studies (see Wichmann [2017] and references therein).

We employ a temporally integrated scenario-modelling approach to assess runout, accepting that, although we know the spatially distributed long-term average sediment-production rate for each landslide trigger, return interval and volume class, we do not know the specific location of landslides in any given event. Instead, we use M_{GPP} to generate a temporally integrated landslide intensity throughout the landscape and propagate sediment down-slope. A significant benefit of this approach is the ability to model the downslope transport of material from landslide sources nominally smaller than the resolution of the input grid. A single iteration of the GPP model effectively tracks a packet of sediment down-slope from each source cell. Each packet is supplied with a set of rules regarding movement, deposition and stop criteria, whose operation is independent of the volume of sediment being moved down-slope. As such, a large volume of sediment, representing multiple sub-pixel landslide sources, can be moved through the topography while obeying rules consistent with a smaller-sized landslide. Although the implementation of this method prevents the capture of specific landslide physics (primarily those associated with momentum and internal interactions, e.g. super elevation and block sliding), it allows us to capture probabilistic debris transport from small landslides across a wide region.

Landslides tend to smooth terrain, as they entrain and deposit soil and rock along the runout path. Although the GPP model includes a sediment-deposition component, this does not account for entrainment and deposition of debris where velocities are high along the landslide path. In order to account for this process and effectively smooth terrain along the runout path, we prepared the DEM by running a median filter with a moving window diameter determined by the cube root of the geometric-mean landslide volume (to conservatively approximate the landslide-footprint area). This reduced the magnitude of topographic irregularities, allowing for increased dispersion and persistence of debris sourced from larger-volume landslides.

We simulated landslide runout using approaches designed to capture the two most common runout types, avalanche- and flow-type movement modes. The avalanche-type movement was modelled using an energy line, or ‘fahrböschung’ principle (Heim 1932), commonly used to capture the travel distance of rockfall, debris flows and rock avalanches. Here, we employ the avalanche-type model to capture the probability of inundation by debris slides, debris avalanches and some rock avalanches (see Section 1.4.2).

Flow-type movements were modelled using the PCM model (Perla et al. 1980), which was initially developed to model avalanche runout and has since been applied to model debris flows and large rock slides. The following sections describe the fundamentals of each runout model, as well as data used to parametrise each implementation. Here, we employ the flow-type model to capture the probability of inundation by debris flows and some rock avalanches (see Section 1.4.2).

In both cases, we use the fully featured GPP model with both material deposition and sink filling enabled, as described in Figure A5.1. The selection of input parameters for each configuration is discussed later in this section. While generally appropriate for regional studies, we must note that this analysis cannot capture dynamic aspects of landslide movement, such as material fragmentation and dispersion, or run-up of the landslide due to the effects of momentum. This latter constraint can lead to errors in path estimation where rock avalanches or debris flows have the energy to run up and over topographic barriers (e.g. ridges or moraine walls).

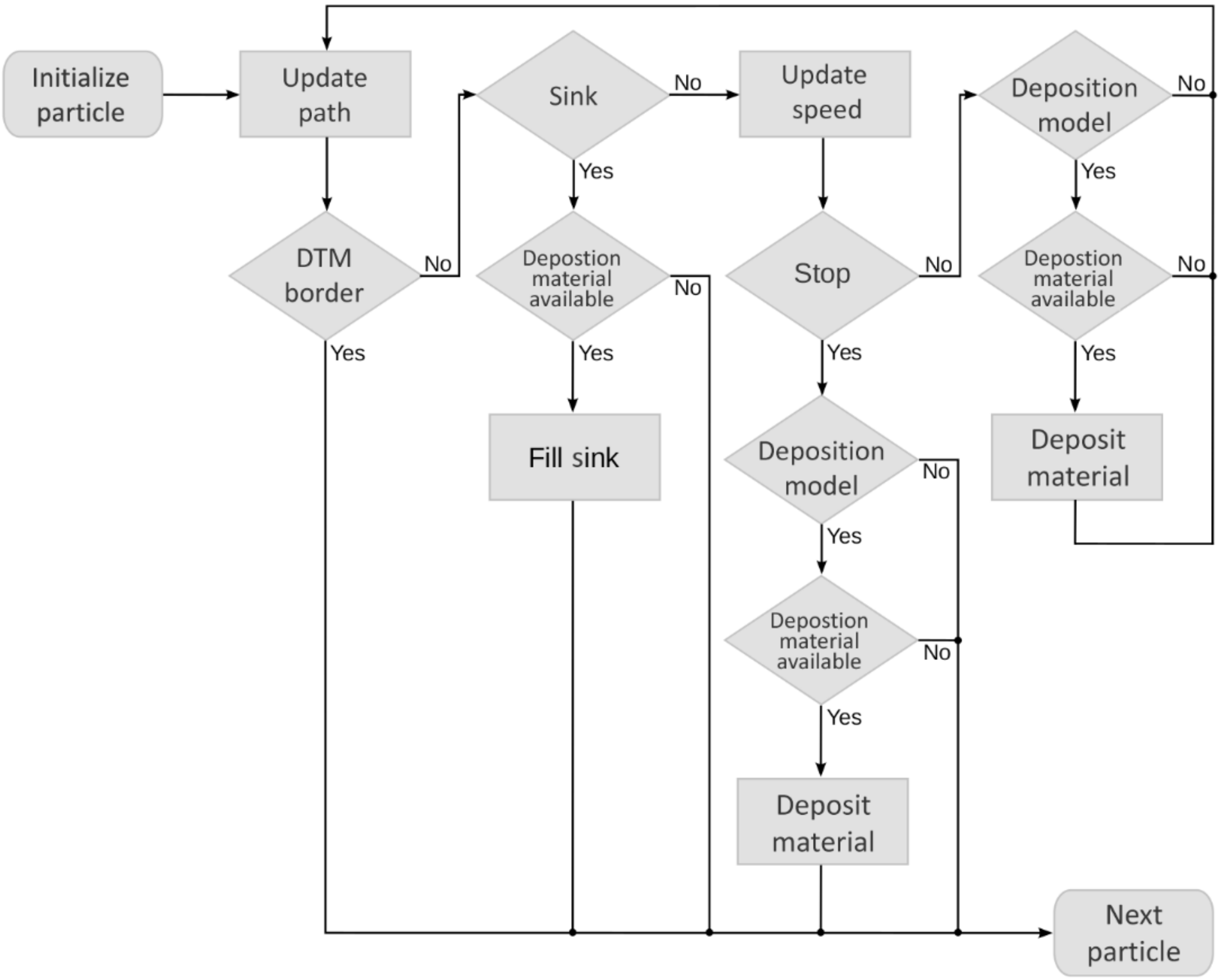

Figure A5.1 Flowchart of the fully featured Gravitation Path Process model used in this analysis. A particle is initiated at each cell in the DEM associated with a potential landslide-source area. 'Sinks' are basins within the DEM, defined as cell (or group of cells) with no down-slope node. Deposit material is derived from the landslide depth grid created during the susceptibility assessment.

A5.4 'Avalanche' Movement Types

A5.4.1 Empirical 'Fahrböschung' (or 'Energy Line') Principle

Heim (1932) proposed that the distance that a landslide travels is proportional to its fall height. The tangent of the ratio of the fall height (*ΔH*) to horizontal runout distance (*L*) between the crest of the source zone and toe of the deposit, known as the energy line, or 'fahrböschung', has subsequently been correlated with landslide volume (*V*) to generate empirical relationships similar to those presented in Figure A5.2 (Corominas 1996). Measurement of the slope crest and deposit toe have since been compiled for many different landslide types and trigger conditions (e.g. de Vilder et al. [2022] and references therein). From these compilations, a best-fit linear regression (in log-log space) between *ΔH/L* and *V* can be derived for each landslide type (debris avalanche, rock avalanche and debris flow) and trigger (seismic/dry and rainfall/wet).

These empirically-based relationships between *ΔH/L* and *V* integrate the effect of different site conditions (e.g. source geology, local topography, grain size of failed material, water content of source material, incorporation of erodible material along the travel path, vegetation, buildings, the presence [or not] of mitigation measures). This range of site-specific conditions results in the variability of observed landslide-debris runout and inundation areas. The variability in the landslide-debris runout and inundation data also allows for the probability of runout exceedance or for limits of confidence to be defined for the prediction of runout for each landslide volume (e.g. Li 1983). For example, the best-fit (blue) line in Figure A5.2 represents an exceedance probability of 50%, i.e. half of the landslides of the given volume and type will travel farther than this line.

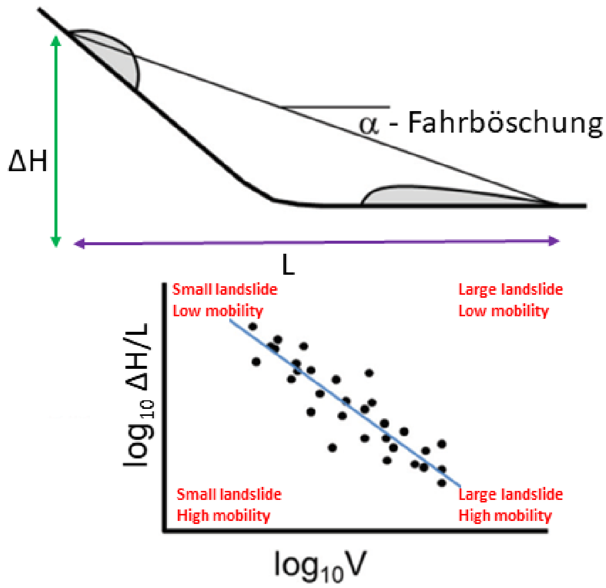

Figure A5.2 Schematic representation of the fall height (*ΔH*) and runout distance (*L*) parameters for a landslide and the conceptual relationship between *ΔH/L* and the landslide volume (*V*) (modified from McDougall [2017]).

A5.4.2 Fahrböschung Data

Parameters controlling avalanche-type runout are varied depending on the simulated volume allowing (for example) larger landslides to travel further than smaller landslides originating from the same location. This is consistent with observed landslide behaviours in a range of settings.

To estimate rainfall- and earthquake-induced avalanche-type movements, we adopt empirical runout relationships derived for (1) dry open-slope debris avalanches for volumes less than 100,000 m^3 and (2) rock avalanches for larger volumes in Brideau et al. (2021a) (Figure A5.3). The dry debris-avalanche and rock-avalanche empirical relationship has been compiled from debris and rock-slope failures that are associated with earthquake-induced landslides (e.g. Port Hills and Kaikōura events) or with large volume (>100,000 m^3) rock avalanches. The bi-linear behaviour (in log-log space) of the relationship between *ΔH/L* ratio and volume had previously been noted by other researchers (e.g. Scheidegger 1973; Hermanns et al. 2012; Brideau et al. 2020). Table A5.1 summarises the fahrböschung (and equivalent *ΔH/L* ratio) for each of the volume classes investigated in this project. The best-fit lines (and associated statistics) for *ΔH/L* as a function of volume plots were determined using a least-squares method. Assuming that the data are normally distributed, the 1%, 10%, 25%, 75%, 90% and 99% runout exceedance probability lines were calculated (Figure A5.3).

Through a process of trial and error, we found the 50th percentile dry open-slope debris avalanche fahrböschung presented in Brideau et al. (2021a) to best represent a majority of landslides in the study region (see Table A1.2). Although this fahrböschung percentile led to a minor over-estimation of the runout of most mapped landslides, the fahrböschung derived for wet channelised debris flows presented in the same reference generated similar, although subjectively worse, representations of more extensive landslide runouts than the flow-type model described below (see Section A5.4.4 for further details on model validation). As few landslides in the region overseen by WCEM have been classified as wet or dry, and none have been classified based on movement mode; objective analysis of the model performance for flow- and avalanche-type landslides is not possible within the scope of this study. Given the 25 m resolution of this study, we found little difference between runout extents for other runout-exceedance probabilities and therefore elect to only model the 50th percentile for each LSD model run. See Section A5.9 for further discussion on related uncertainties.

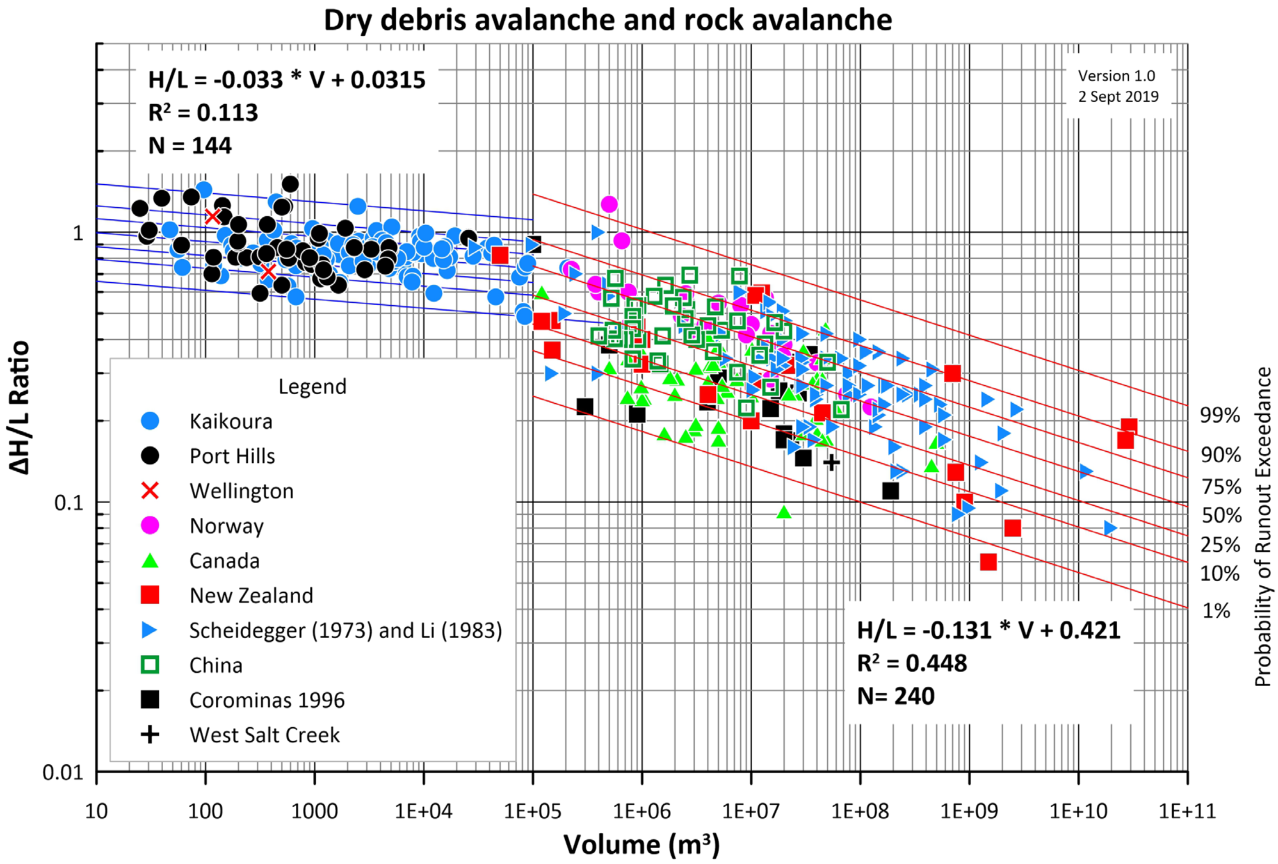

Figure A5.3 Empirical relationship between *ΔH/L* ratio and volume in open-slope dry-debris avalanches (<1,000,000 m^3) and rock avalanches (>1,000,000 m^3) (Brideau et al. 2021a).

Table A5.1 Summary of fahrböschung and *ΔH/L* values for each volume class of avalanche-type movements used in this project. See Figure A5.3 for graphical representation of the data considered.

Volume (m^3)	50% Runout-Exceedance Probability	
	Fahrböschung (°)	*ΔH/L*
10	45	1.0
100	43	0.93
1000	41	0.87
10,000	38	0.78
100,000	30	0.58
1,000,000	23	0.42
10,000,000	18	0.32

A5.4.3 Gravitational Path Process Avalanche-Type Model Implementation

All release areas were run in parallel and processed in ascending elevation order each iteration. This is consistent with our goal to capture mean annual sediment transport rather than simulate discrete sources occurring independent of each other. Given that we run a range of simulations from each source cell to capture all possible runout scenarios, 20 iterations were found to produce a reasonable runout prediction without unnecessary cost on computation time. We selected low values of ‘Initial deposition on stop’ and ‘Deposition slope threshold’ in order to prevent debris dams from forming and to maximise runout on sloping topography. The friction model employed the fahrböschung principle, with angles for each volume class and trigger type determined by dry open-slope debris-avalanche volume-fahrböschung relationships (see previous section).

A ‘Dispersion slope threshold’ of 45° was adopted to prevent dispersion of the random-walk model on steeper topography. We adopt a default ‘Exponent of divergence’ of 2, and the ‘Persistence factor’ (which determines the probability that a particle changes direction) was set to 1 in order to allow maximum dispersion. Additional parameters used in the avalanche-type model are listed in Table A5.2.

Table A5.2 List of input parameters for the Gravitational Path Process (GPP) avalanche-type model.

GPP Avalanche-Type Model Input Parameters	Value	Unit
Friction model	Fahrböschung	-
Deposition model	Slope and on stop	-
Dispersion slope threshold (no dispersion on steeper slopes)	45	°
Exponent of divergence	2	1
Persistence factor	1	1
Processing order	Release areas in parallel	-
Initial deposition on stop	2	%
Deposition slope threshold (no deposition on steeper slopes)	2	°
Minimum path length (fixed to DEM resolution)	25	m
Maximum deposition along path	20	%
Iterations (number of model runs from each start cell)	20	1

A5.4.4 Model Validation

To qualitatively assess the validity of the source area and volume calculations, we compared modelled runouts from landslide-source polygons derived from datasets presented in Table A1.2.

Landslide-debris volumes for each source polygon were calculated using the kinematic-source model presented in Section A4.2. These were used as inputs to simulate landslide runouts from all source areas expected to be associated with avalanche- or flow-type runouts. Over-estimation of landslide-source volumes could be expected to lead to more extensive runouts than mapped, while under-estimation could be expected to generate modelled runouts that do not extend as far as mapped slides. Although the 25 m resolution DEM adopted for this study is likely too coarse to provide a detailed representation of individual landslide runouts, we found a reasonable correlation between modelled runout and mapped landslide outlines, providing confidence in both our source and runout parameter selections. Example outputs for avalanche- and flow-type landslides are provided in Figure A5.4.

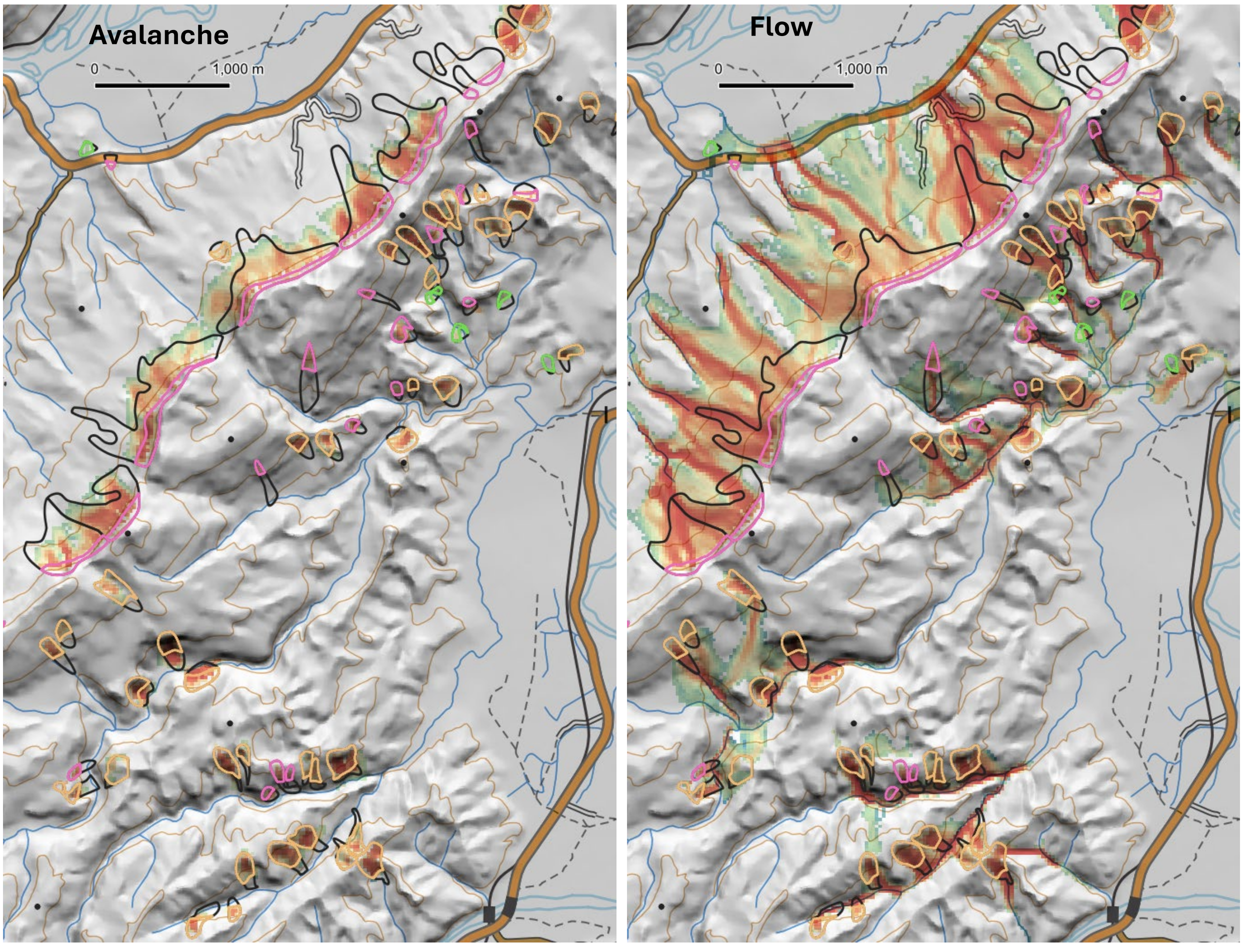

Figure A5.4 Mapped landslide outlines resulting from the 1968 Inangahua earthquake. Landslide-source areas are derived from in-house machine-learning models (coloured polygons), overlain on modelled 50th percentile avalanche-type runouts (left) for mapped landslides resulting from an earthquake trigger and flow-type runouts (right) resulting from the same trigger. Coloured polygons represent landslide sources and are coloured by classification (orange = rock slide – medium, pink = rock slide – small, green = rotational/translational slide).

Runouts associated with the 1968 Inangahua earthquake are most commonly consistent with modelled avalanche-type movement (evident in the correlation of modelled and mapped runout extents; Figure A5.4), although more channelised landslides are better captured by flow-type movements. This may be expected, as the earthquake occurred near the end of summer, when ground conditions are typically dryer. The LSD model assumes that the runout of 83% of all earthquake-induced landslides is consistent with avalanche-type movements, while 16% are assumed to be flow-type movements.

See Section A5.9 for further discussion on the impact of LSD model uncertainties on calculated hazard and risk outputs.

A5.5 'Flow' Movement Types

A5.5.1 PCM Model Principle

The PCM model (Perla et al. 1980) was adopted to model flow-type movements in the region; specifically, debris flows (see Section 1.4.2). This is a two-parameter friction model commonly used to reproduce avalanche- or flow-type behaviours (Wichmann 2017). The model itself takes a centre-of-mass-based approach to evaluate down-slope motion by balancing the accumulation of energy of a particle as it travels down-slope under gravity against two energy-loss terms describing the coefficient of sliding friction and the mass to drag ratio.

A5.5.2 Gravitational Path Process Flow-Type Model Implementation

Similar to the fahrböschung model, the GPP implementation of the PCM model uses a random-walk model to determine the likely path of debris as it moves down-slope, employing an iterative Monte Carlo method to evaluate probable runout paths. We adopt identical persistence and spreading terms as those adopted for the avalanche-type movement models described in Section A5.4.3. Parameters controlling flow-type runout are varied depending on the catchment area that the material flows over, allowing (for example) landslides in channels to travel further than landslides on open slopes. This is consistent with observed landslide behaviours in a range of settings.

Calibration of the PCM model can be complicated, as the inclusion of two energy-loss terms means that back-calculating runout parameters from a mapped debris extent leads to a non-unique solution. In addition, the GPP model allows users to select either a globally consistent, or spatially variable coefficient of sliding friction. A globally consistent coefficient allows for similar treatment of terrain resistance and is ideally suited to unconfined flows over consistent ground cover, while a spatially variable coefficient of sliding friction is commonly combined with metrics describing up-slope catchment area and allows models to incorporate the increased efficiency of debris transport in channelised flows. A recent study by Goetz et al. (2021) presented a method to develop an optimal parameterisation based on a catalogue of 521 mapped rainfall-induced debris-flow sources and deposits in a single river basin in central Chile. Goetz et al. (2021) trialled both spatially consistent and spatially variable coefficients of sliding friction and adopted the spatially consistent option, in part due to the reduced complexity and also a slight improvement in predictive ability of the spatially consistent model with an optimised friction parameter (Mergili et al. 2012; Wichmann 2017). However, it is, important to note that Goetz et al. (2021) elected to adopt previously recommended spatial variability scaling parameters and did not seek to optimise the spatially variable model, which may have yielded improved results.

A lack of suitable mapped landslide data within the study region makes a local calibration of the PCM model difficult, as available landslide inventories do not discriminate between avalanche- and flow-type movements. This invalidates the principal assumption of Goetz et al. (2021), that all mapped landslides are flows, and prevents the adoption of a similar optimisation technique for this study. Instead, we assume that the mode of movement is dominantly 'channelised' flow and adopt a spatially variable friction parameter based on the 'most likely' parameters derived for debris flows in Switzerland (Gamma 1999). We then adopt an intermediate mass-to-drag ratio based on suggested ranges for debris flows (Wichmann 2017; Goetz et al. 2021) to describe the acceleration of debris on steep slopes. A list of all flow-type movement GPP input parameters is provided in Table A5.3 below.

Table A5.3 List of input parameters for the Gravitational Path Process (GPP) flow-type model.

GPP Flow-Type Model Input Parameters	Value	Unit
Friction model	PCM model	-
Deposition model	Slope and on stop	-
Dispersion slope threshold (no dispersion on steeper slopes)	45	°
Exponent of divergence	2	1
Persistence factor	1	1
Processing order	Release areas in parallel	-
Initial deposition on stop	20	%
Deposition slope threshold (no deposition on steeper slopes)	25	°
Minimum path length (fixed to DEM resolution)	25	m
Sliding friction coefficient multiplier (Gamma 1999)	0.19	1

GPP Flow-Type Model Input Parameters	Value	Unit
Sliding-friction coefficient exponent (Gamma 1999)	-0.24	1
Upper sliding-friction coefficient limit (Gamma 1999)	0.3	1
Lower sliding-friction coefficient limit (Gamma 1999)	0.045	1
Mass-to-drag ratio (Wichmann 2017; Goetz et al. 2021)	60	m
Initial velocity (Wichmann 2017)	1	m/s
Iterations (number of model runs from each start cell)	20	1

A5.5.3 Model Validation

We evaluate the flow-type model performance by comparing the extent of modelled debris from flow-type movements against the extent of debris fans within the region. This evaluation was undertaken through a combination of field investigations and GIS (geographic information system) analysis. During the field survey, GNS Science engineering geologists noted the locations and/or extent of 36 individual debris fans (see Section 2.7). Of these, all observations either coincided with landslide-debris fluxes derived from the flow-type models or, in the case of observations marking the extent of a fan, were within 25 m of the modelled extent. As no consistent map of debris-fan extents exists within the region, we undertook a qualitative assessment to compare modelled flow-type extents with landforms demonstrating common debris-flow fan attributes (see Section 1.4.2.2). This assessment was undertaken using a combination of aerial photographs and hillshade DEM models, using either the 8 m national DEM or a 1 m LiDAR DEM where available. Overall, we find an excellent correlation between the extent of modelled debris and the furthest reaches of debris-flow-fan landforms. As expected, maximum fluxes are almost always at the apex of fans and decrease down-slope across the entire surface of fans, with a concentration of modelled debris visible in channels that clearly cross fans in the 8 m DEM. This is consistent with expectations for debris-flow-type landslides, and we are therefore confident that the flow-type models are adequately approximating the distribution of debris fluxes relating to this process with respect to the model input parameters, although we have little data with which to evaluate the magnitude of the annual flux.

See Section A5.9 for further discussion on the impact of LSD model uncertainties on calculated hazard and risk outputs.

A5.6 Deposition Model

The deposition routine in the GPP model employs a sink-filling method that is modified from Gamma (1999). The routine:

1. Identifies the over-flow cell and sink depth.
2. If the current iteration lacks sufficient material to fill the sink's depth, all available material is deposited and the process halts.
3. Otherwise, the sink is filled to a height that maintains a user-defined minimum slope to the overflow cell.
4. To prevent forming another sink, material is placed on the path above the sink, ensuring that enough material remains to maintain the minimum slope.

If the available material is insufficient, the angle is gradually reduced until a minimal downward slope is preserved. Any remaining material is used in subsequent iterations.

For avalanche-type movements, we employ the 'deposition on stop' option with an initial deposition height below 100%. In this configuration, the given percentage of material (available per run) is deposited in the stopping cell and the remaining material (per run) is used to fill the DEM up-slope (in order to preserve a slope for subsequent runs). This necessary approximation allows the model to generate quasi ‘fan’ deposits with constant surface slopes determined by material availability, although this means that the sum of deposited material can be lower than the amount of material in the start cell, depending on the terrain. This may be consistent with our consideration of annualised landslide-debris flux, as fluvial processes can be expected to erode over steepened deposits.

For flow-type movements, we employ the ‘deposition along the path (slope)’ option. In this case, the material flux is reduced by the amount deposited on the path, i.e. below the deposit, the material flux gets lower. If all material available for this run has been deposited, the material flux reduces to zero.

A5.7 Mean Annual Landslide-Debris Flux

The probability of landslide sediment passing a location in the study region can be derived from the material flux returned for each iteration of the GPP model ensemble. Where the input for the model is the calculated landslide sediment-production rate for each scenario (in m/yr), the material flux returned from each iteration of the ensemble [$\Phi_{GPP(\mu)(c)(T,RI)(x,y)}$] therefore reflects the volume of material passing through a given unit area per year (m^3/m^2/yr). Combining the material-flux outputs for flow- and avalanche-type model configurations then requires that the output is scaled by the probability of each movement type in the study region (P_μ, where the subscript denotes the mode of movement). The mean annual landslide-debris flux (Φ_L) can then be written as:

$$\Phi_{L(x,y)} = \sum \frac{\Phi_{GPP(\mu)(c)(T,RI)(x,y)}}{\sigma} \times P_{(\mu)}$$ Equation A5.2

Figure A5.5 presents a selection of landslide-debris-flux outputs from GPP model runs. The three upper panels represent rainfall-induced avalanche outputs overlain on a hillshade derived from the DEM used for each model. The reduction in the detail of each DEM with increasing volume class is a reflection of the smoothing used to prepare the DEM for modelled runout of larger source volumes (see Section A5.3 for further details). Source-volume-class range 4–5 demonstrates the largest debris flux for rainfall-induced landslides, while volume-class range 6–7 presents the highest debris flux for earthquake-induced slides. These volume-class ranges are notably higher than those that may be expected to generate the greatest volume of debris when considering just the mean landslide volume class assigned to each trigger (3.92 and 4.55, respectively; see Section A4.4). This skew toward greater fluxes at larger volumes reflects local characteristics of the area, in particular, a coincidence of higher erosion rates in source areas that support larger landslide volumes. This leads to (1) a greater volume of debris being associated with larger landslide sources and (2) lower fahrböschung angles and therefore greater mobility of larger volume landslides. The increasing mobility of larger avalanche-type landslide volume classes is evident when comparing the extent of volume-class 6–7 earthquake- and rainfall-induced slides, which fan out on the flat terrace around Kokiraki, to that of volume-class 2–3 slides, for which the debris rarely extends to the toe of the hillslopes (upper six panels in Figure A5.5). Flow-type runouts for each trigger in the lower six panels of Figure A5.5 are similar, as we adopt identical flow-type model parameters for earthquake- and rainfall-induced slides (see Section A5.5). The primary difference between the two trigger types is then a result of the increased sediment-production rates calculated for volume-class 4 and 6 earthquake-induced landslides with respect to their rainfall-induced counterparts (see Figure A5.5). Although the probability of earthquake-induced landslides in the vicinity of Kokiraki is notably less than that of rainfall-induced landslides, the impact of this is masked by the larger mean volumes and greater mobility of larger flow-type slides (due to a smoothed topographic model). The mean annual flux of earthquake-induced landslides is therefore similar to that of rainfall-induced slides (see the lower two rows of Figure A5.5).

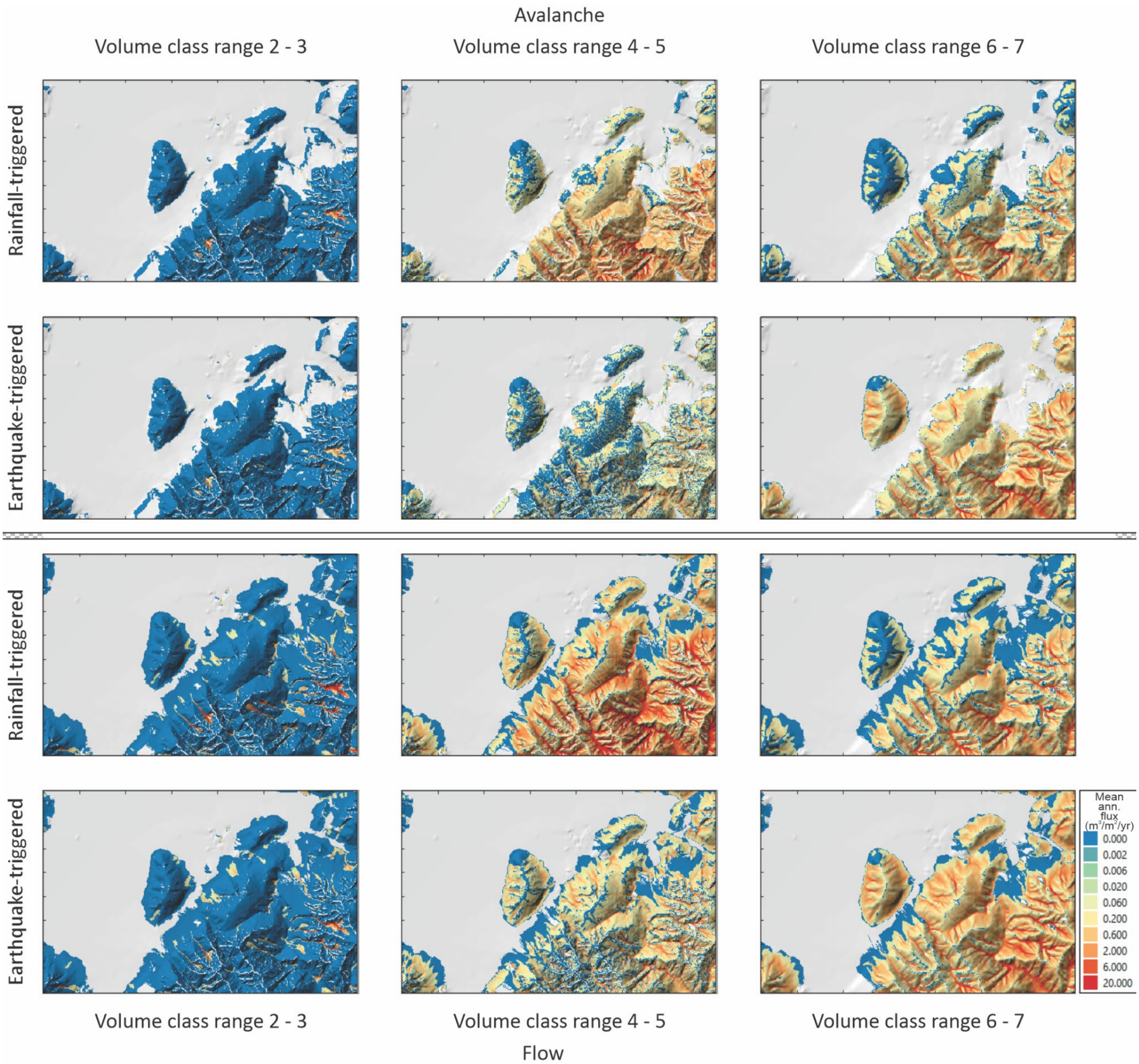

Figure A5.5 Mean annual material flux derived from Gravitational Path Process runout models for selected volume class sizes, triggers and movement types.

A5.8 Scenario-Specific Landslide-Sediment Distribution

Landslide sediment-distribution models for each event-specific scenario were generated using the same model steps as described in Sections A5.1–A5.7, although landslide source-material thicknesses are derived directly from scenario-specific landslide-sediment-production-model depths (see Section A4.6), and only flow- and avalanche-type movement models for the appropriate trigger are simulated.

A5.9 Key Landslide Sediment-Distribution Model Uncertainties and Assumptions

The LSD model variables contribute the most uncertainty in this study due to limited local data constraints, with most parameters varying by 50%.

The proportion of flow-type movements determines the likelihood of landslides occurring as avalanche or flow types. This variable is perhaps the least constrained in the region, as no local data exist that explicitly categorise flow- or avalanche-type landslides. Although not linked to the GPP model, it has the greatest impact on annual property loss risk (APLR), especially at locations far from the landslide source, where shifting to the more mobile flow type can increase APLR by $10^{0.4}\times$. We note a number of uncertainties associated with the proportion of flow-type movements in the calculation:

- Currently, we assume that the proportion is the same for both rainfall- and earthquake-induced landslides; however, this is possibly not the case, as experience suggests that earthquake-induced landslides commonly have a lesser travel distance and therefore are more likely associated with avalanche-type movements. A re-analysis of existing datasets may shed further light on the relative proportions of each movement type in the region overseen by WCEM.
- There may be a seasonal bias to consider, as earthquake-induced landslides may occur during wet periods, potentially increasing the proportion of landslides that transition to flow-type movements. Again, a re-analysis of existing datasets (e.g. the late summer Inangahua and mid-winter Murchison earthquake landslide catalogues [Hancox et al. 2014, 2016]) may shed further light on the relative proportions of each movement type in the region overseen by WCEM.

We note that, although we have undertaken a qualitative evaluation of model performance (see Sections A5.4.4 and A5.5.3), neither the PCM ('flow'), nor Fahrböschung ('avalanche') models have been locally calibrated. Our parameter selection therefore reflects our 'best estimate', although the absolute accuracy of this is difficult to quantify and likely to vary across the region. However, we are able to quantify uncertainties associated with parameter election. These are discussed below:

- PCM model inputs have minimal impact on APLR, as the sliding-friction coefficient, tied to hillslope gradient, strongly controls runout in our 1D model, leading to velocity reductions once the slope falls below a threshold.
- Uncertainty in the fahrböschung angle can alter APLR by up to $10^{-1.7}\times$ near the landslide source, although obviously has no effect beyond the maximum runout extent.
- The GPP persistence factor, which affects both fahrböschung and PCM model runouts, significantly affects APLR, potentially increasing uncertainty from $10^{-1.6}\times$ close to the source to an unconstrained value far from the source, where the 'best estimate' debris flux (and therefore APLR) is almost zero. Although we expect that this solution is a numerical artifact associated with the 1D model employed in our sensitivity analysis, it does highlight the care that needs to be taken when evaluating landslide-debris flux and APLR estimates far from landslide sources. As such, inclusion of a 'maximum credible extent' outline capturing the maximum reach of any debris may be a useful addition to hazard overlays.
- Similarly, DEM resolution influences landslide-debris mobility by altering slope-gradient noise, with APLR varying between $10^{-1.6}\times$ and $10^{6}\times$ at sample locations within 1D models when the grid size changes from 8 m to 25 m. This trend increases with distance from the landslide source, and, while the magnitudes of the values are partly a numerical effect, we expect that debris-flux changes can disproportionately affect APLR in low-flux areas.

Given the above assumptions and uncertainties, we have elected to adopt 'best estimates' for all input variables while adopting conservative ranges for associated uncertainties. This ensures that LSD model results most closely reflect the input datasets and assumptions described in this report, while conveying the overall level of uncertainty associated with LSD model inputs (see Appendix 7). We recommend that West Coast Regional Council consider appropriate precautionary reductions in acceptable hazard or risk metrics based on an evaluation of appropriate confidence intervals and reported model uncertainty (as discussed in Section 5).

APPENDIX 6 Landslide Debris-Inundation-Risk Model

This section describes details of the Landslide Source to Inundation Process Model (LS-IPM) used to convert the landslide-debris-inundation hazard output from the landslide sediment-distribution model into annual property loss risk (APLR).

A quantitative sensitivity analysis is undertaken in Section A7.5.

A6.1 List of Landslide Debris-Inundation-Risk Model Variables

In addition to variables listed in Table A2.1, the following table describes variables introduced in the LS-IPM workflow.

Table A6.1 Landslide debris-inundation-risk model variables.

Variable	Description	Value	Unit
Ω	Characteristic landslide-debris spreading factor	1, 3	1
$\Phi_{L(c)(T)}$	Characteristic landslide-debris volume	-	m^3/m
N_{LS}	Number of potential landslide sources based on source-area calculations	-	1
P_i	Probability of inundation by landslide debris	-	1
Λ	Structural vulnerability	-	1
APL_{LS}	Mean annual property loss risk	-	1/yr
Subscript	Description	-	-
x,y	Spatial location of pixel centroid	-	-
T_0	Lower limit of temporal-integration interval	-	-
T_{max}	Upper limit of temporal-integration interval	-	-
μ	Runout model configuration	-	-
c	Landslide volume class	-	-
T	Landslide trigger type	-	-
RI	Event return interval	-	-

A6.2 Landslide Debris-Inundation-Event Frequency and Magnitude

The landslide-debris flux for a single event is a function of the landslide-source volume, mobility of the landslide debris, topographic routing and proximity to the landslide source. However, mean annual landslide-debris flux is the product of contributing event frequency and inundation event magnitude. As such, separating out the frequency and magnitude of inundation events (as is required for risk analysis) from the LSD model output requires additional assumptions (or site-specific information) with respect to either the frequency of inundation events at a given location or the magnitude of inundation. Here, we evaluate the probability of inundation by rare, independent landslide debris-inundation events by employing a Poisson probability formula. In this case, the annual probability of inundation (P_i) can be derived from the expected number of inundation events per year (λ):

$$P_{i(\mu)(c)(T,RI)(x,y)} = 1 - e^{-\lambda_{(\mu)(c)(T,RI)(x,y)}} \quad \text{Equation A6.1}$$

where λ can be described as a function of the mean annual landslide-debris flux (Φ_{GPP} , i.e. the mean annual magnitude of impact) and the characteristic debris flux at the inundation location for a given landslide source volume (Φ_C, i.e. the magnitude per event):

$$\lambda_{(\mu)(c)(T,RI)(x,y)} = \frac{\Phi_{GPP(\mu)(c)(T,RI)(x,y)}}{\Phi_{C(\mu)(c)(T,RI)(x,y)}} \qquad \text{Equation A6.2}$$

Although the mean annual debris flux for each combination of trigger, volume class, return interval and movement type can be directly derived from individual outputs from the LSD ensemble (see Section A5.7), the characteristic debris flux is not a direct output of the LSD model. As the landslide sediment-production (LSP) and LSD models include a probabilistic consideration of source-debris production, routing of landslide debris and deposition of debris along the travel path, it is not possible to directly correlate the magnitude or frequency of landslide-debris production in source areas to the characteristic debris flux passing a given location down-slope.

To estimate characteristic inundation-event magnitudes, we compare the Gravitational Path Process (GPP) model outputs to the landslide geometries and spreading characteristics defined for the LSP and LSD models. For each LSD iteration, we assume that all inundation events at a given location have a uniform magnitude and that each event results from the failure of a single, independent landslide source. This approach enables us to model characteristic-inundation magnitude by combining assumed landslide-source properties with inputs and outputs from the GPP model.

The characteristic landslide-debris flux can be described as a function of the unit volume of the initial landslide source, the area of landslide sources contributing to a given cell and the degree of spreading between the source and a given location. The unit volume of the landslide source [$\Phi_{L(c)}$] is defined as the average volume of debris that can be expected to pass through one linear metre of slope as a result of a single landslide of a given class size occurring. This is the product of the mean slope-parallel length and mean depth, multiplied by 1 m:

$$\Phi_{L(c)} = \sqrt{A_{L(c)}} \times D_{L(c)} \times 1 \qquad \text{Equation A6.3}$$

If debris were to travel from a landslide source downhill on a planar surface without deposition or spreading, the unit volume of the landslide source could be considered the characteristic debris flux at any given location. However, a combination of debris convergence or divergence due to topographic effects, as well as spreading due to the random-walk component of the GPP model, means that this case becomes increasingly unlikely as (1) topographic effects become stronger with increasing distance from the debris source and (2) the degree of spreading increases with decreasing slope gradient. As such, we develop a simple model to allow for a progressive transition of the characteristic debris flux from the unit-source volume in steeper cells to negligible flux in low-gradient cells with large source areas. We employ a probabilistic model mirroring the random-walk approach adopted in the GPP model (Wichmann 2017) to calculate a debris-spreading factor, separating the characteristic-flux model for steeper source areas from that in shallower-gradient runout areas. In the shallower-gradient runout areas, we calculate a theoretical dispersion of debris based on the distance that debris travels from the landslide source, as well as the gradient of topography along the shortest path. This dispersion factor is employed to calculate a characteristic debris flux (Φ_C) from the unit volume of the landslide source for each volume-class range, as described in Equation A6.4:

$$\Phi_{C(\mu)(c)(T,RI)(x,y)} = \frac{\Phi_{L(c)}}{D_{(x,y)}} \qquad \text{Equation A6.4}$$

where $D_{(x,y)}$ represents the theoretical dispersion of landslide debris between the source and inundation location. The dispersion factor is therefore a function of the distance between the nearest landslide source and a given location, weighted by the spreading factor (ω):

$$D_{(x,y)} = \frac{\int path\ from\ sources\ to\ (x,y) \left(1-\omega_{(x,y)}\right) Rd\ell}{{}^{1}\!/_{2} \times D_{L(c)}} \qquad \text{Equation A6.5}$$

where R is the grid resolution of the GPP model and $D_{L(c)}$ is the mean depth of the landslide-class range (Table A2.1). The spreading factor reflects the probability of debris continuing in the same direction based on the random-walk model outlined in Wichmann (2017):

$$\omega_{(x,y)} = \frac{1 + min\left(p\left(\frac{tan\beta_{i(x,y)}}{tan\beta_{thres}}\right)^{a}, 1\right)}{2} \quad \text{Equation A6.6}$$

Here, all variables reflect GPP model inputs. β_i is the local slope, β_{thres} is the slope threshold (above which no spreading occurs), a is the exponent to control the amount of divergent flow and p is the persistence factor. As β_i decreases from β_{thres} toward zero, ω will decrease from 1 to 0.5. All input parameter values are listed in Tables A5.2 and A5.3. We note that Equation A6.5 considers the shortest path between landslide-source areas and inundation locations rather than the travel path between the material source and a given location. This is a necessary simplification, as each down-slope location can be intersected by multiple travel paths, which prevents derivation of a unique dispersion factor. As the spreading factor is lowest on steeper hillslopes (where landsliding is kinematically feasible) and greatest on flatter slopes (where travel paths typically extend in a linear manner from source areas), this simplification provides a reasonable representation of spreading with increasing down-slope distance from source areas.

Substituting Equations A6.4–A6.6 into Equation A6.2 allows us to estimate the number of landslide debris-inundation events per year (λ). Substituting this frequency into Equation A6.1 then provides an estimate of the annual probability of landslide-debris inundation (P_i) for a given set of conditions.

We note that the model presented in Equation A6.4 provides an approximation of characteristic debris flux at a given location and is not a substitute for local observations or detailed landslide runout analysis. In particular:

- The concentration of debris in convergent, steep topography can lead to an over-estimation of λ, as the flux passing a given location from a single landslide source may be as much as the full landslide volume, rather than the unit volume (as assumed in Equation A6.2). As such, the calculated inundation frequency will exceed the frequency of source events by a factor of $max\left(\frac{\sqrt{A_{L(c)}}}{R}, 1\right)$, depending on the degree of topographic convergence. This effect is most pronounced along valley axes and for larger landslide classes, for which the characteristic length may be up to two orders of magnitude greater than the grid resolution. However, as the DEM is smoothed using a moving window scaled by the landslide volume (see Section A5.3.2), convergent topography is reduced for larger size classes, and this effect is therefore minimised.
- Our consideration of debris spread is not strictly tied to the debris path between the landslide-source and -inundation location. We assume that spreading between the source and inundation location varies as a function of the local slope, without any consideration of topographic concavity, convexity or distinct flow paths along the route. However, the characteristic-flux estimate is based on a conservation of mass approach, bounded by the landslide unit volume on slopes close to or above the slope threshold (presumably near the landslide source; see Equation A6.4), and a proportion of the unit volume is determined as a function of the number of potential contributing landslides on flat ground (presumably distal to the landslide source). While the natural variability in the DEM makes it difficult to quantify associated uncertainties, these bounds suggest that the calculated flux likely has a similar uncertainty to that described above.

The probability of inundation for a given set of conditions can be derived from Equation A6.1. Considering all movement types, volumes, triggers and return intervals, the total annual inundation event frequency (λ_{LS}) can then be calculated as the sum of landslide inundation-event frequencies (Equation A6.2) for all parameter combinations:

$$\lambda_{LS(x,y)} = \sum \lambda_{(\mu)(c)(T,RI)(x,y)}$$ Equation A6.7

In the following section, we present LSP and LSD model results calculated for a simple block model in order to demonstrate inputs and outputs of the characteristic debris flux model. We summarise results in terms of inundation-event frequency, as this can be directly related to the input mean annual sediment-production rates.

A6.2.1 Validation of Landslide Debris-Inundation-Event Frequency Model

The calculation of landslide-inundation frequency can be demonstrated by modelling landslide debris flux from two discrete representative landslide sources (outlined by blue squares in figure below). Figure A6.1a, b illustrates the mean annual debris flux and contributing area outputs from LSD model runs combining avalanche and flow movement types from landslide sources representing the geometric mean of Class 4 and 5 landslides. We specify a mean annual erosion rate for the landslide-source area of 1.5 mm/yr, a sediment bulking factor of 1 and set erosion rates outside of the sources to zero. The slope angle is set at 30°, and the slope threshold is set to 20° to prevent spreading on the hillslope. Based on the area-volume scaling relationship presented in Equations A4.6 and A4.7, the mean depth for this volume class is 10 m. By dividing the landslide depth by the erosion rate, we can determine that the theoretical mean annual reccurrence interval for each slide will be 666 years, or, alternatively, that the frequency of landslide occurrence will be 0.0015 events/yr.

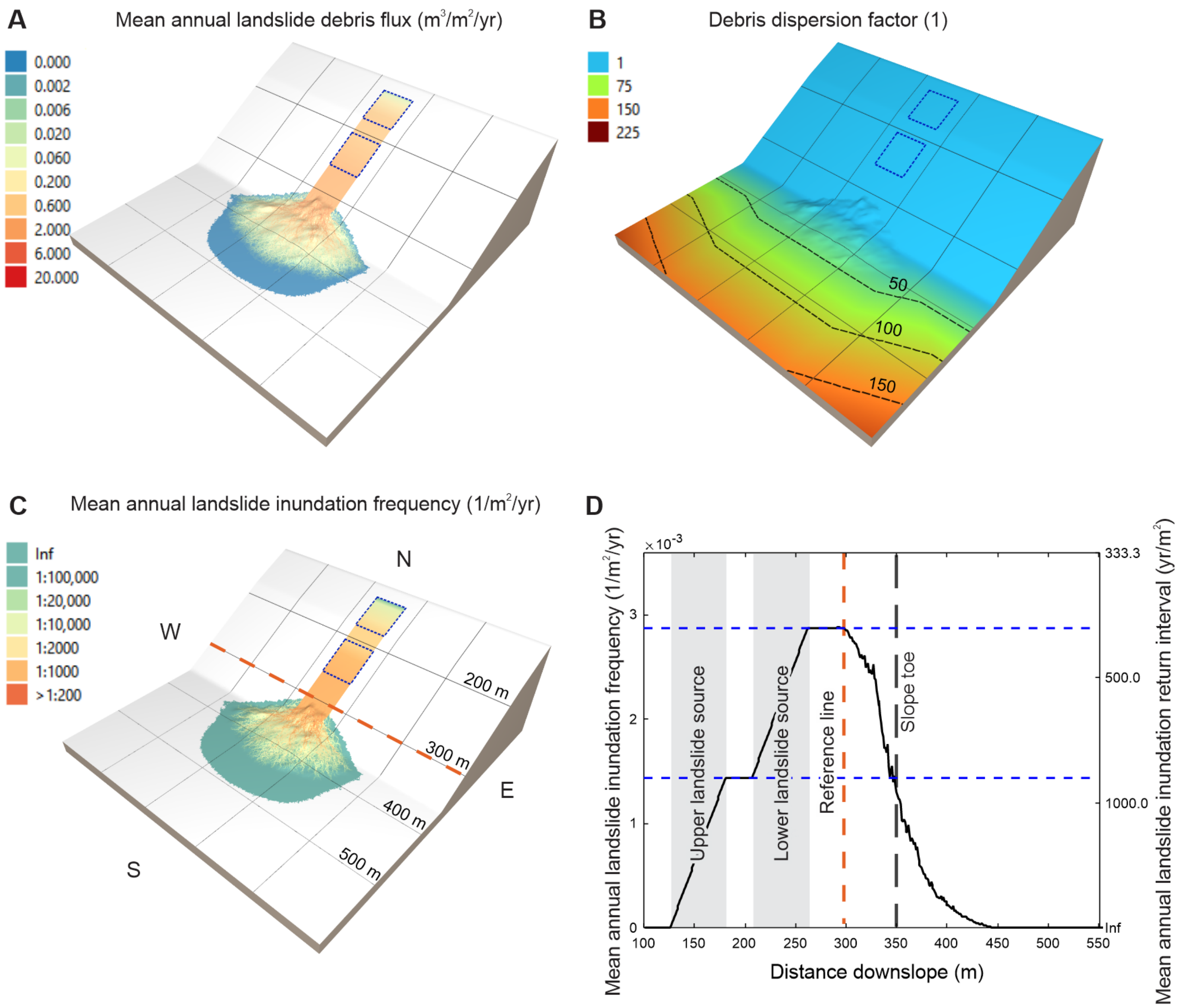

Figure A6.1 Example of model inputs to calculate mean annual landslide debris-inundation frequency from two representative landslide sources.

The mean annual frequency of inundation derived from Equation A6.7 is presented in Figure A6.1c, while Figure A6.1d presents the mean model output along a full-width swath profile from the crest to the toe of the modelled landslide deposit. These two figures indicate that the calculated frequency of inundation increases from zero at the top of the uppermost landslide (125 m down-slope) to almost equal the theoretical mean frequency of landslide occurrence (dashed blue line) at the lower limit of the upper landslide source (175 m downslope). Although the input erosion rate and assumed mean depth of failure is constant throughout the source area, and the frequency of occurrence in this area will also therefore be constant, the calculated frequency of inundation by the characteristic landslide (i.e. geometric mean of Class 4 and Class 5 landslides) increases as the profile progresses down-slope through the source region. This keeps increasing until the contributing area derived from the modelled up-slope area matches the expected contributing area at the lower limit of the upper landslide source (see Figure A6.1). A section of constant inundation frequency from 180 m to 210 m then reflects the lack of a source at this location, and, as such, the mean annual debris flux through these cells is constant. The mean annual inundation frequency then increases to almost the theoretical mean frequency for two events (upper dashed blue line in Figure A6.1; 'Lower landslide source'), before levelling off until the location of the reference line at 300 m (see Figure A6.1). This represents the upper limit of a depositional fan that formed through the model runs and marks the upper limit of debris spreading as a result of a combination of (1) topographic dispersion on a depositional fan formed through the model runs and (2) the initiation of debris spreading as the topographic gradient of the fan and lower model surface were both below the slope threshold.

The reduction of inundation frequency beyond the 300 m reference line reflects the fact that our swath profile captures only a portion of the model along the centerline of the slides. As debris both spreads laterally and is deposited along the path, the material flux, and therefore the derived frequency of inundation along the centerline, reduces respectively. The majority of debris stops prior to 400 m down-slope, with a thin apron extending out to 430 m (note the non-linear colour scale presented in Figure A6.1a). A broader area of zero debris extends out to 500 m down-slope; however, the deposition prior to this point has removed all debris from the runout model, and the continued runout is purely a numerical artefact. As such, the calculated inundation frequency represented in Figure A6.1c, d provides a suitable approximation of the annual probability of inundation from debris derived from the two landslide sources.

A6.3 Probability of Loss (Vulnerability)

The physical vulnerability to landslide-debris-inundation events can be defined as the probability of a building being damaged to a degree at which the cost to repair or restore it (re-instatement cost) would surpass the cost of fully replacing it (replacement cost). APLR therefore describes the likelihood that damage will reach a level where repairs are no longer economically feasible, making full replacement the more cost-effective choice.

In order to evaluate building vulnerability to landslide-debris inundation, we adopt the building damage dataset (n = 168) compiled in Massey et al. (2019) from New Zealand and international data, where the vulnerability of buildings to landslide damage has been related to landslide debris-inundation depth (Figure A6.2). Their analysis suggests that, between 0 m and 4.0 m inundation depth, the building-damage ratio (repair cost divided by replacement value) varies as a sigmoid logistic function, increasing gradually to 30% damage for debris depths up to 1.5 m height and 80% or more damage being incurred for depths greater than 3.0 m. The same vulnerability function was recently employed to evaluate vulnerability to debris flows and rock fall in the Queenstown Lakes District (Woods et al. 2021).

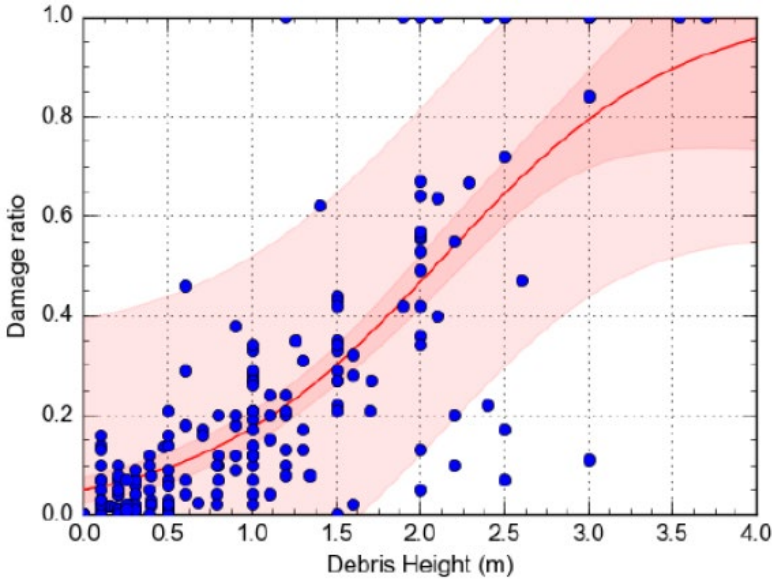

Figure A6.2 Building vulnerability to falling debris and debris flows over a range of common landslide inundation depths (n = 168). Data represents all building types. Darker red shading represents ± one standard deviation, while lighter red shading represents the 95% confidence interval (Massey et al. 2019).

The methods employed in this study do not allow the calculation of debris height for individual landslide events. For the purpose of calculating APLR, we instead assume that the height of debris when it impacts a building is equal to the mean depth of the landslide source. This allows us to then convert the calculated probability of inundation to APLR throughout the study region (see Appendix A6.4 for full details of this calculation). Although debris height will vary in reality as a result of factors such as spreading, channelisation, entrainment and interaction with buildings, we note that the building-vulnerability function adopted in this study (Massey et al. 2019) predicts a mean of 100% damage for debris heights of 4 m and is invariant for all debris heights exceeding 4 m (see Figure A6.2). As the geometric-mean source depth adopted in the LSP model for the 'house'-size landslide-class range (classes 2–3) and above exceeds 4 m (see Table 2.1), this assumption means that we estimate a mean of 100% damage for inundation by any debris for 'house'-sized landslides and above. The geometric-mean depth of 'family-car'-sized landslides therefore results in this class range being assigned a mean damage ratio of 25%, while the damage ratio associated with inundation by debris from 'bus'-sized landslides is 65%. Given the shorter travel distance of lower-volume landslides, and therefore lower potential for spreading, assuming an inundation depth similar to that of the source is not unreasonable for these size classes. On the other hand, the increasing potential for large landslides to transport large volumes of extremely coarse (e.g. house-sized and greater) debris to the full extent of the runout increases the potential damage associated with inundation. Assuming 100% damage for inundation resulting from landslides greater than 'house' size is therefore also not unreasonable. A quantitative analysis of uncertainties associated with this assumption is presented in Section A7.5. Depending on the proximity of the inundation location to the landslide source, we estimate the associated uncertainty to result in an approximate 3% change in calculated APLR.

We note that determining the probability and depth of inundation with a higher level of confidence, as may be suitable for plan changes and building consents in areas where a larger number of properties may be subject to a large hazard event, requires site-specific geological observations and consideration of all potential failure mechanisms and triggers. Such an analysis should be supported by appropriate physical modelling of runout processes (de Vilder et al. 2024).

A6.4 Mean Annual Property Loss Risk

It is assumed that multiple landslides of various source volumes may be triggered at the same time. Therefore, it is important in the risk calculation to ensure that a building is not completely damaged more than once, if it is hit by debris. For example, a building occupying a given grid cell at the time of an earthquake could be damaged by debris from one source volume or from multiple source volumes combined. Therefore, although the probability of damage increases with the increasing volume of debris passing through a given portion of slope, it cannot exceed 1.

To calculate the annual property risk values for each grid cell, the following steps were undertaken:

- **Step 1:** The probability of damage for each landslide-source volume, trigger type and return interval was calculated based on the probability of inundation (Equation A6.1), where:

  $$APR_{LS(\mu)(c)(T,RI)(x,y)} = P_{i(\mu)(c)(T,RI)(x,y)} \times \Lambda(\Phi_{L(c)})$$ Equation A6.8

  Λ is vulnerability, defined as probability of total building damage by debris. If $APR_{LS(\mu)(c)(T,RI)(x,y)}$ ≥ 1, then the value should be 1.

- **Step 2:** The contribution to each grid cell from each landslide-volume class per trigger type and return interval is then calculated as the product of the probability of damage from all landslides within the representative return interval for each trigger type, where:

  $$APR_{LS(T,RI)(x,y)} = 1 - \prod_{i=1}^{n} 1 - APR_{LS(\mu_i)(c_i)(T,RI)(x,y)}$$ Equation A6.9

- **Step 3:** For both rainfall and earthquake triggers, the total building damage risk of a given grid cell is then calculated as a product of the probability of damage from landslides per trigger type and return interval, where:

  $$APR_{LS(x,y)} = 1 - \prod_{i=1}^{n} 1 - APR_{LS(T,RI)(x,y)}$$ Equation A6.10

A6.5 Key Landslide Debris-Inundation-Risk Model Uncertainties and Assumptions

Aside from the uncertainties associated with the landslide source-susceptibility (LSS), LSP and LSD models, uncertainties related to the LDIR model arise from (1) the method employed to estimate the characteristic landslide-debris-inundation event magnitude at locations down-slope of landslide sources (2) the assumed inundation depth for each volume-class range and (3) the vulnerability of structures to inundation by debris of a given depth. While (1) applies to both the probability and APLR calculation, (2) and (3) only affect the calculated APLR. Determining uncertainties resulting from the estimated characteristic landslide-debris-inundation event magnitude is difficult, as this is closely tied to the characteristics of the debris travel path (from landslide sources to inundation locations). However, as we adopt a conservation-of-mass approach to approximately balance the production and spreading of landslide debris, the range of characteristic fluxes is reasonably tightly constrained and variation in calculated event frequency is therefore unlikely to vary by more than an order of magnitude. We test the impact of uncertainties associated with both (2) and (3) by varying the critical inundation depth between 2 m and 10 m, allowing for uncertainties in the inundation depth-vulnerability function presented in Massey et al. (2019), as well as uncertainties associated with spreading and thinning of debris from larger volume landslides. The impact of this reasonably large uncertainty range on calculated APLR is just a $10^{-1.5}$× variation from the ‘most likely’ case at locations close to landslide sources (where inundation by smaller landslides is most likely) and no variation at most distal locations (where only the largest landslide volumes are able to reach). See Section A7.5 for a more detailed discussion of associated uncertainties.

Given the above assumptions and uncertainties, we have elected to adopt 'best estimates' for all input variables while adopting conservative ranges for associated uncertainties. This ensures that LDIR model results closely reflect the input datasets and assumptions described in this report while also conveying the overall level of uncertainty associated with the LDIR model inputs (see Appendix 7). We recommend that West Coast Regional Council consider appropriate precautionary reductions in acceptable hazard or risk metrics based on an evaluation of appropriate confidence intervals and reported model uncertainty (as discussed in Section 5).

APPENDIX 7 Landslide Source to Inundation Process Model Uncertainties and Sensitivity Analysis

A7.1 Sensitivity Analysis

The accuracy of this regional landslide-debris-inundation hazard and risk analysis is dependent on a range of uncertainties associated with the input datasets and model variables. In this section, we adopt likely uncertainty ranges for each variable in order to:

1. Quantify the model sensitivity to each input variable by calculating annual property loss risk (APLR) variation from mean input values.
2. Quantify the total change in APLR from that calculated from 'best estimate' inputs using statistically representative combinations of input uncertainties.

As it is impractical to quantify uncertainties in 2D across the region, we instead adopt a representative 1D topographic profile, assuming that dispersion of debris is consistent with that which may be expected on a planar hillslope. We adopt baseline 'best estimate' input variables either derived from input datasets or regionally consistent variables adopted for this study. The selected topographic profile is described by a steep (~45°), linear hill slope that occupies the first 100 m of the profile length before transitioning to a topographic profile represented by an exponential function that gradually reduces to a ~6° gradient 5000 m from the starting position. We re-calculate a profile for each iteration of the sensitivity analysis and introduce a random gradient noise, calculated based on an assumed vertical digital elevation model (DEM) precision ±50% of the horizontal resolution, in order to reproduce inherent variability in the available DEM models. The profiles are smoothed using the same landslide volume-class-based window used to prepare the DEM for Gravitational Path Process (GPP) model runs (see Section A5.3.2). An example of 1D topographic profiles calculated for each landslide-volume class is presented in Figure A7.1. We note that profiles are only calculated to the maximum extent of flow-type movements, and, as such, profiles for classes 1–5 do not extend across the full 5000 m of the 1D model.

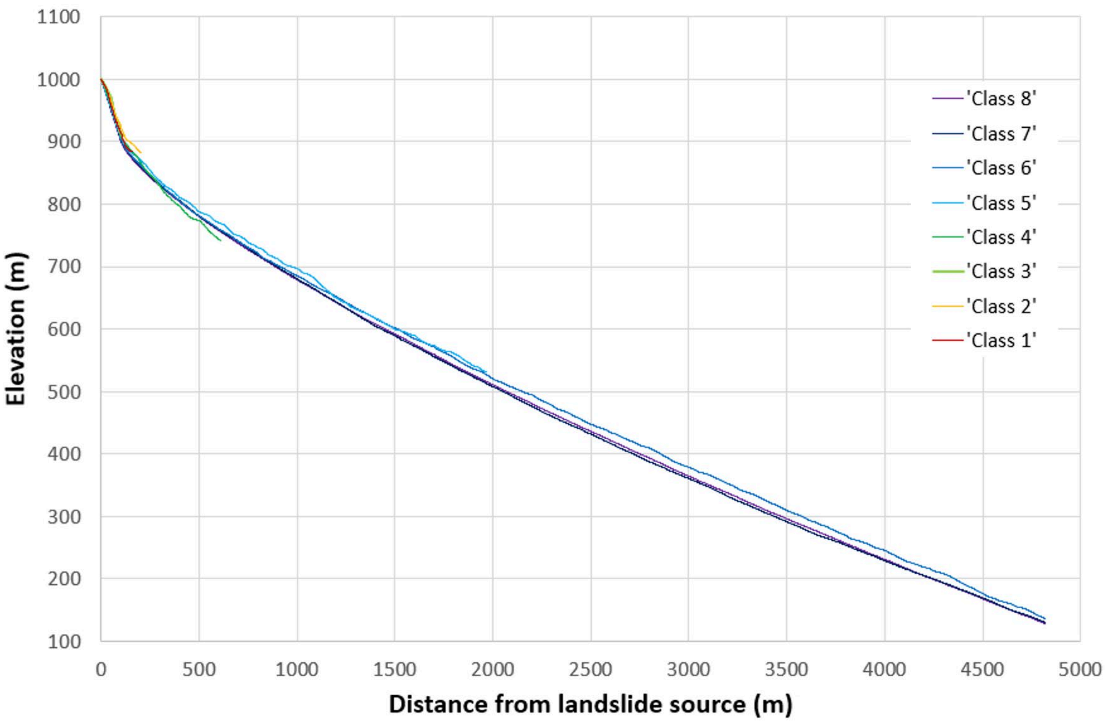

Figure A7.1 Example 1D topographic profiles employed to quantify model uncertainties. Note: the vertical scale is exaggerated for clarity.

In order to quantify model uncertainties, we implemented all equations of the landslide source-susceptibility (LSS) and landslide sediment production (LSP) models for a single landslide-source grid cell in a Microsoft Excel spreadsheet. We then incorporated equations for the fahrböschung and PCM models and calculated the resulting runout for debris derived from the source cell. For the APLR calculation, we assume that the material flux passing a given location is equal to the source volume, as long as that location is within the calculated runout extent. All equations for the APLR model were then implemented in the Microsoft Excel spreadsheet in order to calculate the landslide-debris-inundation risk at fixed locations down-slope of the source cell. Depending on the nature of the input variables, we describe uncertainties as either a mean and standard deviation or as a linear range between maximum and minimum credible limits. The variables tested, along with assumed mean values, standard deviations (for normally-distributed data) and ranges (for linear distributions), are listed in Table A7.1.

Table A7.1 List of variables, assumed baseline values and ranges employed in the sensitivity calculation. Standard deviation / error values are only valid for normally distributed and standard factorial error (SFE) data, while ranges are only valid for linearly distributed data. Variable names contain a prefix denoting the model component that these relate to (LSS, LSP, LSD, LDIR). ARI = annual return interval; RIL = rainfall-induced landslide; EIL = earthquake-induced landslide.

ID	Variable	Description	Mean	Standard Deviation/ Error	Range	Distribution
1	LSS_Pril50	50-year ARI RIL probability (ls_cell/cell/event)	0.000265	6.80E-05	N/A	Normal
2	LSS_Pril100	100-year ARI RIL probability (ls_cell/cell/event)	0.000308	6.80E-05	N/A	Normal
3	LSS_Pril250	250-year ARI RIL probability (ls_cell/cell/event)	0.000375	6.80E-05	N/A	Normal
4	LSS_Peil100	100-year ARI EIL probability (ls_cell/cell/event)	0.00526	6.80E-04	N/A	Normal
5	LSS_Peil250	250-year ARI EIL probability (ls_cell/cell/event)	0.00574	6.80E-04	N/A	Normal
6	LSS_Peil500	500-year ARI EIL probability (ls_cell/cell/event)	0.00624	6.80E-04	N/A	Normal
7	LSS_Peil1000	1000-year ARI EIL probability (ls_cell/cell/event)	0.00692	6.80E-04	N/A	Normal
8	LSP_SEDssy	Suspended sediment yield (kg/m^2/yr)	2	1.8	N/A	SFE
9	LSP_SEDs2t	Suspended to total sediment-yield multiplier (1)	1.5	0.5	N/A	Normal
10	LSP_SEDrho	Bedrock density (kg/m^3)	2650	250	N/A	Normal
11	LSP_SEDnL	Sediment-bulking factor (1)	1.3	0.2	N/A	Normal
12	LSP_SEDw	Proportion of total erosion attributed to landslides (%)	0.6	N/A	0.2–1	Linear
13	LSP_SEDcohesion	Cohesion of critical joints [$\log_{10}$(kN/m^2)]	2	2	N/A	Normal
14	LSP_RILmean	Mean RIL volume [$\log_{10}$(m^3)]	3.92	1	N/A	Normal

ID	Variable	Description	Mean	Standard Deviation/ Error	Range	Distribution
15	LSP_RILstdev	EIL volume standard deviation [$\log_{10}(m^3)$]	0.68	0.5	N/A	Normal
16	LSP_EILmean	Mean EIL volume [$\log_{10}(m^3)$]	4.55	1	N/A	Normal
17	LSP_EILstdev	EIL volume standard deviation [$\log_{10}(m^3)$]	0.68	0.5	N/A	Normal
18	LSD_res	Grid-cell resolution (m)	16.5	N/A	8–25	Linear
19	XSTgradient	Angle of assumed basal failure plane (°)	20	N/A	15–25	Linear
20	LSD_PCMmu	Initial basal friction for PCM model (°)	5	2	N/A	Normal
21	LSD_PCMmd	Mass-to-drag ratio for PCM model [$\log_{10}(1)$]	1.74	N/A	1.3–2.18	Linear
22	LSD_PCMmuExp	Basal friction area scaling exponent for PCM model (1)	-0.24	0.02	N/A	Normal
23	LSD_PCMmuMin	Minimum basal friction for PCM model (H/V)	-0.75	N/A	-1.4 to -0.097	Linear
24	LSD_PCMmuMax	Maximum basal friction for PCM model (H/V)	-0.75	N/A	-1.4 to -0.097	Linear
25	LSD_GPPpersistence	Persistence factor for PCM model	2	N/A	1–3	Linear
26	LSD_GPPspreading	Spreading factor for PCM model	1.75	N/A	1.5–2	Linear
27	LSD_FAHRpercentile	Fahrböschung angle percentile (%)	50	N/A	5–95	Linear
28	LSD_ProbFlow	Proportion of flow-type movements (1)	0.33	0.3	N/A	Normal
29	LDIR_CritFlux	Debris flux at maximum vulnerability [$\log_{10}(m^3/m^2)$]	6	N/A	2–10	Linear

We quantified relative sensitivities to each variable by setting all model inputs to mean values (note: although the ‘mean’ value often represents the ‘best estimate’, it may differ in some cases; for example, where the best estimate does not represent the mid-point of the range) and varying the selected variable across the credible range. Total uncertainty was quantified by setting all model inputs to ‘best estimate’ values and employing statistical models to evaluate the full range of potential input combinations. For both approaches, we determined the change in APLR as a proportion of the baseline APLR value (either the ‘mean’ or ‘best estimate’, depending on the approach) at five positions down-slope of the source (100 m, 150 m, 300 m, 600 m and 1200 m).

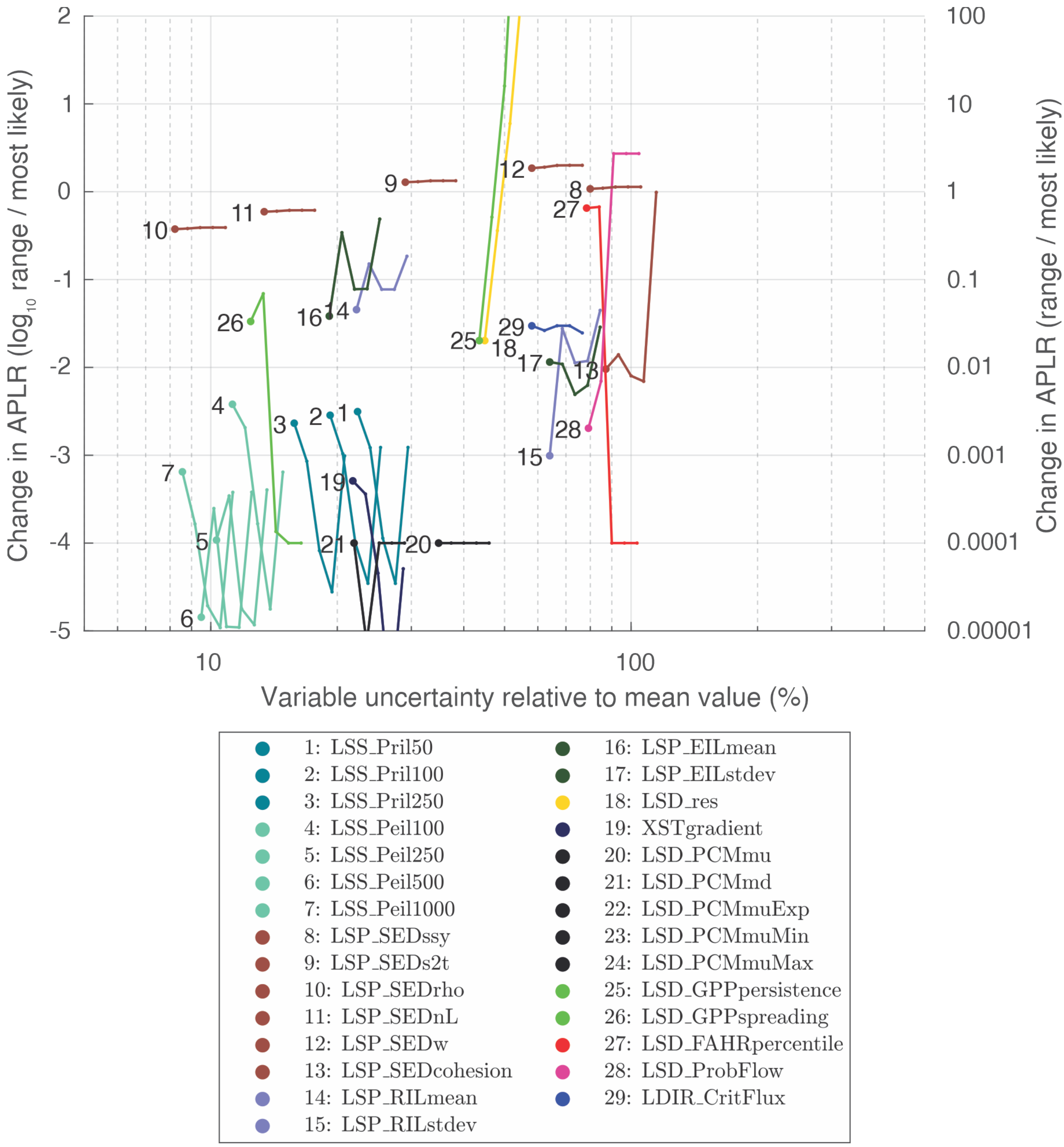

Figure A7.2 Landslide Source to Inundation Process Model sensitivity to uncertainties in model variables. Numbered points correspond to descriptions in the legend. Uncertainties associated with variables 20–24 have no impact on calculated risk at the sample locations and therefore are not plotted here. We note that both cohesion (*c*) (13) and the mass-to-drag ratio of the PCM model (21) are varied on a log scale so that a 100% uncertainty represents an order-of-magnitude increase or decrease in the variable value.

The sensitivity of the calculated APLR to uncertainties in each of 29 key input variables is presented in Figure A7.2. The point and corresponding 'tail' of each trace represents the change in risk at five set distances down-slope of the landslide-source location (100 m, 150 m, 300 m, 600 m and 1200 m). The point marks the change in APLR at 100 m, while the tail marks progressively greater distances from the source. Tails are centred horizontally about the normalised variable uncertainty and offset from left to right to aid visibility.

Traces in the lower left of the plot are associated with both lower relative uncertainties and lower impact on the calculated APLR than those in the upper right (i.e. lower model sensitivity). A general lower-left to upper-right trend indicates increasing model sensitivity to variables with greater uncertainties. For example, the uncertainty on the mean earthquake-induced landslide probabilities (parameters 4–7 in Figure A7.2) is relatively low (approximately ±10% of the mean value) and the resulting impact on the calculated APLR is between 10^{-5}× and $10^{-3.1}$× the most likely APLR value, depending on the proximity to the source. In contrast, the LSP specific-sediment-yield variable (parameter 8 in Figure A7.2) exhibits a high uncertainty, with a standard deviation (1.8) that is approximately 90% of its mean (2), resulting in a variability in the APLR approximately $10^{0.1}$× the calculated 'most likely' solution.

A7.2 Landslide Source-Susceptibility Model Uncertainties

Uncertainties associated with the LSS model inputs are relatively tightly constrained, with a <10% variable uncertainty for earthquake-induced landslide susceptibilities (4–7 in Figure A7.2) and <20% uncertainty tested for rainfall-induced landslide susceptibilities (1–3 in Figure A7.2). These uncertainties result in a ~$10^{-2.5}$× variation from the most likely APLR for most cases; again, with greatest variability associated with more distal locations. Although the earthquake- and rainfall-induced landslide susceptibilities do not affect the total volume of debris generated at a given location, these indirectly impact the APLR by determining the proportion of sediment that is attributed to rainfall- (smaller, less mobile) and earthquake-induced (larger, more mobile) landslides.

A7.3 Landslide Sediment-Production Model Uncertainties

Uncertainties associated with the LSP model inputs (parameters 8–17 in Figure A7.2) lead to the greatest changes in APLR, typically between 10^{-2}× and $10^{0.3}$× of the 'most likely' solution. In particular, we observe an almost 1:1 relationship between variable uncertainty and change in risk for those variables that determine the rate of landslide-debris production (parameters 8–11 in Figure A7.2), with little difference between each sample location. This reflects the first-order control that landslide-debris availability plays in determining risk to down-slope structures and also highlights the importance of refining estimates of present-day landslide sediment-production rates for local or site-specific APLR assessments. The regional-scale datasets adopted in this study should not be considered appropriate for local or site-specific assessments, and failure to recognise localised sources of more rapid debris-generation may, for example, lead to a proportional under-estimation of local APLR. In particular, areas of active erosion (e.g. by fluvial and coastal processes), ongoing slope instability (e.g. creeping or deep-seated landsliding), short-term increases in susceptibility (e.g. due to vegetation loss) and recent anthropogenic modification (e.g. quarries and road cuts) are likely to demonstrate rates of landslide-sediment production several orders of magnitude greater than the assumed regional erosion rates employed in this assessment. These locations can be expected to locally present APLR several orders of magnitude greater than those presented here.

Uncertainties related to DEM resolution and the cohesion of weak joints in the rock mass (c) (parameter 13 in Figure A7.2) affect the landslide area-volume scaling terms in Equations A4.3 and A4.4 and, by proxy, the maximum relief required to support larger landslide-volume classes (Equation A4.5).

Selecting a higher cohesive strength affects landslide-debris-inundation modelling in two opposing ways:

- It increases the theoretical mean depth associated with each landslide volume-class range (Equation A4.3).
- It increases potential failure volumes by steepening the gradient of scarps within hypothetical landslide sources (Equation A4.5).

While these two effects might initially appear to offset each other, the net impact of increasing cohesive strength is a reduction in the proportion of the landscape capable of supporting larger landslides. This occurs because, while the theoretical mean depth of landslide volume-class ranges is unrestricted, the actual depth achievable is constrained by available excess topography.

As a result, a higher cohesive strength increases the proportion (and frequency) of smaller, lower-volume landslides with shorter runout distances. In practical terms, this means:

- Landslide risk increases in areas with high excess topography, where smaller landslides become more frequent.
- Risk decreases at more distal locations, as fewer large, highly mobile landslides are expected.

For further details on the LSP model assumptions and uncertainties, see Section A4.8.

Although the runout distance of given avalanche-type volume classes is dependent on a number of LSD model variables, the relative change in avalanche mobility between volume classes is greater than the uncertainty associated with a single volume class, and the terms determining whether or not a given volume class is feasible at a given location can therefore dominate the variation in APLR. We test a range of cohesion values spanning four orders of magnitude (encompassing all likely conditions from weak soil to intact strong rock). This leads to a variation in APLR of just 10^{-2}× at locations close to the source and 10^{0}× at the farthest location, where a larger-volume ‘avalanche’ failure is able to inundate the position with the lowest cohesion value.

The landslide volume-class distributions for earthquake- and rainfall-induced triggers are determined by two parameters describing the geometric mean and standard deviation of each dataset (parameters 14–17 in Figure A7.2). We test a 0.2× uncertainty in the geometric mean of each volume-class range and 0.75× uncertainty in the standard deviation of each range. We observe a $10^{-1.4}$× to $10^{-0.3}$× change in the most likely APLR as a result of uncertainties in the geometric means of each trigger and 10^{-3}× to $10^{-0.4}$× change in the most likely APLR as a result of standard-deviation uncertainties. As landslide mobility scales non-linearly with volume, the impact of uncertainties in parameters describing earthquake-induced landslide-volume distributions (with a larger geometric-mean volume) are slightly larger than the rainfall-induced landslide uncertainties at equivalent down-slope distances.

A7.4 Landslide Sediment-Distribution Model Uncertainties

With little local data to directly constrain the GPP model-input parameters, we allow the majority of variables to vary by 50%. In general, uncertainties on the PCM model inputs (parameters 20–24 in Figure A7.2) have little to no impact on APLR for all sampled positions. This reflects the strong control of the sliding-friction coefficient on runout, as, once the local slope reduces below the specified limit, the modelled velocity rapidly reduces to zero. As slope gradient varies little between the sample locations in our idealised 1D profile, the calculated extent of flows also varies little for the full range of input values. Testing the full range of fahrböschung angle (parameter 27 in Figure A7.2) uncertainties (5–95% probability of exceedance) leads to a change in calculated APLR of up to $10^{-1.8}$× at locations close to the landslide source, decreasing to 0% at locations beyond the extent of potential ‘avalanche’ runout. We note that, while our 1D profile represents a useful middle-ground to represent natural settings, more complex variations in real-world topography (e.g. waterfalls or cliffs) will lead to non-linear relationships between PCM inputs and runout extents, and, while useful for illustrative purposes, the specific relationships determined here are therefore not applicable to real-world settings.

In contrast to the minor impact that most PCM model inputs have on APLR, variation of the GPP persistence factor (parameter 25 in Figure A7.2) generates a large change in APLR, particularly at greater distances from the landslide source pixel ($10^{-1.6}$× to 10^{9}× the most likely value). The persistence factor determines the probability of debris travelling in the same direction as the previous cell, and a higher persistence factor leads to more debris passing directly from the source cell to inundation cell.

The particularly strong influence of this variable results from two principal sources specific to the Monte-Carlo simulation: (1) as this factor must be determined empirically, its potential range is largely unconstrained; and (b) the spreading behaviour is difficult to reproduce in our 1D model (e.g. 2D effects of debris leaving the travel path and later returning). We therefore consider the large change in APLR to at least, in part, be a numerical anomaly.

The DEM resolution employed in the LSD model (parameter 18 in Figure A7.2) also plays an important role in determining runout distances. In our 1D model, the DEM resolution affects the numerical noise in slope-gradient estimates. A lower DEM resolution smooths topography, reducing noise and therefore the probability of debris encountering conditions that will cause the material to slow to a stop in the LSD model. The runout distance of debris therefore increases with decreasing resolution (see Section A7.1). Varying the DEM resolution from 8 m to 25 m leads to a change in APLR of between $10^{-1.6}$× and 10^{6}×, with associated sensitivity increasing rapidly with increasing distance from the source. Similar to the persistence factor, this is in part a numerical anomaly, as the 1D model adopted here cannot fully capture 2D effects of variations in DEM resolution. However, we do note that the strong increase in sensitivity at greater distances can be expected in the 2D model, as APLR change in areas with no debris flux (for example) will be infinite with even the smallest increase in debris flux. Uncertainties associated with the DEM resolution are further explored in Appendix A7.6.

A7.5 Landslide Debris-Inundation-Risk Model Uncertainties

The LDIR model is affected by the LSD model resolution (parameter 18 in Figure A7.2), the LSD model spreading factor (parameter 26 in Figure A7.2) and the debris height assumed to be associated with 100% damage (parameter 29 in Figure A7.2). As both LSD model variables are discussed in the previous section, we only discuss here the relative impact of variability in the critical debris height. As mentioned in Section A6.3, the debris height is compared against the assumed inundation depth, which for this study is the mean depth of the landslide volume-class range. We vary the critical debris height between 2 m and 10 m, which effectively implies that inundation by anything larger than ‘house’-sized landslides (at the lower end), or ‘supermarket’-sized landslides (at the upper end) will result in 100% damage. Changing this variable therefore only affects the risk calculated as a result of smaller, less mobile landslides. As our 1D model indicates that all sample locations have the potential for inundation by ‘Olympic swimming pool’ (the largest volume class affected) -sized flow-type movements, the critical debris height affects the APLR at all locations. However, this effect is relatively small (approximately $10^{-1.6}$×; see Figure A7.2), as the shape of the sigmoidal function employed to describe vulnerability allows for the greatest change in damage ratio at moderate debris heights, while damage associated with the smallest and largest debris heights varies little irrespective of the critical depth.

A7.6 Total Uncertainty

A7.6.1 Parametric Uncertainties Resulting from Model Assumptions and Inputs

We employed a Monte Carlo approach to evaluate parametric uncertainties resulting from model assumptions and variability in model inputs on the calculated APLR. Combining this approach with Latin Hypercube Sampling (LHS), we undertook a thorough exploration of the input parameter space for linear, standard factorial error and normally distributed inputs.

To represent uncertainties at specific LSD model resolutions, we explored the input parameter space with the resolution fixed at 8 m, then 25 m, and compared results against the ‘most likely’ 25 m output derived from ‘best estimate’ parameters (as this provides a comparison with the outputs of this study). APLR was evaluated for each parameter combination at each of the same five down-slope positions as in the individual parameter analysis. The Monte Carlo simulation results for each location were compiled to generate an empirical cumulative distribution function (CDF), which captured the variability in APLR due to uncertainties in the input parameters at fixed model resolutions. This approach allowed for a robust assessment of APLR under a representative range of input variability.

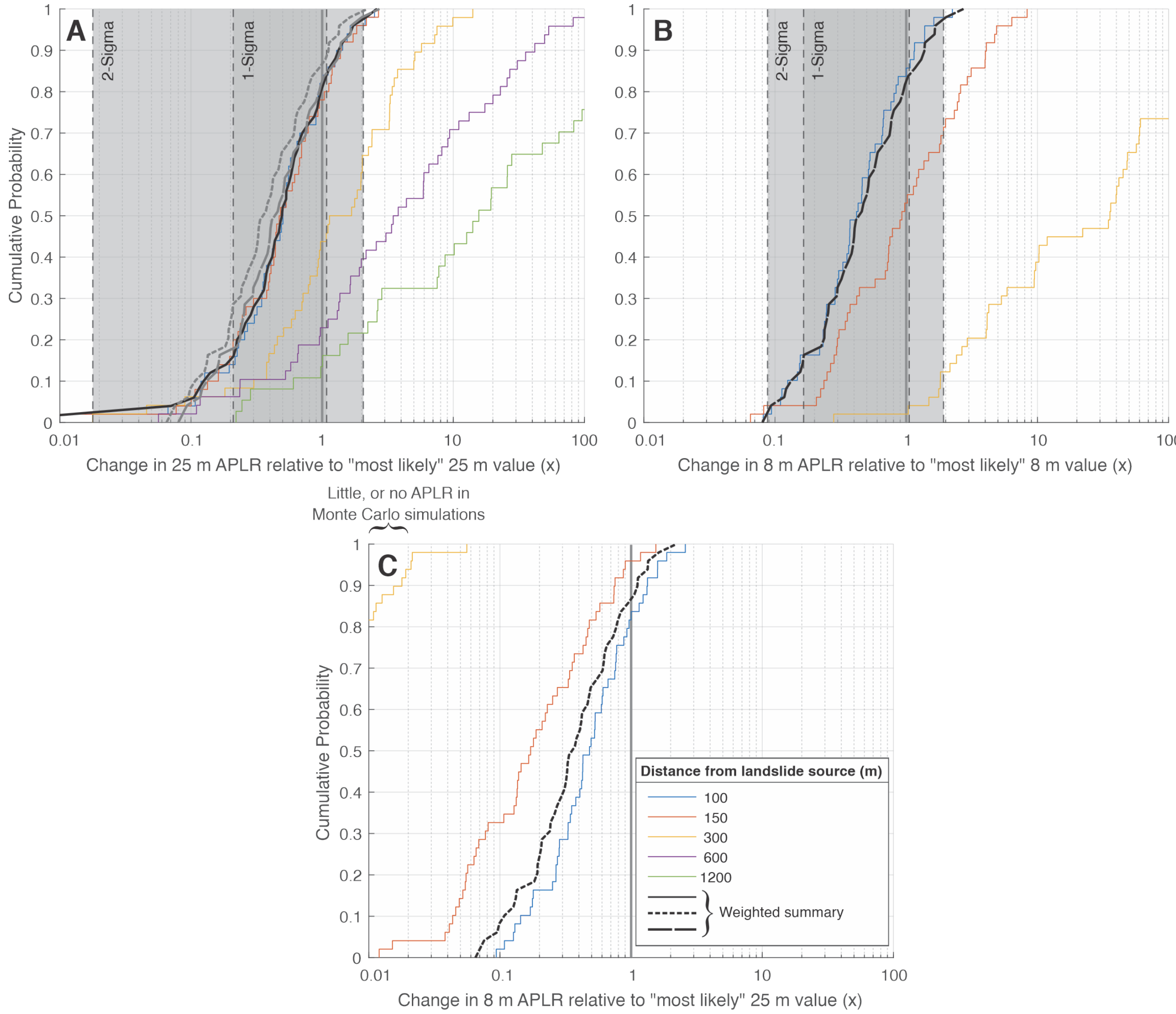

Figure A7.3 Calculated variation in annual property loss risk (APLR) as a result of Monte Carlo simulation of Landslide Source to Inundation Process Model (LS-IPM) inputs for (a) 25 m LS-IPM results with respect to the baseline 25 m model, (B) 8 m LS-IPM results with respect to the baseline 8 m model and (c) 8 m LS-IPM results with respect to the baseline 25 m model. There is no inundation at 600 m or 1200 m in the 8 m LS-IPM instances. An APLR change of 1 indicates that Monte Carlo analysis results are identical to the 'most likely' solution derived from parameters adopted in this study. Black solid and dashed curves represent weighted summaries derived from all sample locations. Grey dashed curves in (a) represent the weighted summaries presented in (b) and (c). Grey shaded regions represent 1- and 2-sigma confidence intervals.

Figure A7.3 presents results of the Monte Carlo analysis for calculated APLR at five sample points located at a range of distances from the landslide-debris source. The point at which each cumulative probability curve passes the dashed vertical line (indicating a match between the CDF and 'most likely' APLR) indicates the proportion of model configurations that return results less than the 'most likely' scenario. In order to generalise APLR uncertainties for both the 25-m- and 8-m-resolution LSD model simulations, we calculated a weighted CDF, normalising the proportional change in APLR by the baseline 25 m APLR at each of the five sample locations (100 m = 1.3 1/yr, 150 m = 7 x 10^{-1} 1/yr, 300 m = 7 x 10^{-3} 1/yr, 600 m = 3 x 10^{-6} 1/yr and 1200 m = 4 x 10^{-13} 1/yr). The generalised uncertainties are presented as heavy black curves in Figure A7.3. A statistical summary of the results is presented in Table A7.3.

Results at 25 m resolution (Figure A7.3a) can be considered an analogue for the outputs of this study. Results at 8 m resolution provide an indication of variability in APLR with respect to the ‘most likely’ baseline of the 8 m model (Figure A7.3b). This can be considered a representation of the impact of uncertainties in input variables at a higher model resolution. In order to provide an indication of the potential change in APLR when re-calculating runout on a higher-resolution DEM, we provide a comparison of results simulated for the 8-m-resolution model referenced to the 25 m model baseline (Figure A7.3c).

We find that locations closer to the landslide source (i.e. 100 m and 150 m locations) generally experience a smaller variation in APLR for both 25 m and 8 m LSD model configurations, and, aside from approximately 5% of the outputs, which indicate little to no inundation potential, all samples for these closer locations plot within an order of magnitude (i.e. between 0.1× and 10×) of the ‘most likely’ value. At farther distances (300 m, 600 m and 1200 m), the proportional variation increases significantly, suggesting a wider range of potential outcomes (Figure A7.3a, b). However, as the calculated ‘most likely’ APLR is lower at greater distances from the source, the ratio between the baseline and re-calculated values can be exaggerated, and the absolute APLR value may remain negligible, even when considering an increase of up to 1000×.

Increasing the DEM resolution from 25 m to 8 m in our 1D model results in a lower APLR at all sample locations, lowering the weighted mean APLR by approximately 2×, as can be observed by comparing the horizontal position of the weighted summaries in Figure A7.3a. This is consistent with the observed change in 2D model results for the Greymouth area, presented later in Section A7.6.2, for which we find the geometric-mean APLR reduced by 3.4× when changing from the 25 m regional DEM to the 8 m LiDAR-derived DEM. The difference between the two values can readily be explained by considering the limitations of the 1D model (described above), the specific topographic characteristics of the Greymouth area and the variation in DEM accuracy when changing from the regional DEM to the more recent LiDAR-derived model.

Although the variability in APLR at the 100 m location is very similar for both the 8 m and 25 m LSD models, APLR at both the 150 m and 300 m sample locations decreases by between 5× and more than 100× (Figure A7.3c). In fact, no debris travels to the 600 m or 1200 m sample points in any of the 8 m simulations. This reflects the cumulative impact of DEM resolution on calculated travel distance, and, in particular, the greater likelihood of smaller landslides either depositing debris or reaching a stop condition earlier on a less smooth (higher-resolution) DEM.

As APLR reduces exponentially with increasing distance from the landslide source, the generalised weighted CDF for both LSD model resolutions closely represents the 100 m and 300 m sample locations. Weighted CDFs for both the 25 m and 8 m configurations (Figure A7.3a and b, respectively) are skewed toward APLR values less than the ‘most likely’ solution, with approximately 85% of configurations returning APLR lower than the ‘most likely’ solution. In other words, there is a higher chance that our 25 m ‘most likely’ scenario over- rather than under-estimates the calculated APLR. We note that this is primarily a function of the input-parameter space and physical controls on landslide runout rather than an indication of conservatism or optimism in our selection of the ‘most likely’ scenario. In some cases, our assumed input values represent the physical upper limit of input parameters (e.g. variation in the proportion of primary erosion by landsliding can only vary below our assumed 100%) and changing parameter values can therefore only decrease APLR from the ‘most likely’ value.

Despite the skewness of the data, we find that 68% of weighted simulation results for the 25 m LSD resolution fall within ±0.35 orders of magnitude of the geometric mean, while 95% of weighted simulation results fall within ±1.0 order of magnitude of the geometric mean (Figure A7.3a). Comparing the change in the weighted 8 m LSD resolution outputs to the baseline 8 m values indicates that 68% of results fall within ±0.40 orders of magnitude of the geometric mean, while 95% of data fall within ±0.67 orders of magnitude of the geometric mean (Figure A7.3b).

Along with reducing the mean APLR with respect to lower-resolution models, running models at higher resolution reduces uncertainty at higher confidence intervals by more tightly constraining outliers in the results (e.g. by eliminating areas to which debris is not able to travel). However, without additional local data, uncertainties in the LSS, LSP, LSD and LDIR model parameters mean that the potential for more extreme variations will always remain (e.g. in association with presently active instabilities not captured in the LSP model-input data).

Table A7.2 Summary statistics for annual property loss risk (APLR) variability based on 1D Monte Carlo simulation results.

Model	Weighted Geometric Mean (x ‘most likely’ solution)	Relative Change in the Weighted Geometric Mean	Variability in APLR at 1-Sigma Confidence Interval (order of magnitude)	Variability in APLR at 2-Sigma Confidence Interval (order of magnitude)
25 m	0.5×	N/A	±0.35	±0.98
8 m	0.42×	N/A	±0.40	±0.67
8–25 m	N/A	2×	N/A	N/A

A7.6.2 Spatial Uncertainties Relating to Digital Elevation Model Accuracy and Resolution

Lower-resolution, less-accurate DEMs tend to produce smoother topography with lower-gradient hill slopes and fewer resolved ridges and channels, particularly around smaller landforms. This introduces several systemic effects:

1. Reduced identification of small landforms as potential landslide-source areas.
2. Lower estimated maximum volumes of kinematically feasible landslides.
3. Increased mobility of landslide debris.
4. Greater spread of debris across the landscape.

In order to evaluate spatial uncertainties associated with DEM accuracy and resolution, we generated two trial APLR outputs for the area around Greymouth at 25 m and 8 m resolution, using a LiDAR-derived DEM collected between 2020 and 2024 as the topographic data source (LINZ 2022). Aside from the input DEM and resolution of the LSP and LSD components of the model (as these two resolutions are tied to one another), all other inputs and parameters were unchanged from the regional study presented in this report. A comparison of theAPLR results derived from the 25 m and 8 m LiDAR-derived studies is presented alongside results of the (25 m resolution) regional analysis based on the national DEM (LINZ 2014) in Figure A7.4.

In general, results of all three studies are similar, with the two 25 m studies (Figure A7.4a, b) demonstrating a consistent range of APLR values across the region. This said, areas of particularly high APLR values in the 8 m study are less extensive than the 25 m studies, reflecting the greater channelisation of debris (i.e. fewer planar slopes supporting spreading of debris) in the better-resolved topography.

However, particularly notable is the progressive increase in the number of potential landslide-source areas resolved when comparing results derived from the regional study presented in this report to those generated from the LiDAR-derived DEM. This is apparent when comparing the extent of landslide debris sourced from hills to the southwest of Wharemoa where the national DEM does not adequately resolve the hill slopes between the plateau and coast (Figure A7.4A). As a result, the LSP and LSD components of the regional study neither generate potential landslide-source areas nor associated debris runout and APLR in areas down-slope. In contrast, the 25 m trial output derived from the LiDAR-derived DEM (Figure A7.4b) captures significant APLR in this area and is supported by a similar result from the 8 m resolution output (Figure A7.4c). In addition, the 8 m results include source areas along smaller landforms, such as the banks of the Grey River and abandoned sea cliffs southwest of Wharemoa not resolved in the 25 m models. Overall, we find that landforms with spatial scales less than 100,000 m^2 are not well represented in the regional study, and debris inundation (and associated APLR) from these smaller source areas may not be identified.

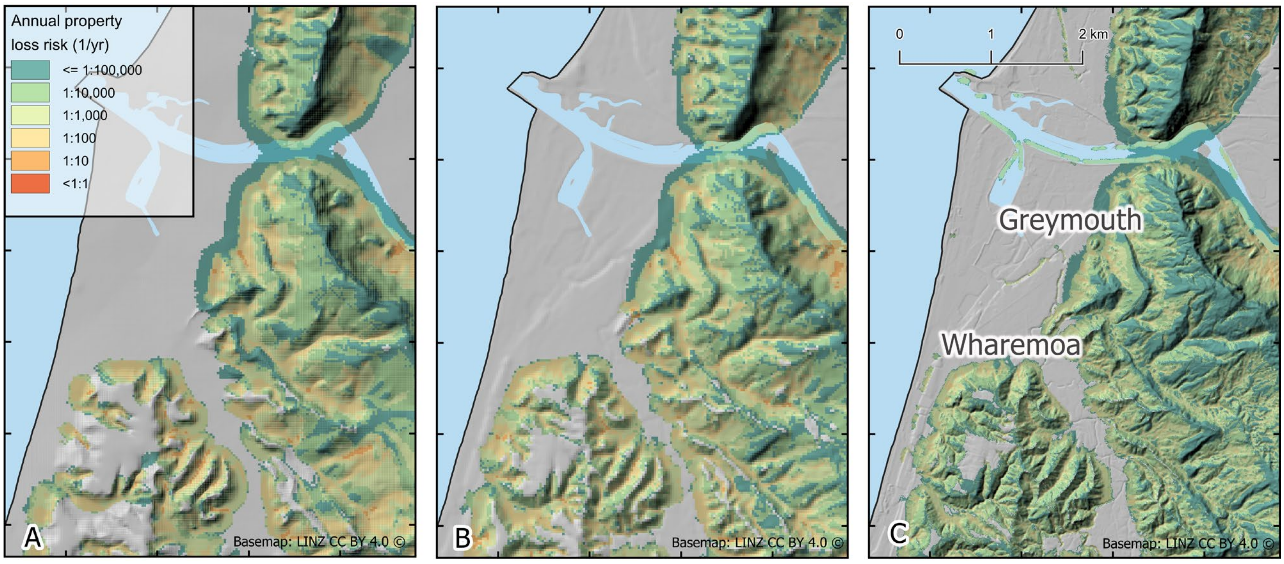

Figure A7.4 Comparison of annual property loss risk in the Greymouth region calculated on (a) the 25 m regional digital elevation model (DEM) employed in this study, (b) the 2020–2024 LiDAR-derived DEM down-sampled to 25 m resolution and (c) the 2020–2024 LiDAR-derived DEM down-sampled to 8 m resolution. The basemap for (a) is the 8 m national DEM, while the recent LiDAR-derived DEM is employed as a basemap at 25 m and 8 m resolution for (b) and (c).

A statistical analysis of the change in APLR from the LIDAR-derived results to the 25 m regional result is presented in Table A7.2 and Figure A7.5. In general, we find that the regional APLR results vary from the LiDAR-derived results in a log-normal manner, with the regional APLR being, on average, 1.1× higher than the 25-m-resolution LiDAR model and 3.4× higher than that of the 8-m-resolution LiDAR model. While the increase in average APLR is primarily a result of debris spreading more and travelling further in the LSD model (see Section A5.9), the broad-variation APLR values (represented by the wide confidence intervals) reflects both increases and decreases in APLR at various locations. This is a result of the combined impact of improved DEM accuracy (e.g. changing the trajectory of debris) and improved performance of the LSP and LSD model components (e.g. altering the stopping position of debris), as evident from the Monte Carlo simulation results presented earlier.

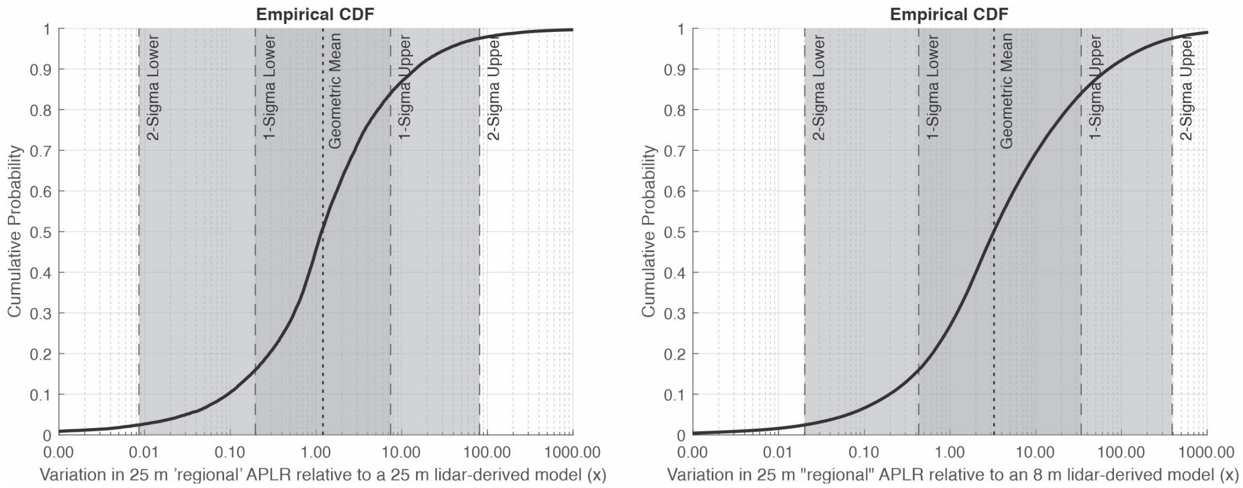

Figure A7.5 Cumulative density function demonstrating the change in predicted annual property loss risk (APLR) in the Greymouth area from LiDAR-derived results to the regional analysis presented in this study. The change in source DEM accuracy and resolution. A change in accuracy is captured in the variation from the 25 m national DEM results to 25 m LiDAR-derived results (left), while the combined effect of accuracy and resolution is captured in the change from the regional analysis results to the 8 m LiDAR-derived DEM results (right). A variation greater than 1 indicates that the regional study presented here likely over-estimates APLR values, while a variation less than 1 indicates that APLR results are higher in the LiDAR-derived models. Grey shaded regions represent 1- and 2-sigma confidence intervals.

Table A7.3 Summary statistics for change in relative annual property loss risk (APLR) in the Greymouth area, from LiDAR-derived results, to the regional analysis presented in this study. DEM = digital elevation model.

	Relative Change in the Geometric Mean	Variability in APLR at 1-Sigma Confidence Interval (order of magnitude)	Variability in APLR at 2-Sigma Confidence Interval (order of magnitude)
25 m LiDAR-Derived DEM to 25 m Regional DEM	1.1×	±0.79	±1.98
8 m LiDAR-Derived DEM to 25 m Regional DEM	3.4×	±0.94	±2.14

We find that the majority of the APLR variability is associated with the accuracy rather than resolution of the 25 m national DEM. Changing the source DEM and maintaining the nominal 25 m resolution leads to a variation in APLR of ±0.79 orders of magnitude at the 1-sigma confidence interval (see Table A7.2), reflecting a significantly more complete catalogue of potential source areas and accurate representation of morphological controls on debris runout. Increasing the resolution of the models to 8 m then only leads to an additional ±0.15 order-of-magnitude change in variability (to ±0.94 orders of magnitude). The increase in resolution causes a similar change in variability at the 2-sigma confidence interval. A qualitative inspection of results in Figure A7.4b and c indicates that, aside from the general decrease in APLR as a result of reduced landslide-debris mobility, as well as limited additional source areas on smaller landforms, the overall pattern of APLR is otherwise consistent with the 25 m LiDAR-derived model results.

A7.6.3 Combined Parametric and Spatial Uncertainties

In order to provide a combined measure of uncertainty, including parametric and spatial uncertainties, we employ the Root-Sum-of-Squares method. This is a widely accepted statistical approach for combining independent uncertainties in log-transformed space. Assuming that the uncertainties are independent and normally distributed, the total uncertainty can be defined as:

$$\sigma_{total} = \sqrt{\sigma^2{}_a + \sigma^2{}_b + \sigma^2{}_c + \cdots}$$ Equation A7.1

where $\sigma_{a,b,c\dots}$ represents the uncertainty of each contributing factor in log-space.

A7.6.3.1 Distinguishing Contributions to Spatial Uncertainties

Although the relationship between topography (including local relief and morphological complexity) and the accuracy of a DEM at various spatial resolutions is complex, we expect that the 8-m-resolution (i.e. 64 m^2 cells) LiDAR-derived DEM will adequately capture landslide debris-production and runout in this region. Further increasing the DEM resolution is likely to result in only minor improvement in APLR accuracy as:

1. The area of cells is significantly less than that of the common 'House to Olympic swimming pool' landslide-size range (geometric-mean source area of 484 m^2; see Table 2.1).
2. The LSD model includes a volume-class-based DEM smoothing step prior to simulating landslide runout (see Section A5.3.2).

We can estimate the relative contributions of DEM accuracy and resolution to the spatial APLR uncertainty by evaluating the various 2D model results for the Greymouth area. We assume that:

1. The total spatial uncertainty associated with the regional DEM accuracy and model resolution is approximately equal to its APLR variability relative to the 8 m LiDAR-derived results (e.g. ±0.94 orders of magnitude at 1-sigma; see Table A7.4).
2. Uncertainties due to the accuracy of the national DEM can be characterised by comparing APLR results from the regional study to those derived from the 25 m LiDAR-derived DEM (e.g. ±0.79 orders of magnitude at 1-sigma, see Table A7.4).
3. Uncertainties associated with the change in resolution from the regional to 8 m model can be isolated by removing the effects of DEM accuracy from the total spatial uncertainty.

Given these assumptions, we can rearrange Equation A7.1 to solve for (*c*) the unknown contribution of combined DEM and model resolution to the total spatial uncertainty. The results of this calculation are presented in Table A7.4.

A7.6.3.2 Total Uncertainty

In order to calculate the total (parametric and spatial) APLR uncertainty on the regional-study results, we combine parametric uncertainties (addressed in the 1D Monte Carlo simulation) and spatial uncertainties (due to DEM accuracy and model resolution) using Equation A7.1. The results are presented in Table A7.4 and indicate that the total estimated uncertainty for the regional LS-IPM analysis based on the national DEM is ±1.04 and ±2.45 orders of magnitude at 1 and 2-sigma, respectively. As the calculated uncertainties do not always follow a normal distribution, these should be considered 'equivalent' to standard deviations rather than directly reflecting the traditional statistical definition.

As this analysis, and those presented below, include significant assumptions, we consider it prudent to conservatively round estimated uncertainties up to the nearest 0.25 order of magnitude, or, alternatively, if a value lies within 0.10 orders of magnitude of the next 0.25 increment, it is rounded up to the next 0.5 interval. For example, a value of 0.97 is rounded up to 1.25, and a value of 1.15 is also rounded to 1.25. (see Table A7.4). This step is based on expert opinion and is intended to prevent over-interpretation of the model results and calculated uncertainties.

Isolating the contributions of DEM accuracy, as well as combined DEM and model resolution, on APLR uncertainty allows us to estimate uncertainties for additional model configurations. In particular:

- Uncertainties for a regional 25-m-resolution analysis based on a LiDAR-derived DEM can be estimated by assuming that the LiDAR-derived DEM accurately represents the ground surface such that the DEM accuracy contribution to the spatial uncertainty can be neglected. Adopting only the model resolution component of the spatial uncertainty then allows us to estimate total uncertainties associated with this configuration to be ±0.67 and ±1.45 orders of magnitude at 1- and 2-sigma, respectively (Table A7.4).
- Uncertainties for an 8-m-resolution analysis based on a LiDAR-derived DEM can be estimated by maintaining the assumption that uncertainties relating to DEM accuracy can be neglected and that uncertainties associated with the 8 m combined DEM and model resolution shall be less than those of the 25 m analysis. In this case, we estimate associated uncertainties to be approximately half those of the lower-resolution model, and, adopting parametric uncertainties relating to the 8 m model presented in Table A7.2, we estimate total uncertainties to be ±0.47 and ±0.83 orders of magnitude at 1- and 2-sigma, respectively.

Table A7.4 Calculation of total annual property loss risk (APLR) uncertainties due to combined uncertainties associated with model assumptions and parameters, DEM accuracy and the combined effects of DEM and landslide debris-inundation-risk model resolution. Uncertainties are presented for 25 m analyses based on the national and LiDAR-derived DEMs, as well as an 8 m analysis based on the LiDAR-derived DEM. Inputs denoted 'estimated' are derived based on expert judgement, as well as assumptions described in the text above.

Uncertainty	Source of Uncertainty	25 m National DEM (order of magnitude)		25 m LiDAR-Derived DEM (order of magnitude)		8 m LiDAR-Derived DEM (order of magnitude)	
		1-Sigma	2-Sigma	1-Sigma	2-Sigma	1-Sigma	2-Sigma
Parametric	Assumptions and parameters (see Section A7.6.1)	±0.35	±0.98	±0.35	±0.98	±0.40	±0.67
Spatial	DEM accuracy	±0.79	±1.98	±0 (estimated)	±0 (estimated)	±0 (estimated)	±0 (estimated)
	Combined DEM and model resolution	±0.58	±1.07	±0.58	±1.07	±0.25 (estimated)	±0.5 (estimated)
Total	Total uncertainty	±1.04	±2.45	±0.67	±1.45	±0.47	±0.83
	Recommended conservative estimate	±1.25	±2.75	±0.75	±1.75	±0.75	±1.00

A7.7 Summary of Uncertainties and Recommendations

A7.7.1 Parametric Uncertainty

Parametric APLR uncertainties associated with assumptions and inputs are estimated based on a 1D Monte Carlo simulation. Spatial uncertainties are estimated based on a 2D analysis of the national and LiDAR-derived DEMs in the area local to Greymouth. Although this analysis has not explored the full parameter space, we expect that the results provide a reasonable representation of both the relative contributions to and absolute magnitude of regional LS-IPM uncertainty.

A7.7.2 Uncertainties due to Digital Elevation Model Inaccuracies

The accuracy of the national DEM (LINZ 2014) employed in this regional analysis is likely the single greatest source of LS-IPM uncertainty. Inaccuracies in the DEM, and its failure to represent smaller landforms (particular those with spatial extents less than 100,000 m^2) can lead to a failure of the analysis to identify landslide-source areas and associated runouts, as well as errors associated with the calculation of landslide-debris mobility and travel paths. The next most significant source of uncertainty is the 25 m resolution of the source DEM and the LS-IPM analysis, which tends to lead to an over-estimation of debris spreading and mobility across the landscape. However, uncertainties associated with model assumptions and input parameters are not dissimilar to those related to resolution at both the 1- and 2-sigma confidence intervals. Of these uncertainties, the greatest contributors to variation in APLR are those that determine the rate of landslide debris production (e.g. the erosion rate and proportion of primary erosion by landslide processes) and empirical GPP model parameters with little constraint on potential ranges (e.g. the persistence factor). Overall, uncertainties are spatially variable and generally increase with increasing distance from landslide-source areas as inaccuracies in the DEM and uncertainties relating to landslide debris mobility are compounded. With the adoption of a LiDAR-derived DEM for the study region, as well as reduction of the resolution of the input DEM and LS-IPM calculation to 8 m or less, we expect model assumptions and parameters to become the largest single source of residual uncertainty.

A7.7.3 Uncertainties due to Digital Elevation Model and Model Resolution

It is more likely that LS-IPM results from this regional analysis over- rather than under-estimate APLR across the study area. This is in part because our selection of ‘best estimate’ input parameters is naturally biased toward higher debris-production rates and greater landslide-debris mobility, as some parameters (such as the proportion of primary erosion by landslides) have an upper limit at, or close to, the adopted value. For the 25 m analysis, our ‘most likely’ solution is approximately 2× the weighted geometric mean derived from the 1D Monte Carlo simulation. Adopting a lower-resolution DEM and LP-ISM analysis tends to lead to greater landslide mobility, as the smoother DEM tends cause debris to travel further and spread more across the landscape. From our 2D models, we find that the geometric mean APLR for the 25 m regional analysis is approximately 3.4× that of the same model on the 8 m LiDAR-derived DEM, while the 1D Monte Carlo simulation similarly indicates that the geometric-mean-weighted APLR for the 25 m resolution model resolution will be approximately 2× that of the 8 m resolution model. Finally, we investigate the effect of DEM accuracy by comparing the 25 m 2D model results for the national and LiDAR-derived DEMs in the Greymouth area. This indicates that the geometric-mean APLR derived from the national DEM is approximately 1.1× that of the identical model based on a LiDAR-derived DEM. We note that this over-estimation relates to geometric-mean APLR result, and includes significant increases in APLR at some locations, as well as significant decreases in APLR in others.

A7.7.4 Present-Day Model Uncertainties

For the present-day 25 m regional LS-IPM analysis presented here, we recommend adopting an uncertainty of ±1.25 orders of magnitude to represent the 1-sigma confidence interval (~68% of results) and ±2.75 orders of magnitude to represent the 2-sigma confidence interval (~95% of results). If a LiDAR-derived DEM is used to represent topography, these uncertainties can be reduced to ±0.75 and ±1.75 orders of magnitude, respectively. Increasing the resolution of the DEM and LS-IPM analysis to 8 m and employing a LiDAR-derived DEM for the analysis is estimated to further reduce the APLR uncertainty to ±0.75 and ±1.00 orders of magnitude at 1- and 2-sigma confidence intervals, respectively. This is described in Table A7.4.

A7.7.5 RCP6 2021–2100 Model Uncertainties

For the RCP6 2081–2100 climate scenario, we recommend adopting a representative 1-sigma uncertainty of ±2.75 orders of magnitude (i.e. the present-day uncertainty at the 2-sigma confidence interval). A lack of constraint on the extreme limits of key input variables does not allow us to provide an RCP6 2081–2100 climate-scenario uncertainty recommendation at the 2-sigma confidence level. For further details of unconstrained variables, see Section 2.3.1.6. For a discussion on recommended uncertainties, see Section 5.3.2.

A7.7.6 Reducing Uncertainties

Reducing uncertainties associated with model assumptions and input parameters will require the employment of new methodologies, or datasets, to constrain key input variables; in particular, those toward the upper right of Figure A7.2. This may include the consideration of sediment-production rates at local scales, employing geological or historical datasets, the probability of avalanche versus flow movement modes by re-analysing existing landslide catalogues, local fahrböschung distributions for rainfall- and earthquake-induced landslides and allowing for depth-dependent and/or material-specific cohesion values.

APPENDIX 8 Alignment with Australian Geomechanics Society Landslide Risk Management Guidelines

A8.1 Introduction

This section presents the steps taken in this basic quantitative regional hazard and risk analysis in terms of the good practise outlined in the Australian Geomechanics Society's Landslide Risk Management Guidelines (AGS 2007).

Using Figure 1 of AGS (2007), this study applies a new methodology to the 'Hazard Analysis' phase of the landslide risk management framework. As in conventional studies, we combine desk- and field-based data on geomorphology, geology, groundwater and slope stability to build a geotechnical model of potential landslide sources.

Traditional event-based approaches then estimate hazard magnitude and frequency from landslide inventories and use empirical or physically based models to predict runout from discrete sources.

In contrast, this study adopts a process-based approach designed for regional-scale application. Instead of modelling a finite set of events, we account for debris production and movement from all feasible sources across the landscape. Hazard is expressed in terms of debris flux (volume per unit area per year) and probability of inundation, providing a spatially comprehensive assessment without the requirement to consider discrete landslide footprints.

Here, hazard magnitude and frequency are defined by debris-production rates, informed by geomorphic-process rates (e.g. tectonic uplift, erosion), landslide inventories and the geotechnical landslide-source model. Spatial impact is calculated with empirical and physically based debris-transport models, using conventional approaches to derive model inputs from international datasets and landslide behaviours in the study area. We employ a deterministic model of characteristic landslide debris flux to convert the spatial hazard output to a magnitude-frequency relationship for landslide-debris inundation, supporting consequence analysis and completing the 'Risk Analysis' phase of the AGS (2007) framework.

The 'Consequence Analysis' considers the vulnerability of buildings to debris inundation, using depth-dependent damage ratios to estimate APLR. Buildings are treated as permanent elements at risk, and inundation depth is used to quantify the likelihood of economic loss.

More specific detail on how this new approach aligns with, deviates from or does not use the steps outlined in AGS (2007) is provided in the sections below.

A8.2 Hazard Analysis

A8.2.1 Data Gathering / Desk Study

1. **Assemble relevant data and record their sources.**

   Data employed in this study are summarised in Appendix 1.

A8.2.2 Field Investigation Requirements

1. **Complete investigations sufficient to establish a geotechnical model, identify geomorphic processes and associated process rates.**

   The geotechnical and geomorphological models employed in this study are presented in Sections 2.2 and 2.3). The LSP model presents geotechnical and kinematic constraints on landslide debris production, while the LSS model describes spatiotemporal patterns in landslide debris production in response to a range of triggers.

2. **Inspect the site and surrounds, including field mapping of the geomorphic features.**

   Limited field mapping and geomorphological analyses undertaken in this study were undertaken to validate model outputs and refine the geotechnical model. This is detailed in Section 2.7.

3. **Determine the subsurface profile from exposures or subsurface investigation, such as by boreholes and/or test pits.**

   This element is not considered appropriate for this level of regional hazard analysis.

4. **Assess likely groundwater levels and responses to trigger rainfall events.**

   Antecedent groundwater conditions based on climatological models are considered as an input to the LSS model; see Section A3.3.

5. **Prepare a cross-section drawing (to scale) through selected parts of the site to demonstrate the geotechnical model of site conditions and on which landslides may be identified.**

   This element is not considered appropriate for this level of regional hazard analysis. However, we do calculate a kinematic source model for the whole region within the LSP model. A 3D representation of the largest potential landslide at given locations (defined by the kinematic source model) is detailed in Section A4.2.

6. **Take into account slope-forming process rates associated with the geotechnical model and landslides.**

   The landscape is considered to be in a steady state, such that slope-forming processes reflect the balance between bedrock uplift and denudation through, for example, fluvial, glacial and hillslope erosion; see Section A4.1.1. Landslides are considered to be the primary erosional processes on geomorphically active hillslopes, an observation supported by a comparison of catchment-wide uplift and erosion rates with calculated landslide debris-production rates (see Section A4.1.1). The rate of landsliding is considered to be limited by the generation of unstable sediment (regulated by the rates of relief production and rock strength degradation); see Section 2.1.2.

7. **Identify landslides types/locations appropriate to the geotechnical model based on local experience and general experience in similar circumstances.**

   The potential for landslides of a given volume class range to occur at a specific location is informed by the kinematic source model; see Section A4.2. Parameterisation of the model is based on frictional and cohesive strength properties of representative hillslope materials derived from global datasets. We justify the appropriateness of our parameter selection and discuss opportunities to employ a more detailed kinematic source model in Section A4.2. We assume that landslide debris production at a location is the result of landslide volume-class ranges (encapsulating all landslide types) up to the maximum volume determined from the kinematic source model; see Section A4.4.

8. **If required, further detailed investigations should be completed to better define the model, landslides, triggers, frequency (likelihood) or design of stabilisation measures to control the risk.**

   This element is not considered appropriate for this level of regional hazard analysis.

A8.3 Landslide Characterisation

1. **Characterise the landslides based on the desk study and field investigations.**

   The probable landslide volume characteristics for rainfall and earthquake triggers are informed by regional landslide catalogues and comparison with international datasets; see Section A4.3.

The probability of landslides moving as slides or flows in response to potential triggers is based on experience from previous landslide events both elsewhere in New Zealand and globally; see Section A5.2.

A8.4 Frequency Analysis

A8.4.1 Techniques for Frequency Analysis

1. Adopt a frequency-analysis technique appropriate to the level of study and complexity of the geotechnical model and slope-forming process.

As we employ a process-based, rather than event-based, methodology, the explicit determination of landslide initiation frequency is not used. Instead, the method presented here requires quantification of the rate of landslide-debris production per unit area (i.e. $m^3/m^2/yr$); see Section A4.5. This is numerically equivalent to the frequency of landslide initiation events, where each event has a known debris-production volume per unit area (i.e. 1/yr x m^3/m^2). However, the intrinsic relationship between the landslide debris-production rate and slope-forming processes, as well as the lack of a requirement to evaluate individual landslide frequencies, has significant numerical advantages over event-based approaches. This is particularly true for the scale and geotechnical complexity of the regional hazard analysis presented here. See Section 2.1 for further details.

2. Gather local and historical knowledge of slope performance and landslide characteristics and occurrence. The resulting inventory enables assessment of frequency.

We measure ‘slope performance’ through a combination of landslide susceptibility and sediment-production rates. The LSS model is trained on catalogues of previous landslide events; see Section A3.1. Landslide sediment-production rates are compared against both local basin-averaged erosion rates and denudation rates from mapped landslides in Section A4.1.1.

3. Empirical methods based on slope-instability ranking systems.

These methods are not employed in this study, as the LSS and LSP models provide the required metrics.

4. Relationship to geomorphology and geology.

The LSS and LSD models allow the probability of a volume of landslide debris being produced at a given location to be tied to geological and geomorphological attributes; see Sections 2.2 and 2.3. Assumptions required to project these slope-performance indicators into a future climate scenario, as well as possible sources of error, are discussed in Sections A3.5 and A4.7.

5. Prepare a statistical evaluation of rainfall and relate to history of landsliding and population of slopes within area of similar slope type.

The RIL and EIL components of the LSS model allow a correlation between the magnitude of landslide-triggering events (24-hour precipitation, or PGA) and the probability of slope failure; see Section 2.2.

6. Consider use of simulation models and Monte Carlo sampling analyses to derive a frequency of failure.

These methods are not employed in this study, as the LSS and LSP models provide the required metrics.

7. Use a knowledge-based expert judgment or ‘degree of belief’ method that combines experience, expertise and general principles.

A ‘degree of belief’ approach is employed to convert specific sediment yield to landslide sediment-production rates. This is based on general geomorphological principles and is appropriate for regional studies where objective data are lacking. Constraints on model variables are derived from regional and global datasets; see Section 2.1.

8. Other methods.

The mean annual rate of landslide-debris production (or alternatively, frequency of landslides of a given size occurring) at a given location in response to any trigger is determined as a function of slope-forming processes; in particular, the landslide sediment-production rate, the relative annual probability of rainfall- and earthquake-triggered landslides and the volume characteristics of landslides associated with either trigger; see Section A4.5. The probable volume of debris produced at a given location in response to a given event is determined by comparing the probability of failure in the given event to the mean annual probability calculated for that location; see Section A4.6.

A8.4.2 Estimation of Annual Probability (Frequency) of Each Landslide

1. Use 'best estimates' for frequency but consider range, uncertainty and sensitivity.

As stated in Section A8.3 (1), the process-based approach adopted here does not require an evaluation of the frequency of initiation of individual landslides. Instead, we employ a related metric that describes the rate of debris production by feasible landslides at a given location. 'Best estimates' of contributing parameters are derived from regional and global datasets. Various scenarios are tested through a Monte Carlo analysis of variables contributing to the geological model (e.g. the sediment production rate, the proportion of sediment contributing to landslides and the suspended load to total sediment yield multiplier). See Sections A4.1 and A7.3 for further details.

2. Estimates of frequency may be derived by partitioning the problem to *(Annual probability of trigger event) x (Probability of sliding given the trigger event)* over the range of trigger events.

The rate of debris production is estimated by partitioning the mean annual rate of debris production by kinematically feasible volume-class ranges and the relative probability of triggering events; see Section A4.5.

3. Complete a review of the assessed frequency in relation to the implied cumulative frequency of the event occurring within the design life and known performance within the area.

An example of the proportion of landslide debris generated by various landslide volume-class ranges in response to both rainfall and earthquake triggers and all considered return intervals is presented in Section 2.3.1.4. We discuss the consistency between the modelled and theoretical distribution of debris production by various triggers and landslide volume ranges in the same section.

A8.4.3 Assess the Travel Distance and Probability of Spatial Impact of the Elements at Risk

The LSD model is employed to assess the volume of debris travelling from kinematically feasible landslide-source areas downslope through the landscape (landslide-debris flux). The model employs a combination of empirical and physically-based methods and accounts for slope characteristics, the mechanism of debris movement and characteristics of the downhill path. See Section 2.4 for an introduction to the LSD model. A sensitivity analysis of parametric and spatial uncertainties is presented in Sections A7.4 and A7.6.

The LDIR model is employed to convert the calculated landslide-debris flux (from the LSD model) to a probability of spatial impact. See Sections 2.5 and 2.1.3 for a brief overview.

We note that the metric from which we calculate the probability of spatial impact differs slightly from that described in AGS (2007), which states that it is important to estimate the movement of a 'slide mass' (commonly accepted to be the total volume of landslide debris) downslope by landslide processes. Instead, we consider the movement of a unit volume of landslide debris from portions of a potential landslide-source area. The specific volume of debris is determined using a probabilistic model (see Section A5.1). Although physically related quantities (the probability of a landslide occurring in an area can be considered unity where the sum of landslide-debris production equals the volume of a representative 'slide mass'), there are significant differences in the manner in which the probability of spatial impact needs to be calculated from these two metrics.

Determining the probability of spatial impact from the metric specified in AGS (2007) requires the consideration of (1) the probability of a given failure occurring and (2) the probability of the slide mass travelling to a specific location. In the simplest case, a location can be considered as being impacted by a 'slide mass' when any portion of the calculated movement overlaps with that location. Although not explicitly specified in AGS (2007), determining the probability of impact has typically involved the calculation of landslide movement either from discrete sources or a discrete-source region and subsequent mapping of spatial impacts back to the combined probability of a range of failure and transport scenarios. While calculating the probability of impact from discrete sources provides the best possible representation of spatial impact probabilities, it is computationally infeasible to calculate all possible landslide types from all possible sources in regional studies. However, reducing the range of discrete sources employed in inundation calculations to computationally feasible numbers can significantly degrade the spatial accuracy of the resulting impact probability assessment. The consideration of discrete-source regions, on the other hand, allows a complete consideration of the probability of 'slide masses' initiating within a region, as well as empirical estimates of inundation extents. However, this provides little to no insight into the probability of spatial impact within the calculated extent of inundation.

In the process-based model presented here, the probability of failure is encoded into the unit volume of debris released from all valid sources distributed across a hillslope. Rather than mapping discrete movement paths back to the probability of a given failure occurring, we can therefore calculate the probability of spatial impact by directly comparing the volume of debris passing a location (the 'landslide-debris flux') to a 'characteristic landslide-debris flux' expected if a landslide of a given size were to inundate that location. When the mean annual, or scenario-based, landslide-debris flux equals the characteristic flux at a location, the probability of a landslide inundating that location is considered to be unity. By pre-calculating the characteristic landslide-debris flux for all landslide-volume classes at all locations across a region, and tying this to the physically based calculation of probabilistic landslide-debris transport from all possible source cells, we are able to shortcut the requirement to explicitly tie inundation to discrete landslide sources and provide a reasonable representation of inundation probability at full resolution, while cutting computational cost by several orders of magnitude. Uncertainties relating to the calculation methodology are presented in Section A7.5.

We note that the specification of a method to assess the travel distance and calculate spatial probability of inundation is outside of the scope of AGS (2007). As such, the method presented here only deviates from the guidelines in its adoption of a unit debris volume, rather than the 'slide mass', as the metric from which the probability of spatial impact is calculated.

A8.5 Consequence Analysis

A8.5.1 Elements at Risk

We consider undifferentiated buildings to be the elements at risk; see Section 2.1.3 for a brief overview.

A8.5.2 Temporal Spatial Probability

We consider buildings to be permanently located, therefore the temporal spatial probability can be neglected.

A8.5.3 Evaluation of Consequence to Property

We assume that the height of landslide debris is equal to the mean depth of the representative landslide source; see Section A6.3. This allows us to adopt a vulnerability function to relate the height of landslide debris (i.e. the extent of damage likely to property arising from each potential landslide) to a 'damage ratio', describing the ratio of the indicative cost of the damage to the estimated market value (see Section A6.3).

A8.5.4 Evaluation of Consequence to Persons

Consequence to persons is beyond the scope of this study.

A8.6 Risk Estimation

A8.6.1 Quantitative Risk Estimation

In order to calculate APLR, we evaluate the product of the probability of total economic damage from all landslides for every assessed trigger type and return interval. This is described in Sections 2.5 and A6.4.

A8.6.2 Semi-Quantitative and Qualitative Risk Estimation for Risk to Property

As we undertake a quantitative risk estimation, this step is not required.

A8.6.3 Risk Matrix for Property Loss

This is beyond the scope of the current study.

A8.6.4 Estimation of Risk of Loss of Life

This is beyond the scope of the current study.

APPENDIX 9 External Review and Responses

On 12 November 2024, GNS Science (now part of Earth Sciences New Zealand as of 1 July 2025), engaged Manaaki Whenua – Landcare Research (now part of the Bioeconomy Science Institute) to undertake peer-review of this GNS Science consultancy report (CR2025/28) written for the West Coast Civil Defence & Emergency Management Group (now West Coast Emergency Management). Deliverables from the review included a brief written statement outlining an assessment of methods, quality of analysis and robustness of key findings, as well as any suggestions for improvement in these aspects or improvements in report clarity. Feedback on document formatting, spelling and style were not required. In addition, two one-hour meetings were held online to discuss any issues identified in the report that required further discussion. The review and all related documentation were delivered to GNS Science on 17 January 2025.

The brief written statement (italics) and responses from Earth Sciences New Zealand (in blue) are as follows:

17 January 2025

INSTITUTE OF GEOLOGICAL AND NUCLEAR SCIENCES LIMITED, 1 Fairway Drive, Avalon, Lower Hutt, New Zealand (GNS SCIENCE)

Dear Kerry Leith,

This letter serves as project deliverable for the peer-review of a GNS Science consultancy report titled 'WCCDEM regional landslide debris inundation assessment' written for the West Coast CDEM group. As commissioned by GNS, this letter and the accompanying commented report, give "a brief written statement outlining an assessment of methods, quality of analysis, and robustness of key findings, and any suggestions for improvement in these aspects or improvements in report clarity."

The aim of the WCCDEM regional landslide debris inundation assessment report is to produce a regionally consistent estimate of landslide debris inundation risk. The level of suitability is 'screening or basic'. The methodology does not nor claim to assess local landslide susceptibility. Also, it does not model initiation or flow paths from individual events. Rather the model applies a probabilistic approach over a long timescale to approach regionally consistent coverage. We think the authors did a tremendous job in developing their methodology and we support the basic principles of the approach. Given the available data and the large extent of the West Coast region, the approach is sensible.

As with all modelling, but especially here with data limitations, the authors are required to make simplifications and assumptions. These should be chosen consciously in such a way that results still reflect reality and/or reliably answer research objectives. Transparent communication is important. We think in general the authors do a good job of this communication by summarizing uncertainty under each module chapter. In certain sections of the methodology, we urge the authors to provide more clarity. These are mostly related to the validity of the probabilistic approach. We listed our points in the corresponding subsections below. This is prefaced by general points that we'd like to raise attention to and is followed by general miscellaneous comments.

General Points

We have three key observations. (1) The assessment assumes all sediment transport happens through landslides. (2) sediment becomes available at a constant rate at each location through uplift (one for the current climate and one for RCP6, scaled by increased RIL probability as we understood it.) (3) The scenario is applied to 10,000 years to account for sufficient sediment production. These points mean that the model output depends mainly on where and at which spatial extent landslides occur. Where is treated relatively simply. The slope threshold (>20°) and logistic regression on an assumed *representative sample gives landslide susceptibility. One model is for those earthquake-induced and one for rainfall-induced. The volume of landslides follows a probability distribution from an inventory and is capped by 'kinematic feasibility'. Our interpretation of all mentioned above is that the quality of results ultimately hinges on the realistic representation of topography. This goes for both the landslide initiation and subsequent runout using kinematic models.*

Generally, this accurately captures the concept of the LSS, LSP and LSD models. However, some clarification is required. Specifically:

1. All primary sediment production occurs as a result of landslides. Primary sediment production differs from sediment transport.

   As described in Section 2.3.1.1:

   > *"We assume that landslides are the sole driver of mass wasting (the initial mobilisation and movement of soil or rock material) on hill slopes where landslides are determined to be kinematically feasible. Landslide-debris production is therefore assumed to be equal to the long-term erosion rate. We derive the long-term erosion rates from a combination of suspended-sediment-yield observations, estimates of soil and rock densities and measures of long-term tectonic uplift and erosion. This is a necessary simplification, and, while observational evidence suggests that landslides dominate mass wasting processes in much of the region, processes such as slope creep, gully formation, glacial erosion or fluvial under-cutting can also contribute to initial movement of soil and rock. Once sediment is mobilised, additional erosion processes (such as gullying and fluvial transport) contribute to the long-term transport of sediment through the landscape."*

2. Sediment availability is correlated with a specific sediment-yield model, which itself has been developed based on observations of suspended sediment yield in rivers. We apply a uniform scaling factor to convert suspended sediment yield to total sediment yield based on a correlation of spatially averaged erosion rates derived from ^{10}Be data from catchments along the range front. Although we find that these also correspond to long-term uplift rates, as well as landslide erosion rates in the same catchments, we are not specifically correlating uplift (such that an area of subsidence may have negative sediment-production rates).

   This is described in Section 2.3.1.1:

   > *"We base our estimation of erosion rates on previous studies quantifying specific sediment yield from hill slopes to rivers across New Zealand, as well as the specific density of geological units mapped throughout the country. This is calibrated against rates of long-term erosion and tectonic uplift."*

3. The 10,000-year factor is simply a numerical adjustment for the modelling. It has little impact on the results.

   This is described in Section A5.1:

   > *"We adopt an integration interval of 10,000 years, reflecting the approximate interval since deglaciation of the region following the Last Glacial Maximum. This effectively ensures that the magnitude of debris deposited in each model run is similar to the scale of post-glacial sedimentary landforms in the region (such as debris-flow fans and incised river channels), enabling modelled runouts to overcome topographic obstacles where sufficient landslide debris is available. While increasing the integration interval is an effective means of reducing the effects of minor topographic features on local flow paths, it has little impact on the overall model output. An increase of two orders of magnitude (from 0.1 to 10 kyr), for example, decreased the mean annual debris flux in a sample region by <1% while increasing the proportional area affected by debris flux by 2.7% (see Section A5.6 for further details)."*

4. We agree, the realistic interpretation of topography has a fundamental influence on calculated LDF and LDIR. This is a fundamental dataset for the study.

   This is discussed in Section A4.8:

   > *"We assume that the topography in the DEM is an accurate representation of the ground surface. The 8 m DEM is derived from the January 2012 Land Information New Zealand (LINZ) Topo50 20 m contours, which largely reflect topography digitised from 1940 aerial photographs. We have down-sampled this data to 25 m resolution for the purposes of this regional study. The DEM therefore likely under-represents the smaller landforms (less than approximately 100,000 m^2), and smaller landslide source areas may therefore not be identified …"*

   and Section 2.4.2:

   > *"Aside from uncertainties associated with previously discussed LSS and LSP model inputs, landslide-debris flux outputs are a function of … (3) the DEM used to simulate the runout paths."*

   > *"As landforms represented by the DEM determine the travel path of landslide debris, inaccuracies resulting from (for example) topographic changes since the original elevation data were generated in the 1940s (see Section 2.3.1.2), digital noise, interpolation errors or failure to accurately resolve landforms with lesser spatial extents can significantly change the travel path of debris sourced from smaller landslides. Smoothing of the DEM to improve runout-model performance for larger landslides mitigates much of the uncertainty associated with this input data (see Section A5.3.1 for further details). The accuracy of the national DEM employed here is estimated to generate spatial uncertainties of more than 6× the most likely APLR, while the 25 m resolution of the regional study is expected to generate uncertainties greater than 4× the most likely result. These two factors are the largest single source of uncertainty in this study, and care must therefore be taken when interpreting results (for example) in locations subject to inundation by smaller landslides, down-slope or smaller landforms (<100,000 m^2) or where topographic changes may significantly alter the path of landslide debris runout. See Sections A7.4 and A7.6.2 for further discussion on DEM-related LSD model uncertainties, as well as mitigation strategies involving the use of up-to-date LiDAR datasets."*

This is important to state because this means the resolution used in the analyses, the DEM quality and possible resampling techniques should be well thought out. We understand the authors are obliged to use a generalisable elevation model so a description of the quality and the degree of feature preservation at a resolution of 25 and 32 m is vital. Specifically related to this is the computation of slope angle with resolution. A smooth down-sampled DEM reduces slope angle depending on the method used. This could affect landslide susceptibility as it is based on a slope threshold …

These are fair points. The susceptibility model is trained on DEM data at the same resolution as the model is applied. As such, the specific gradient values are somewhat irrelevant, as we employ a statistical rather than physical approach. Although this is a possible source of error, the error is captured in the uncertainty estimates of the earthquake- and rainfall-induced landslide models.

In Section A3.6, we note:

> *"The model is trained on a 32 x 32 m grid of pixels containing landslide scars. This neither represents the exact number, nor exact area, of mapped landslides in the dataset. The uncertainty associated with calculating either of these two fundamental metrics from the rainfall-induced landslide output is dependent on grid resolution, landslide-area characteristics and landslide clustering in the landscape. Currently, this uncertainty is only constrained with respect to the training dataset; elsewhere, it is unconstrained."*

... and likely the 'kinematic feasibility' (see further below). To summarise, the authors should state clearly the quality of the DEM and its derivatives and if possible, conduct and present a sensitivity analysis for various DEM resolutions.

In terms of capturing the kinematic feasibility, this is also a possible source of error. However, we note that kinematic feasibility is not entirely necessary, as in Section A4.2:

> *"Shallow failures originating from soil or weathered bedrock may initiate on hill slopes with gradients less than that assumed for the kinematic model. In order to capture these features, we assigned a depth of failure equivalent to a Class 1 landslide to all cells not already classified with a surface gradient of more than θ_{NAT} (see Figure A4.3)."*

That said, we now note the impact of DEM resolution on model uncertainties:

In Section 3.2:

> *"The down-slope movement of landslide debris is the principal hazard considered in this study, and, as such, uncertainties associated with factors controlling the potential size of landslides and long-term landslide debris-production rates have some of the greatest impacts on modelled APLR. These uncertainties include those associated with determining kinematic feasibility and deriving long-term debris-production rates, quantifying variability across the landscape (e.g. due to recent erosion, excavation or rejuvenation of existing creeping landslides) and forecasting the impact of climate change on future fracturing, weathering and erosion rates. Associated individual variable uncertainties can cause variations in the calculated APLR of up to about 2× the most likely value or more, depending on the scale of the landform, its history of modification or instability and the location of elements at risk."*

Section A4.8:

> *"We assume that the topography in the DEM is an accurate representation of the ground surface ... The DEM therefore likely under-represents the smaller landforms (less than approximately 100,000 m^2), and smaller landslide source areas may therefore not be identified ..."*

Section 5.5:

> *"The effect of locally increasing the resolution of landslide-debris-flux and APLR predictions is particularly easy to test, and an example is presented for the Greymouth area in Figure A7.4 (see Section A7.6.2). Increasing the resolution of the LSP and LSD models can provide better representation of potential landslide sources and improve the tracking of potential landslide-debris-inundation paths. This is most relevant for locations close to hill slopes, down-slope of landforms with spatial extents less than 100,000 m^2 and areas of subtle channelisation. Incorporation of a higher-resolution topographic model may result in both increases and decreases in APLR, depending on the scale and variability of local landforms and their representation in the DEM. However, we overall find that reducing from 25 m to 8 m resolution and employing a recent LiDAR-derived DEM can be expected to reduce the mean APLR by approximately 3.4×, while also reducing 2-sigma (95th percentile) uncertainties from ±2.75 to ±1.0 order of magnitude (see Section A7.7)."*

Section 6:

> *"Residual uncertainties vary spatially and increase with distance from landslide sources. These are particularly large in areas adjacent to topography with spatial extents less than 100,000 m^2."*

We now include a full quantitative assessment of spatial uncertainties associated with the DEM accuracy and model resolution in Section A7.6.2.

Landslide Source Susceptibility [LSS]

We don't quite get whether the return interval for RIL or EIL is lower. First the text explicitly states: "For example, the predicted mean annual RIL probability in the Kokiraki area is approximately 0.30 kyr^{-1}, while the mean annual EIL probability in the same area is approximately 0.10 kyr^{-1}". But then: "higher probabilities of landsliding for the shortest return interval events will result in a larger proportion of debris being assigned to earthquake-triggered events,". Further, we don't understand whether and why EIL are larger. Is it because the rarer occurrence in susceptible areas makes for more sediment availability or because of the superimposed size distribution from the inventory? This is generally an interesting point that should be stated and compared to research more clearly. For example, research by de Vilder et al. (2023) for the Kaikoura district indicates that RIL dominate the risk profile. If you conclude EIL is dominant on the West Coast, we're curious for a discussion on the difference.

The relative importance of earthquake- or rainfall-induced landslides varies spatially, based on the estimated PGAs or 24-hour rain amounts for the given ARIs used. This can be observed by comparing rainfall- and earthquake-induced probability in Figure 2.2d, e.

This is discussed in Section 2.2.2:

> *"Mean annual rainfall- and earthquake-induced landslide probabilities, as well as total annual probabilities of landslide initiation, are presented in Figure 2.2. Overall, the LSS model indicates that the greatest earthquake- and rainfall-induced landslide probabilities are in areas with steep topography, primarily in the region between Fox Glacier and Kokiraki. Relative probabilities for the two triggers vary across the study region, with rainfall-induced landslide probabilities being generally higher along the Southern Alps and earthquake-induced landslide probabilities being higher in the north of the region. Overall, mean annual rainfall-induced landslide probabilities are more variable, with maximum values commonly an order of magnitude greater than earthquake-induced landslide probabilities at the same location."*

Regarding the proportion of debris assigned as a result of LSS outputs, this is discussed in the LSP model (Section 2.3.1.4). However, we discuss potential implications in Section 2.2.2:

> *"The LSS model probabilities for rainfall- and earthquake-induced landslides determine how landslide-sediment production is distributed across the LSD model runout simulations (described in Section 2.3). While these probabilities do not affect the total amount of debris produced in a given cell, they do influence how debris is allocated across 112 individual runout simulations in the LSD model (described in Section 2.4). These simulations represent various combinations of landslide triggers, return intervals and landslide-size classes."*

Regarding the use of aspect (page 71). Including it as 0 to 360 is not a good application in regression because it's circular and not a gradient. Rather use Northerness and Easterness, the cosine and sine of aspect respectively.

This is a good point, and we agree that aspect can be circular rather than a gradient. Aspect control on landslide susceptibility was initially checked using the frequency-ratio method. The frequency ratio is the relative frequency of grid cells that are affected by landslides (Y = 1) and their associated factors (e.g. aspect), compared with the relative frequency of cells that are not landslides (Y = 0), within the given factor. All grid cells within each GeolCode grouping were used in these analyses. The frequency-ratio results showed that aspects in the north to east orientations – at the lower end of the aspect gradient (0–60°) – were found to be most susceptible to landslides.

To investigate whether using a circular versus gradient approach had any statistical importance in the LR regressions, we re-ran the LR models adopting the cosine and sine approach. Overall, the results were similar, with either a minor decrease or increase in the overall model performance (AUC and R^2) – for each GeolCode – when compared to the original corresponding model results. These results are thought to be because: (1) aspect has a relatively small statistical significance in the models compared to the other factors; and (2) the landslide susceptible aspects – based on the datasets used – represent a gradient, noting that this may not be the same for other landslide datasets. Given these results, it was decided to keep the original model results.

Performance is measured using AUC and R^2. It is not clear to us how they are related to the landslide inventory. If they are all based on the inventory points, what are the control, i.e. landslide absence points? If you use every cell in the study area you are inflating the accuracy.

The landslide absence points are the Y = 0 grid cells, used in each 'bootstrap' sample. For model training, LR models were fitted to the data (grid cells) in each bootstrap sample (each sample comprised 75% of the data), randomly taken from each GeolCode-specific dataset. A total of 100 bootstrap samples were taken from each GeolCode-specific dataset. The best-fit models were then used to calculate the AUC and R^2 of each LR model. The values presented represent the mean values based on the results from all 100 models.

Landslide Sediment Production [LSP]

In nature, landslide size is constrained on the low end by the ratio between mass (increasing with volume) to passive earth pressure (cross-sectional area dependent). The high-end is constrained by landscape heterogeneity (paraphrased from Milledge et al. 2014). We don't fully understand the approach the authors take to landslide dimensions. Especially the often mentioned 'kinematic constraints' and specifically the background to Figure A5.7a are not apparent? The authors need to be clearer in their methods here.

This is clarified in Section A4.2:

> *"Identification of potential landslide-source areas was based on an analysis of landscape morphology, with the intention of determining the greatest kinematically feasible landslide-volume classes within the digital elevation model (DEM).*
>
> *Our kinematic landslide source model allows us to estimate the largest hypothetical landslide that can occur at a given location based on an assumption of basic material-strength parameters (friction and cohesion) and an assessment of required geometric freedom through an analysis of local topography. The purpose of this step is not to evaluate slope stability but rather to define geometric constraints for the largest potential landslide sources. Therefore, we do not explicitly calculate the balance of driving and resisting forces for each hypothetical source.*
>
> *We then assume that smaller landslides are able to occur anywhere that larger ones can occur. This is a notable simplification, as present-day local topography may have insufficient relief to support the generation of smaller landslides at some locations within a larger landslide body. However, given that (1) larger landslides can only occur on slopes with average gradients in excess of an assumed critical-failure angle (and mean slope angles must therefore equal or exceed this angle) and (2) failure of these slopes may occur progressively (such that future topography may support smaller failures where it is not currently possible), we suggest that this simplification is reasonable for a regional analysis."*

The fixed relationship between volume and area (and hence depth) of a landslide does not do justice to the constraints mentioned above and to complex local soil depth variation. While we agree with the necessary simplification, we think the authors should state this shortcoming more explicitly.

Technically, yes, we agree – although many studies adopt landslide area-volume relationships with one or two parameters and no consideration for non-linearity or spatial variability. However, in our study, the area-volume relationship is tied to cohesion. In this case, we have added the following statements:

In Section A4.2, we state:

> *"As discussed here, cohesive strength is highly dependent on the type of materials present and their physical condition (compaction, weathering, fracture density, etc.). These properties tend to vary with depth from the surface, and landslide area-volume relationships should therefore theoretically also vary with increasing depth from the surface. Although we currently have no data to better constrain this relationship in the study area, explicitly accounting for spatially variable, depth-dependent cohesion values could reduce uncertainties in the landslide-debris flux and annual property loss risk (APLR) datasets. Further discussion regarding selection of the cohesive strength and associated uncertainties can be found in Section A7.3."*

In Section 5.5, we state:

> *"Better characterising landslide-source geometries. In particular, explicitly accounting for spatially variable, depth-dependent cohesion and friction estimates based on geological data."*

In Section A4.8, we state:

> *"We assume that the adopted cohesion is spatially consistent and invariant with landslide volume. In reality, this is likely to vary with rock or soil strengths. Varying the cohesion will alter the distribution of the maximum feasible landslide volumes. A lower cohesion will bias sediment production toward lower volume and more frequent landslide classes."*

In Section A7.3, we state:

> *"Selecting a higher cohesive strength affects landslide-debris-inundation modelling in two opposing ways:*
>
> - *It increases the theoretical mean depth associated with each landslide volume-class range (Equation A4.3).*
> - *It increases potential failure volumes by steepening the gradient of scarps within hypothetical landslide sources (Equation A4.5).*
>
> *While these two effects might initially appear to offset each other, the net impact of increasing cohesive strength is a reduction in the proportion of the landscape capable of supporting larger landslides. This occurs because, while the theoretical mean depth of landslide volume-class ranges is unrestricted, the actual depth achievable is constrained by available excess topography.*
>
> *As a result, a higher cohesive strength increases the proportion (and frequency) of smaller, lower-volume landslides with shorter runout distances. In practical terms, this means:*
>
> - *Landslide risk increases in areas with high excess topography, where smaller landslides become more frequent.*

- *Risk decreases at more distal locations, as fewer large, highly mobile landslides are expected.*

For further details on the LSP model assumptions and uncertainties, see Section A4.8."

As sediment flux is the key output of the model, derivation of source volumes for both RIL and EIL is critical. The total combined source volume for RIL and EIL is determined by the suspended sediment yield estimator of Hicks et al. (2011). It is important for the authors to consider whether or not the sediment gauging records used by Hicks et al. appropriately represent earthquake events, and if they span suitable time periods to capture the time taken for all source material to work through the system. In section 5.1.1 the authors state that the observations in Hicks et al. (2011) almost certainly reflect interseismic sediment production. The model is therefore likely underestimating the total debris flux. If the sediment yield estimator loads can be thought of as not containing EIL loads, are there alternative options to estimate an EIL component, such as a scaling factor or alternative modelling approach that could be used estimate an additional EIL component?

This is now clarified in Section A4.1.1:

"Employing recent observations of river-borne sediment yield or denudation rates through ^{10}Be concentrations can raise questions with respect to the influence of earthquake-induced landslide-sediment contributions. Specifically, (1) are observed rates elevated as a result of recent earthquake-induced landsliding? (2) If these do not include a direct earthquake-induced landslide signal, do observed rates exclude the contribution from earthquake-induced landslides?

Regarding question (1): Observations of lacustrine sedimentation in Lake Ellery immediately to the west of the Alpine Fault indicate that seismically generated sediment may temporarily increase mean erosion rates by ~40% (Howarth et al. 2016). This is supported by seismically generated landslide models from Robinson et al. (2016), who suggested that co-seismic landsliding may increase erosion rates in some catchments by around 35%. Global studies indicate that the period of enhanced landslide-sediment production commonly decays exponentially to background levels over a period of up to seven years, depending on the return interval of the triggering event (Marc et al. 2015; Fan et al. 2018), with the phase of enhanced post-seismic sedimentation (incorporating enhanced instability and sediment transport) lasting on average 58 ± 15 years (Howarth et al. 2016). This reflects a period over which landslide deposits directly connected to river networks become exhausted of readily transportable debris (see Croissant et al. [2019] and references therein). Given that the last earthquake to trigger regional landsliding in the region was the 1968 Inangahua earthquake (>56 years ago), suspended sediment yields observed by Hicks et al. (2011) almost certainly reflect rates of inter-seismic sediment transport. As such, these do not carry the short-term 35–40% increase in sediment output associated with fluvially connected post-seismic landslides and instead reflect more or less constant background rates of undifferentiated (earthquake- and rainfall-induced) landslide debris export via the river network. This is facilitated by a combination of secondary sub-aerial and fluvial processes, modulated by climatic factors (Croissant et al. 2019). We can therefore rule out the possibility that observed rates are elevated as a result of recent earthquake-induced landsliding.

Regarding question (2): Accounting for the relatively modest initial increase in earthquake-induced erosion rates, as well as rapid exponential decay, the associated increase in long-term erosion rates can therefore be expected to be approximately 4% over a 100-year seismic cycle, dropping to roughly 1–1.5% for a 300-year cycle (consistent with Alpine Fault recurrence intervals [Howarth et al. 2016]). These increases are negligible when compared to uncertainties associated with erosion-rate estimates in the study region (discussed later *in this section). We therefore assume that the observed rates represent the combined transport of earthquake- and rainfall-induced landslide debris through secondary sub-aerial and fluvial processes and thereby capture the contribution of both triggers."*

The model also appears to use the gridded sediment yield estimator pixel values to determine source volumes. Is the spatial variability in the grid representative of EIL processes?

This is now discussed in Section A4.8:

> *"We base our estimates of present-day landslide-sediment-production rates on a derivative of rates of specific sediment yield (SSY) presented in Hicks et al. (2011). They report a standard factorial error (SFE) of between 1.55 and 1.8 for the majority of studied catchments, noting that glaciated catchments on the West Coast may be associated with SFEs of ~2–3 (an SFE of 1.8 is equivalent to a geometric standard deviation of 1.8, meaning one 'sigma' on the log scale corresponds to multiplying or dividing by 1.8). The authors recommend against applying the models to predict sediment yields from catchments less than 10 km^2, raising the question of applicability at the local slope scale, as applied here. In this study, we do not expect SSY, and therefore calculated landslide debris-production rates, to accurately represent present-day activity on individual hill slopes across the approximately 25,000 km^2 of the region overseen by WCEM. However, evidence suggesting that the landscape is in a steady state (see Section A4.1.1) and that, on average, denudation rates derived from SSY estimates represent long-term, spatially integrated erosion rates provides confidence that this dataset is adequately capturing regional variability in landslide debris-production rates. That said, we note that uncertainties associated with SSY inputs generate some of the greatest uncertainties in APLR predictions (see Section 8.3), and therefore identify local refinement of the landslide sediment-production models with appropriate local input data as a high priority for local re-evaluation of hazard and risk (see Section 5.5)."*

Landslide Sediment Delivery [LSD, Section 2.4]

GPP is applied for avalanche movements, PCM for flow types. A division of 2/3 avalanche type and 1/3 flow type landslides is mentioned based on data from Cyclone Gabrielle. Is this sampled randomly and assigned to each 'chunk' of available sediment coming down as landslide flux?

For each class size and return interval, we run two models with identical source debris inputs. One for flow and one for avalanche. The outputs are then averaged using the 2/3 to 1/3 ratio for rainfall-induced landslides and 5/6 to 1/6 ratio for earthquake-induced landslides.

Section 2.4.1.4:

> *"In order to calculate the mean annual landslide-debris flux, we added together all calculated debris fluxes for all avalanche- and flow-type models, then applied a weighting to reflect the relative proportion of avalanche- and flow-type movements in the landscape before adding the output of both movement types together (see Section A5.7 for full details)."*

This is also detailed in Equation A5.2.

The PCM model is designed snow avalanches (Perla et al., 1980). Why did you choose this one for flow type landslides? Snow does have different properties than soil/rocks. This should be explicitly stated with one or multiple examples where it is proven this model can be applied to landslides as well.

In Section 2.4.1.2, we note:

> *"The PCM method is commonly used to represent debris-flow-type runouts (e.g. Gamma 1999; Mergili et al. 2012; Goetz et al. 2021)."*

This is expanded upon in Section A5.5.2.

The LSD model is described as allowing deposition of source material to occur along the flow path, yet the primary assumption of the model framework is that inputs and outputs of material from a slope are balanced, and this assumption is used to validate the results. These two points are at odds. As the deposited material appears to remain on slope without subsequent re-entrainment, the sediment load delivered to the stream network must no longer equate to that estimated by Hicks et al. (2011), and fluxes of sediment down the flow path may be underestimated. Are the authors able to quantify what proportion of sediment remains on slope? If material does remain on slope, then the assumption also needs to be made that the data used in Hicks represents net delivery to stream and not the gross erosion from slopes and would need to be scaled to provide gross erosion rates.

We can quantify the sediment that is deposited on hill slopes by the primary landslide movement. However, we do not expect it to stay there long-term, as secondary processes move the debris into the rivers.

This is described in Section 2.1.2:

> *"The landslide-debris-inundation hazard assessment is based on a geomorphologically consistent evaluation of landslide-sediment production and distribution across the region by landslide processes. We consider the volume and rate of landslide initiation to be limited by the rate of debris production on hill slopes (Figure 2.1). Once initiated, landslide debris then travels through the hill-slope system as primary 'runout' (i.e. as debris flows or debris avalanches from the landslide source) and is either directly deposited in river channels, which then flush the sediment from the landscape, or deposited on hill slopes before being moved to river channels by secondary debris-transport processes such as sheet wash, rilling, gullying and other fluvial or glacial mechanisms. These secondary processes are not considered in the current study; however, these play an important role in the geomorphological system, as they act as a buffer between landslide deposits and the river system. As secondary transport processes operate at a more or less constant rate through time (e.g. Croissant et al. 2019), we can expect average rates of sediment transport in rivers, for example, to reflect long-term rates of landslide-debris production in the contributing landscape."*

Landslide Debris Inundation Risk [LDIR, Section 2.5]

The resolution of the modelling at 25m (or 32m depending on the module) is too coarse to model small and median scale landslides in a meaningful way. The highest available regionally consistent resolution is 8m and using this could improvement the quality of the analysis. However, the authors choose the coarser resolution due to computational constraints, which is understandable. After re-reading it is however not clear how small landslides are still included in the analysis as claimed. For example, the class of 40- 100 m^2 house-sized landslides occupy less than 1/5th of a single cell. If, as the authors claim, the centerpoint is key would that mean a whole cell (625 m^2) is considered an active landslide? This would then affect characteristics and runout length. All in all, the authors need to write this part of the methodology more clearly and double check whether small landslides are accurately represented.

This is discussed in A5.3.2:

> *"We employ a temporally integrated scenario-modelling approach to assess runout, accepting that, although we know the spatially distributed long-term average sediment-production rate for each landslide trigger, return interval and volume class, we do not know the specific location of landslides in any given event. Instead, we use M_{GPP} to generate a temporally integrated landslide intensity throughout the landscape and propagate sediment down-slope. A significant benefit of this approach is the ability to model the downslope transport of material from landslide sources nominally smaller than the resolution of the input grid. A single iteration of the GPP model effectively tracks a packet of sediment down-slope from each source cell. Each packet is supplied with a set of rules regarding movement, deposition and stop criteria, whose operation is independent of the volume of sediment being moved down-slope. As such, a large volume of sediment, representing multiple sub-pixel landslide sources, can be moved through the topography while obeying rules consistent with a smaller-sized landslide. Although the implementation of this method prevents the capture of specific landslide physics (primarily those associated with momentum and internal interactions, e.g. super elevation and block sliding), it allows us to capture probabilistic debris transport from small landslides across a wide region."*

Miscellaneous

Comparisons of contemporary and long-term degradation rates should be reported in proportional terms as well as absolute terms, as the small units (mm/yr) can be misleading.

Reporting of units has now been adjusted for consistency.

Certain references (see commented report) include links that don't work. For transparency these should be addressed.

All references have now been checked for consistency.

Frequently the manuscript reads wordy. It is understandable as it is challenging to correctly describe many interdependent assumptions on complex processes. A critical check for conciseness could nonetheless improve quality of the manuscript. Specific sections are commented on in the attached manuscript.

The manuscript has now been edited for conciseness.

References

Milledge D G, Bellugi D, McKean J A, Densmore A L, & Dietrich W E 2014. A multidimensional stability model for predicting shallow landslide size and shape across landscapes. Journal of Geophysical Research: Earth Surface, 119(11), 2481-2504.

Perla R, Cheng T T, McClung D M 1980. A two–parameter model of snow–avalanche motion. Journal of Glaciology, 26(94), 197-207.

de Vilder S, Massey C, Brideau, M, Lukovic B, Morgenstern R, Townsend D, Rosser B 2023. Including the impact of climate change in quantitative risk analysis: example Kaikoura, New Zealand.

With kind regards,

Feiko van Zadelhoff
Andrew Neverman

earthsciences.nz